UNIVERSITY OF SOUTHAMPTON

FACULTY OF NATURAL AND ENVIRONMENTAL SCIENCES

SCHOOL OF CHEMISTRY

Transient Studies at Microelectrodes

by

Samuel C. Perry

Thesis for the degree of Doctor of Philosophy

October 2015

UNIVERSITY OF SOUTHAMPTON

ABSTRACT

FACULTY OF NATURAL AND ENVIRONMENTAL SCIENCES
SCHOOL OF CHEMISTRY

Doctor of Philosophy

TRANSIENT STUDIES AT MICROELECTRODES

by Samuel C. Perry

Transient studies of electrochemical systems at microelectrodes allow analysis under rapid mass transport conditions. The small active area allows rapid resolution of charging currents, giving access to meaningful information even at short times. Sampled current voltammetry at microelectrodes (MSCV) is a multistep technique whereby data is collected from a series of potential step experiments along the redox wave of interest. Varying the sampling time allows comparison of how a reaction proceeds at varying timescales, whilst simultaneously showing the potential dependence. Selection of an appropriate sampling time tunes the rate of mass transport to give quasireversible conditions, allowing facile kinetic analysis using quasireversible models. Application to the oxygen reduction reaction (ORR) revealed unreasonably large currents at short times. This work suggests that pre-adsorbed oxygen at the electrode surface is responsible. The presence of the pre-adsorbed oxygen was confirmed by its direct reduction in argon purged solution, and its strong dependence on the metal substrate. The resultant peak potentials were used to calculate the binding energies of varying metals towards oxygen (ΔG_O), which are in excellent agreement with the literature. This is useful, as ΔG_O is a popular descriptor for oxygen reduction activity. Once the pre-adsorbed oxygen is consumed, MSCVs for the ORR can be used for standard kinetic analysis using Tafel or Koutecky-Levich analyses, with the advantage of the electrode being oxide free before each data point is recorded.

Contents

List of Tables

List of Figures

List of Equations

Declaration of Authorship

I, Samuel C. Perry, declare that the thesis entitled *Transient Studies at Microelectrodes* and the work presented in the thesis are both my own, and have been generated by me as the result of my own original research. I confirm that:

- this work was done wholly or mainly while in candidature for a research degree at this University;
- where any part of this thesis has previously been submitted for a degree or any other qualification at this University or any other institution, this has been clearly stated;
- where I have consulted the published work of others,this is always clearly attributed;
- where I have quoted from the work of others, the source is always given. With the exception of such quotations, this thesis is entirely my own work;
- I have acknowledged all main sources of help;
- where the thesis is based on work done by myself jointly with others, I have made clear exactly what was done by others and what I have contributed myself;
- parts of this work have been published as:
  - S. C. Perry, L. M. Al Shandoudi, G Denuault; *Anal. Chem.*, **2014**, *86*, 9917-9923.
  - S. C. Perry, G. Denuault; *Phys. Chem. Chem. Phys.*, **2015**, *17*, 30005-30012.

Signed:.....

Date:.....

Acknowledgements

I would like to take this opportunity to thank Dr Guy Denuault for all of his help and guidance through all aspects of this work, from the initial conceptualisation of ideas right through to guiding my first experiences of scientific writing. Also to all group members past and present, including but not limited to Mara, Nawal, Laila, Aziz, Ana and Saiful for all of their discussions and feedback. Last but by no means least a huge thank you too all of my family, especially my wife Sam, for their constant support and encouragement for all aspects of this work, from successful experiments through to broken electrodes.

List of Parameters

Symbol	Name	Units
A	Electrode geometric area	cm^2
A_{echem}	Electrochemically active surface area	cm^2
a	Electrode radius	cm
$a_{O,R}$	Activity of oxidised or reduced species	
α	Transfer coefficient for an electrochemical reaction	
α	Free energy of activation for a diffusing cation	J mol^{-1}
b	Gradient of a Tafel slope	V
β	Free energy of activation for a diffusing anion	J mol^{-1}
C	Capacitance of an electrode	F cm^{-2}
C_{dl}	Double layer capacitance	F
c	Concentration	mol cm^{-3}
γ	Free energy of activation for diffusing water	J mol^{-1}
D	Diffusion coefficient	cm^2 s^{-1}
d	Distance between SECM tip and substrate	cm
E	Applied potential	V
E^0	Standard electrode potential	V
E_e	Equilibrium potential	V
E_X	Thermodynamic potential for reaction 'X'	V
ΔE_O	Binding energy of oxygen	eV
E_p	Peak potential from voltammetry	V
F	Faraday's constant	C mol^{-1}
$\Delta G^0_{\ddagger}$	Standard free energy of activation	J mol^{-1}
$\Delta G^{\ddagger}_e$	Free energy of transition state	J mol^{-1}
ΔG_O	Theoretical Gibbs energy of oxygen adsorption from DFT	J mol^{-1}
ΔG_{peak}	Experimentally determined Gibbs energy of oxygen adsorption	J mol^{-1}
h	Planck's constant	J s
i	Current	A

Symbol	Name	Units
I	Current Density	A cm^{-2}
I_0	Exchange current density	A cm^{-2}
i_{ads}	Current from the reduction of pre-adsorbed O_2	A
i_b	Recorded current from background processes	A
i_C	Charging current	A
i_{exp}	Experimentally measured current	A
i_k	Kinetically controlled current	A
i_L	Mass transport limited current	A
i_{O_2}	Current from the reduction of pre-adsorbed O_2	A
i_{theo}	Mass transport limited current from a theoretical model	A
θ_{O_2}	Number of monolayers of adsorbed O_2	
j	Flux to an electrode	mol cm^{-2} s^{-1}
K	Dimensionless kinetic parameter k_s / k_m	
$K^{\ddagger}$	Surface pre-equilibrium constant for electron transfer	
k^0	Standard electrochemical rate constant	cm s^{-1}
k_B	Boltzmann's constant	J K^{-1}
k_m	Rate of mass transfer to an electrode	cm s^{-1}
k_f	Rate constant for the forward reaction	cm s^{-1}
k_s	Rate of electron transfer	cm s^{-1}
κ	Solution conductivity	Ω^{-1} cm^{-1}
κ_{el}	Transmission coefficient for electron transfer	
L	Normalised tip-substrate distance for SECM	
M_i	Formula mass of species i	g mol^{-1}
m	Number of moles	mol
μ	Solution viscosity	g m^{-1} s^{-1}
n	Number of electrons transferred	
ν	Scan rate in voltammetry	V s^{-1}
ν	Kinematic viscosity of a solution	cm^2 s^{-1}
ν_s	Frequency of ligand reorganisation	s^{-1}

Symbol	Name	Units
N_A	Avogadro's constant	mol^{-1}
N_X	Number of adsorption sites on surface 'X'	
N_{O_2}	Number of adsorption sites for dioxygen	
P_t	Barometric pressure	atm
P_{O_2}	Partial pressure of O_2	atm
p	Vapour pressure of water	atm
Q	Charge density	C cm^{-2}
$Q_{ads,step}$	Charge density from reduction of pre-adsorbed O_2 by reductive step method	C cm^{-2}
$Q_{ads,sub}$	Charge density from reduction of pre-adsorbed O_2 by the subtraction method	C cm^{-2}
$Q_{ads,sweep}$	Charge density from reduction of pre-adsorbed O_2 by reductive sweep method	C cm^{-2}
R	Ideal gas constant	J K^{-1} mol^{-1}
R_f	Roughness factor	
r_g	Radius of glass around the metal of the electrode	cm
r_{max}	Radius of the solution domain for simulations	cm
R_u	Uncompensated solution resistance	Ω
ρ	Density of a solution	g cm^{-3}
T	Temperature	K
t	Time	s
τ	Sampling time	s
τ	Characteristic time for resolution of charging currents	s
τ_{factor}	Correction factor for timescales used in regression analyses	
V	Volume of solution	dm^{-3}
V_m	Molar volume	cm^3 mol^{-1}
X_D	Diffuse layer thickness	cm
x	Distance between working electrode and Luggin capillary	cm
x	Distance between the electrode and the edge of the diffuse layer	cm

Symbol	Name	Units
x_+	Mole fraction of a cation in solution	
x_-	Mole fraction of an anion in solution	
z_{max}	Height of solution above domain floor for simulations	cm
z_{ede}	Height of electrode above domain floor for simulations	cm
ω	Rotation rate for rotating disc electrodes	Hz

List of Abbreviations

Abbreviation	Meaning
CE	Counter electrode
CV	Cyclic voltammetry
DFT	Density functional theory
EELS	Low energy electron loss spectroscopy
EQCM	Electrochemical quartz crystal microbalance
MSCV	Sampled current voltammetry at microelectrodes
O	Oxidised species
OCP	Open circuit potential
OER	Oxygen evolution reaction
ORR	Oxygen reduction reaction
R	Reduced species
RDE	Rotating disc electrode
RE	Reference electrode
RHE	Reversible hydrogen electrode
SCE	Saturated calomel electrode
SCV	Sampled current voltammetry
SECM	Scanning electrochemical microscopy
SECCM	Scanning electrochemical cell microscopy
SEM	Scanning electron microscope
SHE	Standard hydrogen electrode
SMSE	Saturated mercury mercurous sulfate electrode
UPS	Ultraviolet photoemission spectroscopy
WE	Working electrode

1 Introduction

1.1 Structure of the introduction

The work presented in this report will focus on the study of electrochemical systems under transient conditions; that is at sufficiently short sampling times to give rapid rates of mass transport, in order to reveal previously hidden information. As such, the introduction will focus on the theory and techniques associated with transient electrochemistry.

Section 1.2 will look at the kinetics of redox processes, linking the measured current with applied potential and flux to the electrode surface, in order to show how varying the acquisition conditions of an experiment will affect the kinetic regime of the studied system. This will form the basis of the study of kinetic parameters in Chapter 4, as well as help understand the difference between diffusion controlled redox reaction and the redox reaction of adsorbed surface species, which will be key in Chapter 5.

Section 1.3 gives a summary of voltammetric techniques. This will comprise of both novel techniques proposed and used throughout this work, as well as a description of more commonly used techniques in order to provide a comparison. Common uses and practical limitations are discussed in each case in order to emphasise the usefulness of the proposed techniques in all results sections.

Section 1.4 will present the theory associated with electrochemistry at microelectrodes. The structure and diffusion profile will be discussed in comparison with larger planar electrodes, and the advantages of the small active area in terms of recorded data will be discussed. These differences will be essential in understanding the motivation behind the development of the techniques presented in all research sections, as well as explaining why such data would not be accessible at a larger electrode.

Section 1.5 provides details for the oxygen reduction reaction. This shall first cover the elementary steps of the reaction, as well as a summary of alternate mechanistic routes that

have been proposed. The importance of the adsorption of oxygen in the mechanism will be discussed, which shall be important in explaining the data here presented in Chapter 5. A summary of common materials for oxygen reduction catalysts will then be presented, including a brief discussion on the varying diagnostic criteria used for the determination of effective catalytic materials. The final section will then give a summary of the main research aims of this work, as well as giving a summary of the structure of the report.

1.2 Kinetics in electrochemistry

Electrochemistry can be broadly defined as the study of reactions involving the transfer of a charged species across an interface; most commonly at an electrode - electrolyte interface. The progress of a reaction can be monitored by the perturbation in the measured current. The current recorded at the working electrode is therefore a measure of the rate of reaction at the electrode surface, which is related to the flux of oxidisable or reducible species to said electrode (j). The flux itself is determined by the the rate of diffusion of the redox active species and its concentration gradient at the surface of the electrode, according to Fick's first law.

$$I = nFj = -nFD\left(\frac{\mathrm{d}c}{\mathrm{d}x}\right)_{x=0} \tag{1.1}$$

Equation 1.1: *Current density at an electrode (I) from the number of electrons transferred (n), Faraday's constant (F), the flux to an electrode (j), diffusion coefficient (D), and the concentration gradient at the electrode surface (dc/dx).*

The environment at an electrode surface is never static, rather it is in a state of dynamic equilibrium. At a point of zero current, rates of oxidation and reduction at the electrode are equal, giving a net zero flux to the electrode. This is the so called equilibrium potential (E_e). Application of a potential gradient across the interface may be used to shift the equilibrium in a specific direction, with more positive potentials favouring oxidation, and more negative potentials favouring reduction. The equilibrium potential is dependent

on the ratio of oxidised and reduced species at the electrode surface, as determined by the Nernst equation.

$$E_e = E_e^0 + \frac{RT}{nF} \ln \left[\frac{a_O}{a_R} \right] \tag{1.2}$$

Equation 1.2: *Nernst equation for the calculation of the equilibrium potential (E_e) from the standard equilibrium potential (E_e^0), ideal gas constant (R), temperature (T), number of electrons transferred (n), Faraday's constant (F), and the activities of the oxidised (a_O) and reduced species (a_R).*

The rate of a single electrochemical reaction in any given system is determined by both the kinetic rate constant of that system (k), and the concentration of the species present in the reaction media (c). The driving force for an electrochemical reaction at the electrode surface is dependent on the potential gradient across the electrode-solution interface, and so the relative rates of the forward and reverse reactions are dependent on the electrode potential. The potential difference needed to drive the reaction is dependent on the nature of the oxidised and reduced species involved in said reaction. For example, many oxidation or reduction reactions result in a change in the coordination environment of the redox species. This may be subtle, such as a slight change in metal-ligand bond length. Any change in bond length is due to the change in the charge on the central metal ion. The key behaviour is that the coordination shell remains intact throughout the redox process, and electron transfer occurs across empty space. This is known as an outer sphere electron transfer, and is very fast.

Alternatively, the redox reaction may result in a complete change in the geometry of the species involved. It is also possible that the redox species may need to directly bind to the electrode surface for electron transfer to proceed. This is known as inner sphere electron transfer, and is considerably slower. This is due to the movement of electrons being orders of magnitude faster than nuclear motion. Any molecular reorganisation will considerably slow the rate of electron transfer, with bond breaking or forming being considerably slower still than simple changes in bond length. The degree of reorganisation of a species during a redox process is therefore a good indication as to how facile the reaction will be. This is well illustrated by the difference in the rate of electron transfer

for different iron complexes, which are dependent on the solvent environment. Fe-H_2O bonds for aqueous Fe^{II} are longer than for Fe^{III} (2.08 Å compared to 1.96 Å[1]) due the the greater positive charge on the metal ion. The necessity of this change in bond length for electron transfer results in a slow rate constant for electron self exchange of 4 mol^{-1} dm^3 s^{-1}. However, for the ferricyanide-ferrocyanide redox couple, the length of both species are much closer in size (1.93 Å[2] and 1.91 Å[3] respectively), leading to a much faster rate of self exchange of 300 mol^{-1} dm^3 s^{-1} [4].

As electrochemical systems exist in a dynamic equilibrium, the direction of the overall reaction is determined by the relative stabilities of the reduced and oxidised species. These are made more of less stable around the electrode depending on the potential difference across the electrode. A positive potential means the oxidised species is more stable, and therefore drives the oxidation reaction. The transfer coefficient (α) is a measure of how sensitive the transition state is to changes in the potential difference. It is a number between 0 and 1, most commonly close to 0.5. In this way α is a key parameter when it comes to the kinetics of electrochemical systems. Another key parameter is the standard electrochemical rate constant. This is a measure of the speed of electron transfer, and is dependent on a number of factors, according to Equation 1.3.

$$k^0 = K^{\ddagger}\nu_s\kappa_{el}\exp\left\{\frac{-\Delta G_e^{\ddagger}}{RT}\right\} \tag{1.3}$$

Equation 1.3: *Standard electrochemical rate constant (k^0) from the surface pre-equilibrium constant ($K^{\ddagger}$), the frequency of ligand reorganisation (ν_s), the free energy of the transition state ($\Delta G_e^{\ddagger}$), the transmission coefficient (κ_{el}), the ideal gas constant (R) and the temperature (T).*

The free energy of the transition state ($\Delta G_e^{\ddagger}$) comes from the relative stabilities of the oxidised and reduced species. The frequency of reorganisation (ν_s) comes from the need for the solvent sphere or ligands to reorganise on electron transfer, due to the change in charge on the species in question. This is orders of magnitude slower than the physical movement of electrons, and so is a limiting factor when it comes to the rate of electron transfer. Combining terms for the rate of electron transfer and the nature of the transition

state allows a complete expression for the rate of an electrochemical reaction, taking into account the nature of the species involved and the potential difference applied.

$$k_f = k^0 \exp\left\{\frac{-\alpha n F(E - E_e^0)}{RT}\right\} \tag{1.4}$$

Equation 1.4: *Rate constant for an electrochemical reduction (k_f) from the standard electrochemical rate constant (k^0), Faraday's constant (F), the applied potential (E), the standard potential (E_e^0), the transfer coefficient (α), the ideal gas constant (R) and the temperature (T).*

Combining the relative contributions of the forward and backward reactions allows the expression of the net current density of a real electrochemical system according to the Butler-Volmer equation.

$$I = I_0\left\{\exp\left(\frac{(1-\alpha)nF\eta}{RT}\right) - \exp\left(\frac{-\alpha n F\eta}{RT}\right)\right\} \tag{1.5}$$

Equation 1.5: *Butler-Volmer equation for the net current density of an electrochemical reaction (I) from the transfer coefficient (α), the number of electrons transferred (n), Faraday's constant (F), ideal gas constant (R), temperature (T), the overpotential (η, given by $E - E_e$) and the exchange current density (I_0).*

The Butler-Volmer equation therefore provides a means to elucidate kinetic information of a redox active system. A plot of $\ln(I)$ against η allows α to be calculated from the gradient, and I_0 from the intercept of the linear region with zero overpotential. I_0 can then be used to find the standard electrochemical rate constant through Equation 1.6.

$$I_0 = nFk^0 c_O^{1-\alpha} c_R^{\alpha} \tag{1.6}$$

Equation 1.6: *Exchange current (I_0) from the standard electrochemical rate constant (k^0), the transfer coefficient (α), the number of electrons transferred (n), Faraday's constant (F), and the concentrations of oxidised (c_O), and reduced species in solution (c_R).*

These concepts will all be further discussed in Chapter 4, where the kinetic parameters will be determined from a novel voltammetric technique.

1.3 Voltammetry

1.3.1 Typical electrochemical cell design

Most electrochemical cells are based around a three electrode system, as shown in Figure 1.1.

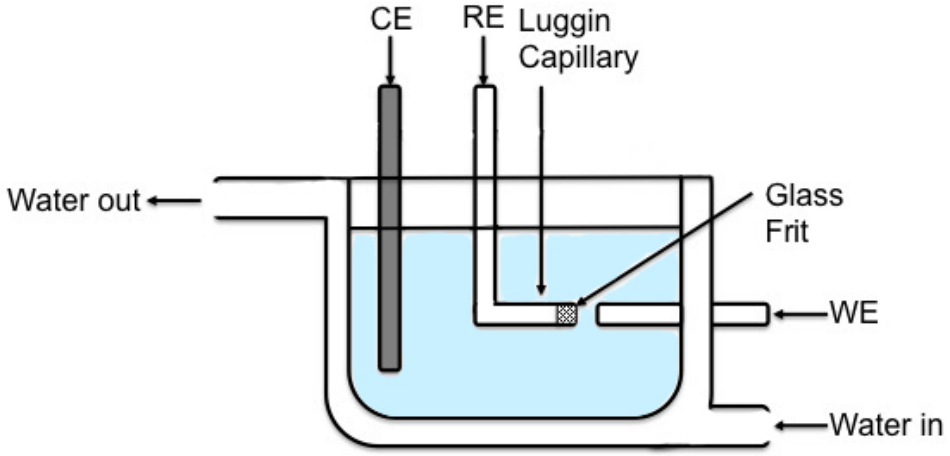

Figure 1.1: *Typical three electrode cell design featuring a working electrode (WE), reference electrode (CE) reference electrode (RE) and luggin capillary. The cell used is a jacketed cell, which allows the external flow of water from a thermostatically controlled water bath, giving reliable temperature control.*

The working electrode is the electrode that performs electrochemistry on the system of interest. The materials vary hugely across electrochemistry. Platinum and glassy carbon are two of the most common, but many conductors and semiconductors can be used depending on the research aims.

The reference electrode provides a standard for measuring the potential difference applied to the working electrode. The standard hydrogen electrode (SHE) is the universal standard for reference electrodes, and is obtained by bubbling hydrogen gas over platinum metal in 1 M acid solution.

$$\mathrm{H^+ + e^- \rightleftharpoons \frac{1}{2}H_2} \qquad E = 0.0\ \mathrm{V} \tag{1.7}$$

Equation 1.7: *Established equilibrium at a SHE reference electrode.*

Clearly having a constant stream of hydrogen gas in an experimental set up is not desirable, so a number of other reference electrodes are more commonly used in everyday practice. These commonly use an established equilibrium between solid metal and a metal salt, such as the equilibrium between silver and silver chloride (Ag/AgCl), mercury and mercurous chloride (SCE), or mercury and mercurous sulphate (SMSE).

$$\mathrm{AgCl} + \mathrm{e}^- \rightleftharpoons \mathrm{Ag} + \mathrm{Cl}^- \qquad E = \mathrm{SHE} + 0.199\ \mathrm{V} \tag{1.8a}$$

$$\frac{1}{2}\mathrm{Hg_2Cl_2} + \mathrm{e}^- \rightleftharpoons \mathrm{Hg} + \mathrm{Cl}^- \qquad E = \mathrm{SHE} + 0.244\ \mathrm{V} \tag{1.8b}$$

$$\frac{1}{2}\mathrm{Hg_2SO_4} + \mathrm{e}^- \rightleftharpoons \mathrm{Hg} + \frac{1}{2}\mathrm{SO_4^{2-}} \qquad E = \mathrm{SHE} + 0.640\ \mathrm{V} \tag{1.8c}$$

Equation 1.8: *Half cell reactions for the Ag/AgCl, SCE and SMSE reference electrodes, along with their potentials vs. SHE.*

As long as the salt solution in which they are contained is saturated, they provide a well established and reliable potential that can be used as a reference. The reference electrode is brought into the close proximity to the working electrode via a Luggin capillary. This reduction in distance is necessary to reduce the iR drop in the cell, caused by the uncompensated solution resistance.

$$R_u = \frac{x}{\kappa A} \tag{1.9}$$

Equation 1.9: *Uncompensated solution resistance (R_u) from the distance between the working electrode and Luggin capillary (x), electrode area (A) and solution conductivity (κ).*

The iR drop is an artefact of solution resistance that acts to distort the data recorded, and is proportional to the distance between the working and reference electrodes[5]. Equation 1.10 gives the iR drop during a chronoamperometric response at a large planar electrode. The origin of the current term comes from the Cottrell equation, which shall be discussed in Section 1.3.2.

$$iR_u \approx \frac{nFAD^{1/2}c}{\pi^{1/2}t^{1/2}} \frac{x}{\kappa A} \tag{1.10}$$

Equation 1.10: *iR drop at an electrode from the number of electrons transferred (n), Faraday's constant (F), electrode area (A), diffusion coefficient (D), concentration (c), time (t), distance between the working electrode and Luggin capillary (x), and solution conductivity (κ).*

The counter electrode is there to carry out the opposite reaction to the working electrode. This maintains charge neutrality in the cell. Counter electrodes are therefore chosen to have a larger surface area than that of the working electrode. This ensures that the current density on the counter is much lower than on the working, so that the overall current reflects the redox reaction on the working, rather than on the counter. Carbon rods and platinum gauze are popular choices.

1.3.2 Chronoamperometry

Chronoamperometry is a potential step experiment. It is typically performed by starting from a solution containing only one part of the redox couple in question, say the oxidised form O, although chronoamperometry with both species present is also possible. The electrode is polarised so that the potential difference corresponds to a net current of zero. According to Equation 1.1 this means the concentration gradient at the electrode surface must be zero, and so the concentration of O at the surface is equal to the concentration in bulk solution. The potential is then stepped to one where the reduction of O is under diffusion control.

This potential step causes O at the surface of the electrode to be consumed. This generates a steep concentration gradient at the electrode surface, and thus gives a large current response. As this potential is maintained, O diffuses towards the surface down the concentration gradient, whilst R diffuses away from the surface into the bulk. The area where O is actively moving towards the electrode surface down a concentration gradient is known as the diffusion layer. The thickness of this layer is known as the characteristic

distance ($X_D(t)$), and is dependent on the diffusion coefficient of the species involved, and the time at which it is measured, as given by Equation 1.11.

$$X_D(t) = \sqrt{\pi D t} \tag{1.11}$$

Equation 1.11: *Characteristic distance* ($X_D(t)$) *from the number of electrons transferred* (n), *diffusion coefficient* (D) *and time observed* (t).

As time goes on and more O is consumed, the concentration of O close to the electrode surface is less than that of the bulk for an increasingly large distance from the electrode surface. The concentration gradient at the electrode surface is therefore decreasing as the diffusion layer of the electrode expands, as is shown in Figure 1.2.

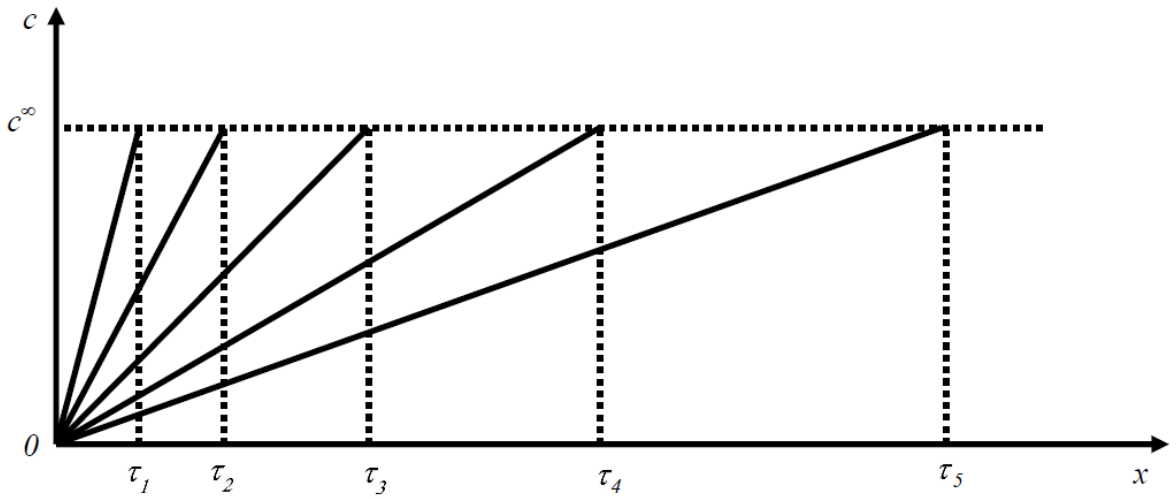

Figure 1.2: *Schematic representation of the concentration profiles of a reducible species, showing the change in concentration* (c), *vs. coordinate* (x) *as time* (τ) *increases from* τ_1 *to* τ_5, *showing the concentration gradient from zero at the electrode surface, to the bulk concentration* (c^∞) *at the edge of the diffusion layer.*

The continually decreasing concentration gradient means that the current recorded during the chronoamperogram is also decreasing. This gives the characteristic current response for a potential step experiment. The measured current is initially large, which then initially reduces at a rapid rate as the diffusion layer expands and the concentration gradient decreases. As the diffusion layer continues to expand the gradient decreases at a slower rate, and so the current also decreases at a slower rate. This continues until

the concentration gradient is decreasing at a sufficiently slow rate to make it appear that the current has levelled off, although a closer inspection would show a slight continual reduction in the measured current. When the potential is stepped back to the starting potential the opposite reaction is driven, where the previously generated R is oxidised to O. This results in a positive current, which decays to zero once all R in close proximity to the electrode surface has been consumed. These features can be seen in Figure 1.3.

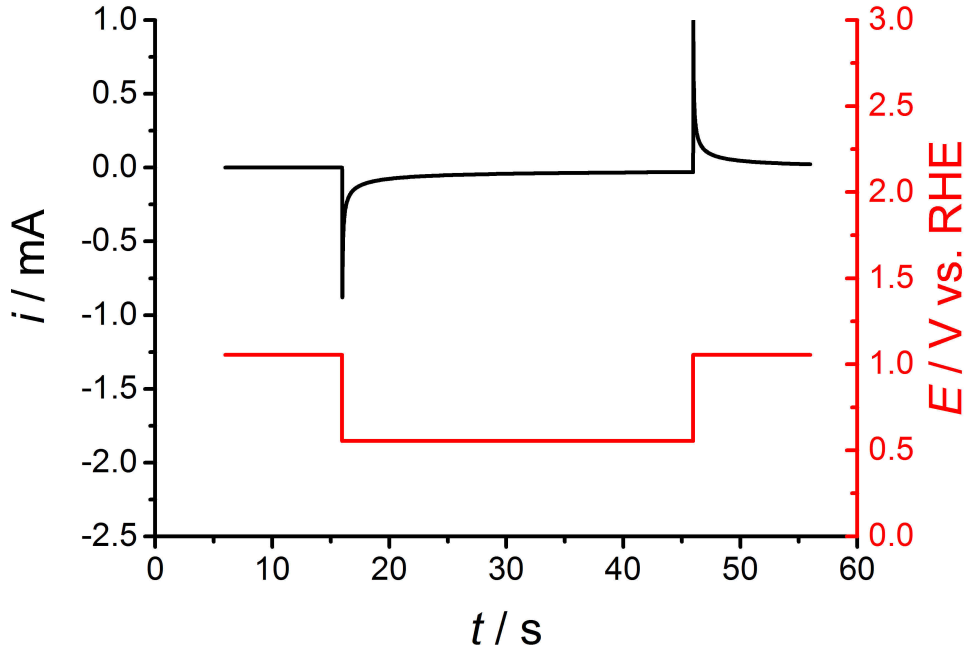

Figure 1.3: *Potential step for 5 mM $K_3Fe(CN)_6$ in 0.5 M KCl at a 5 mm diameter Pt electrode.*

The concentration gradient at the surface of the electrode is dependent on the diffusion coefficient of the species involved and the time at which it is being measured. Therefore, the current is also dependent on these parameters, following Equation 1.1. During the potential step the surface concentration of O is zero. This means that the concentration gradient at the electrode surface is essentially the bulk concentration of O divided by the characteristic diffusion distance at a given time. Substitution of this equivalence into Equation 1.1 allows the expression of the current during a chronoamperogram purely in terms of easily measurable parameters, known as the Cottrell equation.

$$|i| = \frac{nFAD^{1/2}c^{\infty}}{\pi^{1/2}t^{1/2}} \tag{1.12}$$

Equation 1.12: *Cottrell equation for the current at a planar electrode during a chronoamperogram (i) from the number of electrons transferred (n), Faraday's constant (F), electrode area (A), bulk concentration (c^{∞}) and the time (t).*

The current from the Cottrell equation will be a measure of the entire Faradaic current. However, it will not be the only current measured during a potential step experiment. There is also a significant contribution from the capacitance of the electrode being used. At the onset of the potential step, the surface of the electrode becomes charged. The scale of this capacitance is given by Equation 1.13.

$$C_{dl} \approx \pi a^2 R_f C \tag{1.13}$$

Equation 1.13: *Approximate capacitance of the double layer at an electrode (C_{dl}), from the electrode radius (a), capacitance of the electrode (C) and the roughness factor (R_f).*

When this happens in the presence of charged species in solution the metal/solution interface acts like a capacitor, as oppositely charged ions are attracted to the electrode surface. This generates a flux to the electrode, which in turn produces a capacitive current. The flux is made up of all species in solution, mostly the charged electrolyte. This should not affect the mass transport of the redox active species, so long as the electrolyte concentration is sufficiently large. The magnitude of this current is given by Equation 1.14[5].

$$i_C = \frac{E}{R_u} \exp\left\{\frac{-t}{R_u C_{dl}}\right\} \tag{1.14}$$

Equation 1.14: *Charging current during a chronoamperogram (i_C) from the applied potential (E), uncompensated resistance (R_u), sampling time (t), and the double layer capacitance (C_{dl}).*

Equation 1.14 shows how the charging current decreases exponentially with time. This means that on the short time scale after the onset of the potential step, there is a significant contribution to the measured current from the charging current. After a certain amount of time has passed the charging current will become negligible, and so the measured current

is due to the Faradaic processes at the electrode surface. The characteristic time for the charging current at a large planar electrode is given by Equation 1.15.

$$\tau \approx R_u C_{dl} \approx \frac{R_f C x}{\kappa} \tag{1.15}$$

Equation 1.15: *Characteristic time for the charging current during a chronoamperogram (τ) from the uncompensated resistance (R_u), double layer capacitance (C_{dl}), roughness factor (R_f), electrode capacitance (C), distance between the working electrode and Luggin capillary (x) and solution conductivity (κ).*

Equation 1.15 shows how the time taken to resolve the capacitive current is independent of the electrode area, but can be reduced by increasing the conductivity of solution, or more simply by reducing the distance between the Luggin capillary and the working electrode. As a general rule, when $t < \tau$, the charging current is greater than the Faradaic current. In order to guarantee the sole recording of Faradaic information with little of no contribution from the charging current, the sampling time must be greater than 3τ. The charging current at $t = 3\tau$ is approximately equal to 5 % of the charging current at $t = 0$ s[5]. This can be seen by the crossover in charging and Faradaic currents in Figure 1.4.

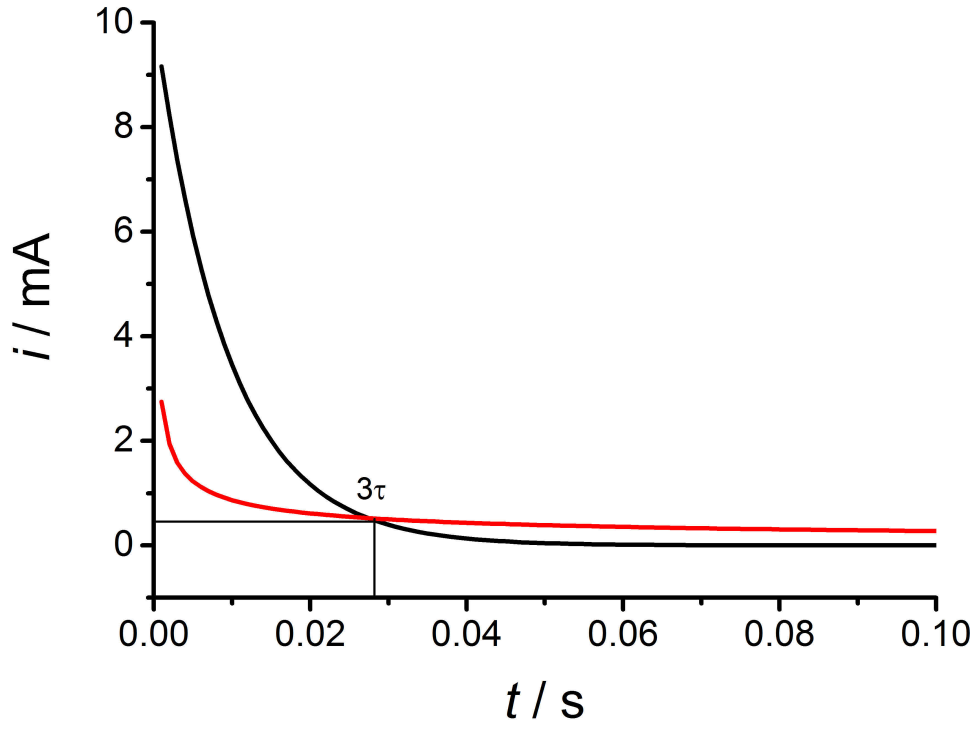

Figure 1.4: *Schematic plot of charging current (i_C, black) and Faradaic current (i, red) against time (t) during a potential step, showing how the Faradaic current is masked by the charging current until $t = 3\tau$.*

1.3.3 Cyclic voltammetry

In cyclic voltammetry the potential is swept backwards and forwards between predefined limits at a specified scan rate (ν). Plots of current vs. potential give information about redox active species both in solution and at the electrode surface. Cyclic voltammograms for a simple, single electron redox species in solution at a large planar electrode give a characteristic twin peak shape, as is seen in Figure 1.5.

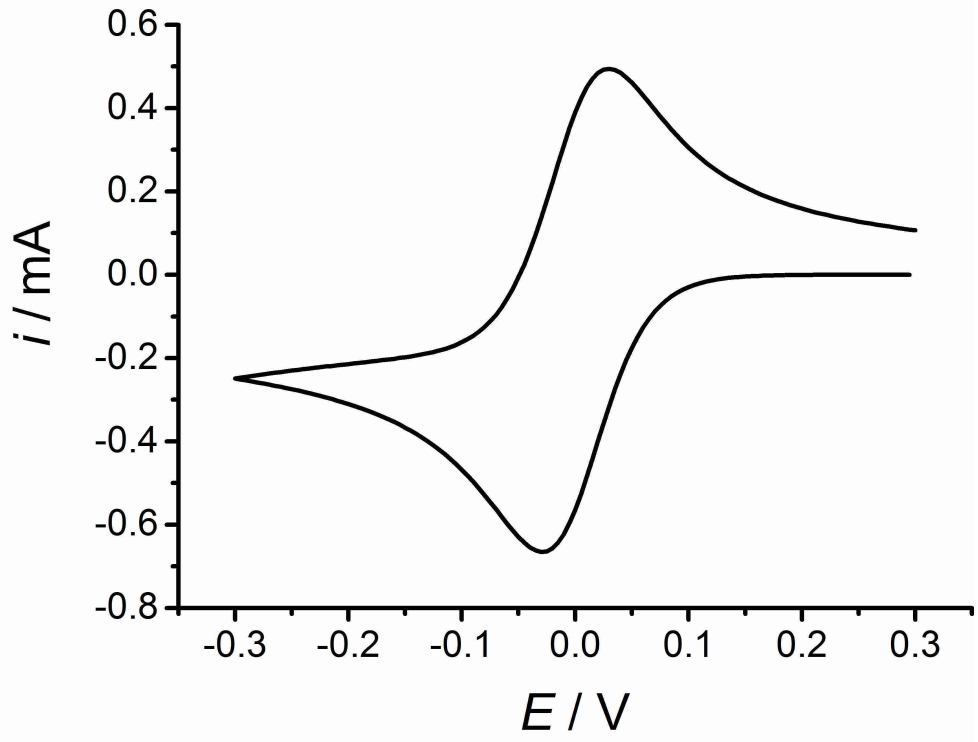

Figure 1.5: *Cyclic voltammogram for a single electron redox process at a large planar electrode, where a = 0.5 cm, E^0 = 0.0 V, c = 1 mM, ν = 1 V s^{-1}, and D = 1 × 10^{-5} cm^2 s^{-1} simulated using the DigiElch simulation package.*

The shape of the voltammogram shown can be explained in terms of the constantly evolving concentration gradient at the electrode surface. This example takes a large planar electrode in a solution containing only the oxidised species of a redox couple (O). At the start of the CV, there is not enough of a potential difference at the electrode solution interface to drive the reduction reaction, and so the concentration of O at the electrode surface is equal to that in the bulk. The concentration gradient is zero, and so the measured

current is also zero. As the potential is ramped more negative, O at the electrode surface is consumed and a concentration gradient is established, generating a current. As the potential difference is increased, the gradient increases and so does the current. This continues until a maximum concentration gradient is achieved, corresponding to the peak in the CV. After a further increase in overpotential, the surface concentration of O reaches zero. Further reduction of O leads to an extension of the diffusion field into the bulk solution, causing a decrease in concentration gradient, and therefore a decrease in current. The magnitude of the peak current is proportional to the square root of the scan rate, as given by the Randles-Ševčik equation.

$$i_p = 2.69 \times 10^5 n^{3/2} A D^{1/2} c \nu^{1/2} \tag{1.16}$$

Equation 1.16: *Peak current at 298 K in A (i_p) from the number of electrons transferred (n), electrode area in cm^2 (A), diffusion coefficient in $cm^2\ s^{-1}$ (D), concentration in mol cm^{-3} (c) and the scan rate in $V\ s^{-1}$ (ν). 2.69×10^5 is a contant that applies when the given units are used.*

In this way, a plot of i_p against $\nu^{1/2}$ is a common, simple way of determining the diffusion coefficient for a reversible redox couple. It is also possible to learn a lot about the reversibility of the redox system. The degree of reversibility is determined by the relative magnitudes of the rate of mass transport, as given by the mass transfer coefficient (k_m), and the rate of electron transfer (k_s), according to table 1.1

Table 1.1: *Degree of reversibility from the ratio of the rate of mass transport (k_m) to the rate of electron transfer (k_s).*

k_m **vs.** k_s	**Reversibility**
$k_s > k_m \times 10$	Reversible
$k_s \approx k_m$	Quasireversible
$10 \times k_s < k_m$	Irreversible

The degree of reversibility indicates how much kinetic information is apparent in the slope of the voltammogram. For a reversible system, the rate of electron transfer is so rapid that the wave contains no apparent kinetic information. At the surface of the electrode,

the Nernst equation (Equation 1.2) will apply. The degree of reversibility will therefore be independent of potential, and so will be reflected in the whole of the voltammogram. For quasireversible or irreversible systems the rate of electron transfer is sufficiently slow for the wave to reveal kinetic information. An irreversible system essentially means that a greater driving force is needed to give a Faradaic response. This means that an increasing degree of irreversibility is observed in a cyclic voltammogram as an apparent stretching of the voltammogram, with the peaks being shifted to a greater overpotential, as can be seen in Figure 1.6.

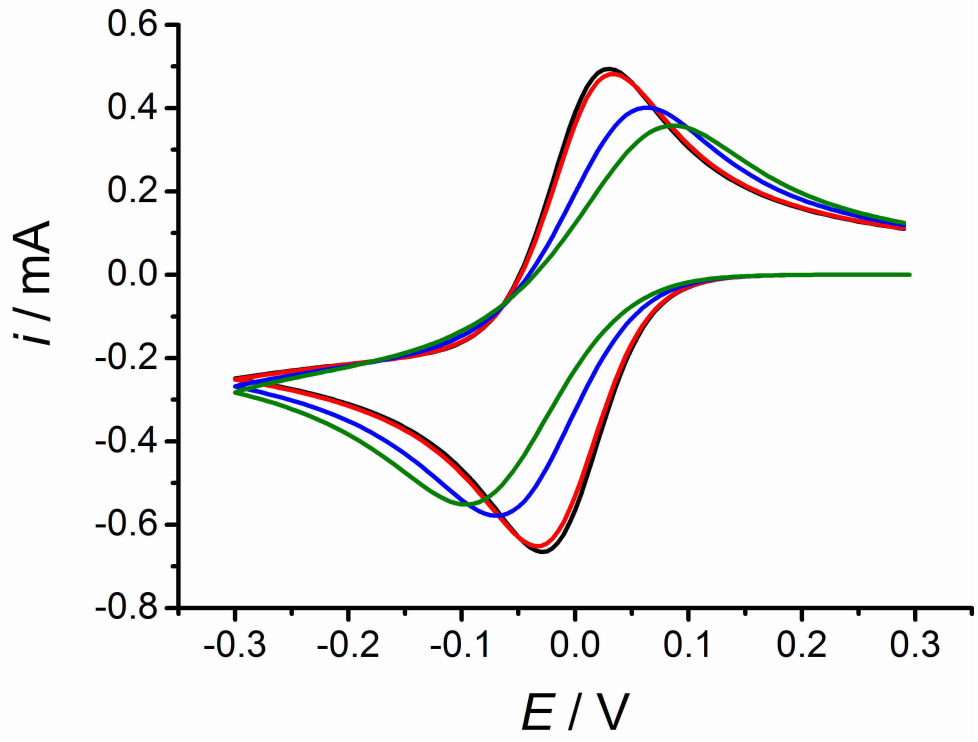

Figure 1.6: *Cyclic voltammograms for a single electron redox process at a large planar electrode, where* $a = 0.5$ *cm,* $E^0 = 0.0$ *V,* $c = 1$ *mM,* $\nu = 1$ *V* s^{-1}*, and* $D = 1 \times 10^{-5}$ cm^2 s^{-1} *simulated using the DigiElch simulation package, showing the decrease in peak separation and increase in peak current as the standard heterogeneous rate constant is increased from 0.005 cm* s^{-1} *(green), to 0.01 cm* s^{-1} *(blue), to 0.05 cm* s^{-1} *(red) to 0.1 cm* s^{-1} *(black).*

As such, the separation between peaks in a cyclic is a simple measure of the reversibility of the system. A fully reversible system would have a peak separation of 59/n mV, with a greater separation indicating a more irreversible system. As the system becomes more irreversible, the peak potential separation (ΔE_p) will continually increase. However, a

fully irreversible system is indicated by the difference between the peak potential and the half peak potential ($|E_p$ - $E_{p/2}|$) is now given by $48/\alpha$n mV at 298 K. The peak potentials also become a function of scan rate, as given by Equation 1.17 [6]

$$E_p = E^0 - \frac{RT}{\alpha nF}\left[0.78 - \ln\left(\frac{D^{1/2}}{k^0}\right) + 0.5\ln\left(\frac{\alpha nF\nu}{RT}\right)\right] \tag{1.17}$$

Equation 1.17: *Peak potential for an irreversible redox system (E_p) from the standard potential (E^0), ideal gas constant (R), temperature (T), transfer coefficient (α), number of electrons transferred (n), Faraday's constant (F), standard electrochemical rate constant (k^0), diffusion coefficient (D), and the scan rate (ν).*

The peak current in the irreversible case is still proportional to the square root of the scan rate, but the kinetic limitation on the system now adds a proportionality to the transfer coefficient as well.

$$i_p = 2.99 \times 10^5 n(n\alpha)^{1/2} AD^{1/2} c\nu^{1/2} \tag{1.18}$$

Equation 1.18: *Peak current at 298 K in A (i_p) from the number of electrons transferred (n), transfer coefficient (α), electrode area in cm^2 (A), diffusion coefficient in $cm^2\ s^{-1}$ (D), concentration in mol cm^{-3} (c) and the scan rate in V s^{-1} (ν). 2.69×10^5 is a contant that applies when the given units are used.*

It is therefore possible to find kinetic parameters k^0 and α using Equations 1.17 - 1.18. A plot of i_p vs. $\nu^{1/2}$ will give α in the gradient, then parameters can be simply entered into Equation 1.17 to give k^0. It is worth noting that the calculation for the peak current of an irreversible system may only be accurate for the forward scan. The rapid mass transport in relation to the rate of electron transfer would lead to a significant amount of material generated during the forward scan being lost into the bulk solution before it may be oxidised in the reverse sweep. This leads to a decrease in the size of the reverse peak, or even a loss of the reverse peak entirely if the kinetics are sufficiently slow.

In the quasireversible system the situation is more complicated, as the current receives significant contributions from both kinetic and mass transport effects. Nicholson was able to show that the balance between mass transport and kinetic control allows for a simplistic expression of the peak separation as a function of a dimensionless parameter ψ [7].

$$\psi = \frac{(D_O/D_R)^{\alpha/2} k^0}{(\pi D_O \nu F/RT)^{1/2}} \tag{1.19}$$

Equation 1.19: *Dimensionless kinetic parameter (ψ) diffusion coefficients of the oxidised (D_O) and reduced species (D_R), transfer coefficient (α), standard electrochemical rate constant (k^0), scan rate (ν), Faraday's constant (F), ideal gas constant (R) and temperature (T).*

Numerous textbooks provide a data table whereby a user can look up their measured ΔE_p and read off the corresponding value for ψ, which can then be used to calculate k^0 [5,8]. An alternative method is to find an expression that allows for the approximation of ψ from experimental ΔE_p values. There are a number of possibilities in the literature, with varying degrees of accuracy [9–12]. Equation 1.20 shows the model that is used in this work.

$$\Delta E_p = 0.08314 \text{ V} - \frac{0.00306 \text{ V}}{\psi} - \frac{0.149 \text{ V}}{\psi^{1/2}} - \frac{0.1445 \text{ V}}{\psi^{1/3}} \tag{1.20}$$

Equation 1.20: *Suggested model for the approximation of ψ from experimental values of ΔE_p from Siraj et al.[12].*

With the aid of this model, it is therefore possible to calculate values for k^0 and α simply via a non-linear regression analysis of ψ vs. $\nu^{-1/2}$. ψ would be calculated for multiple peak separations that were measured from cyclic voltammograms of varying scan rates. Calculation of ψ by this method has the advantage that a true experimental peak separations can be used, rather than having to round to the nearest tabulated value.

It is important to consider the sources of error in this method. Probably the most significant is that the method assumes no contribution to ΔE_p from factors such as iR drop. Cyclic voltammograms are sensitive to the resistance of the solution in the cell. An increase in the resistance results in a greater potential needed to generate the same current, according to Ohm's law. This leads to the peak current being shifted away from the equilibrium potential as a greater overpotential is needed to reach the maximum surface concentration gradient, as can be seen in Figure 1.7.

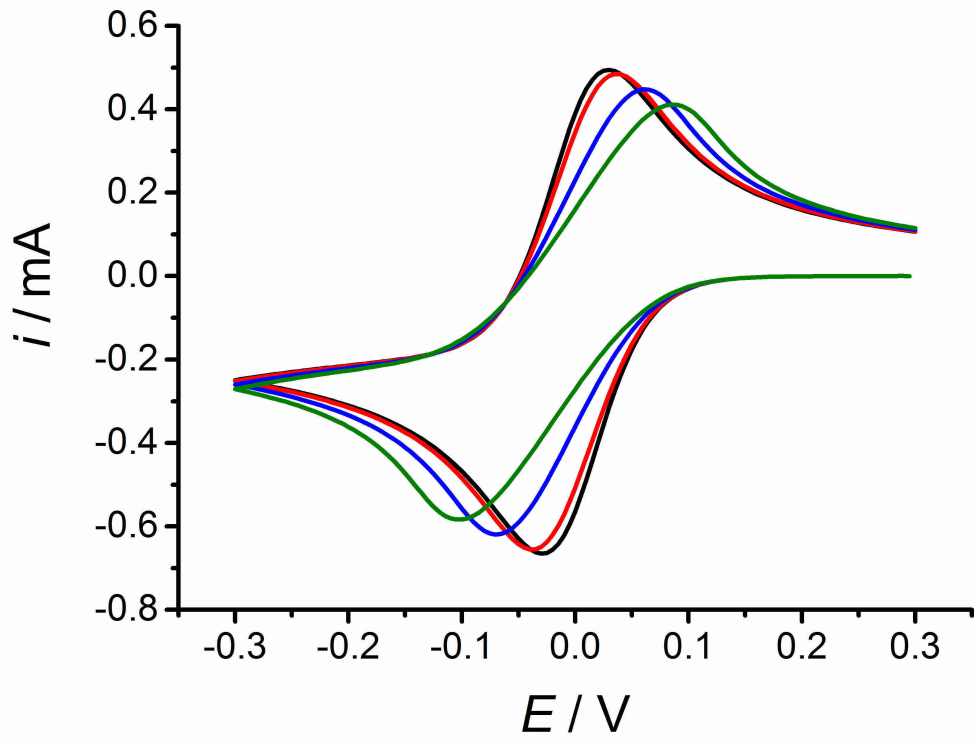

Figure 1.7: *Cyclic voltammograms for a single electron redox process at a large planar electrode, where* $a = 0.5$ *cm,* $E^0 = 0.0$ *V,* $c = 1$ *mM,* $\nu = 1$ *V* s^{-1}*, and* $D = 1 \times 10^{-5}$ cm^2 s^{-1} *simulated using the DigiElch simulation package, showing the increase in peak separation and drop in peak current as the resistance is increased from 0* Ω *(black), to 0.01* Ω *(red), to 0.05* Ω *(blue) to 0.1* Ω *(green).*

The effects can usually be minimised with the use of a relatively concentrated electrolyte and a Luggin capillary, but some shifting of the peaks may still be present despite best efforts. This makes measuring peak separation such that ΔE_p is entirely due to kinetic effects experimentally challenging, and fairly unlikely. Any values gained by this method would certainly need to be corroborated with a second method, such as a digital simulation.

As well as being affected by the resistance of the system, the shape of a cyclic voltammogram will also be altered by the capacitance of the electrode in use, as was previously discussed for chronoamperometry in Section 1.3.2. The resolution of the charging current however is different to that of chronoamperometry due to the cyclic nature of the process. The charging current observed is now proportional not only to the time at which it is measured, but also to the scan rate of the voltammogram. Considering

a sweep from a low potential (E_1) to a higher potential (E_2), the charging current is given by Equation 1.21.

$$i_C = \nu C_{dl} + \left[\left(\frac{E_1}{R_s} - \nu C_{dl}\right)\exp\left(\frac{-t}{R_s C_{dl}}\right)\right] \tag{1.21}$$

Equation 1.21: *Charging current in a cyclic voltammogram (i_C) from the scan rate (ν), starting potential of the sweep (E_1), uncompensated resistance (R_u), double layer capacitance (C_{dl}), and time after the onset of the sweep (t).*

As with chronoamperometry, the charging current is decreasing with time during the sweep. As the sweep direction is changed from the forward to the reverse scan, the sign of ν is changed from positive to negative. This results in the charging current changing sign from positive to negative as well. This gives the recognisable charging current rectangular shape about the x axis. The charging current is also a function of the scan rate. A faster scan rate causes a more rapid perturbation in the potential difference at the electrode surface, which therefore generates a larger charging current response.

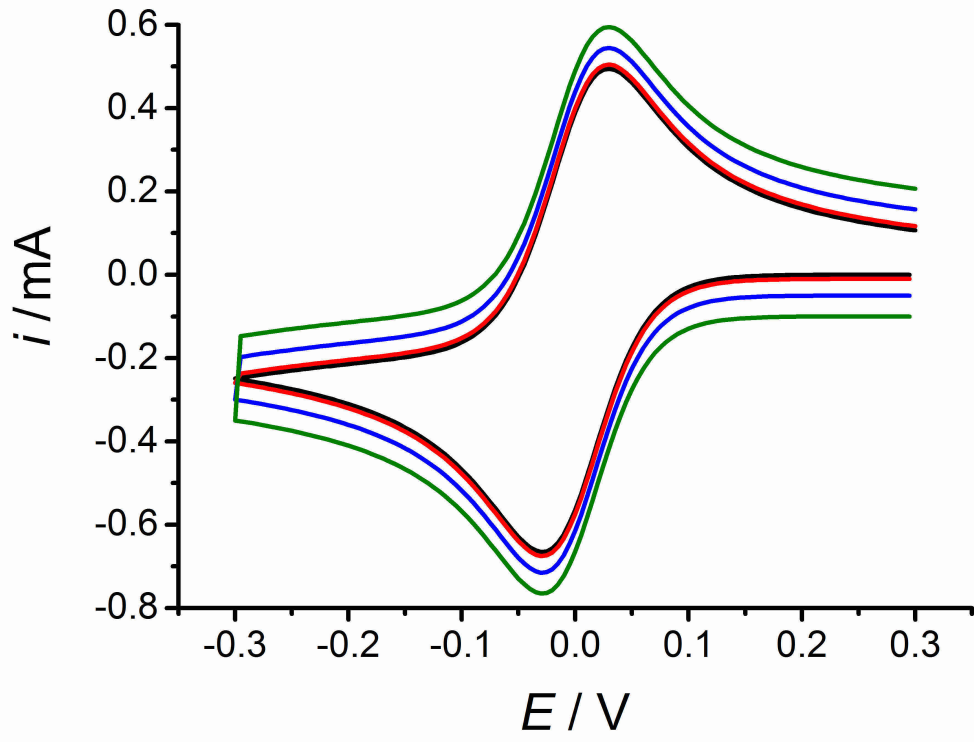

Figure 1.8: *Cyclic voltammograms for a single electron redox process at a large planar electrode, where a = 0.5 cm, E^0 = 0.0 V, c = 1 mM, ν = 1 V s^{-1}, and D = 1 × 10^{-5} cm^2 s^{-1} simulated using the DigiElch simulation package, showing the increase in peak current and thickening of the double layer region as the capacitance is increased from 0 mF (black) to 20 mF (red), 50 mF (blue) and 100 mF (green).*

In the absence of a reducible species in solution, it is possible to electrochemically observe processes occurring at the electrode surface. A well known example is the cyclic voltammogram of polycrystalline platinum electrodes in deaerated sulfuric acid electrolyte.

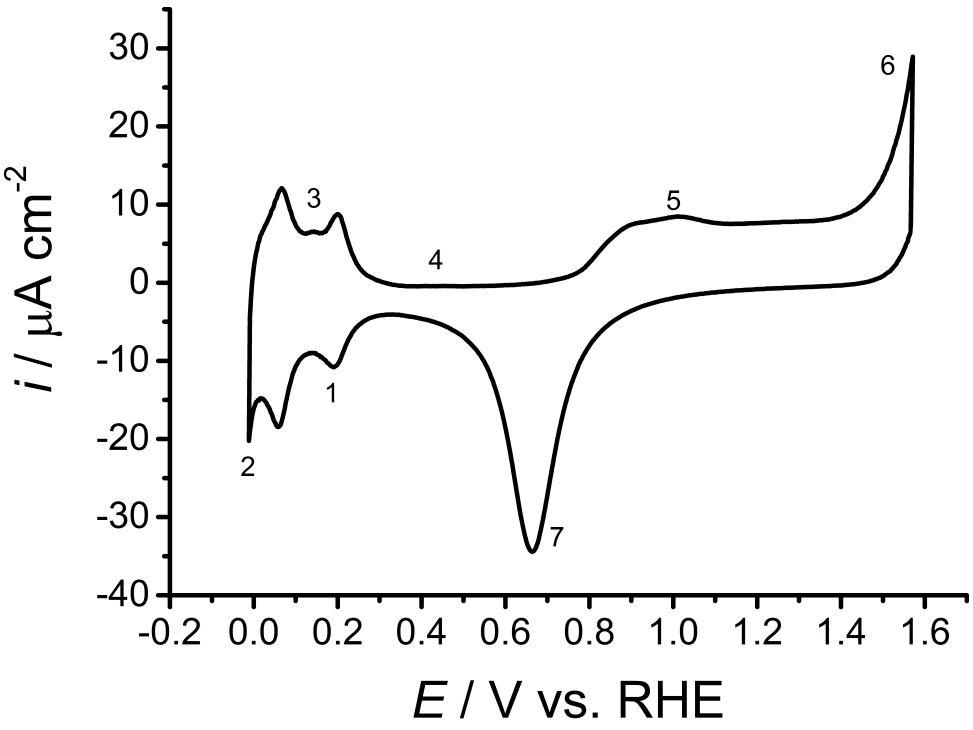

Figure 1.9: *Cyclic voltammogram recorded at a 10 mm diameter Pt electrode in 1 M H_2SO_4, ν = 20 mV s^{-1}, that has been deoxygenated with Ar gas for 20 min. The numbered regions show hydrogen adsorption (1), hydrogen evolution (2), hydrogen stripping (3), double layer region (4), oxide formation (5), oxygen evolution (6) and oxide stripping (7).*

The acid CV of platinum shows a number of distinct regions that give clear indication of the reactions occurring at the electrode surface. Starting from the bottom left quadrant, labelled "1", this region is due to the adsorption of hydrogen onto the electrode surface by the Volmer mechanism.

$$\mathrm{Pt} + \mathrm{H^+} + \mathrm{e^-} \rightarrow \mathrm{Pt - H^{\bullet}_{ads}} \tag{1.22}$$

Equation 1.22: *Adsorption of hydrogen onto a platinum electrode surface.*

There can clearly been seen to be two distinct peaks for the adsorption of hydrogen onto the electrode, which correspond to two distinct strengths of hydrogen adsorption.

The more positive peak corresponds to stronger adsorption and the more negative peak corresponds to weakly adsorbed hydrogen. These peaks are strongly surface dependent, with their positions being dependent on the crystallographic orientation of the platinum surface. As the potential is made more negative, the onset of a sudden increase in current is seen, labelled "2". This corresponds to the evolution of hydrogen gas, as hydrogen atoms adsorbed on neighbouring sites combine and are released as molecular hydrogen by the Tafel mechanism[13].

$$Pt - H^{\bullet}_{ads} + Pt - H^{\bullet}_{ads} \rightarrow H_2 \tag{1.23}$$

Equation 1.23: *Direct evolution of hydrogen from a platinum electrode surface.*

Alternatively a single adsorbed proton may form hydrogen gas through combination with an aqueous proton as it is reduced, as described by the Heyrovsky mechanism[14].

$$Pt - H^{\bullet}_{ads} + H^{+} + e^{-} \rightarrow H_2 \tag{1.24}$$

Equation 1.24: *Reductive evolution of hydrogen from a platinum electrode surface.*

The evolution of hydrogen from the platinum surface requires a reasonably large coverage with hydrogen in order to increase the likelihood of two adsorbed species being next to each other. The process itself is passive, as the required electrons are transferred during the adsorption stage and the electrons needed for bonding are already present.

Directly above in the upper left quadrant, labelled "3", are two symmetrical peaks at positive currents. These peaks correspond to the stripping of the hydrogen that had been adsorbed in the lower left quadrant. The peaks are fairly symmetrical, indicating the reversibility of hydrogen adsorption and desorption.

The thin region in the centre of the plot, labelled "4", is known as the double layer region. This is an area where no reduction of oxidation is occurring at the surface. What is observed is a small capacitive current due to the charging of the electrode surface with ionic species, due to the potential bias at the electrode surface.

In the upper right hand quadrant, labelled "5", is the oxide formation region. Rather than a simple adsorption of singular atoms on the metal electrode, the oxide formation is complex, and forms a number of phases. The initial formation takes place via the oxidative adsorption of water onto the metal surface[15].

$$Pt + H_2O \rightarrow Pt - OH + H^+ + e^- \qquad E = 0.85 \text{ - } 1.10 \text{ V vs. RHE} \qquad (1.25)$$

Equation 1.25: *Formation of platinum oxide* $(Pt - OH)$ *via the oxidative adsorption of water onto the electrode surface.*

As the coverage of OH at the surface increases, repulsion between adsorbed oxygen atoms increases the enthalpy for the formation of the adsorbed layer. As the coverage increases further, the enthalpy for the formation of further adsorbed species becomes greater than the formation of a bulk metal oxide. Above this specific coverage, oxygen atoms will give a metal oxide[16]. This occurs via a place exchange reaction from PtOH in the surface to HOPt as a bulk oxide[17]. A full coverage of OH is achieved at around 1.1 V vs. RHE[18]. Above this potential the formation of bulk PtO oxide is observed.

$$Pt - OH \rightarrow Pt - O + H^+ + e^- \qquad E = 1.10 \text{ - } 1.40 \text{ V vs. RHE} \qquad (1.26)$$

Equation 1.26: *Further oxidation of platinum oxide* $(Pt - OH)$ *to Pt-O.*

Further oxidation of this Pt-O layer is then possible by the same mechanism as for the initial oxidation[19,20].

$$Pt - O + H_2O \rightarrow Pt - O_2 + 2H^+ + 2e^- \qquad E = 1.20 \text{ V vs. RHE} \qquad (1.27)$$

Equation 1.27: *Further oxidation of platinum oxide* $(Pt - O)$ *to Pt-*O_2*.*

The multifaceted nature of these reactions explains the asymmetrical nature of the peak for oxide formation. For a simple adsorption process, as with the hydrogen adsorption, a symmetrical peak was seen. In the case of oxide formation different oxides are constantly being formed at different times, as the energy required for formation is constantly changing with the coverage. This gives the broad feature seen at positive potentials. As the potential

is made more positive, a further increase in the current is seen, labelled "6". This is the onset of oxygen evolution. This occurs via the combination of adjacent adsorbed oxygen atoms[21].

$$Pt - O + Pt - O \rightarrow 2Pt + O_2 \tag{1.28}$$

Equation 1.28: *Evolution of dioxygen from adjacent platinum oxides* ($Pt - O$).

Alternatively, oxygen evolution may come from the oxidation of Pt-OH, via the formation of a surface peroxide species[22].

$$Pt - OH + H_2O \rightarrow Pt - OOH + 2H^+ + 2e^- \tag{1.29a}$$

$$Pt - OOH \rightarrow Pt + O_2 + H^+ + e^- \tag{1.29b}$$

Equation 1. 29: *Oxygen evolution from the oxidation of platinum oxide* (*Pt-OH*) *via a peroxide intermediate* (*Pt-OOH*).

This process is in competition with Equation 1.26, as formed Pt-OH may be oxidised to Pt-O or to bare platinum with a liberated O_2 molecule. Once sufficiently positive potentials have been maintained for long enough and a full monolayer of Pt-O is obtained, Equation 1.28 is the dominant pathway for oxygen evolution.

Finally, peak 7 is the oxide reduction. The oxide reduction mechanism appears to mirror its formation. Starting with a Pt-O surface, the Pt-O is first protonated, and then reduced to give HOPt bulk oxide[17].

$$Pt - O + H^+ + e^- \rightarrow HOPt \tag{1.30}$$

Equation 1.30: *Reduction of platinum oxide* ($Pt - O$) *to HOPt bulk oxide.*

This HOPt then undergoes a place exchange to give the Pt-OH surface oxide, which is then also reduced to give bare platinum once more.

$$Pt - OH + H^+ + e^- \rightarrow Pt + H_2O \tag{1.31}$$

Equation 1.31: *Reduction of platinum oxide* ($Pt - OH$) *bare platinum.*

The symmetrical reduction peak is indicative of a surface reduction process, as the reduction is not hindered by diffusion, presumable due to the low pH allowing large concentrations of rapidly diffusion protons for the protonation steps. It is also noticeable that there is a large separation between the oxide formation and reduction regions of around 200 mV[22], highlighting the irreversibility of the oxide formation and removal reactions.

1.3.4 Rotating disc electrodes

The rotating disc electrode (RDE) is a large planar disc electrode in an insulating surround. The disc is rotated at a constant rate, which acts to pump fresh solution over the electrode surface in a predictable and reproducible manner. The diffusion layer at a RDE is a thin stagnant layer of solution at the electrode surface that rotates with the electrode. Its thickness (X_D) is given by Equation 1.32.

$$X_D = 0.643\nu^{1/6}D^{1/3}\omega^{-1/2} \tag{1.32}$$

Equation 1.32: *Diffusion layer thickness in cm (X_D) from kinematic viscosity of the solution in cm^2 s^{-1} (ν), diffusion coefficient in cm^2 s^{-1} (D) and rotation rate in Hz (ω). 0.643 is a constant that applies when the given units are used.*

As the rotation rate is increased the flux of solution to the electrode surface is increased, and the diffusion layer becomes increasingly thin. The rate of mass transfer to the electrode is determined by how quickly the redox species can diffuse across the diffusion layer. A faster rotation rate will therefore give a faster rate of mass transport. The mass transport limited current is given by the Levich equation.

$$i_L = 1.554nFAD^{2/3}\nu^{-1/6}c\omega^{1/2} \tag{1.33}$$

Equation 1.33: *Mass transfer limited current for a rotating disc electrode in A (i_L), from the diffusion coefficient in cm^2 s^{-1} (D), electrode area in cm^2 (A), kinematic viscosity in cm^2 s^{-1} (ν), number of electrons transferred (n), Faraday's constant in C mol^{-1} (F), concentration in mol cm^{-3} (c) and rotation rate in Hz (ω). 1.554 is a constant that applies when the given units are used.*

The given example is for a linear sweep voltammogram for the reduction of O to R at a RDE. At a potential of zero current the concentration of O at the surface will be equal to that in the bulk. As the potential is increased, O at the surface is reduced to R, giving a concentration gradient at the surface. This diffusion layer thickness is fixed by the rotation rate, and so as the potential is increased and more O is consumed, the concentration gradient will increase and so will the current. Eventually the concentration at the surface reaches zero. As the diffusion layer thickness is fixed the concentration gradient can increase no further, and the limiting current has been reached. This means that a thinner diffusion layer also results in a larger concentration gradient at the electrode surface, as bulk concentration is reached at a shorter distance from the electrode surface. Larger rotation rates will therefore generate larger limiting currents, as can be seen in Figure 1.10.

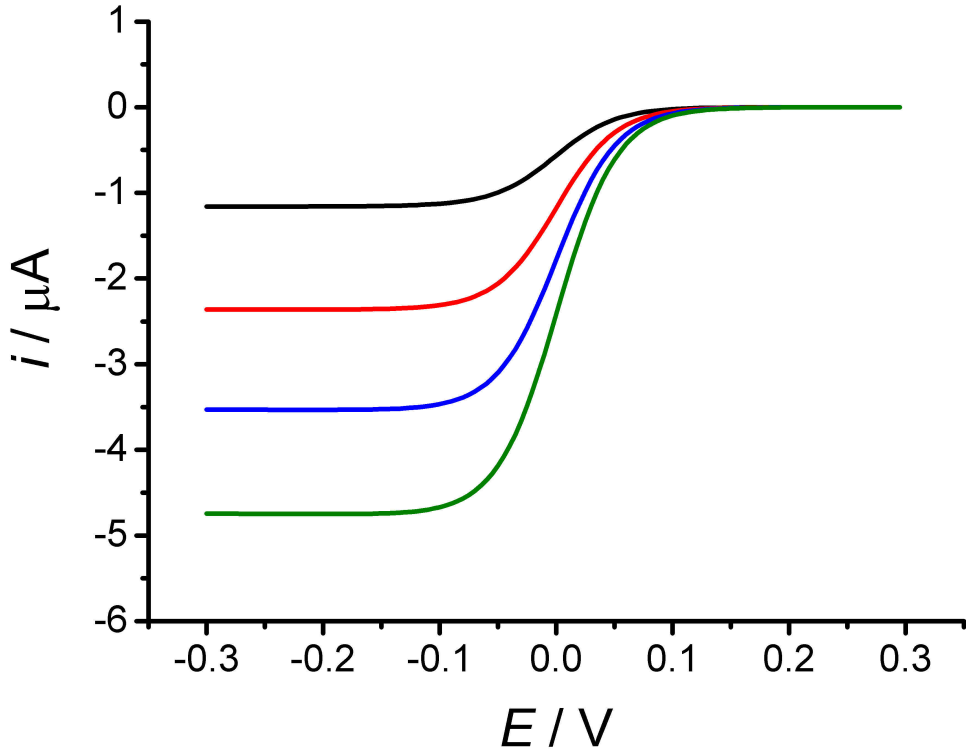

Figure 1.10: *Simulated linear sweep voltammograms for a single electron reduction at a 5 mm diameter rotating disc electrode, where* $D = 1 \times 10^{-5}$ cm^2 s^{-1}, $c = 1$ mM *and* $\nu = 1$ mV s^{-1}, *showing how the mass transport limited current becomes larger as the rotation rate is increased from 1 Hz (black), to 4 Hz (red), 9 Hz (blue) and 16 Hz (green).*

A linear sweep of potential from a potential of zero current to one of mass transport limited current will give a sigmoidal voltammogram. The plateau at large overpotential will correspond to the limiting current from the Levich equation. The slope of the observed sigmoid will reflect the kinetics of the system. Slow kinetics require a greater overpotential to drive the reaction, and so is observed as a more shallow slope in the sigmoid, as can be seen in Figure 1.11.

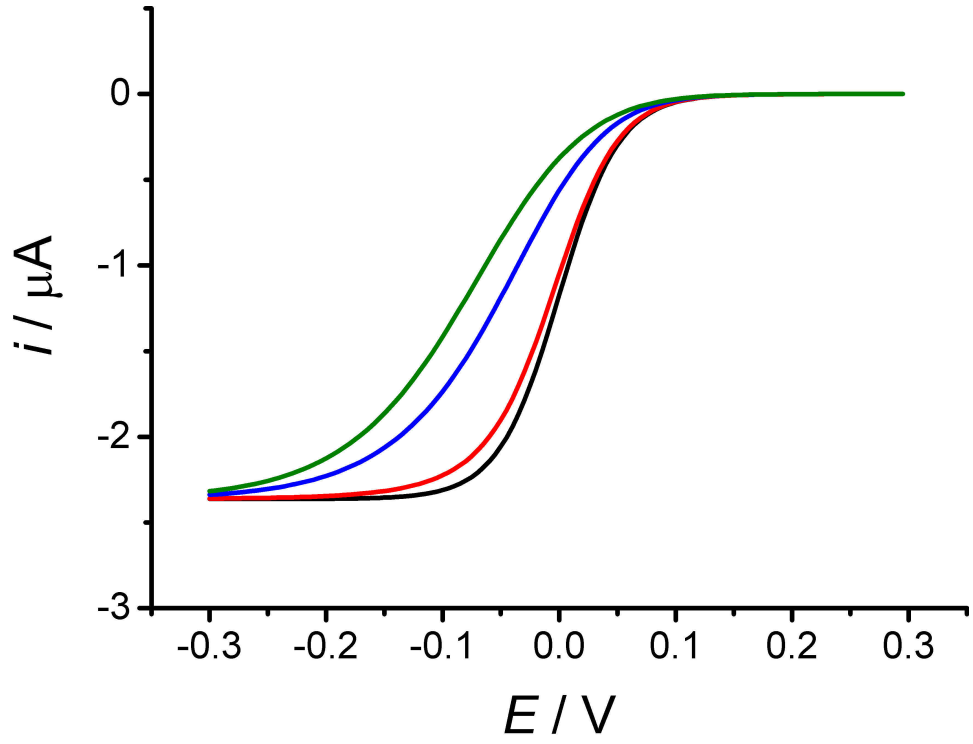

Figure 1.11: *Simulated linear sweep voltammograms for a single electron reduction at a 5 mm diameter rotating disc electrode, where* $D = 1 \times 10^{-5}$ cm^2 s^{-1}, $c = 1$ mM, $\nu = 1$ mV s^{-1}, *and* $\omega = 4$ Hz, *showing how the slope of the CV becomes steeper as* k^0 *is increased from 0.005 cm* s^{-1} *(green), to 0.01 cm* s^{-1} *(blue), 0.1 cm* s^{-1} *(red) and 1 cm* s^{-1} *(black).*

For a reversible reaction the voltammogram is described by Equation 1.34.

$$E = E_e^0 + \frac{RT}{nF} \ln \left\{ \frac{I}{I_L - I} \right\} \tag{1.34}$$

Equation 1.34: *Shape of a linear sweep voltammogram at a RDE from the potential* (E), *standard equilibrium potential* (E_e^0), *ideal gas constant* (R), *temperature* (T), *number of electrons transferred* (n), *Faraday's constant* (F), *the experimental current* (I) *and the limiting current* (I_L).

For a voltammogram of a first order redox reaction at a RDE under kinetic limitations, the measured current is a combination of the kinetically controlled and mass transport limited currents.

$$\frac{1}{i_{exp}} = \frac{1}{i_k} + \frac{1}{i_L} = \frac{1}{i_k} + \frac{1}{1.554nFAD^{2/3}\omega^{1/2}\nu^{-1/6}c} \tag{1.35}$$

Equation 1.35: *Experimentally measured current for a reduction process at a rotating disc electrode in A (i_{exp}), from the mass transfer limited current in A (i_L), the kinetically controlled current in A (i_k), diffusion coefficient in cm^2 s^{-1} (D), kinematic viscosity in cm^2 s^{-1} (ν), number of electrons transferred (n), Faraday's constant in C mol^{-1} (F), concentration in mol cm^{-1} (c) and rotation rate in Hz (ω). 1.554 is a constant that applied when the given units are used.*

The assumption that $1/i_{exp} = 1/i_k + 1/i_L$ requires the reaction to be first order with respect to the species being reduced or oxidised at the electrode surface. Under these conditions, a plot of i_L vs. $\omega^{-1/2}$ will therefore give $1/i_k$ at the intercept.

$$i_k = nFAck^0 \exp\left\{\frac{-\alpha nF}{RT}(E - E^0)\right\} \tag{1.36}$$

Equation 1.36: *Kinetically controlled current for a rotating disc electrode (i_k), from the number of electrons transferred (n), Faraday's constant (F), electrode area (A), concentration (c) ideal gas constant (R), temperature (T), potential (E), standard potential (E^0), standard electrochemical rate constant (k^0) and transfer coefficient (α).*

Calculating the kinetically controlled current at varying potentials will therefore allow the calculation of kinetic parameters k^0 and α from a plot of $\ln(i_k)$ vs. $E - E^0$.

1.3.5 Sampled current voltammetry

Previously described cyclic and linear sweep voltammetry techniques have involved sweeping the potential between two potential limits and then measuring the current response. This is commonly thought of as a continuous sweep. However, when using a digital potentiostat, the potential will be incrementally increased. It is therefore more appropriate to think of it as a series of potential steps, with the start point of each potential step being the potential at which the current was previously measured. Sampled current

voltammetry (SCV) is an alternate means of probing redox mechanisms. It is a well-known experimental technique, and has been previously reported in multiple textbooks[6,23], yet it seems to have fallen out of favour as a practical technique in recent years.

SCV is a multi-step procedure that builds a recognisable voltammogram by recording the current separately for each potential on the reduction wave, using a series of potential step experiments. This allows the current to be recorded from the same starting point of zero current at each potential. It also allows the electrode to be pre-treated between each data run using a conditioning waveform. This could be a simple sweep between positive and negative limits prior to the chronoamperogram being recorded. This means that the current is not just recorded from the same starting potential, but also from the same starting surface conditions, as any adsorbed species can be stripped off by the cleaning waveform. The development and application of this waveform will be later discussed in Chapter 2. To our knowledge, no previously published work takes this extra step to pre-treat the electrode to ensure it is clean throughout the data collection. Sampling the current at the same time after the potential step allows an SCV to be constructed[5].

In this way multiple SCVs can be constructed from a single set of current transients (see Figure 1.12), making SCV a powerful tool for the analysis of redox processes. By sampling data at short times (τ_1, Figure 1.12a) a pseudo-steady-state voltammogram can be constructed. By sampling the same data at long times (τ_4, Figure 1.12a), a steady-state voltammogram can be constructed. This allows the comparison of pseudo-steady-state voltammograms (τ_1, Figure 1.12b) with steady-state voltammograms (τ_4, Figure 1.12b) within the same set of experimental data. The time at which steady-state voltammograms could be sampled can be approximated as the point in the current transients at which a plateau is reached.

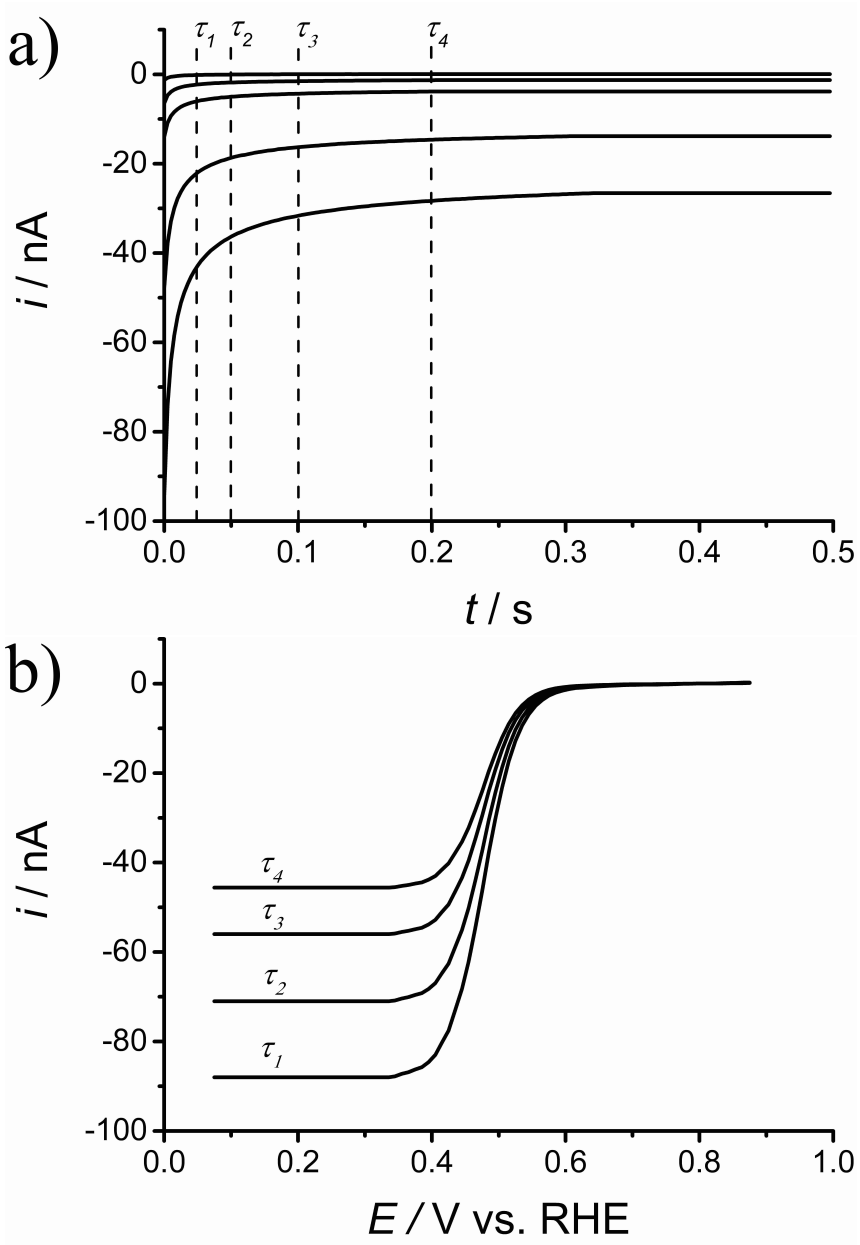

Figure 1.12: *Plots showing raw data of current vs. time transients (a) and the constructed SCVs from currents sampled at times τ_1, τ_2, τ_3 and τ_4 (b).*

This construction process can also be visualised on a 3D plot of current vs. time vs. potential (Figure 1.13). Here, both the shape of the original current vs. time transients (red) and the constructed SCV (green) can be clearly seen on the same plot. By moving the green SCV line along the time axis, it can be seen how multiple SCVs can be constructed from the same collection of current transients.

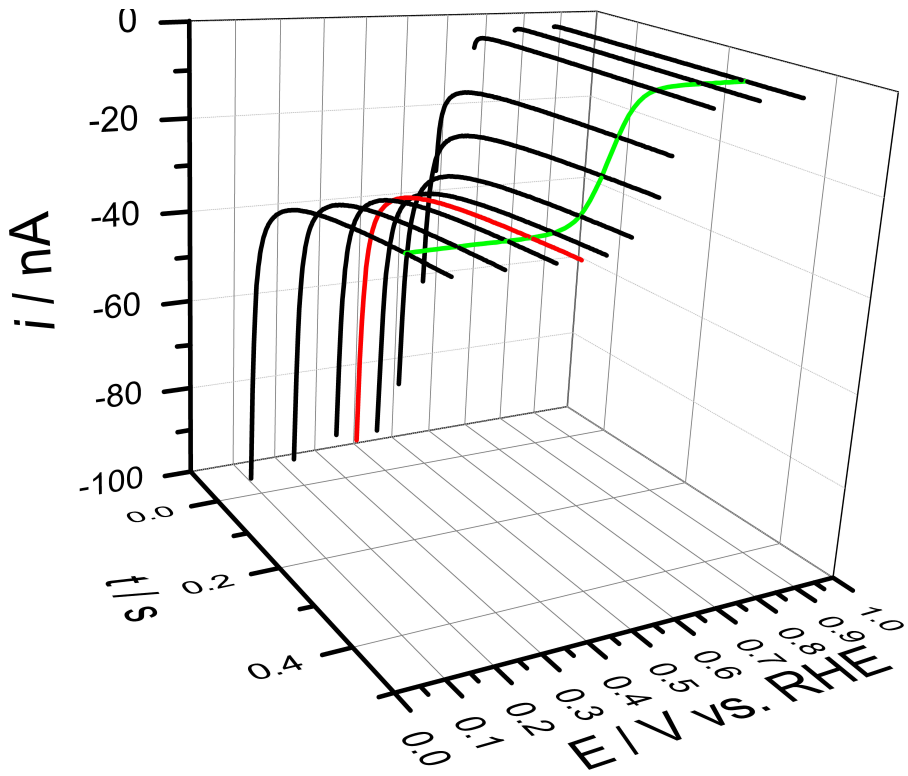

Figure 1.13: *Plot showing unprocessed current vs. time transients (black and red) and constructed current vs. potential SCV (green).*

The magnitude of the current in any SCV is dependent on the time at which it is sampled, in the same way that the current in the raw chronoamperograms is time dependent as well. This makes it impossible to compare SCVs sampled at different times. This can easily be resolved through a normalisation procedure, by dividing the SCVs by the diffusion limited current for that particular sampling time. This is given by the Cottrell equation, as shown in Equation 1.12.

The sigmoid that is constructed contains useful kinetic information, with more irreversible systems exhibiting a more shallow slope. The slope can therefore be used to calculate the standard electrochemical rate constant and transfer coefficient by simply fitting the constructed voltammogram to a theoretical model. Bard and Faulkner give the shape of a quasireversible SCV as a function of a dimensionless kinetic parameter, λ[5].

$$\lambda = \frac{k_f t^{1/2}}{D^{1/2}}(1 + \zeta\theta) \tag{1.37a}$$

$$\zeta = \left(\frac{D_O}{D_R}\right)^{1/2} \tag{1.37b}$$

$$\theta = \exp\left\{\frac{nF(E - E^0)}{RT}\right\} \tag{1.37c}$$

Equation 1.37: *Dimensionless kinetic parameter for a SCV at a large planar electrode (λ) from the forward rate constant (k_f), diffusion coefficient for the oxidised (D_O) and reduced species (D_R), sampling time (t), Faraday's constant (F), potential (E), standard potential (E^0), ideal gas constant (R) and the temperature (T).*

The shape of the sigmoid is then given by the following function of lambda.

$$i = \frac{i_d}{(1 + \zeta\theta)}\pi^{1/2}\exp(\lambda^2)\mathrm{erfc}(\lambda) \tag{1.38}$$

Equation 1.38: *Current of a sampled current voltammogram (i) from the diffusion limited current (i_d) and ζ, θ and λ from Equation 1.37.*

For a totally irreversible system, kinetic limitations result in the backward reaction being negligible, and so the model can be simplified.

$$i = i_d\pi^{1/2}\lambda\exp(\lambda^2)\mathrm{erfc}(\lambda) \tag{1.39a}$$

$$\lambda = \frac{k_f t^{1/2}}{D_O^{1/2}} \tag{1.39b}$$

Equation 1.39: *Current of an irreversible sampled current voltammogram (i) from the diffusion limited current (i_d), the dimensionless kinetic parameter for a SCV at a large planar electrode (λ) the forward rate constant (k_f), diffusion coefficient for the oxidised species (D_O) and sampling time (t).*

For a large planar electrode, i_d is given by the Cottrell equation, as given in Equation 1.12. Kinetic parameters can then be found through non-linear regression to find λ at multiple potentials. λ can then be used to find the forward rate constant at each of the given potentials. Using Equation 1.4, k^0, α and E^0 can be calculated from the intercept and gradient of a plot of $\ln(k_f)$ vs. $E - E^0$. This method of using non-liner regression of a current-potential curve against a theoretical model to find kinetic parameters will form

the basis of the kinetic analysis performed in Chapter 4. The use of non-linear regression will be a constant technique, whilst the model will be altered to fit to the experimental technique used, taking into account to the nature of the diffusion to the electrode, timescale of measurements and other similar parameters.

1.4 Microelectrodes

Microelectrodes have distinctly different behaviours to the larger planar electrodes that have previously been described. There are multiple types of microelectrode used in the literature, the main variance being the shape and therefore properties of the active area. Microelectrode geometries are large in number, including spherical, hemispherical, disc, line and ring shapes. In this project only microdisc electrodes have been used, and so only these will be discussed in detail.

The electrochemistry of a microdisc electrode occurs at the cross section of a platinum wire at the tip of the microelectrode. This is surrounded by glass insulation, and connected to a copper wire by a metal epoxy. The glass insulation is then sealed shut with a non-conductive epoxy resin to prevent the copper wire from detaching. A schematic diagram for this design is shown in Figure 1.14. Metal wire for the construction of microelectrodes is available in multiple diameters. Anything less than around 50 μm is generally considered to be a microelectrode.

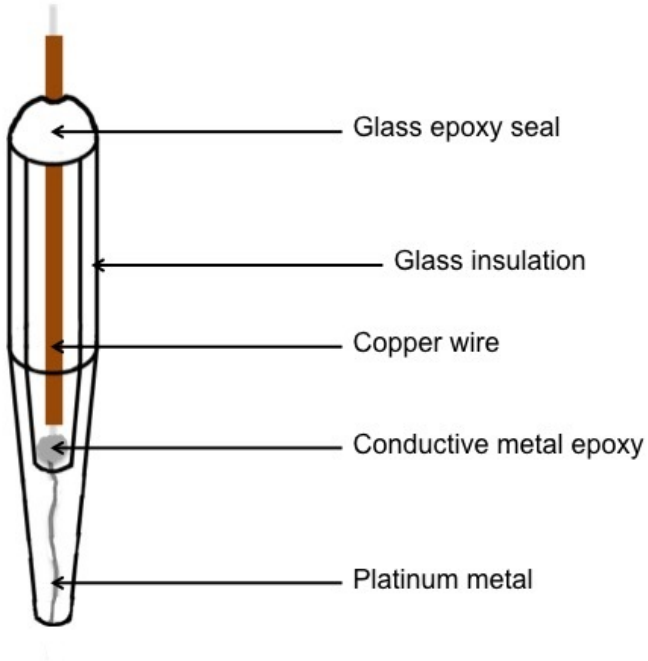

Figure 1.14: *Schematic diagram showing the principle components of a microelectrode.*

There are alternative construction methods available, including sealing the metal wire in epoxy resin rather than glass, and the use of metal solder in place of a conductive epoxy. As long as connections are sound and the insulation is effective and inert, these materials should have little impact on the behaviour of the electrode. The key parameter of a microelectrode that determines most of its properties is the electrode radius. The small size of the active area, commonly between 10^{-8} cm^2 and 10^{-4} cm^2, gives a microelectrode a number of distinct advantages over macroelectrodes.

For instance, when the surface of the electrode is biased, a layer of oppositely charged ions will become attracted to the electrode surface. The surface will therefore become charged, behaving like a capacitor. The scale of this capacitance has been previously discussed, and is approximated by Equation 1.13. The characteristic time taken to resolve this capacitance (τ) is determined by the product of the electrode capacitance and the uncompensated resistance. Whilst the term for the capacitance at a microelectrode is the same as for a large planar electrode, the small size of the electrode gives a different term for the uncompensated solution resistance to that previously discussed for a large planar electrode[24].

$$R_u = \frac{1}{4\pi\kappa a}\left(\frac{x}{x+a}\right) \tag{1.40}$$

Equation 1.40: *Uncompensated solution resistance at a microelectrode (R_u), from the distance between the working electrode and the Luggin capillary (x), electrode radius (a) and solution conductivity (κ).*

When the electrode radius becomes small, shortening the distance between the Luggin capillary and the working electrode has a negligible effect on the the uncompensated solution resistance. The bracketed term can therefore be removed from standard calculations. The characteristic time for the resolution of the charging current at a microelectrode is therefore given by Equation 1.41.

$$\tau \approx R_u C_{dl} \approx \frac{R_f a C}{4\kappa} \tag{1.41}$$

Equation 1.41: *Characteristic time taken to resolve the double layer charging from the double layer capacitance (C_{dl}), uncompensated resistance (R_u), roughness factor (R_f), electrode radius (a), electrode capacitance (C) and solution conductivity (κ).*

The characteristic time is therefore proportional to the radius of the electrode used and so a very small electrode allows the double layer charging current to be very rapidly resolved. As with large planar electrodes, the sampling time must be greater than 3τ in order to guarantee the sole recording of Faradaic information with little of no contribution from the charging current. The charging current at $t = 3\tau$ is approximately equal to 5 % of the charging current at $t = 0$ s[5]. For example, for a 25 μm diameter platinum electrode in 0.1 M NaCl, where the roughness factor is 3, the capacitance is 30.1 μF cm^{-2} [25] and the conductivity is 0.013 Ω^{-1} cm^{-1} [26], it takes 6.5 μs to discharge the double layer. This gives access to meaningful information even at very short times. Recording data at microelectrodes offers the clear advantage that voltammograms are able to be constructed on the millisecond time scale, whereas equivalent data collected on macroelectrodes would be obscured by capacitive currents.

Another key feature of microelectrodes is the predictable size and shape of the diffusion field based on the geometry of the microelectrode. It is therefore essential for the electrode tip to be polished until smooth, as a rough surface would give a larger active surface area,

which would not be taken into account by formulae involving the electrode radius. For this, consider chronoamperometry at an electrode, where the potential is stepped from a region of zero current to one of mass transport limited current. At a large, planar electrode, the size of the diffusion layer increases proportionally to the square root of time, following $\sqrt{\pi Dt}$. As the diffusion layer gets larger, the concentration gradient at the electrode surface decreases. This decrease in concentration gradient with time is shown in Figure 1.2, where the gradient can be seen to decrease as time progresses from τ_1 to τ_5.

Microelectrodes, on the other hand, show a more complex diffusion behaviour. At the onset of a potential step for the reduction of O → R, any O at the electrode surface will be immediately consumed. This gives an effective infinite concentration gradient at the electrode surface and so the current is also assumed infinite, although in practice the response time of the potentiostat limits the measured current to a finite value. At this point, diffusion to the electrode surface is rapid and linear, and so can be compared to planar diffusion to a macroelectrode. However, as time progresses, the small size of the electroactive area starts to affect the shape of the diffusion field. Atoms at the end of the disc may receive material radially as well as linearly, and so receive a much greater flux compared to atoms in the centre of the disk. This is known as edge effects. The effect can be readily observed by looking at the deposition of metal onto a microelectrode surface. The greater mass transport to the edge of the electrode when compared to the centre leads to the formation of a contoured shape resembling a red blood cell, rather than a smooth and even deposit.

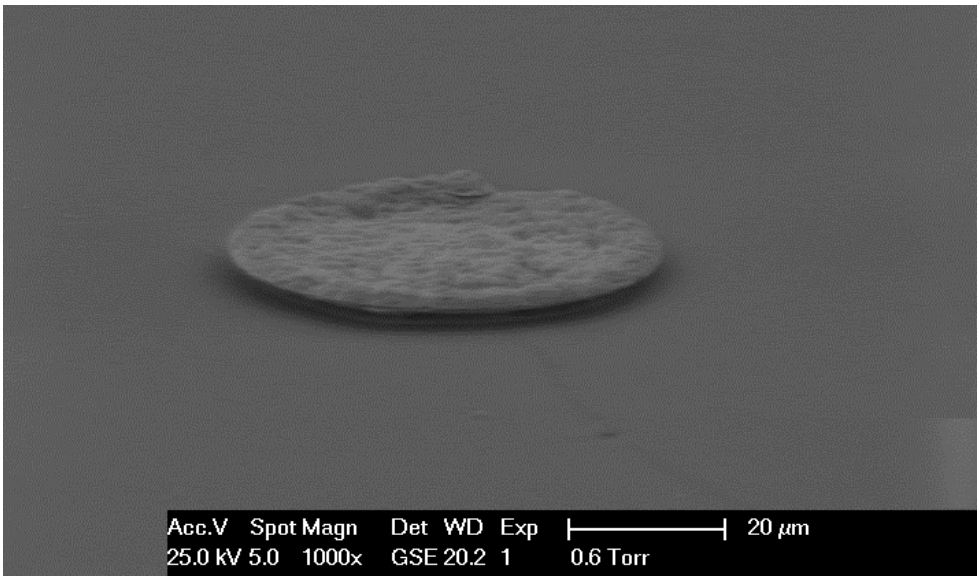

Figure 1.15: *5 μm thick nanostructured platinum deposited on the 50 μm diameter platinum microelectrode, showing the characteristic thick deposits at the edge of the electroactive disc due to the increased mass transport to edge sites.*

When edge effects come in to play and radial diffusion starts to become more influential, the diffusion field starts to take a hemispherical shape. This hemisphere then becomes larger and more well defined as the steady state is approached. At a microelectrode, once the hemispherical diffusion layer is established, the diffusion field still increases according to $\sqrt{\pi Dt}$. However, the area of the diffusion layer is now a function of time as well as the coordinate. This means that as time increases, the diffusion layer area will get larger, as well as the thickness. This means that the diffusion layer thickness increase will not affect the concentration gradient at the surface, as the electrode gets access to an increasingly large volume of solution as the field extends.

This will give a constant current regardless of sampling time, once the steady state is established. This expansion of the diffusion field is represented by Figure 1.16. At the microelectrode, the expansion from τ_1 to τ_3 can be seen to incorporate a larger area than the planar electrode thanks to its hemispherical shape.

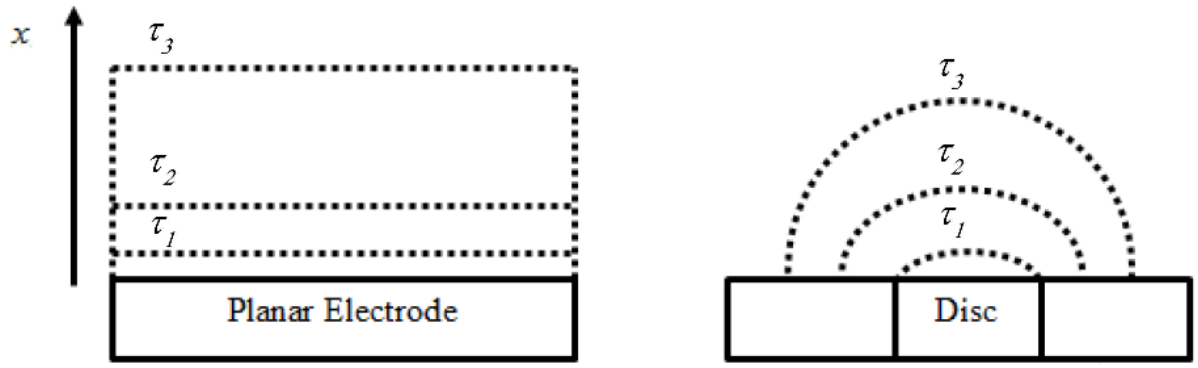

Figure 1.16: *Diagram showing the evolution of a diffusion field at a planar electrode (left) vs. a microdisc electrode (right), showing that only the area of the diffusion layer of the microelectrode is a function of time (τ).*

At a microdisc electrode, the current measured at any point during a potential step experiment can be approximated by the relative contribution of transient and steady state currents.

$$i = \frac{nFAD^{1/2}c}{\pi^{1/2}t^{1/2}} + \frac{4nFADc}{\pi a} \tag{1.42}$$

Equation 1.42: *Theoretical current during a potential step experiment at a spherical electrode, from the number of electrons transferred (n), Faraday's constant (F), diffusion coefficient (D), concentration (c), time (t), area (A) and radius (a), made up of a time dependent transient term (left) and a time independent steady state term (right).*

Equation 1.42 shows the current during a potential step experiment is made up of a transient term, which is a function of time, and a steady state term, which is independent of time. At very short times after the potential step, mass transport to the electrode surface is rapid, and so diffusion can be assumed to be linear. This is where the transient function is dominant, and so the current is time dependent. As time progresses, edge effects on the microelectrode begin to dominate. Soon, hemispherical diffusion is established, leading to a well-defined, hemispherical diffusion field. This is where the steady state function is dominant, and so the current is independent of the time at which it is measured. The steady state current can therefore be calculated from the second term, assuming the time of observation is sufficient long.

$$i = 4nFDca \tag{1.43}$$

Equation 1.43: *Theoretical steady state current a spherical electrode (i) from the number of electrons transferred (n), Faraday's constant (F), diffusion coefficient (D), concentration (c) and radius (a).*

In practice Equation 1.42 is a poor approximation for the measured experimental current at a microelectrode. At very long or very short times, when the model deviates to either planar or hemispherical diffusion, the model works reasonably well. However, the model becomes less accurate at intermediate times when there are contributions from both terms. A number of more complex models have been proposed to give a more accurate representation of the current response at a microelectrode. These tend to originate as two expressions, one for short times and one for long times as with Equation 1.42. Greater care is then taken in the stitching of the two halves together to give a more accurate model at intermediate sampling times. One example was presented by Shoup and Szabo, which gave a single unified equation to simulate the entire current transient [27].

$$i_{theo} = 4nFDc^{\infty}a \cdot f(t), \quad f(t) = 0.7854 + 0.4431\theta^{1/2} + 0.2146\exp\left\{-0.3912\theta^{1/2}\right\} \tag{1.44}$$

Equation 1.44: *Equation for calculating the theoretical limiting current (i_{theo}) as given by Shoup and Szabo [27] from the dimensionless time dependent mass transfer coefficient ($\theta = \frac{Dt}{a^2}$), the number of electrons transferred (n), Faraday's constant (F), bulk concentration (c^{∞}), diffusion coefficient (D), electrode radius (a), and the sampling time (t).*

An alternate model was then proposed by Mahon and Oldham, which gave separate time dependent functions depending on the magnitude of the time dependent, dimensionless mass transfer coefficient θ [28].

$$i_{theo} = \pi nFDc^{\infty}a \cdot f(t), \quad f(t) = \begin{cases} \frac{1}{\sqrt{\pi\theta}} + 1 + \sqrt{\frac{\theta}{4\pi}} - \frac{3\theta}{25} + \frac{3\theta^{3/2}}{226} & \text{if} \quad \theta \leq 1.281 \\ \frac{4}{\pi} + \frac{8}{\sqrt{\pi^5\theta}} + \frac{25\theta^{-3/2}}{2792} - \frac{\theta^{-5/2}}{3880} - \frac{\theta^{-7/2}}{4500} & \text{if} \quad \theta \geq 1.281 \end{cases} \tag{1.45}$$

Equation 1.45: *Equations for calculating the theoretical limiting current (i_{theo}) as given by Mahon and Oldham [28] (b), from the dimensionless time dependent mass transfer coefficient ($\theta = \frac{Dt}{a^2}$), the number of electrons transferred (n), Faraday's constant (F), bulk concentration (c^{∞}), diffusion coefficient (D), electrode radius (a), and the sampling time (t).*

Comparison of these models with experimental transients showed a great improvement with respect to Equation 1.42. Out of the two, preliminary studies indicated that the model by Mahon and Oldham seemed the most accurate, particularly when the sampling time was of the order of milliseconds. This is especially important for the transient studies in this work, and so is the model used here.

With microelectrodes, the time taken for the steady state to be established is determined by how rapidly the transient term becomes negligibly small in comparison to the steady state term; the transient term can clearly be seen to reduce as time increases. As the transient term is proportional to the square of the radius of the electrode, microelectrodes follow the trend that the smaller the radius, the faster the steady state is reached. These behaviours can be clearly seen in the cyclic voltammetry at microdisc electrodes, shown in Figure 1.17. By cycling slowly (right), the hemispherical diffusion field is maintained throughout the voltammogram, and so a steady state voltammogram is obtained. By cycling quickly (left), mass transport is made rapid, giving planar diffusion, and so a transient state voltammogram is obtained.

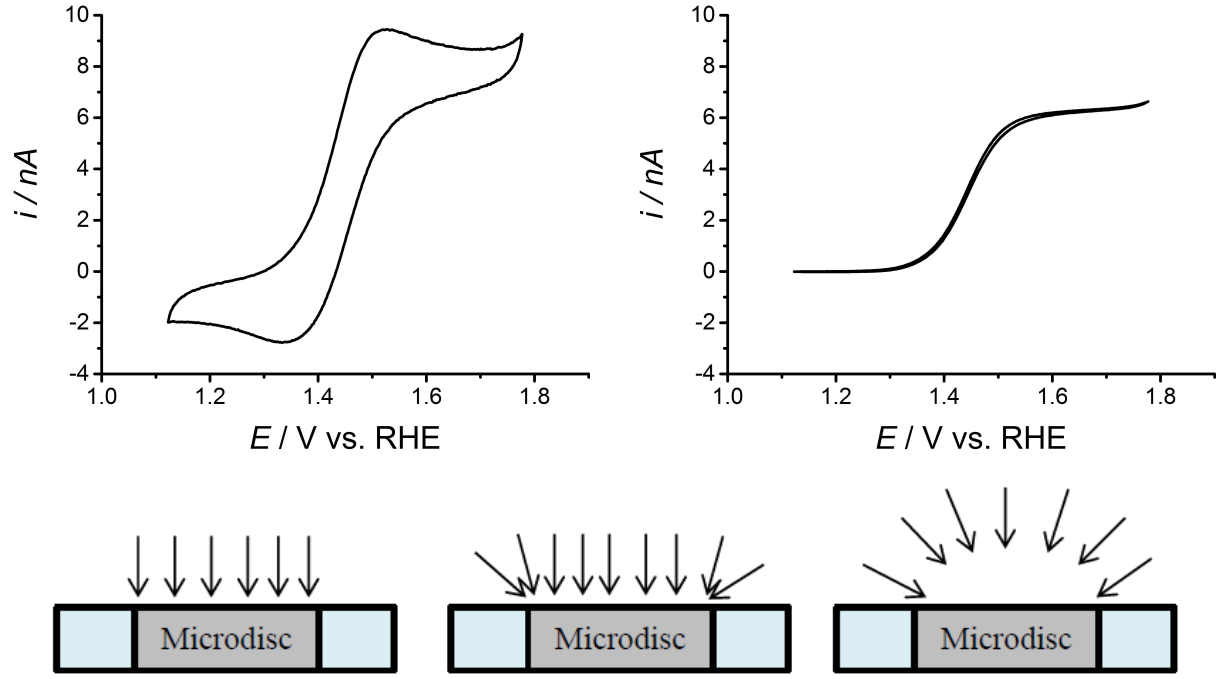

Figure 1.17: *Schematic diagram of diffusion towards a microelectrode during a potential step experiment, showing the direction of mass transport (→) at short times, with transient voltammogram (left), intermediate times (middle) and long times with steady state voltammogram (right).*

The change in the transient and steady state behaviour also affects the iR drop of the system. Assuming that the system is under diffusion control, at short times the iR drop is related to the current as determined by the Cottrell term.

$$iR \approx \frac{nFDc4\pi a^2}{\pi^{1/2}t^{1/2}} \frac{1}{4\pi\kappa a} \tag{1.46}$$

Equation 1.46: *iR drop at a microelectrode (iR), from the number of electrons transferred (n), Faraday's constant (F), diffusion coefficient (D), concentration (c), electrode radius (a), time (t) and solution conductivity (κ).*

At short times, the iR drop is seen to be proportional to the radius of the electrode used, with the iR drop decreasing as the electrode is made smaller. Once the sampling times becomes sufficiently long, the iR drop is determined by the steady state current.

$$iR \approx \frac{nFDc4\pi a^2}{a} \frac{1}{4\pi\kappa a} \tag{1.47}$$

Equation 1.47: *iR drop at a microelectrode (iR), from the number of electrons transferred (n), Faraday's constant (F), diffusion coefficient (D), concentration (c), electrode radius (a) and solution conductivity (κ).*

Now, the iR drop is not a function of the electrode radius. However, experimental evidence shows that the iR drop still decreases as the electrode is made smaller. As yet, there is no theoretical explanation for this.

Clearly the nature of the transport of material is a key factor when it comes to predicting the difference in the behaviour between planar and microdisc electrodes. The mass transfer coefficient (k_m) is a measure of the rate of transport of material from the bulk of the solution to the electrode surface. For a planar electrode, this can be calculated by simple division of the diffusion coefficient by the characteristic distance given by Equation 1.11.

$$k_m = \sqrt{\frac{D}{\pi t}} \tag{1.48}$$

Equation 1.48: *Mass transfer coefficient for a planar electrode (k_m), from the diffusion coefficient (D), and the time (t).*

For a microelectrode, the expression is more complicated due to the hemispherical nature of the diffusion layer. The rate of transport of redox species to the electrode is not only dependent on the thickness of the layer, but also on its area. In the steady state, the rate of mass transport is given by Equation 1.49

$$k_m = \frac{4D}{\pi a} \tag{1.49}$$

Equation 1.49: *Mass transfer coefficient for a microelectrode (k_m), from the diffusion coefficient (D), electrode radius (a).*

The origin of the difference between the transient response under planar diffusion and the steady state response under hemispherical diffusion is clear here. The planar mass transport term is inversely proportional to time, making it large at short times, when it will outweigh steady state diffusion. As t increases, the planar mass transfer term decreases as the denominator becomes large. This continues until the hemispherical diffusion term is the larger, and now dominates diffusion to the electrode surface. This also shows why there is an upper size limit for microelectrodes, as the steady state diffusion term is inversely proportional to the electrode radius. A small radius is needed to give a fast enough hemispherical diffusion term to outweigh the planar diffusion term over an observable timescale.

It is also noticeable that the rate of mass transport at a microdisc electrode is proportional to the radius of the electrode, with a smaller electrode giving a larger k_m. In this way k_m can be readily manipulated. This is often compared to the rotating disc electrode (RDE). Here, the rate of mass transport is varied by changing the rotation rate of the electrode, according to Equation 1.50.

$$k_m = 1.554\nu^{-1/6}D^{2/3}\omega^{1/2} \tag{1.50}$$

Equation 1.50: *Mass transfer coefficient for a rotating disc electrode (k_m), from the diffusion coefficient in $cm^2\ s^{-1}$ (D), kinematic viscosity in $cm^2\ s^{-1}$ (ν) and rotation rate in Hz (ω). 1.554 is a constant that applies if the given units are used.*

The rapid rotation of the RDE acts to pump fresh solution over the electrode surface. In this way, the mass transfer coefficient is readily manipulated by varying the rotation rate, with faster rotation generating a greater rate of mass transport. It is clearly easier to vary mass transport with a RDE rather than with a microelectrode. With RDE, k_m can be altered using the software without having to touch the set up, where as microelectrodes require the fabrication of a new microelectrode with a different radius for every data point. However, the use of microelectrodes allows a far greater range of mass transfer coefficients to be accessed, as shown in Table 1.2.

Table 1.2: *Mass transfer rates (k_m) at microeletrodes of specified radii (a) and rotating disc electrodes at specified rotation rates (ω), assuming $D = 1 \times 10^{-5}$ cm^2 s^{-1} and $\nu = 0.01$ cm^2 s^{-1}.*

k_m / **cm s^{-1}**	ω / **Hz**	a / **μm**
0.0001	0.09	1273
0.001	8.92	127
0.01	892	12.7
0.1	89,214	1.27
1	8,921,364	0.13

Microelectrodes have the key advantage that it is far easier to reduce the size of an electrode diameter than it is to achieve rotation rates in the megahertz range without the appearance of significant noise due to the vibrations of the instrument. This is a key limitation in the operational range of a rotating disc electrode. The models used in RDE theory require the mass transport to the disc to be laminar flow; that is with the flow being in parallel layers. Vibrations in the RDE equipment introduce turbulence into the flow, and so the experimental data would not be valid.

If the microelectrode geometry is sufficiently small and the scan rate is sufficiently slow, then a steady state voltammogram is obtained. The thin sigmoid obtained provides a means of analysing the kinetics of the system being studied, with steeper slopes indicating faster kinetics.

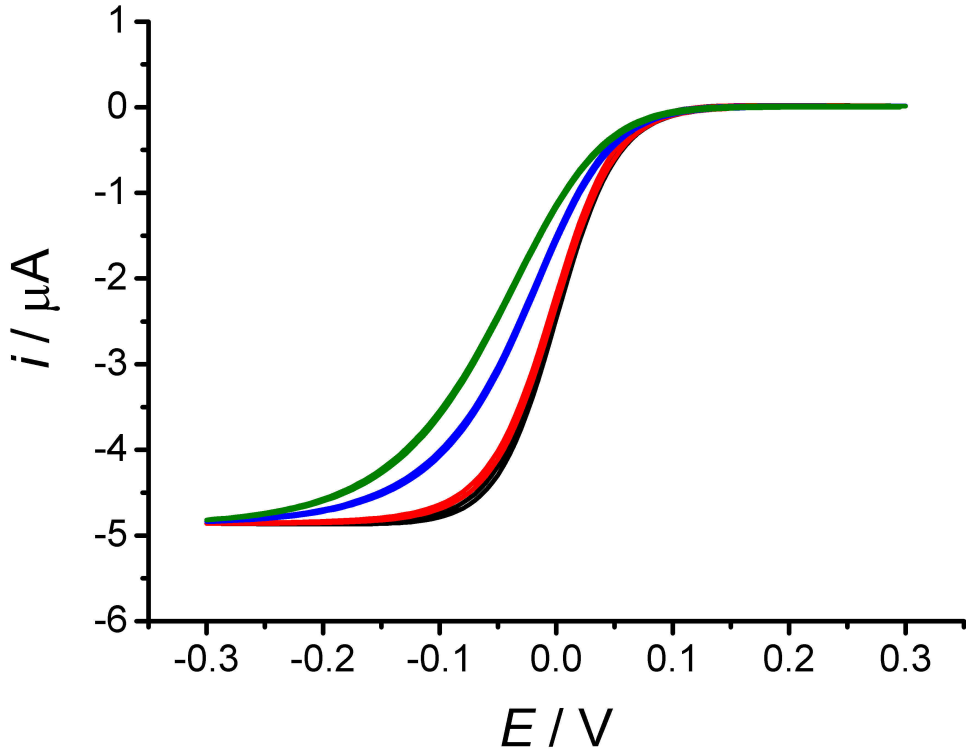

Figure 1.18: *Simulated cyclic voltammograms for a single electron reduction at a 25 µm diameter electrode, where* $D = 1 \times 10^{-5}$ *cm*^{2} *s*$^{-1}$, $c = 1$ *mM,* $\nu = 1$ *mV s*$^{-1}$, *and* $\omega = 4$ *Hz, showing how the slope of the CV becomes steeper as* k^0 *is increased from 0.005 cm s*$^{-1}$ *(green), to 0.01 cm s*$^{-1}$ *(blue), to 0.1 cm s*$^{-1}$ *(red) to 1 cm s*$^{-1}$ *(black).*

For a quasireversible system, Oldham provides the following model for a steady state voltammogram at a microdisc electrode[29], which was verified by Michael *et al.*[30].

$$i_{theo} = \frac{i_d}{\theta}\left[1 + \frac{\pi}{\kappa\theta}\left(\frac{2\kappa\theta + 3\pi}{4\kappa\theta + 3\pi^2}\right)\right]^{-1} \tag{1.51a}$$

$$\kappa = \frac{\pi k^0 a}{4D_O}\exp\left\{\frac{-\alpha n F(E - E^0)}{RT}\right\} \tag{1.51b}$$

$$\theta = 1 + \frac{D_O}{D_R}\exp\left\{\frac{nF(E - E^0)}{RT}\right\} \tag{1.51c}$$

Equation 1.51: *Theoretical model for a steady state voltammogram at a microdisc electrode* (i_{theo}) *from the number of electrons transferred* (n), *diffusion coefficient for the oxidised* (D_O) *and reduced species* (D_R), *electrode radius* (a), *standard electrochemical rate constant* (k^0), *transfer coefficient* (α), *Faraday's constant* (F), *potential* (E), *standard potential* (E^0), *ideal gas constant* (R), *temperature* (T), *and the mass transport limited current as given by Equation 1.43* (i_d).

For a totally irreversible system the situation becomes simpler, as the greater kinetic limitations on the system make mass transport less significant. This results in the θ term approaching one as the kinetics becomes slower, allowing the expression of the following simplified model.

$$i_{theo} = i_d\left[1 + \frac{\pi}{\kappa}\left(\frac{2\kappa + 3\pi}{4\kappa + 3\pi^2}\right)\right]^{-1} \tag{1.52}$$

Equation 1.52: *Theoretical model for a steady state voltammogram at a microdisc electrode (i_{theo}) from the kinetic parameter κ, as given by Equation 1.51b, and the mass transport limited current at a microelectrodes, as given by Equation 1.43 (i_d).*

It is therefore quite simple to find values for k^0, α and E^0 by using a non-linear regression to fit the model to experimental data. It is important to select the correct model based on the reversibility of the species being probed. The reversibility is predominantly determined by the nature of the redox species involved. Differences in the rate of electron transfer due to the reasons discussed in Section 1.2 tend to have a greater effect than changes in the rate of mass transfer, as most diffusion coefficients are relatively similar providing the temperature, pressure and electrolyte are kept reasonably constant.

The driving force of the reaction is dependent on the applied potential, as was described in Equation 1.4. At low overpotentials, the driving force of the reaction is decreased, and so the rate of electron transfer is low. Therefore, it may be possible to apply an irreversible model to the foot of a quasireversible or reversible steady state voltammogram, providing the overpotential is not allowed to get sufficiently large. This does come with the notable disadvantage of the reduction in the number of usable data points for the application of the model. This would therefore result in a far less precise results than if a model is applied to a full wave.

Alternatively, Oldham shows a graphical method, whereby a plot of $\ln \frac{i}{i_L - i}$ vs. E gives two linear regions[31]. A value for α is found in the gradient of the more shallow linear region, and E^0 and k^0 are found from the x and y coordinate at the point of intersection between the two lines, as is demonstrated in Figure 1.19.

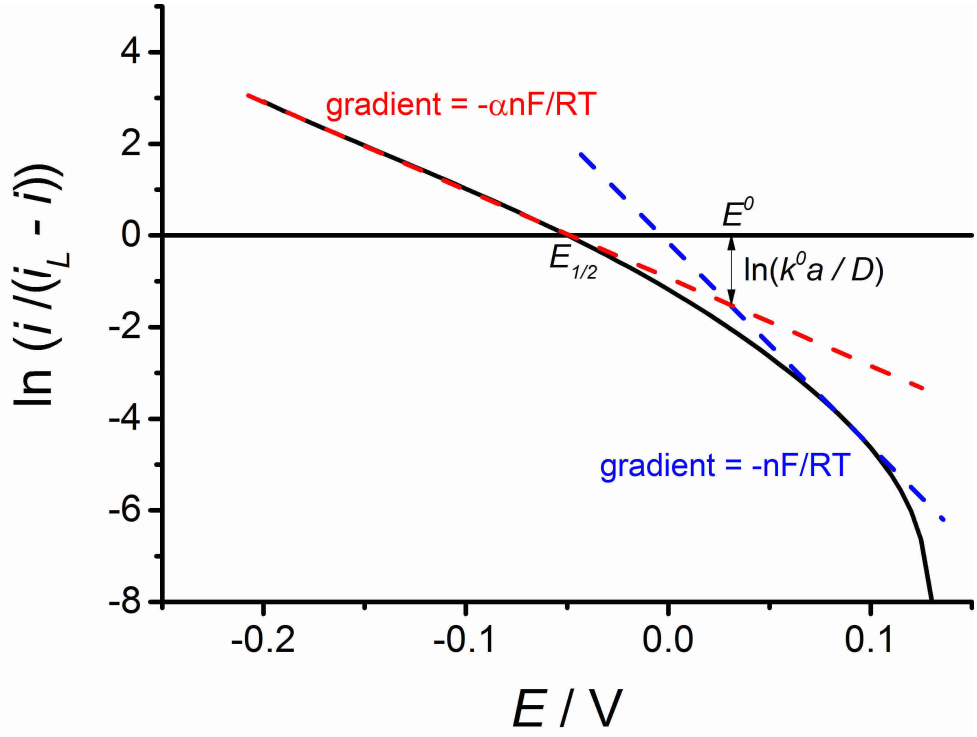

Figure 1.19: *Linear sweep voltammogram for the determination of kinetic parameters for a single electron reduction at a 25 µm diameter electrode plotted as* $ln\frac{i}{i_L - i}$ *vs E, showing how* α, k^0 *and* E^0 *may be determined from the gradients and intercepts of extrapolated linear regions.*

Whilst this is a simple method, it does introduce an element of error, as linear regions are not always clear, and have to be chosen by eye. It would therefore be preferable to use the method given in Equations 1.51 - 1.52.

1.5 Oxygen reduction reaction

1.5.1 Oxygen reduction mechanism

The oxygen reduction reaction (ORR) is a much discussed reaction in electrochemistry. The ORR is a complex multi-electron reduction, and may proceed via multiple pathways. Which pathway is followed seems to be determined by a combination of factors, including pH, electrode material, crystal face, roughness, electrolyte and rate of mass transport. The simplest pathway possible is the direct, four-electron reduction. Even this can occur

by two different pathways, depending on the pH. Under acidic conditions, the reduction involves four electrons and four protons[32].

$$O_2 + 4H^+ + 4e^- \rightarrow 2H_2O \qquad E^0 = 1.229 \text{ V vs. SHE} \qquad (1.53)$$

Equation 1.53: *Four electron reduction of oxygen to water in acidic aqueous solution.*

Under basic conditions, when the concentration of protons is low, the reduction uses two water molecules as a proton source. This produces four equivalents of hydroxide ions[33].

$$O_2 + 2H_2O + 4e^- \rightarrow 4OH^- \qquad E^0 = 0.401 \text{ V vs. SHE} \qquad (1.54)$$

Equation 1.54: *Four electron reduction of oxygen to water in basic aqueous solution.*

Whether the reduction proceeds via the acidic or basic route clearly depends on the concentration of protons available in close proximity to the electrode surface. This results in an interesting behaviour when the proton concentration reaches an intermediate value. At the onset of oxygen reduction there is a significant amount of protons available for oxygen reduction, and so the acidic route is taken (Equation 1.53). After a short time during the reduction, enough of the protons have now been consumed to cause the reduction to be limited by the concentration of protons at the electrode surface. At this point, the mechanism switches to the basic route (Equation 1.54). This results in two distinct waves being observed during a simple cyclic voltammogram for oxygen reduction at the point where proton concentration becomes a limiting factor. Investigations into the point at which the mechanisms switch are available in the literature, with the pH at which proton concentration becomes a limiting factor proposed to be 2.7[34] by Mentus, and in the range of 2.5 - 4 by Li *et al.*[35] . The exact pH will be dependent on the mass transport regime in place. Faster rates of mass transport result in a more rapid loss of protons from around the electrode surface, resulting in the switch to the basic mechanism occurring at a lower pH. This two wave voltammetry is shown in Figure 1.20. The apparent alignment of the hydrogen adsorption regions for pH 2.7 and 7.3 is likely due to transient change in the local pH during the experiments.

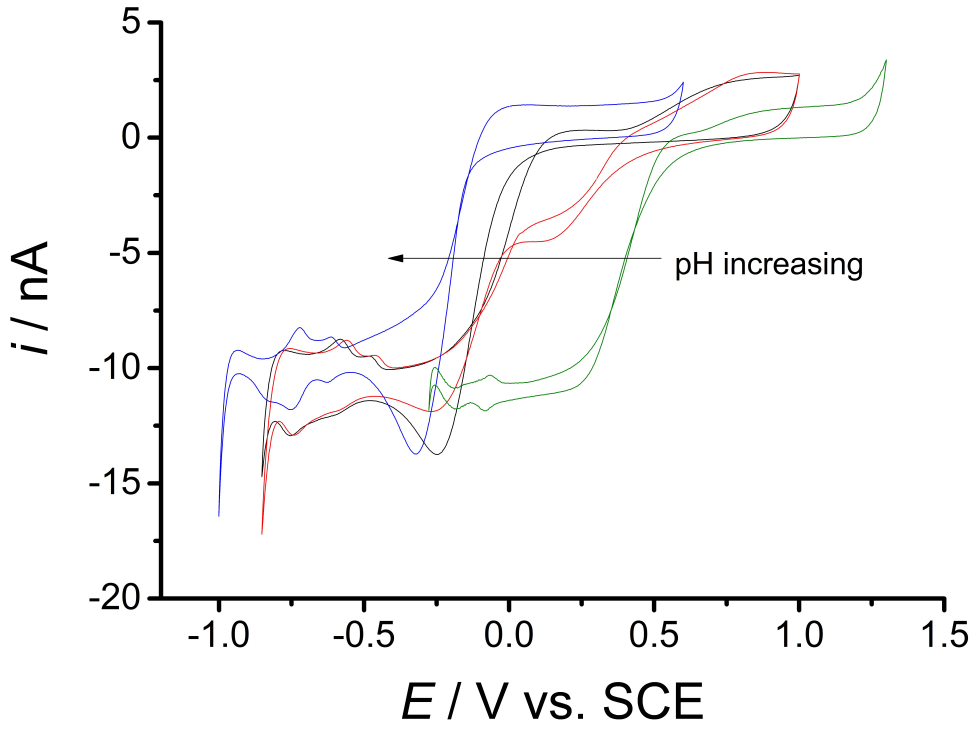

Figure 1.20: *CVs recorded at 200 mV s^{-1} recorded at a 25 µm diameter Pt microelectrode in aerated 0.1 $KClO_4$ after using $HClO_4$ and KOH to give pH 1 (green), 2.7 (red), 7.3 (black) and 13 (blue).*

Very little work on the oxygen reduction reaction is done in this area, with most fuel cell studies in particular favouring either strongly acidic or strongly basic electrolytes. Also, the diffusion of protons is considerably faster than the diffusion of large molecular dioxygen; 9.3×10^{-5} cm^2 s^{-1} [35] compared to 2.16×10^{-5} cm^2 s^{-1} [36], both recorded in 0.5 M electrolyte. This means that the involvement of proton concentration as a limiting factor is rarely seen. However, it may become an important consideration when using ion exchange membranes, which can hinder the rate of proton mass transfer around the electrode surface.

As well as the four electron reduction pathway, the ORR may instead proceed via a two electron pathway, going via a peroxide intermediate. The generated peroxide may be subsequently reduced to give water, or may diffuse into the bulk solution and dissociate. It is possible for the oxygen produced from the decomposition of peroxide to be subsequently reduced, provided the peroxide is not lost to the bulk solution before the decomposition occurs. This can be thought of as a cyclic process, with two electrons transferred to

give peroxide, followed by a chemical step to regenerate the starting dioxygen. If the regenerated oxygen is completely reduced to water, then the overall reduction is then a complete four electron reduction process. As with the four electron process, the mechanism differs depending on whether the environment is acidic or basic.

$$O_2 + 2H^+ + 2e^- \rightarrow H_2O_2 \qquad E^0 = 0.700 \text{ V vs. SHE} \qquad (1.55a)$$

$$H_2O_2 + 2H^+ + 2e^- \rightarrow 2H_2O \qquad E^0 = 1.760 \text{ V vs. SHE} \qquad (1.55b)$$

$$O_2 + H_2O + 2e^- \rightarrow HO_2^- + OH^- \qquad E^0 = \text{-}0.065 \text{ V vs. SHE} \qquad (1.55c)$$

$$HO_2^- + H_2O + 2e^- \rightarrow 3OH^- \qquad E^0 = 0.867 \text{ V vs. SHE} \qquad (1.55d)$$

$$H_2O_2 \rightarrow H_2O + \frac{1}{2}O_2 \qquad (1.55e)$$

Equation 1.55: *Two electron reduction of oxygen to hydrogen peroxide in acidic (a) or basic aqueous electrolyte (c), followed by further two electron reduction to water in acidic (b) or basic aqueous electrolyte (d), or alternatively resulting in dissociation (e).*

During the ORR at an electrode surface, a combination of both the two and four electron pathways may be observed at any one time. This leads to the complex reaction scheme proposed by Wroblowa *et al.*[37], as is shown in Figure 1.21.

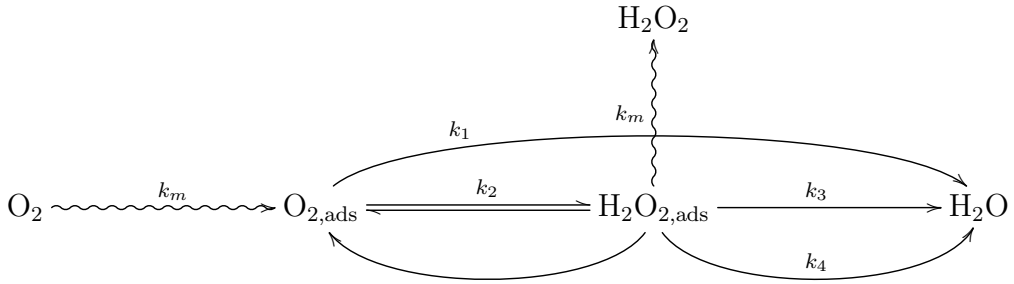

Figure 1.21: *Schematic diagram for the two and four electron ORR pathways, depicting the mass transport of O_2 from bulk solution to be adsorbed on the electrode surface (k_m), then four electron reduction to water (k_1). Alternatively, two electron reduction to H_2O_2 (k_2), followed by further two electron reduction to water (k_3), diffusion in to the bulk (k_m), or decomposition to O_2 and H_2O (k_4).*

A further method of peroxide decomposition is also possible, whereby the peroxide splits in to two $HO^\bullet$ radicals[38]. These can then undergo a further single electron reduction each, to give an overall four electron reduction[39].

$$O_2 + 2H^+ + 2e^- \rightarrow H_2O_2 \qquad E^0 = 0.670 \text{ V vs. SHE} \qquad (1.56a)$$

$$H_2O_2 \rightarrow 2HO^\bullet \qquad (1.56b)$$

$$HO^\bullet + H^+ + e^- \rightarrow H_2O \qquad E^0 = 2.330 \text{ V vs. SHE} \qquad (1.56c)$$

Equation 1.56: *Two electron reduction of oxygen to hydrogen peroxide (a) followed by decomposition to the hydroxide radical (b) and subsequent reduction to water (c).*

More complex mechanisms have also been proposed, whereby the oxygen is reduced via a series of single electron reduction steps via radical intermediates. Adzic *et al.* suggest that superoxide is an important intermediate for the ORR after identifying it using surface enhanced infra-red adsorption spectroscopy (SEIRAS)[40]. The formation of radical species during ORR was confirmed via SECM experiments by Hapiot, who proposed that the ORR is initiated by a single electron reduction to superoxide, which then undergoes a further single electron reduction to peroxide, which then behaves as above[39].

$$O_2 + e^- \rightarrow O_2^{\bullet-} \qquad E^0 = \text{-}0.330 \text{ V vs. SHE} \qquad (1.57a)$$

$$O_2 + 2H^+ + 3e^- \rightarrow HO^\bullet + HO^- \qquad E^0 = 0.803 \text{ V vs. SHE} \qquad (1.57b)$$

$$HO_2^- + H_2O + e^- \rightarrow HO^\bullet + 2OH^- \qquad E^0 = 0.184 \text{ V vs. SHE} \qquad (1.57c)$$

Equation 1.57: *Proposed methods for generation of radicals during the ORR by Hapiot et al[39,41].*

$$O_2^{\bullet-} + AH \rightleftharpoons HO_2^\bullet + A^- \qquad (1.58a)$$

$$O_2^{\bullet-} + HO_2^\bullet \rightarrow HO_2^- + O_2 \qquad (1.58b)$$

$$HO_2^\bullet + e^- \rightarrow HO_2^- \qquad E^0 = \text{-}0.744 \text{ V vs. SHE} \qquad (1.58c)$$

$$HO_2^- + AH \rightleftharpoons H_2O_2 + A^- \qquad (1.58d)$$

Equation 1.58: *Subsequent reaction of electrochemically generated radical species via reaction with a proton donating species (AH) to give hydrogen peroxide[41].*

Referring to Figure 1.21, if the rate of mass transport (k_m) is greater than the rate of peroxide reduction (k_3), then the rate of diffusion of peroxide away from the electrode increases. This leads to less oxygen being completely reduced, and so the apparent number

of electrons involved in the reaction becomes less than four. This has previously been observed on rotating disc electrodes at varying rotation rates[42,43], on microelectrodes of varying size[43] and on nanoelectrodes of varying size[32]. If the number of electrons transferred was measured during this process, this would give an idea of the interplay between the two and four electron pathways. The efficiency of a metal when it comes to catalysing the ORR is a fair indicator of whether the reduction will proceed via an overall two or four electron reduction, as it will determine the relative sizes of k_m and k_3. Different metals also exhibit a preference for different mechanisms. Whether by direct two electron reduction, or by the above steps via radical intermediates, hydrogen peroxide is inevitably formed in some small amount during the ORR. This may be subsequently reduced to give an overall 4 electron pathway, or may diffuse into the bulk solution. Interestingly, as well as the pH changing the mechanism of the reduction, it can also change the number of electrons transferred during the reduction. A larger pH decreases the number of electrons transferred from four to two. It has been proposed that this reduction is due to the increased degree of surface poisoning by hydroxide ions, which are available in greater concentrations in basic solution[44]. Adsorbed hydroxide favours the desorption of hydrogen peroxide and so inhibits further reduction, resulting in only two electrons being transferred per oxygen molecule[35].

Another important question in the ORR mechanism is which step is the rate determining step. Damjanovic *et al.* proposed that the rate determining step is the first electron transfer, as they found that the activation energy for the first electron transfer is larger than those for subsequent electron transfer steps[45]. Yeager *et al.* proposed a different scenario, where the dissociative adsorption of oxygen onto the electrode surface is rate determining, whether or not electron transfer has occurred[46,47]. Sidik *et al.* used DFT to analyse the adsorption of molecular oxygen onto Pt_2, where they found that the energy requirement for the dissociation of oxygen was higher than that for the first electron transfer. This suggested that it is the initial electron transfer rather than the dissociation of oxygen that is the rate determining step[48]. Sidik *et al.* also raised the importance of solvent effects in the dissociation of oxygen on the platinum metal surface. In acidic

solution, when a hydronium ion hydrogen bonds to the adsorbed oxygen, electron density is donated into the O_2 π^* orbital. This lengthens the O-O bond distance, and so reduces the energy requirement for bond dissociation. This would therefore have a significant impact on the calculated activation energies for oxygen dissociation.

It is generally agreed that the rate determining step is complicated, containing contributions from a number of different chemical and electron transfer steps. Rather than try to discern the difference between these, most analysis refers to a pseudo-elementary step, which is assumed to be a simple one or two electron transfer depending on the electrode material and the applied potential[33]. Ghoneim *et al.* found a negligible difference between the rate of the ORR when moving from phosphoric acid to deuterated phosphoric acid, which seems to indicate protonation steps are not involved in the rate determining step[49]. Much analysis of the rate determining step comes from the slope of a Tafel plot, which is a plot of E vs. $\ln(i)$. The gradient of this plot is defined by Equation 1.59[47].

$$\frac{1}{b} = \left\{\frac{\partial \ln(i)}{\partial E}\right\}_T = -\left\{\frac{\partial(\Delta G^0_{\ddagger})/RT}{\partial E}\right\}_T \tag{1.59}$$

Equation 1.59: *Observed gradient* $(1/b)$ *of a plot of the natural log of current* (i) *against potential* (E) *at a specific temperature* (T)*, and its relationship to the free energy of activation* $(\Delta G^0_{\ddagger})$ *and the ideal gas constant* (R)*.*

If $\Delta G^0_{\ddagger}$ is assumed to be potential independent, this expression reduces to the following.

$$b = \left\{\frac{\partial E}{\partial \ln(i)}\right\}_T = \frac{-RT}{\alpha n F} \tag{1.60}$$

Equation 1.60: *Potential independent expression for the gradient* (b) *of a plot of potential* (E) *against the natural log of current* (i) *at a specific temperature* (T)*, from the ideal gas constant* (R)*, transfer coefficient* (α) *number of electrons transferred* (n) *and Faraday's constant* (F)*.*

This gradient comes from the simplification of the Butler-Volmer equation (Equation 1.5) at large overpotentials to give the Tafel equation.

$$\eta = -\frac{2.3RT}{\alpha nF}\log\{i\} + \frac{2.3RT}{\alpha nF}\log\{i_0\} \tag{1.61}$$

Equation 1.61: *Tafel equation, relating the applied overpotential (η) to the measured current for a reduction (i), the exchange current density (i_0) the ideal gas constant (R), temperature (T), transfer coefficient (α), number of electrons transferred (n) and Faraday's constant (F).*

From the Tafel equation, it is clear how a plot of η vs. $\log(i)$ would give i_0 in the intercept and $-2.3RT/\alpha nF$ as the gradient. From the relationship in Equation 1.60, if the first electron transfer is rate determining it would be expected that the Tafel slope would have a gradient of around 120 mV dec^{-1}, assuming the transfer coefficient α is 0.5. A Tafel slope of 60 mV dec^{-1} would indicate a pseudo-two electron transfer rate determining step.

In practice, it is commonly seen that a Tafel analysis of oxygen reduction on platinum results in a curved plot. From this, two distinct Tafel slopes can be observed, with a slope of 60 mV dec^{-1} seen at low overpotential, and a 120 mV dec^{-1} seen at high overpotential. These two distinct slopes represent the difference in oxygen reduction kinetics at low and high overpotentials. At relatively positive potentials, it is possible for the metal surface to be partially oxidised, resulting in a Pt/PtO surface. At more negative potentials the electrode surface is in a more reducing environment and therefore is oxide free. The ORR is hindered by the presence of the surface oxide, which is reflected in the 60 mV dec^{-1} Tafel slope, and a pseudo-two electron reduction rate determining step is seen. On the oxide free surface, the ORR is more kinetically favoured, giving the 120 mV dec^{-1} Tafel slope, and single electron reduction rate determining step[50,51].

As well as determining the number of electrons transferred in the rate determining step, a Tafel plot also contains information about the catalytic activity of the electrode in use. The intercept of a Tafel plot allows calculation of the exchange current density (i_0). This is an important parameter for electrocatalysis. For a system at equilibrium where the net measured current is zero, the associated oxidation and reduction reactions are occuring at equal rates. The magnitude of the reductive or oxidative current at equilibrium is i_0. As the reduction at this point is not driven potentiostatically, it is instead related to the catalytic activity of the material being used. It is therefore a good indicator of the catalytic

activity of a material. The exchange current density is related to the electrocatalytically active surface area of the electrode, and also to the partial pressure of oxygen. Correction of the observed exchange current density to give the intrinsic exchange current density should therefore be made before comparing results from different literature sources[52].

$$i_{0,exp} = i_0 A_{echem} \left(\frac{P_{O_2}}{P^0_{O_2}} \right)^{\alpha} \tag{1.62}$$

Equation 1.62: *Experimentally determined exchange current density ($i_{0,exp}$) from the intrinsic exchange current density (i_0) the electrochemically active surface area (A_{echem}), partial pressure of O_2 (P_{O_2}), standard partial pressure of O_2 ($P^0_{O_2}$), and the transfer coefficient (α)*

As the ORR produces two Tafel slopes, it is also possible to record two values of i_0 for each experiment. Generally in the literature both are quoted along with the potential range over which they are measured. Alternatively, a direct comparison of catalysts can be made by simply comparing Tafel slopes, as a high exchange current will be indicated by a shift of the Tafel plot to the right. However, care must be taken here to make sure that the experimental conditions are indentical when making such comparisons.

1.5.2 Adsorption on platinum metal surfaces

All mechanisms for oxygen reduction begin with an initial adsorption of oxygen onto the electrode surface[53], and with platinum being one of the most popular materials for oxygen reduction catalysts, the adsorption of oxygen onto its surface has been well researched. The adsorption of oxygen onto the catalyst surface is clearly a hugely important stage in the oxygen reduction mechanism. A number of different possibilities exist for the adsorption of oxygen onto a metal surface[54].

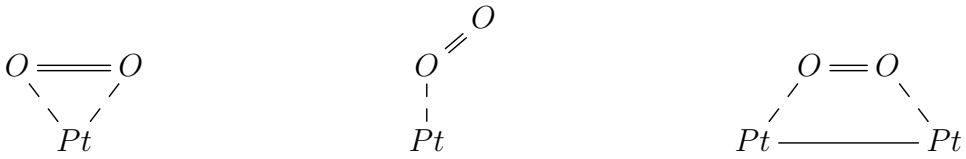

Figure 1.22: *Schematic diagrams for varying modes of adsorption of oxygen on platinum*

The Griffith model is a side on adsorption mode, with two oxygen atoms bound to a single metal atom[55]. Oxygen adsorbs by binding 2π orbitals with the empty $5d_z^2$ of the metal atom, with some degree of back bonding from partially filled d_{xy} or d_{yz} metal orbitals to the antibonding $2\pi^*$ of the oxygen molecule[56]. The bridge model is a similar arrangement, but with one oxygen atom adsorbing per metal atom[47]. Strong adsorption indicates a greater degree of back bonding, which weakens the oxygen-oxygen bond, thus promoting dissociative adsorption. Both of these models result in the adsorption of both oxygen atoms to the metal surface. This favours the four electron reduction pathway, as two bonds formed per oxygen molecule helps to hinder the diffusion of peroxide away from the electrode surface[21,48,56]. The Pauling mode of adsorption is an end on adsorption mode[57]. Adsorption is through a σ bond between the σ orbital of the oxygen molecule into the metal d_z^2 orbital. The oxygen molecule is now kept perpendicular to the metal surface. This does not give the oxygen molecule the chance to dissociate at the electrode surface, and so favours two electron reduction, with peroxide being the end product.

A number of high vacuum studies have looked into the adsorption of oxygen onto single crystal metal surfaces. Gland *et al.* used ultraviolet photoemission spectroscopy (UPS) and low energy electron loss spectroscopy (EELS) to show that oxygen dissociates upon adsorption on Pt(111) when the temperature is between 150 and 500 K. This indicated that singly bound atomic oxygen is the predominant adsorbed species[58]. The adsorption energies increase as the surface coverage increases due to repulsion between adsorbed oxygen species. This likely explains why the saturation of adsorption of oxygen on platinum is reached at around 0.2 - 0.25 monolayers[44]. The same nature of adsorption was seen on Pt(100) surfaces, where dissociative adsorption of oxygen was observed as low

as 125 K, and adsorbed oxygen was found to be entirely adsorbed as atomic oxygen at 300 K[59].

There are also other factors that will affect how oxygen reduction proceeds. The rate of oxygen reduction is proportional to the active area of the electrode in question. This means that the ORR current can be reduced by poisoning the electrode surface with a strongly binding species. In the case of platinum, a very effective poison is CO gas. CO is able to strongly bind to the platinum when held at a negative potential, and will out compete any other gaseous species adsorbing[60]. Poisoning the surface of an electrode with CO gas could therefore give an indication of the rate of oxygen reduction in the absence of any adsorbed O_2 gas prior to the start of the reduction. A similar effect is seen when using certain electrolytes. In the case of the potassium salts used as electrolytes in this study, the binding energy of the anion in decreases following $I^- > Br^- > Cl^- > ClO_4^-$[61]. It would therefore be expected that the rate of the reduction of O_2 dissolved in $KClO_4$ would be faster than O_2 dissolved in the same concentration of KI. In fact, it has been reported that the addition of as little of 4 ppm of Cl^- gives an order of magnitude decrease in the ORR activity[62]. Yano *et al.* observered a similar effect by the addition of H_2SO_4 into $HClO_4$, which showed a decrease in the apparent rate constant for the ORR without affecting the activation energy[63]. Collman *et al.* specifically designed their catalyst to prevent anion poisoning by constructing an environment such that anions are unable to bind. They used a face to face Co-Co porphyrin as a catalyst for the ORR. This gave good selectivity for the four electron pathway, as the Co-Co distance corresponded the distance expected for a dioxygen bridge to form across the two metal sites, whilst being too small for the larger anions to fit[64].

Perchlorate has been observed to not adsorb at all, but instead remains as part of the double layer around the electrode surface. This was shown by Teliska *et al.*, as the addition of perchlorate to a bisulfate solution does not alter the amount of bisulfate adsorbed onto the electrode surface[65]. Interestingly, bisulfate does adsorb onto the metal surface despite being analogous in structure to the perchlorate. It has been suggested that this is due to the sulfur receiving a greater back donation than the chlorine thanks to a lower

HOMO-LUMO gap in the sulfate than in the perchlorate[65]. The binding of sulfate to Pt metal surface is also quite different to the binding of halide ions in nature as well as bond strength due to the shape of the anion. The bisulfate anions bind most strongly to the Pt(111) crystal face due to the symmetry match between the C_{3v} bisulfate anion and the (111) surface. The adsorption of bisulfate has been shown to reduce the catalytic activity of platinum by blocking active sites by Ciapina *et al.*, who dosed the surface of Pt(111) electrode with cyanide. This reduced the availability of the four-fold atomic sites needed for bisulfate binding whilst allowing the ORR to proceed, giving the expected increase in catalytic activity[66]. The poisoning effect of bisulfate results in the ORR activity in sulfate solutions following the trend Pt(111) < Pt(100) < Pt(110)[67]. The spherical halides on the other hand can pack more closely onto the Pt(100) crystal face, resulting in increased adsorption onto this surface. Catalytic activity in halide anions therefore follows the trend Pt(100) < Pt(111) < Pt(110). This same pattern is also seen in perchlorate experiments[51], and so much ORR research is conducted in perchlorate based electrolytes.

It is worth noting that, although there is a clear trend in the activities of single crystal faces, the ORR mechanism may not be so simple on polycrystalline or mutlifaceted surfaces. Komanicky *et al.* proposed that oxygen may initially adsorb onto the 100 face, and then migrate onto the 111 face for reduction. This would be favourable as the OH_{ads} produced would readily desorb from the more weakly adsorbing 111 face than the more strongly adsorbing 100 face, increasing the turnover rate of the catalyst surface[68]. Attard *et al.* have also reported that the high activity commonly reported for the Pt(110) face is due to the presence of a highly disordered 1x2 arrangement, and that the increased activity is down to the greater number of steps and defects in this face[69]. Clearly the crystal structure is hugely important when it comes to predicting the activity of a catalyst material. A similar effect can be seen by manipulating the size of platinum particles. Imaoka *et al.* used the addition of adatoms to an icosahedral Pt cluster, which changed the nature of the adsorption sites available, having the corresponding effect on catalytic activity[70].

A strong adsorption onto the metal surface corresponds to greater donation of electron density from the metal surface onto oxygen. The donation of electron density reduces the activation energy of the first three electron reduction steps, but raises the energy for the reduction of Pt-OH. This is why a strong binding energy of oxygen acts to reduce the catalytic activity of a material, as adsorbed OH_{ads} acts to poison the electrode surface when the activation energy for its reduction becomes too high[21]. Differences in the nature of adsorption can also explain differences in the reduction pathway. Strong adsorption of oxygen allows the oxygen to dissociate on the metal surface. This allows complete four electron reduction, which is observed on platinum and platinum family metals. Metals on which oxygen adsorbs more weakly cannot break this O-O bond, and so two electron reduction is favoured. Such materials include mercury, gold and also carbon and oxide covered metals[21]. Single free adsorption sites result in an end-on adsorption of oxygen. This favours the production of peroxide as an end product, as formed peroxide is easily released before further reduction takes place. Side-on adsorption of oxygen requires two adsorption sites side by side adsorption sites to be free. When this form of adsorption is seen, four electron reduction is favoured as both oxygen atoms are direct contact with the electrode surface[56].

1.5.3 Materials for oxygen reduction

Many different materials have been probed for their use as potential oxygen reduction catalysts. These range from pure metal catalysts such as Pt[32,51,68,69,71–77], Ag[78] or Au[79], binary or ternary alloys of these metals with other transition metals such as PtCo[71,72,80–83], PtAu[84], PtCr[81,85], PtNi[72,80,82], PtTi[85,86], PtFe[81,87], PdCo[88], PtV[85,89], PtRhFe[72] or PtCoSn[90], zero platinum catalysts such as Fe/C/N[91,92] or TiO_2/C[93] and also metal free catalyst materials such as nitrogen doped carbon[94–97], multiply doped carbon[98] or carbon nanotubes[96,99]. In all cases, platinum is used as a benchmark for comparing catalytic activity of varying materials.

Platinum electrodes show a preference for the complete four electron reduction. It has been suggested that platinum follows an ECE mechanism, whereby the first electrochemical step generates the peroxide via two electron reduction, which then undergoes a chemical change, such as a decomposition or protonation step, before undergoing the further two electron reduction[43]. However, it is worth noting that ECE mechanisms tend to feature a homogeneous chemical step, where the chemical reaction occurs in solution. This is not the case for the ORR as the chemical step would involve the oxygen species adsorbed onto the electrode surface. These steps are all rapid, and so the voltammetry shows the four electron total reduction as one simple reduction wave, as can be seen in Figure 1.23.

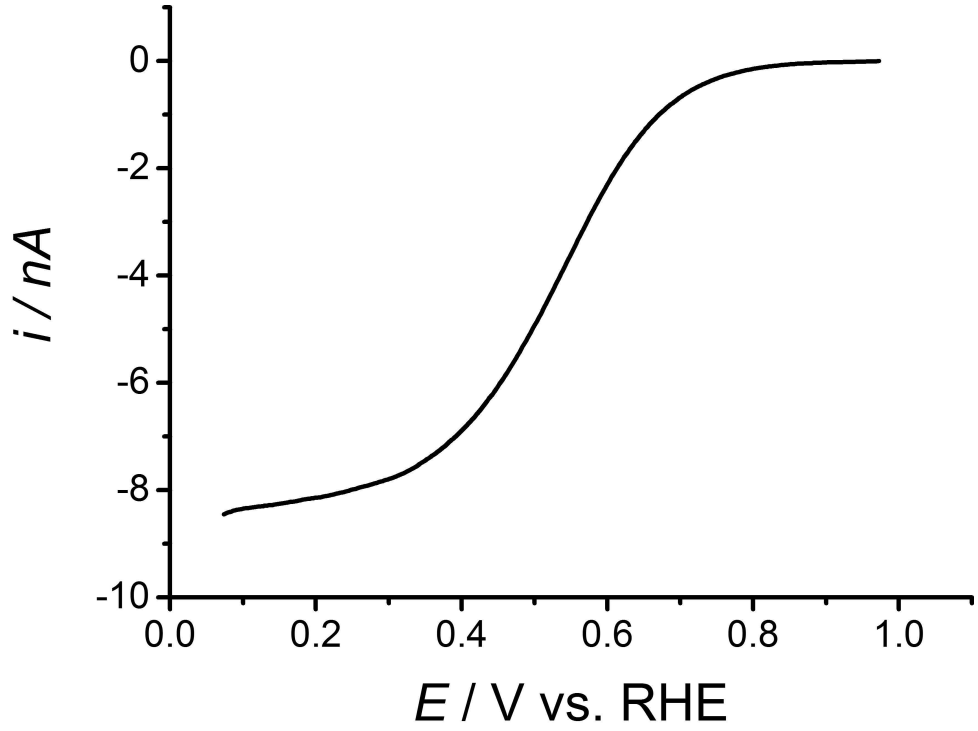

Figure 1.23: *2 mV^{-1} linear sweep voltammogram of ORR in aerated 0.1 M $KClO_4$ on a 25 μm diameter Pt electrode. The sweep started at 1 V vs. RHE, proceeding in a negative direction.*

Gold, on the other hand, gives a well-defined 'two-wave' reduction. This features a plateau in the mid-range potentials where there is a stable region of two electron reduction of oxygen to peroxide, as seen in Figure 1.24. This difference between gold and platinum has also been seen when reducing oxygen at platinum nanoparticles on a

gold support, where it has been observed that the two electron reduction at the gold substrate is facilitated by the removal of the peroxide by further two electron reduction at the platinum nanoparticles[79]. At more negative potentials a second wave is seen, which corresponds to the two electron reduction of peroxide, although this requires a considerable overpotential due to the low energy of binding between peroxide and gold[100]. It was found that the rate of the second two electron reduction exhibits very little potential dependence, even at very negative potentials, suggesting that the issue of the large overpotential needed to give the reduction is avoided by the peroxide decomposing into more easily reducible species, such as OH_{ads}[101].

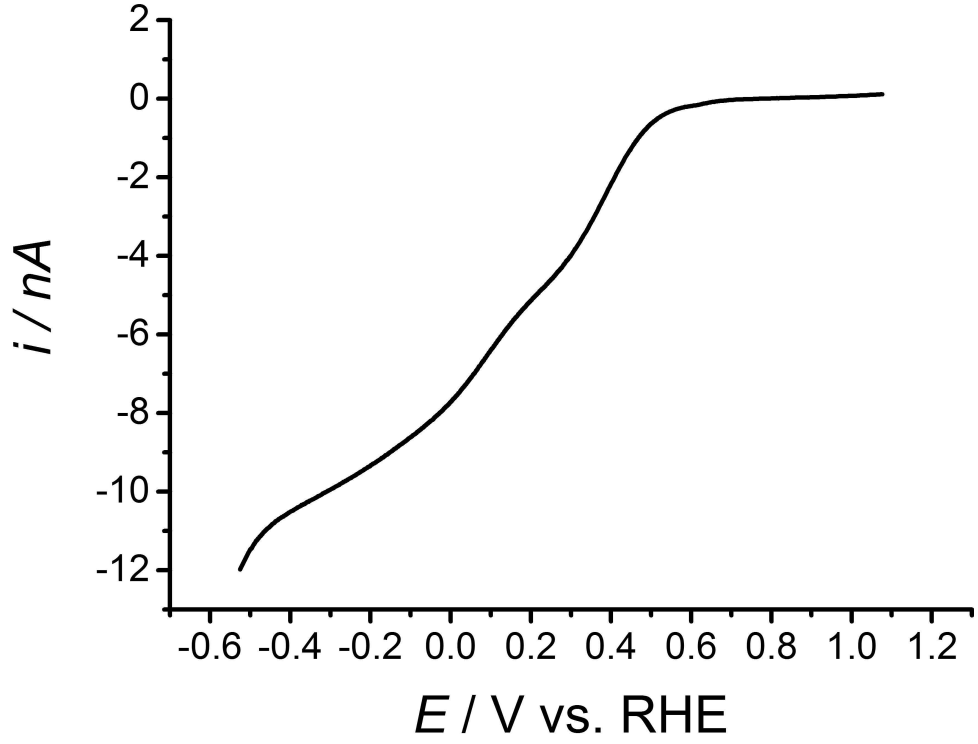

Figure 1.24: *2 mV s^{-1} linear sweep voltammogram of ORR in aerated 0.1 M $KClO_4$ on a 25 μm Au electrode. The sweep started at 1.1 V vs. RHE, proceeding in the negative direction.*

Platinum metal is a popular electrode material thanks to its well defined electrochemistry, and due to its excellent catalytic activity for the ORR. One reason that it is suitable for this is that its metal-oxygen binding energy (ΔE_O) is of an intermediate value. This means that it is not so weak that oxygen binding is disfavoured, but not so strong that binding is irreversible. This is important because the oxygen reduction

reaction proceeds via adsorption steps. This results in a high catalytic activity for the reaction, which is demonstrated in the volcano plot shown in Figure 1.25.

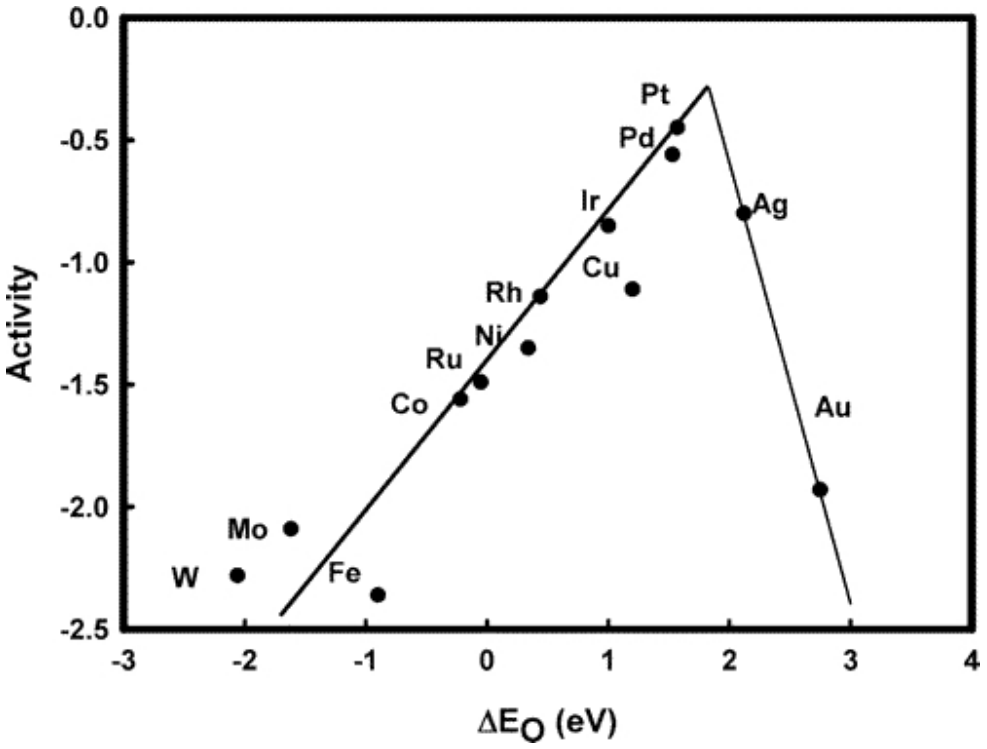

Figure 1.25: *Volcano plot showing the catalytic activity for ORR for various metals against their oxygen binding energies (ΔE_O). Values for ΔE_O were taken from reference 102.*

The excellent correlation between binding energy and catalytic activity shows that the strength of the interaction between oxygen and the metal catalyst is incredibly important, which makes ΔE_O a useful descriptor for the evaluation of catalytic materials. It can be seen that, whilst platinum is the highest metal listed in Figure 1.25, it is not the highest catalytic activity possible. According to the trend across the other metals, it appears that a slight reduction in ΔE_O could in fact provide an increase in the catalytic activity of the material. The strength of the Pt-O bond is also an indicator of whether the metal will favour two of four electron reduction, as strong Pt-O bonds can facilitate the breaking of the O-O bond. Weaker Pt-O bonding will therefore make it more likely that the O-O bond will not be broken until after two electron reduction steps, favouring the formation of hydrogen peroxide[73].

When developing a material for the efficient catalysis of the ORR, it is common to aim for the peak of the volcano plot. One well researched way to achieve this is by alloying platinum with other metals, which has the effect of altering the binding energy towards oxygen. However, calculation of binding energies of alloyed metals is far more complicated than performing the same calculations for a pure metal. It is computationally difficult to simulate the presence of both metal atoms in appropriate number and position, as well as accounting for interactions between both atoms affecting the energies of their orbitals. Inevitably, a number of approximations have to be used. One commonly used approximation is to use the calculation of the d-band energy as an approximation for ΔE_O. The d-band energy is defined as the difference between the d-band centre and the Fermi level. The d-band centre itself is determined by the number of occupied d orbitals and the d-band width, which is a function of coordination number, orbital size, and interatomic distance[84].

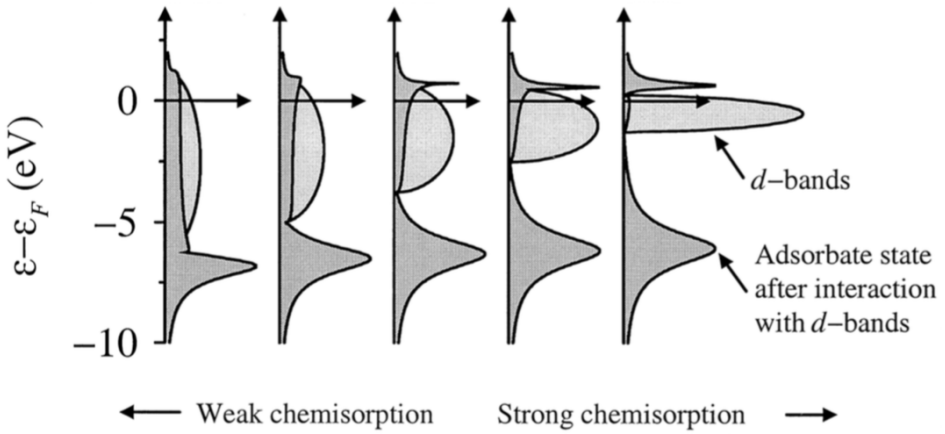

Figure 1.26: *Diagram of the change in the shape and position of the substrate (dark grey) and metal (light grey) orbitals after adsorption onto a metal surface, showing the narrowing of the metal d orbital when adsorption is stronger, resulting in a higher d-band centre, and a smaller energy cap between the d-band centre and the Fermi level (→). Figure taken from Hammer and Nørskov, reference 103.*

The Hammer-Nørskov model uses the d-band energy to evaluate the reactivity of a catalyst surface. Metals with a low d-band energy bind most adsorbates more strongly than an equivalent site on a different metal with a higher energy[104]. A plot of d-band energy against catalytic activity would therefore produce a volcano plot in the same way as a plot of catalytic activity against ΔE_O. Alloying platinum with a 3d transition metal

lowers the platinum d-band center, giving weaker adsorption of oxygen. This effect has been found to be greatest for early and smaller transition metals[105].

A number of other methods have also been suggested after study using DFT. Lee *et al.* used the dissociative binding energy of oxygen on the metal surface as a descriptor for the catalytic activity of a number of palladium alloys[88]. Xin *et al.* used M-OH bond strength, M-OH bond distance and d-band width to model catalytic activities of platinum alloys[106]. Jalan *et al.* focused on the alloy lattice parameter as a descriptor for oxygen reduction activity. They found that alloying platinum with smaller metals resulted in an overall decrease in the lattice parameter, which correlated with the oxygen reduction activity for those metals. Smaller lattice parameters resulted in an increased activity by favouring the dissociative adsorption of dioxygen[85]. A similar effect was observed by Mukerjee *et al.*, who found an increase in d-band energy and a decreased Pt-Pt bond distance on alloying with transition metals for carbon supported platinum catalysts correlated with increased catalytic activity, with PtCo/C being the most efficient[81].

It has also been suggested that alloying can be exploited to reduce the impact of poisoning species on limiting the ORR. Stamenković *et al.* looked at the poisoning effect of OH_{ads} on the ORR on Pt_3Ni and Pt_3Co alloys. They found that the cobalt alloy could effectively weaken the adsorption of the poisoning OH_{ads} layer, making the catalyst more efficient[80]. Spanos *et al.* found that this increase in catalytic activity was proportional to the Co content of the PtCo alloy[83], and Gentil *et al.* suggested that the increased catalytic activity of PtV alloys was due to the same effect[89]. A similar effect was also observed by Gasteiger *et al.*, where the changes in nanoparticle size altered adsorption behaviour of OH_{ads}, having the corresponding impact on catalytic activity[71]. Importantly, Stamenković *et al.* also found that the ORR followed the same mechanism despite the alloying, as no change in the amount of peroxide produced was observed on the ring of a rotating ring disc experiment[82]. Paulus *et al.* also observed no change in the rate determining step or apparent activation energy for the ORR on the alloy surface[72], meaning that comparison of the alloys to pure platinum metal is appropriate. A further practical reason for alloying platinum with other metals is simply cost. A

platinum nanoparticle with a core of a transition metal minimises the amount of platinum metal involved in catalyst. All platinum used is kept on the electrode surface, and so is in contact with the solution and therefore is catalytically active[107].

It is of course worth noting that these theoretical calculations come with a number of limitations. Most of the calculations will assume a single crystal face, single metal atom, or small cluster of atoms for the substrate material, which is rarely representative of a real experimental system. Also, it has been reported that predicting the d-band for alloys is difficult, as it is hard to be sure of the extent of hybridisation and/or charge transfer between the orbitals of the differing neighbouring metals[108]. There is also the added complication of which metal the adsorbate may preferentially bind to in a bi-metallic system. This is often circumvented by assuming the co-alloyed metal is beneath the surface, and so only a single metal is involved in the adsorption. This seems appropriate, as it has been reported that for PtCo alloys, a place exchange occurs between Pt and Co. This results in a Pt skin forming on top of a PtCo alloy sublayer[80]. The same group also reported that, in the case of a Pt_3Fe alloy, an annealed alloy with a significant Pt skin has significantly different electronic characteristics to an alloy with the same atomic ratio, but with the iron sputtered on the surface[87]. The calculations also assume a static metal lattice during the adsorption. This may not be appropriate, as it has recently been shown that platinum undergoes a significant lattice expansion during oxygen adsorption. This binding affects the electronic character surface by raising the d-band centre, stabilising the binding of adsorbates[109].

1.6 Research aims

The aim of this work was to investigate the application of transient studies at microelectrodes as an alternative to the more commonly used electrochemical methods. Chronoamperometry at microelectrodes was analysed on the millisecond timescale in order to give access to a high mass transport regime. Comparison to well established theoretical models was then used to elucidate kinetic information. Deviations from the expected

theoretical values for a mass transport controlled redox process indicated the presence of pre-adsorbed redox active species. Quantification of these adsorbates provided information regarding the catalytic activity of that particular electrode material towards the reduction of the adsorbed species when in solution. This work focused on the application of this method towards the oxygen reduction reaction.

Chronoamperograms at microelectrodes also allowed simple construction of recognisable, sigmoidal reduction waves, as would be expected for experiments at larger rotating disc electrodes. As such, these voltammograms were analysed as if they were linear sweep voltammograms recorded with rotating disc electrodes in the traditional way. This provided insights into the kinetics of the redox system, and the catalytic activity of the material being used. However, as the voltammograms were recorded at microelectrodes, corrections for iR drop were not necessary, highlighting the usefulness of the method compared to the more commonly used rotating disc technique.

1.7 Structure of thesis

This thesis is comprised of eight chapters. Chapter 2 will provide details of the chemicals, instrumentation and experimental techniques used throughout the bulk of this work. Standardised procedures for the fabrication and preparation of electrodes and conditioning waveforms will be provided, along with details of all potentiostatic waveforms used, so that all work here presented can be reproduced if desired.

Chapter 3 will focus on the construction and subsequent normalisation of sampled current voltammograms at microelectrodes (MSCV). This technique allows the construction of sigmoidal voltammograms from a collection of chronoamperograms recorded at a microelectrode. Examples of the voltammetry accessible by this technique will be given, along with a verification of a proposed normalisation technique. This normalisation takes advantage of a model in the literature for the calculation of the theoretical diffusion controlled current at a microelectrode, when recorded at a specific

time. Effects of sampling conditions, cleaning waveforms and choice of equipment will also be discussed regarding their impact on the acquired MSCVs.

Chapter 4 will look at the kinetic analysis of MSCVs. The slope of the MSCV will become steeper as the kinetics of the redox system become faster, and so can be used to calculate the kinetic parameters k^0, α and E^0. This was achieved through the application of a novel equation for the modelling of MSCVs, based on one previously described for modelling steady state voltammograms at microelectrodes. Examples will be given for the application of this model to real electrochemical systems, and the accuracy of extracted parameters will be discussed. The practical range of the model will also be described in terms of a range of accessible values of k^0. This was assessed through the calculation of several theoretical MSCVs constructed using the COMSOL simulation package.

Chapter 5 will look at the application of MSCV to detecting the presence of pre-adsorbed oxygen at a microelectrode surface. Pre-adsorbed oxygen will first be discussed in terms of unreasonable large values for the apparent number of electrons transferred (n_{app}), as calculated by the normalisation method proposed in Chapter 3. Experimental conditions were manipulated in order to confirm that the extra current was caused by the pre-adsorption of oxygen, as opposed to other contaminating adsorbates or accidentally deposited oxides. Subsequent analysis of the unprocessed current transients quantifies the amount of oxygen that pre-adsorbs in a specific time in terms of charge (Q), a number moles, and an approximate number of monolayers (θ). The likely accuracy of each parameter and limitations of a number of different methods for their calculation will be discussed.

Chapter 6 will look at the application of the MSCV to the determination of the catalytic activity of the electrode material by a number of methods. The amount of extra charge will be discussed as related to the binding energy (ΔE_O) of the metal towards aqueous oxygen. This was done for a number of different metals with varying binding energies, and the resultant relationship was then used to express catalytic activity. This is appropriate as ΔE_O is already being used as a descriptor for the oxygen reduction reaction. Analysis of

MSCVs as if they were linear sweep voltammograms recorded rotating disc electrodes was then done in order to calculate the kinetic current (i_k) of each metal. Plotting i_k against Q then provided an entirely experimental calibration curve for the relationship between catalytic activity and pre-adsorption of oxygen. Through inspection of the correlation between Q, i_k and ΔE_O, Q will be discussed as a potential descriptor for ORR catalytic activity.

Chapters 7 and 8 will then provide a conclusion for the entirety of the report, as well as a discussion for potential future work. This will then be followed by a list of references and an appendix of supplementary information and data.

2 Experimental

2.1 Electrode preparation

Working electrodes were constructed by first sealing a piece of metal microwire in a glass pipette using a blow torch. This closed the end of the pipette around the wire, leaving the rest of the pipette open. The sealed pipette was then fixed in a clamp with a heated filament around the tip. The open end of the pipette was connected to a vacuum pump. The vacuum was established and the heated filament turned on. The heated filament softened the glass and the vacuum acted to seal the open glass around the wire. The filament coil was then moved up the glass pipette, following the seal, to give a couple of centimetres of sealed glass around the microwire. A small portion of microwire was left exposed within the glass pipette. The exposed microwire was then connected to a copper wire to form an electrical connection to the microelectrode tip. This was done with either silver paint, or a small piece of metal solder, which was melted to form the seal using the same heater filament. Once the connection was confirmed, the open end of the microelectrode was sealed using epoxy resin to make sure that the copper wire could not become separated from the microwire due to mechanical stress. A schematic diagram of the process is shown in Figure 2.1.

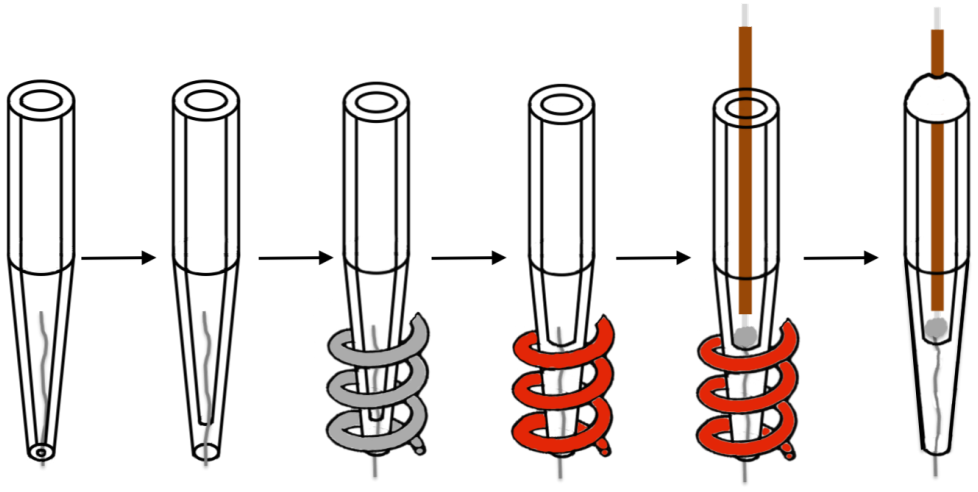

Figure 2.1: *Schematic diagram showing the construction of a microelectrode by the sealing of a metal microwire in a glass pipette and subsequent sealing under vacuum and connection to a copper wire via a conductive metal solder.*

Once constructed, the electrode was polished to ensure a smooth surface. This was done by polishing the electrode tip with silicon carbide paper on a lapping machine, until the tip is flat. Polishing was then repeated with increasingly smooth grades of lapping film, starting at 50 μm going down to 0.3 μm at the smoothest. The electrode tip was sonicated in water for three minutes in between each polishing to remove any remnants of the previous grade of polishing material from the tip prior to a smaller grade being used. The electrode was deemed to be suitably smooth when the voltammetry in argon purged sulfuric acid resembled that in Figure 1.9, specifically noting the detail in the hydride adsorption region, and the thin double layer. The electrode tip was polished for 20 minutes using 0.3 μm alumina powder prior to each experiment to ensure a clean and reproducible surface at all times. Examples of voltammograms for clean metal surfaces of all metals used in this work can be found in the appendix.

Once smooth the electrode radius was accurately measured via scanning electron microscopy (SEM). Images were recorded using the gaseous secondary electron detector under the environmental mode of a Philips XL30 SEM with 0.6 Torr of water. All calculations involving the electrode radius used radii measured in this way, with the radius measured to the nearest 0.01 μm. Further error is introduced as the metal wire used is rarely perfectly circular. An average value was therefore taken by measuring the diameter at multiple points around the wire. This minimised the error on the value of the radius used in theoretical calculations. At the same time, the seal between then microwire and the glass surround was inspected. This was done to ensure that there were no cracks or defects that could allow solution to access the sides of the wire, which would give access to a larger surface area than was described by the cross sectional area of the wire. This was also confirmed through comparison of experimental current transients for the reduction of $[Ru(NH_3)_6]^{3+}$ with the theoretical model given in Equation 1.45. A good agreement indicates that the current is proportional to the electrode radius, and so the $[Ru(NH_3)_6]^{3+}$ is not also being reduced by the sides of the microwire.

The reference electrodes used in this work were the saturated calomel electrode (SCE) and saturated mercury mercurous sulfate electrode (SMSE). The mercury / mercurous

salt couple was placed in the reference electrode cap, in contact with an external copper wire, and was sealed into the cap using glass wool. The rest of the electrode was made up of a glass pipette with a screw top and a glass frit at the other end. The reference electrode was filled with saturated potassium salt solution, with a few crystals of pure salt being added to ensure full saturation. This was important to give a reliable reference potential. The electrodes were stored with the glass frit submerged in saturated potassium salt solution to further ensure the concentration of salt within the electrode is maintained.

Most experiments in this report did not require the use of a counter electrode due to the low magnitude of current passed at such small working electrodes. When experiments were conducted at electrodes with larger surface areas, a platinum gauze was used as a counter electrode. This was cleaned before use by exposing the gauze to a gas flame, before being rinsed with deionised water.

2.2 Experimental Rig

Most electrochemical experiments were conducted in a two-electrode cell, as the low currents associated with microelectrodes meant that a counter electrode was not necessary. When necessary, a platinum gauze was used as a counter. The working and reference electrodes were introduced to the same cell via different necks in a five-necked, jacketed cell, allowing the bubbling of gas to take place by inserting the frit in to one of the other necks. Before bubbling, the gas was passed through the same electrolyte as was found in the cell using a Drechsel bottle. This ensured a constant humidity and therefore a constant rate of gas dissolution across all experiments. Glass tubing was used between the Drechsel bottle and the electrochemical cell to prevent any exchange of gases between the two points. The cell was connected to a water bath set at 25°C via plastic tubing. The entire set-up was kept inside a Faraday cage to minimise interference from external electronic equipment. All water tubing was surrounded by a grounded metal wire mesh to prevent the conduction of electrical noise.

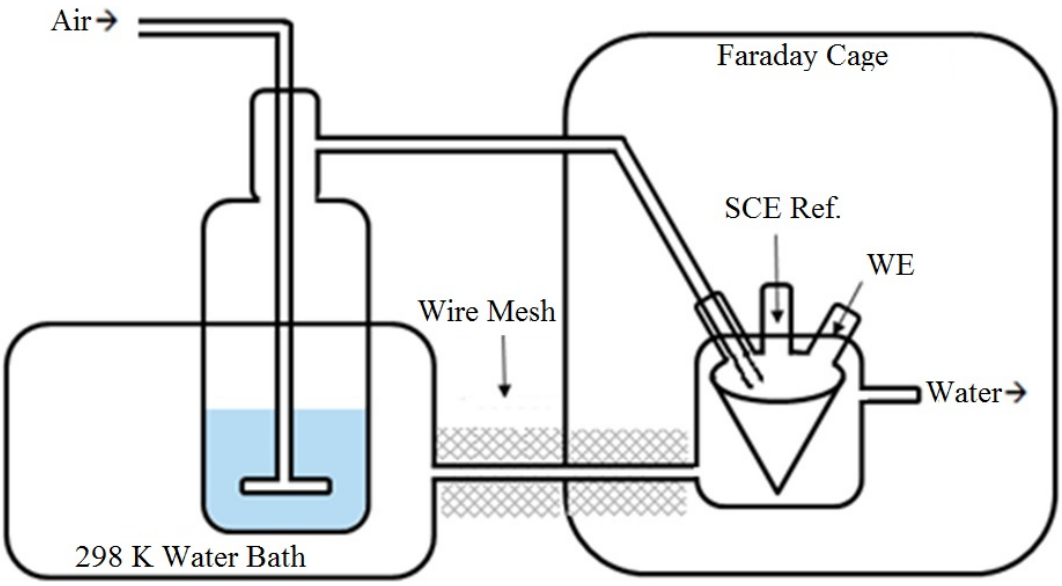

Figure 2.2: *Schematic diagram of the equipment set up used, showing the working electrode (WE) and reference electrode (SCE) in a jacketed cell inside a Faraday cage. Air was bubbled through the Drechsel bottle kept at the same temperature as the cell.*

For experiments regarding the ORR, air was bubbled through a Drechsel bottle containing the electrolyte studied, then bubbled through a frit into the cell for 30 min. For the study of other redox active species, the cell was purged with argon by the same method for the same period of time. The electrodes were connected to a PC controlled PGSTAT101 potentiostat from Metrohm, run using NOVA 1.10. Prior to every experiment, the electrode was cycled at 200 mV s^{-1} until a stable voltammogram was seen.

2.3 MSCV procedure

A command list was written using NOVA 1.10 to give full automation of the following procedure. The electrode was first electrochemically cleaned by sweeping between upper and lower cleaning potentials at 500 mV s^{-1} six times. The importance of this waveform will be discussed in Section 3.5. The potential was then held at the open circuit potential (OCP) for 10 s, and then stepped to the most negative potential of the desired MSCV, where the current was measured for 0.5 s. The potential was then held at the open circuit

potential for 10 s once more. OCP was determined by leaving the electrode at open circuit for several minutes before observing the potential. After this, the electrode was biased at the previously measured value. The value was assumed constant provided the experimental conditions were unchanged. A new OCP was therefore measured whenever the electrode, electrolyte or pH was changed. This procedure was then repeated, with the stepped potential being increased by 0.01 V each time. The waveform used can be seen in Figure 2.3.

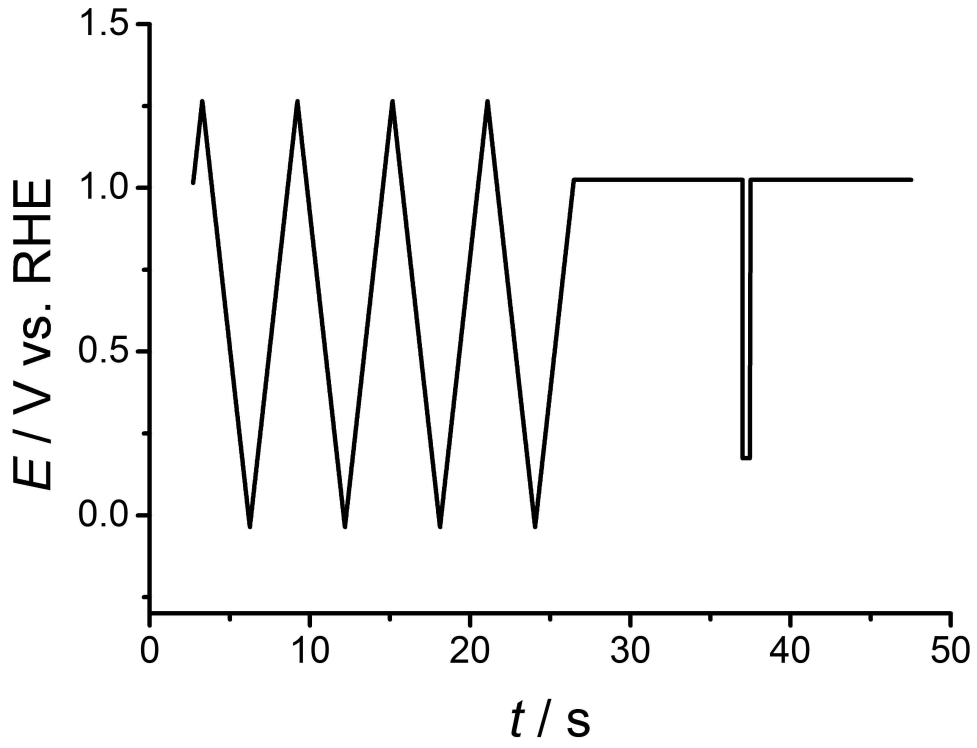

Figure 2.3: *Waveform used for collecting the MSCV data, showing the cleaning waveform, rest at OCP, potential step, and then further rest at OCP.*

A second nested procedure was used to collate the transients and save them as a text file. A third procedure then reorganised the current vs. time transients collected at multiple potentials into current vs. potential MSCVs collected at multiple times.

Constructed MSCVs were displayed in terms of the time after the potential step at which they were sampled. The sampling time can be related to an equivalent scan rate through Equation 2.1[5].

$$\nu = \frac{RT}{Ft} \tag{2.1}$$

Equation 2.1: *Calculation of the equivalent scan rate (ν) when sampling at a specified time (t), where R is the ideal gas constant, and T is temperature.*

Table 2.1 shows the times at which MSCVs were sampled, and their equivalent scan rates. This highlights the effectiveness of the MSCV procedure, as the same data set can produce voltammograms corresponding to scan rates between 50 mV s^{-1} and over 10 V s^{-1}.

Table 2.1: *Equivalent scan rates (ν) for MSCVs when sampling at a specified time (t).*

Sampling Time / s	**Equivalent Scan Rate / V s^{-1}**
0.0025	10.27
0.005	5.14
0.01	2.57
0.02	1.28
0.05	0.51
0.1	0.26
0.2	0.13
0.5	0.05

2.4 Verification of normalisation procedure conditions

The normalisation procedure detailed in Section 3.1 was verified by recording a MSCV for $Ru(NH_3)_6Cl_3$ reduction, and then normalising the resultant MSCVs using Equation 1.45. This MSCV was recorded using the materials and potentials listed in Table 2.2.

Table 2.2: *Potentials and materials used for MSCVs of $Ru(NH_3)_6Cl_3$.*

				Potentials / V vs. RHE			
Metal	**Electrolyte**	**pH**	**OCP**	**Upper Cleaning Potential**	**Lower Cleaning Potential**	**Upper MSCV potential**	**Lower MSCV potential**
Pt	0.5 M KCl	7	0.85	0.95	-0.05	0.85	0.05

2.5 Kinetics of Fe^{II} / Fe^{III} conditions

Once the MSCV data collection procedure was established and verified, multiple conditions could easily be probed by simply replacing the electrolyte or working electrode. For the study of a quasireversible Fe^{II} / Fe^{III} couple, a solution of 5 mM $Fe(ClO_4)_3$ in 0.5 M $HClO_4$ was probed, using the potentials in Table 2.3.

Table 2.3: *Potentials and materials used for MSCVs of $FeClO_4$.*

				Potentials / V vs. RHE			
Metal	**Electrolyte**	**pH**	**OCP**	**Upper Cleaning Potential**	**Lower Cleaning Potential**	**Upper MSCV potential**	**Lower MSCV potential**
Pt	0.5 M $HClO_4$	0.3	0.85	1.05	0.15	0.95	0.25

2.6 Kinetics of ferro/ferricyanide conditions

As well as sampling naturally slow systems such as the Fe^{II}/Fe^{III} redox couple, faster redox systems can also be sampled by simply shortening the sampling time of the MSCV. This raises the rate of mass transfer whilst the rate of electron transfer stays constant, thus allowing the quasireversible model to be applied. For the study of the application of a

quasireversible model to a reversible system, a solution of 5 mM $K_3Fe(CN)_6$ in 0.5 M KCl was probed, using the potentials in Table 2.4.

Table 2.4: *Potentials and materials used for MSCVs of $K_3Fe(CN)_6$.*

				Potentials / V vs. RHE			
Metal	**Electrolyte**	**pH**	**OCP**	**Upper Cleaning Potential**	**Lower Cleaning Potential**	**Upper MSCV potential**	**Lower MSCV potential**
Pt	0.5 M KCl	7	1.0	1.25	0.35	1.05	0.45

2.7 ORR conditions studied

MSCV was first used to observe oxygen reduction in $KClO_4$ to probe the time dependence of n_{app} in neutral, unbuffered conditions. Perchlorate was chosen to prevent the poisoning of the electrode surface by halide adsorption, which could reduce the electrode activity by blocking adsorption sites[61,62]. There is still the possibility of poisoning of chloride by trace quantities of chlorides, which should be considered. In the case of the TraceSELECT $HClO_4$ from Sigma-Aldrich, a 0.1 M solution contains around 0.114 ppm of Cl^-, which should not have too great an effect[62]. A more significant source of Cl^- would likely be leakage from the SCE reference electrode. To combat this, experiments should be kept as short as possible, the SCE electrode should be introduced to the cell as late as possible, and fresh solutions should be used in all cases.

MSCVs were recorded in the presence of phosphate buffer to observe ORR at a fixed pH. A comparison was made between MSCVs recorded at a glass sealed electrode vs. an epoxy sealed electrode to probe the effect of the buffering capacity of glass by dealkalization. The ORR was probed at different metal surfaces by recording MSCVs using electrodes made of Au, Ag, Pt, Cu and Ni, as well as at two Pt alloys, $Pt_{0.9}Ir_{0.1}$ and $Pt_{0.9}Rh_{0.1}$. The effect of poisoning the electrode surface with increasingly strongly binding anions was also investigated to ascertain the role of adsorption steps.

Changes in electrode metal and pH will shift the ORR wave, and so different potential limits are needed in each case. These are summed up in Table 2.5. Potentials for the upper cleaning potential was determined by stepping slightly past the onset of the oxide formation region. The lower cleaning potential was determined as being more negative than the ORR plateau without leading to sudden increase in current associated with the evolution of hydrogen. Changes in electrode insulation or presence of a buffer did not affect the position of the ORR wave, and so have not been included in the table.

Table 2.5: *Potentials used for MSCVs in various electrolytes, with different metal electrodes for the investigation in the oxygen reduction reaction.*

			Potentials / V vs. RHE				
Metal	**Electrolyte**	**pH**	**OCP**	**Upper Cleaning Potential**	**Lower Cleaning Potential**	**Upper MSCV potential**	**Lower MSCV potential**
Au			0.60	0.85	-0.35	0.85	-0.25
Ag			0.70	0.95	-0.15	0.75	0.05
Cu			0.60	0.65	-0.15	0.65	-0.05
Ni	0.1 M $KClO_4$		0.35	0.85	-0.45	0.35	-0.45
$Pt_{0.9}Rh_{0.1}$		7.34	0.95	0.85	-0.45	0.35	-0.45
$Pt_{0.9}Ir_{0.1}$			0.95	0.85	-0.45	0.35	-0.45
			0.95	1.25	-0.05	1.15	0.15
	0.1 M KCl		0.95	1.25	-0.05	1.15	0.15
Pt	0.1 M KBr		0.95	1.25	-0.05	1.15	0.15
	0.1 M KI		0.55	0.95	-0.05	0.55	-0.15
	0.1 M KOH	13	0.95	1.20	0.10	1.20	0.40
	0.1 M $HClO_4$	1	0.90	1.15	0.05	0.90	0.20

2.8 Materials Used

Table 2.6: *Chemicals and materials used during this work*

Name	Formula	Purity /%	Manufacturer
Metal Wires			
Platinum Wire	Pt	99.9	Goodfellow
Gold Wire	Au	99.9	Goodfellow
Silver Wire	Ag	99.9	Goodfellow
Copper Wire	Ag	99.9	Goodfellow
Nickel Wire	Ni	99.9	Goodfellow
Platinum/Rhodium Wire	$Pt_{0.9}Rh_{0.1}$	99.9	Goodfellow
Platinum/Iridium Wire	$Pt_{0.9}Ir_{0.1}$	99.9	Goodfellow
Electrolytes			
Sulfuric Acid	H_2SO_4	95	Fisher
Potassium Perchlorate	$KClO_4$	99	Sigma-Aldrich
Potassium Chloride	KCl	99.6	Fisher
Potassium Bromide	KBr	99	Acros Organics
Potassium Iodide	KI	98	May&Baker
Potassium Hydroxide	KOH	85	Fisher
Perchloric Acid	$HClO_4$	72	Sigma-Aldrich
Redox Species			
Ruthenium Hexamine Trichloride	$Ru(NH_3)_6Cl_3$	99.6	Fisher
Iron Perchlorate Hydrate	$Fe(ClO_4)_3$	99	Aldrich
Potassium Ferricyanide	$K_3Fe(CN)_6$	99	Aldrich
Additives			
Sodium Dihydrogen Phosphate	NaH_2PO_4	99.2	Fisher
Sodium Sulfite	$NaSO_3$	98	Sigma-Aldrich
Argon	Ar	Pureshield	BOC

Solutions were made up using deionised water from a 'Select Range' water purification system from Pur1te, outputting 18.2 MΩ cm resistivity water. All glassware was regularly cleaned by soaking in a diluted solution of Decon 90 (BDH) overnight. Each piece was then rinsed with deionised water and then soaked in deionised water overnight to help remove all traces of the Decon 90. The glassware was then thoroughly rinsed again with deionised water before being left to dry in an oven at 40 °C. The chemicals used in this report are detailed in Table 2.6. The compressed air used for air saturation of electrolytes was from the laboratory's compressed air supply. The air was scrubbed by bubbling through a Drechsel bottle, which contained the same electrolyte as was used in the cell. This acted to humidify the air, as well as remove any trace organics that may have been present.

2.9 Practical Considerations

The procedure to normalise MSCVs, as will be outlined in Section 3.1, requires accurate knowledge of the concentration of the redox species and its concentration. For MSCVs of simple redox compounds the concentration is simply determined by making accurate measurements when making up solutions. Diffusion coefficients are determined from plots of limiting currents measured on microelectrodes of varying size against the respective electrode radius. As the diffusion limited current of a redox species is proportional to the electrode radius (see Equation 1.43) a plot of the limiting current against the electrode radius will give the diffusion coefficient in the gradient. This assumes the concentration, number of electrons transferred and electrode radius are well known, which is a fair assumption in these cases.

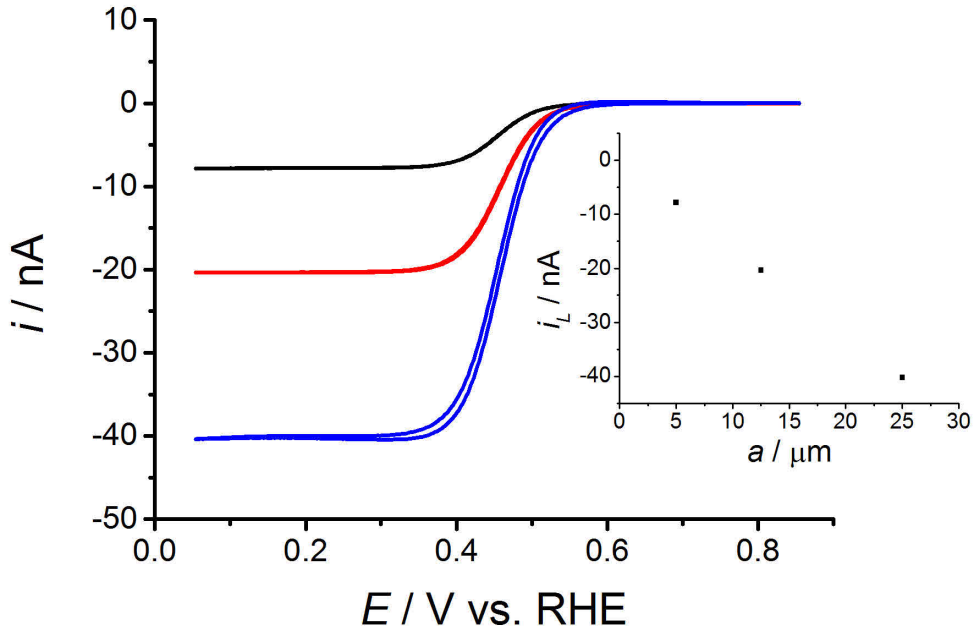

Figure 2.4: *2 mV s^{-1} CVs for 5 mM $[Ru(NH_3)_6]^{3+}$ at 10 µm (black), 25 µm (red) and 50 µm (blue) diameter microdisc electrodes in Ar purged 0.5 M KCl. Insert shows the the linear relationship between limiting current (i_L) and radius (a).*

In the case of studies of the ORR, the concentration of dissolved oxygen (c_{aq}) and its diffusion coefficient (D) could not be simply calculated in the same way, as the combination of two and four electron reduction pathways gave uncertainty over the average number of electrons being transferred during the reduction. Diffusion coefficients were instead calculated using Equation 2.2 from Akita[110], which was found to give values in good agreement with the literature by Sosna[111,112].

$$D = \left(\frac{k_B}{h}\right)\left(\frac{V_m}{N_A}\right)^{2/3} T \exp\left(-\frac{\Delta\alpha x_+ + \Delta\beta x_- + \gamma}{RT}\right) \qquad (2.2)$$

Equation 2.2: *Calculation of the diffusion coefficient (D) from Boltzmann's constant (k_B), Planck's constant (h), the molar volume (V_m) Avogadro's number (N_A) temperature (T), gas constant (R), molar fractions of the cation (x_+) and anion (x_-), and temperature independent components of the free energy of activation of diffusing solute in aqueous solution due to the cation (α), anion (β) and water (γ), where $\Delta\alpha = \alpha - \gamma$ and $\Delta\beta = \beta - \gamma$.*

Values for $\Delta\alpha$, $\Delta\beta$ and γ are tabulated in the literature, and are available for a number of individual cations and anions[110]. The molar volume is defined as follows.

$$V_m = \left(\Sigma c_i + c_w\right)^{-1} \tag{2.3}$$

Equation 2.3: *Calculation of the molar volume (V_m) from sum of the molar concentration of species i (c_i) and the molar concentration of water (c_w).*

The molar concentration of water can be readily calculated for any solution using Equation 2.4.

$$c_w = \frac{\rho - \sum_i M_i c_i}{0.01802} \tag{2.4}$$

Equation 2.4: *Calculation of the molar concentation of water (c_w) from density of the solution (ρ) and the sum of the molar concentrations of species i (c_i) with their corresponding formula masses (M_i).*

Oxygen solubility was determined using the model by Tromans[113], shown in Equation 2.5.

$$c_{aq} = P_{O_2} \exp\left\{\frac{0.046T^2+203.35T\cdot\ln\left(\frac{T}{298}\right)-(299.378+0.092T)(T-298)-20591}{8.3144T}\right\}\left\{\frac{1}{1+\kappa(c_i)^y}\right\}^{\eta} \tag{2.5}$$

Equation 2.5: *Calculation of the solubility of O_2 (c_{aq}) from the partial pressure of oxygen (P_{O_2}), temperature (T), the concentration of the solute (c_i) and solute specific coefficients (κ, y, η).*

The collection of current transients for all potentials across a potential range takes a fairly long time. Care therefore needs to be taken to ensure these values of D and c are accurately known, and also that they remain constant throughout the course of the experiments. This is essential for achieving a high level of reproducibility between experiments. This means that temperature and humidity control is essential, and the degree of air saturation of the solution needs to be reproducible. Humidity was controlled by bubbling air through a sintered Drechsel bottle containing the same electrolyte as in the cell at 25°C. The air was bubbled for 20 minutes before all experiments to ensure a reproducible degree of oxygen saturation. Dissolved oxygen concentration is also affected by the atmospheric pressure, which changes from day to day. The effect of changes in atmospheric pressure on the concentration of dissolved oxygen is taken into account with equation put forward by Colt[114], shown in Equation 2.6. The pressure was measured

and updated hourly by a barometer belonging to the University of Southampton weather station.

$$c_{aq} = \frac{c_{aq,760\ \text{mm Hg}}(P_t - p)}{760\ \text{mm Hg} - p} \tag{2.6}$$

Equation 2.6: *Modification of calculated concentration of dissolved O_2 (c_{aq}) from the concentration found at 760 mm Hg atmospheric pressure ($c_{aq,760\ \text{mm Hg}}$) barometric pressure (P_t) and the vapour pressure of water (p).*

3 Normalisation Procedure

3.1 SCVs at Microelectrodes

Although sampled current voltammetry has been widely studied, it has mostly been used for large electrodes, such as the mercury drop electrode. However, SCV at microelectrodes (MSCV) offers a number of distinct advantages over other voltammetric techniques. Most of the literature focuses on probing reactions under steady state conditions at planar electrodes[115]. However, when employed on a microelectrode, this technique has great potential for the study of transient behaviour of electrochemical systems, as will be discussed.

Microelectrodes allow the recording of both transient and steady state data depending on the time at which the current is sampled. By sampling data at short times (τ_1, Figure 1.12a) transient data is obtained, and a pseudo-steady-state voltammogram can be constructed. By sampling the same data at long times (τ_4, Figure 1.12a), a true steady-state voltammogram can be constructed. This is the key advantage of microelectrodes, as it allows the comparison of pseudo-steady-state voltammograms (τ_1, Figure 1.12b) with true steady-state voltammograms (τ_4, Figure 1.12b) within the same set of experimental data, with both types of data providing high quality sigmoids for easy analysis. The time at which steady-state voltammograms could be sampled can be approximated as the point in the current transients at which a plateau is reached.

The magnitude of the current in any MSCV can be seen to depend on the time at which it is sampled. This makes it difficult to compare MSCVs sampled at different times. To allow comparison of MSCVs regardless of sampling time, a procedure was developed to normalise the voltammograms by dividing the current by the theoretical diffusion controlled current, calculated using Equation 1.45 from Mahon and Oldham[28]. Entering the corresponding sampling times into Equation 1.45 will give a theoretical mass transport limiting current for each MSCV. Division of every data point of the MSCV by

the appropriate theoretical diffusion limiting current will give a normalised MSCV, where the wave at high overpotential will intersect with one on the y axis. Importantly, the overall shape and proportions of the wave are maintained after the normalisation.

$$i_{norm} = \frac{i_{exp}}{\pi n F D c^{\infty} a \cdot f(t)} \tag{3.1}$$

Equation 3.1: *Calculation of the normalised MSCV current (i_{norm}) from the experimental current (i_{exp}), Faraday's constant (F), diffusion coefficient (D), bulk concentration (c^{∞}), electrode radius (a), and the time dependent function from Equation 1.45.*

The normalisation to one on the y axis requires all parameters in Equation 1.45, specifically c, D, a, n and τ, to be well known. Alternatively, if the theoretical value of n is set to be one, the data will then normalise to the apparent number of electrons that were transferred (n_{app}).

$$n_{app} = \frac{i_{exp}}{\pi F D c^{\infty} a \cdot f(t)} \tag{3.2}$$

Equation 3.2: *Calculation of the apparent number of electrons transferred (n_{app}) from the experimental current (i_{exp}), Faraday's constant (F), diffusion coefficient (D), bulk concentration (c^{∞}), electrode radius (a), and the time dependent function from Equation 1.45.*

In this way, the normalisation procedure can be exploited to calculate the number of electrons transferred in a complex, multi-electron redox reaction.

3.2 Verification of normalisation method with Ruthenium

The normalisation method outlined in Section 3.1 was first validated using the single electron reduction of $[Ru(NH_3)_6]^{3+}$ as a model system. In this case, n_{app} will always be one regardless of sampling time, and so it was expected that all MSCVs would be identical post normalisation. MSCVs were recorded from data sampled 2.5 ms, 5 ms, 10 ms, 20 ms, 50 ms, 100 ms, 200 ms and 500 ms after the potential step.

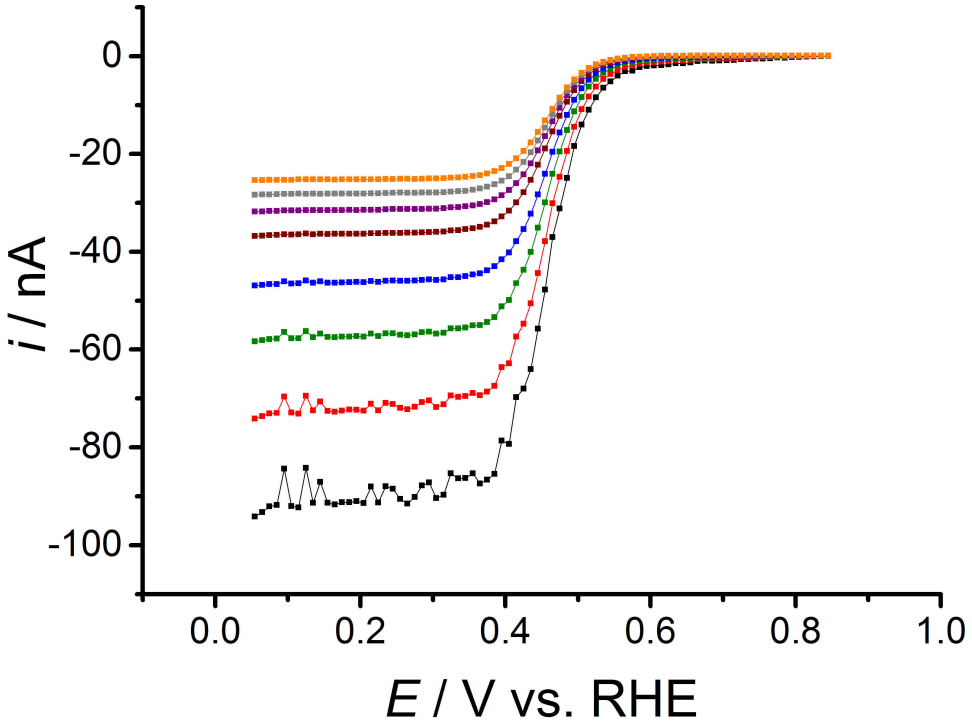

Figure 3.1: *MSCV for 5 mM* $[Ru(NH_3)_6]^{3+}$ *reduction at a 25 µm diameter platinum electrode in Ar purged 0.5 M KCl, sampled 2.5 ms (black), 5 ms (red), 10 ms (green), 20 ms (blue), 50 ms (brown), 100 ms (purple), 200 ms (grey), and 500 ms (orange) after the potential step.*

A negative experimental current was normalised using a positive theoretical current, so that the normalised current will remain negative. This was done intentionally so that the normalised MSCV retains the same orientation as the original. Normalisation was done as described in Section 3.1, using Equation 1.45. The diffusion coefficient was determined from a plot of limiting currents against microdisc radii for differently sized microelectrodes. Electrode radii were accurately measured using the environmental mode of a SEM. The resultant normalised MSCVs are shown in Figure 3.2.

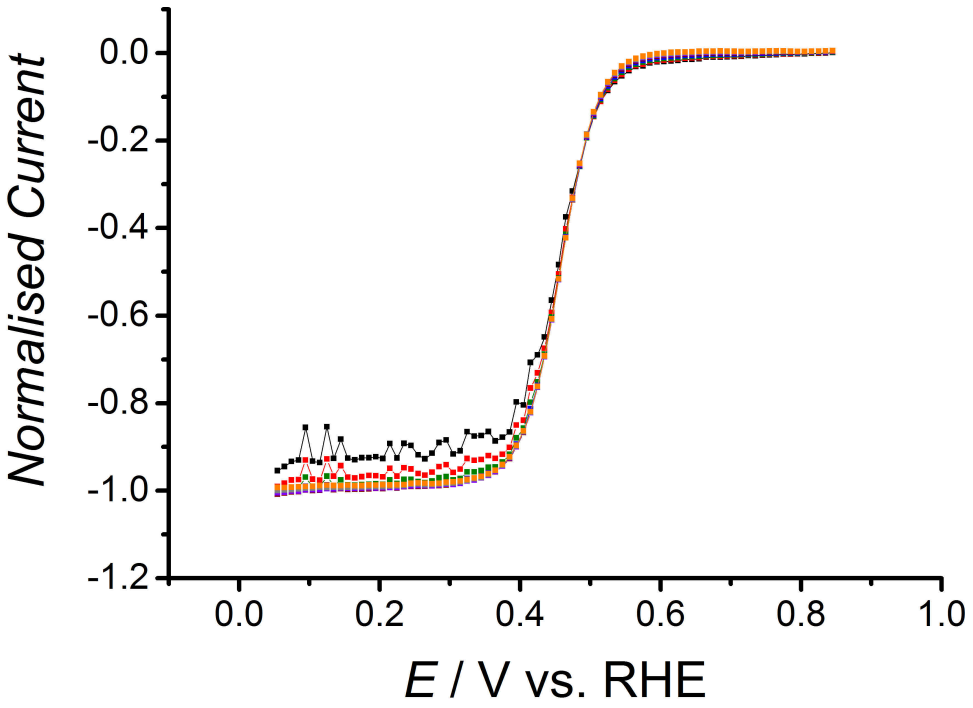

Figure 3.2: *MSCV for 5 mM* $[Ru(NH_3)_6]^{3+}$ *reduction at a 25 μm diameter platinum electrode in Ar purged 0.5 M KCl, sampled 2.5 ms (black), 5 ms (red), 10 ms (green), 20 ms (blue), 50 ms (brown), 100 ms (purple), 200 ms (grey), and 500 ms (orange) after the potential step, normalised using the theoretical limiting current from Equation 1.45, using* $D = 8.4 \times 10^{-6}$ cm^2 s^{-1}, $c = 5$ mM, $a = 12.85$ μm.

It can be seen from these normalised MSCVs that, regardless of sampling time, the voltammograms are made to look identical by the normalisation. Indeed, the difficulty in discerning the MSCV from one sampling time to another indicates how effective the normalisation procedure is. This validation is important, as it not only shows that the normalisation procedure is functioning correctly, but also that the equipment is able to accurately record the current even when sampling at very short times. It is worth noting that some caution should clearly be used when analysing data sampled at 2.5 ms (■, Figure 3.2).

Figure 3.2 shows a key advantage of the MSCV technique in that the constructed sigmoids are identical at 10 ms and 500 ms, despite the mass transport regimes being entirely different at these two sampling times. Shortening the sampling timescale results in an increased rate of mass transport yet the smooth sigmoidal voltammogram is maintained. This is in contrast to cyclic voltammetry at microelectrodes, where increasing the mass

transport through the scan rate results in the appearance of peaks and an increase in the overall charging current across the entire voltammogram, as can be seen in Figure 1.17. This allows the simple visual comparison of MSCVs regardless of the timescale, which is not possible to do for CVs at varying scan rates.

3.3 Influence of acquisition conditions

One slight exception to the success of the normalisation procedure is the MSCV sampled at 2.5 ms (■ in Figure 3.2), which seems to be a little way off of the other values. This seems to be a common observation regardless of the experimental conditions used, and so it is likely down to the limitations of the instrument when it comes to sampling at such a short time. When the current is recorded the corresponding time elapsed since the onset of the potential step (τ) is also recorded. Accuracy of τ is essential for the normalisation procedure, and even small error in its measurement could have a significant impact in the calculated theoretical diffusion controlled current, from Equation 1.45. For instance, a 0.1 ms error in sampling time would have little impact of data sampled at 500 ms, but may equate to a significant error when it comes to sampling on the millisecond timescale.

The error seen in the 2.5 ms MSCV can be shown to be due to inaccuracies in the time measurement by varying the acquisition procedure used when collected the raw data. In Nova 1.10, and indeed in many other electrochemical softwares, current acquisition at short timescales can be made more accurate by using the high speed mode rather than the high stability mode. Further increase in the accuracy of short timescale measurements is achieved by using a faster potentiostat, in this case the PGSTAT30. This has a dedicated ADC750 high speed card, and therefore allows the shortening of the interval between the acquisition of data points. By sampling data points at 10 µs intervals using the faster potentiostat, the deviation from $n_{app} = 1$ can be entirely removed, as is seen in Figure 3.3.

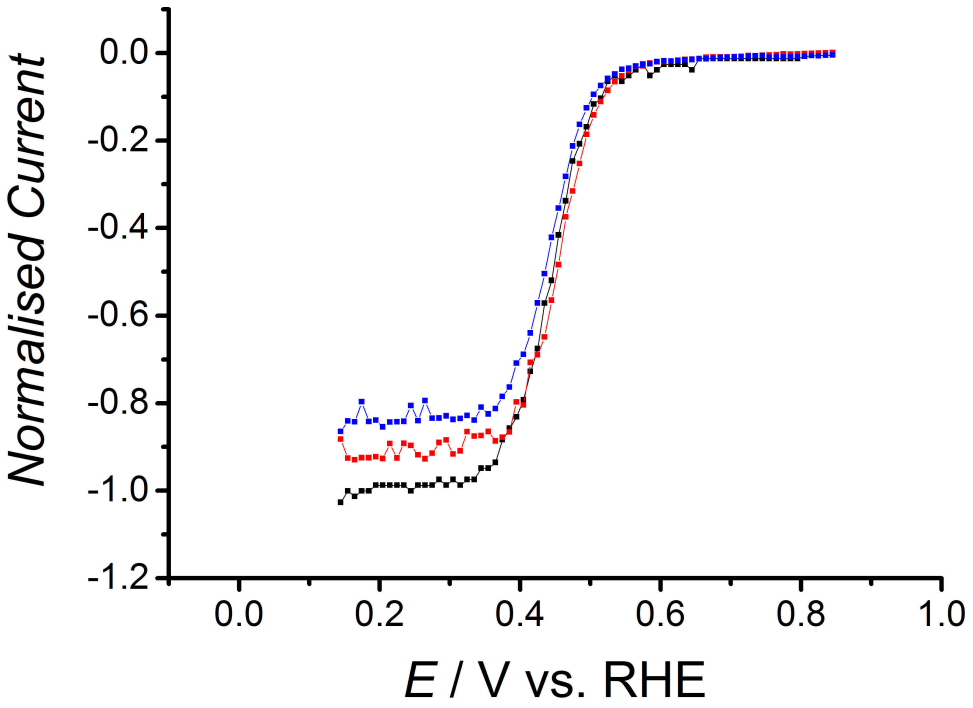

Figure 3.3: *MSCV for 5 mM* $[Ru(NH_3)_6]^{3+}$ *reduction at a 25 µm diameter platinum electrode in Ar purged 0.5 M KCl, sampled 2.5 ms after the potential step, where data was sampled every 2.5 ms under high stability (blue), and high speed conditions (red) with the PGSTAT101, and every 10 µs under high speed conditions (black), with the PGSTAT30, normalised using the theoretical limiting current from Equation 1.45, using* $D = 8.4 \times 10^{-6}$ cm^2 s^{-1}, $c = 5$ *mM,* $a = 12.85$ *µm.*

Sampling on the microsecond timescale removes the error after the normalisation of the 2.5 ms MSCV. However, when sampling at such short times, it is not possible to simultaneous reach the steady state conditions, as sufficiently long transients cannot be recorded before the capacity of the memory buffer of the high speed card is exceeded. A compromise is therefore made so as to allow the recording of undistorted data at short times, whilst sampling for a sufficiently long time as to allow simultaneous recording of transient and steady state data.

3.4 Influence of current ranging

Current ranging is a key parameter when it comes to analysis on the millisecond timescale. Potentiostats function by allowing a current to flow across a resistor. The current is then

determined by measuring the potential drop across the resistor, with the signal being amplified by an operational amplifier (Op Amp) in current follower configuration. Passing a current across a resistor with a low resistance will therefore generate a small potential difference. Selecting a greater resistance will give a greater potential difference. As such, the careful selection of the current range is needed to accurately measure the current. As the current becomes smaller, the potential difference across the resistor becomes smaller, and so the accuracy of the measurement also decreases. Decreasing magnitudes of current therefore requires a larger resistance for accurate measurement. Current ranging is a means of selecting an appropriate resistor for the system being measured. Selecting a smaller current range results in the current being measured across a higher resistance resistor, giving a greater accuracy of measurements at low magnitudes of current.

Many modern potentiostats come with an auto ranging option, which allows the instrument to adjust the assigned current range based on the current being measured. Manually selecting the current range involves initiating the measurement across a set resistor in the potentiostat circuit. Auto current ranging involves the potentiostat switching between resistors at the onset of the measurement until the optimum current range is selected. As the measurement progresses, the system stays active and the current range may be further modified should the magnitude of the current change.

This is a simple option as the ideal range is automatically selected based on the magnitude of the current being recorded. However, this automatic ranging comes with limitations, predominantly due to the limitations associated with the speed of the electronics being used. By definition, a few data points must be recorded before the correct current range may be selected, and so the initial data recorded under automatic ranging may not necessarily be recorded under ideal conditions. Switching the current range in the middle of a measurement comes with a second flaw. The switch in current range is often accompanied by a spike in the measured current. These spikes are due to the switch from one resistor to the next. Say a 100 μA current is measured across a 10 kΩ resistor. This gives a potential difference of 1 V across the resistor. If potentiostat then switches to a 1 kΩ resistor, the potential difference will drop to 0.1 V. This potential drop will not

be instantaneous, but will take a short time to take effect. This delay in the drop of the potential difference across the resistance is observed as spikes in the measured current, as can clearly be seen in Figure 3.4.

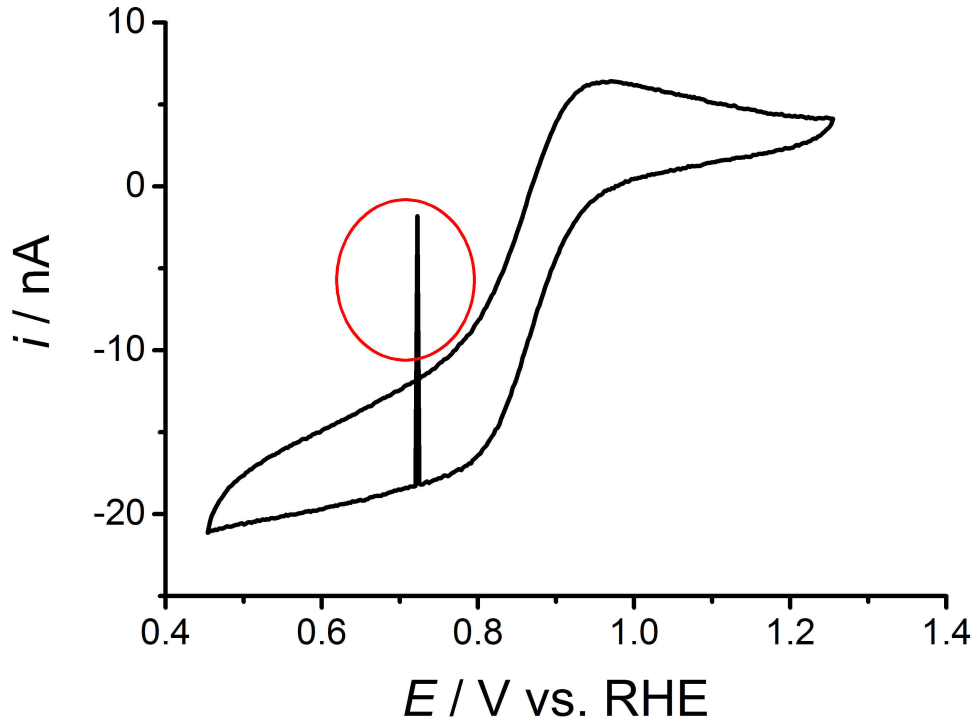

Figure 3.4: *Current spike seen on a CV for 5 mM $K_3Fe(CN)_6$ at a 25 µm diameter platinum electrode in Ar purged 0.5 M KCl, caused by switching the current range during data acquisition.*

In many cases, the problems with automatic current ranging are not significant. However, when making measurements on the millisecond timescale they can obscure transient data. For transient experiments, the current range must therefore be fixed. This means care must be taken to select the correct current range prior to experiments being performed. If the current range selected is too high, then data is often obscured by background noise from surrounding electrical equipment, as is seen in Figure 3.5. This is despite best efforts to ground equipment and with the use of a Faraday cage. If the selected current range is too low then it leads to an overload of the operational amplifier in the current follower being used. This results in the loss of current measured on the short timescale until the Op Amp recovers, as can be seen in Figure 3.6.

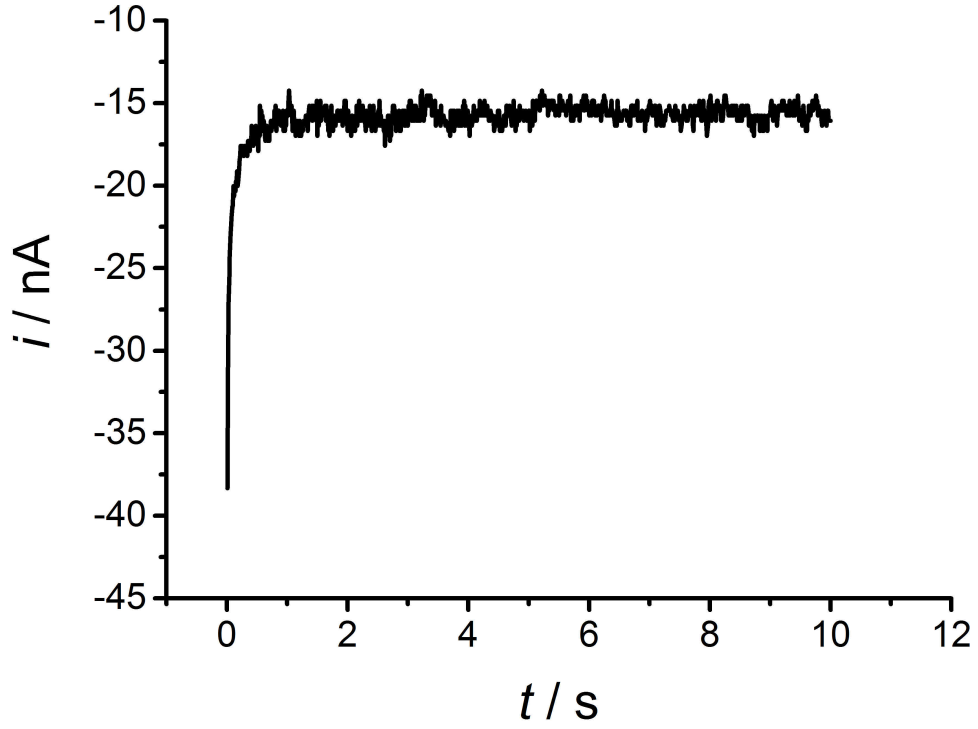

Figure 3.5: *Chronoamperogram for 5 mM $K_3Fe(CN)_6$ at a 25 µm diameter platinum electrode in Ar purged 0.5 M KCl, where the selected current range was too high, showing the masking of data by electrical noise.*

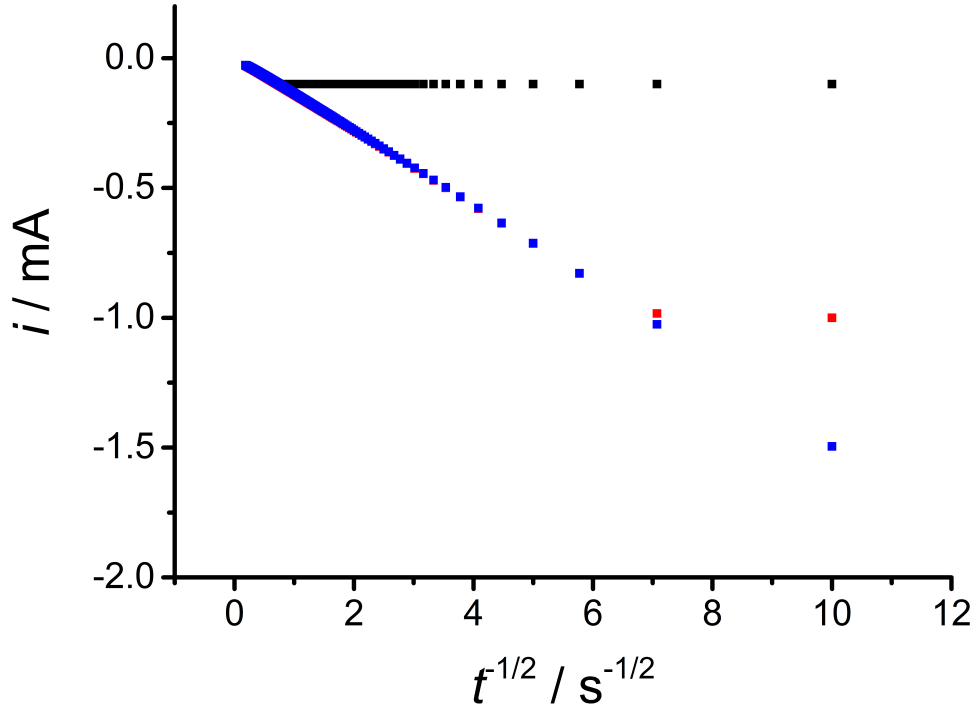

Figure 3.6: *Chronoamperogram for 5 mM $K_3(FeCN)_6$ at a 5 mm diameter platinum electrode in Ar purged 0.5 M KCl, where the selected current range was 0.1 mA (black), 1 mA (red), and 10 mA (blue), showing that data at short times gets cut off when too low a current range is selected.*

Ideally, the current should be measured using a logarithmic amplifier in order to precisely measure the entire range of the transient. However, commercially available potentiostats are fitted with linear amplifiers and so a compromise must be selected. The chosen current range should be low enough to minimise the interference of noise whilst being high enough to prevent data loss due to saturation of the Op Amp. Saturation of the Op Amp may be technically impossible to avoid, in which case the range should be selected such that the Op Amp is entirely recovered before the first data point is measured. Recovery times vary across different Op Amps, and may differ from the saturation time. As a rule of thumb, the current range selected should be a maximum of three times the current being measured.

3.5 Importance of the cleaning waveform

The importance of the cleaning waveform in giving reliable and reproducible MSCVs can be demonstrated by normalising MSCVs that were constructed from chronoamperograms that were collected without the waveform in place. These MSCVs deviated from the expected sigmoidal shape that was seen in the case of MSCVs recorded with the cleaning waveform, particularly for short sampling times. The normalised MSCVs still appear to be sigmoidal but the currents are larger than the diffusion controlled values and systematically increase as the sampling time is decreased, as is seen in Figure 3.7.

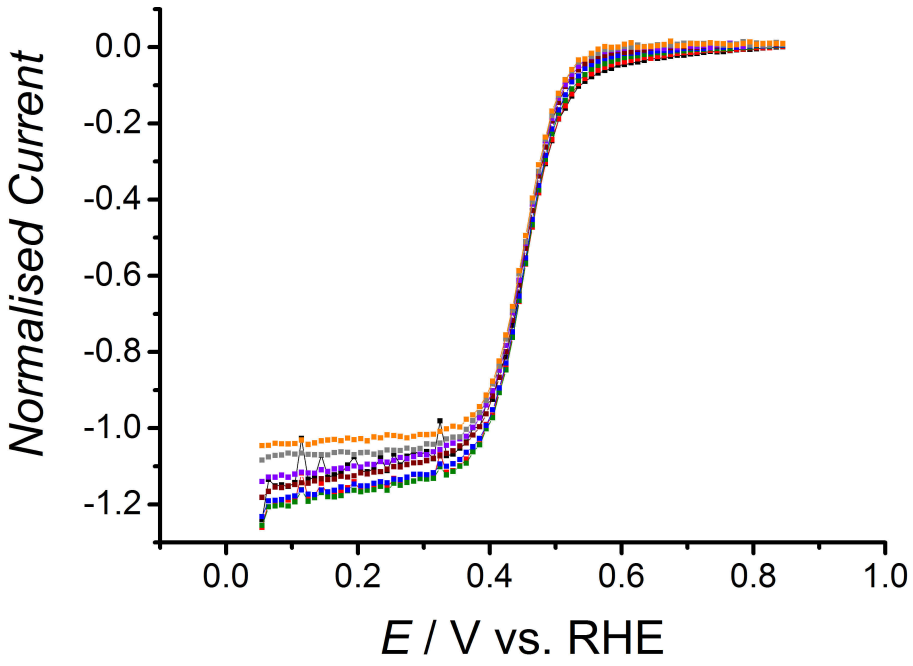

Figure 3.7: *MSCV for 5 mM* $[Ru(NH_3)_6]^{3+}$ *reduction at a 25 μm diameter platinum electrode in Ar purged 0.5 M KCl with no cleaning waveform, sampled 2.5 ms (black), 5 ms (red), 10 ms (green), 20 ms (blue), 50 ms (brown), 100 ms (purple), 200 ms (grey), and 500 ms (orange) after the potential step, normalised using the theoretical limiting current from Equation 1.45, using* $D = 8.4 \times 10^{-6}$ cm^2 s^{-1}, $c = 5$ *mM,* $a = 12.85$ *μm*

This deviation was not observed when the electrode was preconditioned before each step, so non-Faradaic processes such as double layer charging can be ruled out. The extra current therefore reflects the contribution from surface bound redox processes such as the reduction of Pt oxides. The adsorption of hydrogen could also affect the current but only at sufficiently negative potentials of less than around 0.15 V vs. RHE in neutral $KClO_4$. Comparison of Figure 3.7 with a cyclic voltammogram recorded in the absence of $[Ru(NH_3)_6]^{3+}$ (Appendix, Figure 10.1) shows the extra current in Figure 3.7 occurs over a significantly wider range than where hydrogen adsorption is observed.

Certainly the quality of the voltammetry is greatly improved by the implementation of the cleaning waveform. As described previously, the conditioning waveform was carefully designed to ensure every point on the MSCVs was recorded in identical conditions and to remove the Faradaic contribution from surface-bound redox processes. The cleaning potentials and sweep directions guarantee that the electrode surface is first oxidised and

then reduced. The last conditioning sweep in particular guarantees that the open circuit potential is approached from a more negative potential after having reduced the oxide and desorbed all hydrogen. Comparison of Figure 3.2 with Figure 3.7 illustrates the dramatic improvements that the conditioning waveform made to the shape of the voltammograms at short sampling times.

In all experiments using MSCV in this report the cleaning waveform was applied, with the potentials being adjusted depending on the redox species being probed. In the case of single electron redox probes, the success of the cleaning waveform is indicated by the neat alignment of all MSCVs on top of each other and a normalisation to one on the y axis. For more complicated multi-electron reductions where this is often not possible, the success of the cleaning waveform is indicated by clean and reproducible voltammetry across separate experiments. Small variations to the cleaning potentials have a negligible impact on the constructed MSCV, indicating that the waveform is sufficient for the system in question.

An alternative means of providing identical MSCVs at all sampling times was the use of a background subtraction method. Here, MSCV experiments were carried out without the conditioning waveform and without $[Ru(NH_3)_6]^{3+}$ to produce a background MSCV for each sampling time. These were subtracted from the corresponding MSCVs recorded in presence of ruthenium hexamine before the normalisation was performed as before. The background subtraction approach was not only far more cumbersome, requiring two mathematical steps and taking considerably more time, it also turned out to give a far poorer result when it came to producing identical sigmoidal curves at varying sampling times, when compared to the use of the cleaning waveform.

The ability to condition the electrode before each potential step is a key advantage of MSCV. This had been exploited when normal pulse voltammetry was applied to dropping mercury electrodes, since each step was recorded with a fresh drop. With programmable computerised instrumentation, any form of electrochemical waveform can be implemented within the MSCV protocol to refresh the surface of solid electrodes before each step. To our knowledge this unique advantage of MSCV has been overlooked.

4 Kinetic Analysis of MSCVs

4.1 Development of a kinetic model for MSCVs

With the normalisation procedure verified in Chapter 3, it was then possible to use MSCV to find the kinetic parameters for a redox system. As with SCV at planar electrodes, the MSCV sigmoid allows calculations of the standard electrochemical rate constant, standard electrode potential and transfer coefficient by fitting the constructed voltammogram to a theoretical model. However, the model given in Equation 1.38 cannot be simply used, as it does not take into account the onset of the hemispherical diffusion field that is found at microelectrodes. For the same reason, it is not possible to use the model for determining kinetic parameters from the model for steady state voltammetry at microelectrodes as given in Equation 1.51, as this model assumes a well developed hemispherical diffusion field, which would not be present when sampling at short times.

In order to glean kinetic information from MSCVs, a novel model was constructed. The Oldham model for the calculation of kinetic parameters from steady state linear sweep voltammograms at microelectrodes, as shown in Equation 1.51, was used as the basis of the new model[29]. As the model only applies to steady state linear sweep voltammetry, it assumes the presence of a hemispherical diffusion field. However, Equation 1.51 does not account for the change in the size of the diffusion layer as the timescale of the measurements change, and so could not be applied to short timescale MSCVs, where the hemispherical diffusion field is not fully developed. A time dependent mass transfer coefficient was therefore proposed[116].

$$k_m = \frac{D}{a} \cdot f(t) \tag{4.1}$$

Equation 4. 1: *Time dependent mass transfer coefficient (k_m), from the diffusion coefficient (D), electrode radius (a) and the time dependent function from Equation 1.45 ($f(t)$).*

This mass transfer coefficient was then inserted into Equation 1.51 to allow for the calculation of kinetic parameters at a given sampling time for a quasireversible system.

$$i_{theo} = \frac{i_D}{\theta}\left[1 + \frac{\pi}{\kappa\theta}\left(\frac{2\kappa\theta + 3\pi}{4\kappa\theta + 3\pi^2}\right)\right]^{-1} \tag{4.2a}$$

$$\kappa = \frac{k^0 a}{D_O \cdot f(D_O, t)} \exp\left\{\frac{-\alpha n F(E - E^0)}{RT}\right\} \tag{4.2b}$$

$$\theta = 1 + \frac{D_O \cdot f(D_O, t)}{D_R \cdot f(D_R, t)} \exp\left\{\frac{nF(E - E^0)}{RT}\right\} \tag{4.2c}$$

Equation 4. 2: *Theoretical current at a MSCV under quasireversible conditions (i_{theo}) from the number of electrons transferred (n), diffusion coefficient for the oxidised (D_O) and reduced species (D_R), sampling time (t), electrode radius (a), standard electrochemical rate constant (k^0), transfer coefficient (α), Faraday's constant (F), potential (E), standard potential (E^0), Boltzmann's constant (R) temperature (T) and the theoretical limiting current (i_D) and time dependent function ($f(t)$) from Equation 1.45.*

This is where MSCV offers a clear advantage over the other given models for the calculation of kinetic parameters. For the methods given in earlier chapters, the system is required to be subject to a specific level of reversibility in order for the model to be valid. This constrains the application of these methods, and also makes them inapplicable for the calculation of kinetic parameters for reversible systems. With MSCV, the degree of reversibility is controlled by the sampling time. Shorter sampling times give faster rates of mass transport, which therefore decrease the reversibility of the system. By careful selection of the sampling time for a MSCV, it is therefore possible to tune the reversibility of the system so that the desired model may be applied.

This is where the use of a microelectrode is essential. The rapid resolution of the charging current at a microelectrode means that Faradaic information is accessed even at incredibly short time scales. This makes it possible for the sampling time to be sufficiently decreased to make a reversible system behave quasireversibly. In this way, MSCV can be used for the calculation of kinetic parameters for a fast redox system without the need of complicated experimental rigs or expensive equipment. As was previously described for the case of steady state voltammograms at microelectrodes in Chapter 1.4, the degree of reversibility is also dependent on the applied overpotential, as well as the sampling time. This means that for MSCV, it is possible to make the system behave irreversibly by manipulating the sampling time, the potential range, or possibly both simultaneously. Whilst manipulating the reversibility via the potential has the disadvantage of reducing the

number of data points being analysed, a combination of both methods allows a considerable reduction in the reversibility of the system being analysed. This unique combination means that MSCV is able to use quasireversible models to analyse much faster systems than any of the other models previously described would allow.

4.2 Kinetics of the Fe^{II}/Fe^{III} redox system

The system first chosen for kinetic analysis was the Fe^{II} / Fe^{III} couple, as it is a simple, single electron transfer with well documented kinetic parameters in the literature for comparison[117,118]. MSCVs were recorded for the reduction of $Fe(ClO_4)_3$ in 0.5 M $HClO_4$ using a 25 μm platinum electrode, and are shown in Figure 4.1.

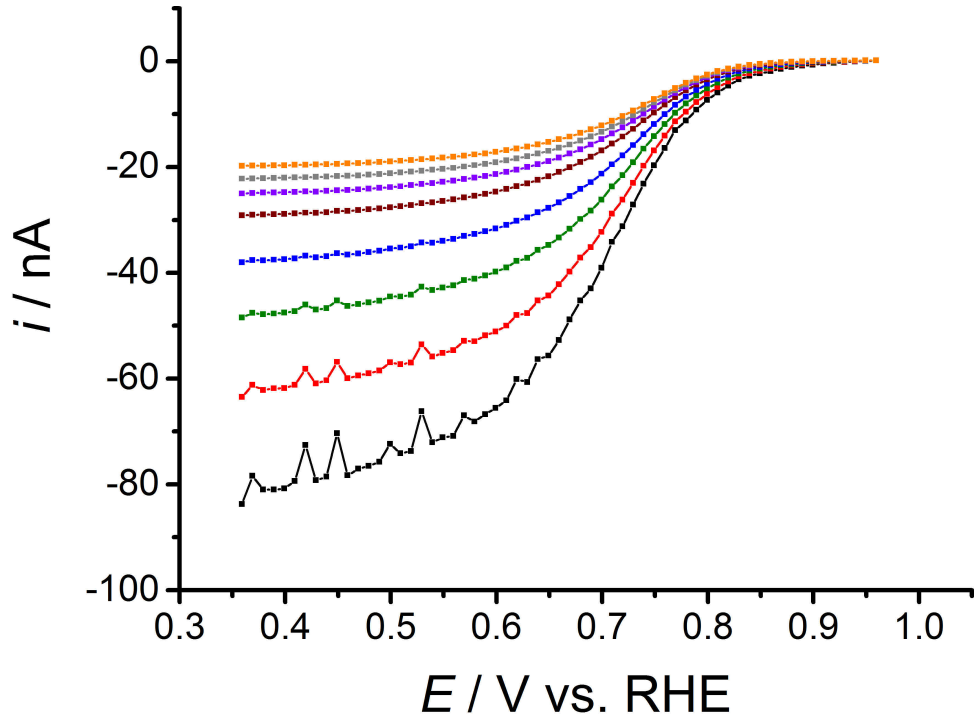

Figure 4.1: *MSCV for 5 mM $Fe(ClO_4)_3$ reduction at a 25 μm diameter platinum electrode in Ar purged 0.5 M $HClO_4$, sampled 2.5 ms (black), 5 ms (red), 10 ms (green), 20 ms (blue), 50 ms (brown), 100 ms (purple), 200 ms (grey), and 500 ms (orange) after the potential step.*

MSCVs were then normalised as described in Chapter 3.1 using Equation 1.45. D_O was calculated from a plot of limiting currents against microdisc radii for differently sized

microelectrodes. D_R was calculated assuming that $D_O/D_R = 0.83$[118]. Electrode radii were accurately measured using the SEM, as described in Section 2.1. All parameters used are given in Table 4.1. The resultant normalised MSCVs are shown in Figure 4.2.

Table 4.1: *Parameters used for normalisation and subsequent kinetic analysis of MSCVs for the Fe^{II}/Fe^{III} redox couple.*

Symbol	Parameter	Value
a	Electrode radius	12.85 μm
n	Number of electrons transferred	1
D_O	Diffusion coefficient for Fe^{III}	6.29 x 10^{-6} cm^2 s^{-1}
D_R	Diffusion coefficient for Fe^{II}	7.60 x 10^{-6} cm^2 s^{-1}
c	Concentration of $Fe(ClO_4)_3$	5 mM
T	Temperature	298 K

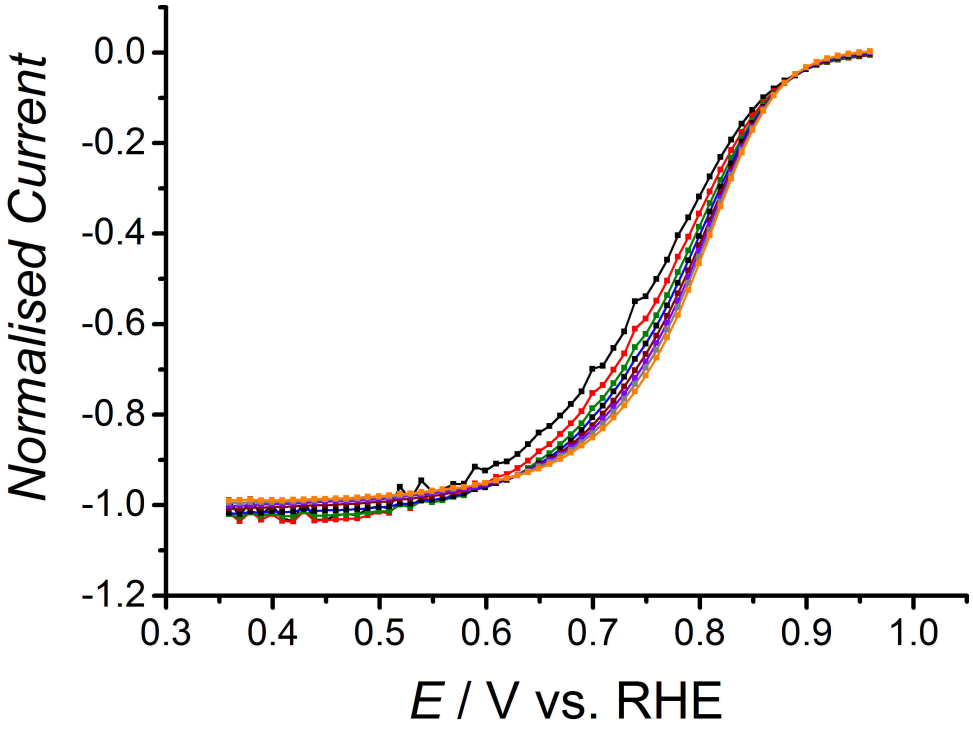

Figure 4.2: *MSCV for 5 mM $Fe(ClO_4)_3$ reduction at a 25 μm diameter platinum electrode in Ar purged 0.5 M $HClO_4$, sampled 2.5 ms (black), 5 ms (red), 10 ms (green), 20 ms (blue), 50 ms (brown), 100 ms (purple), 200 ms (grey), and 500 ms (orange) after the potential step, normalised using the theoretical limiting current from Equation 1.45, using the parameters listed in Table 4.1.*

As with $[Ru(NH_3)_6]^{3+}$ (Figure 3.2), at large overpotentials all MSCVs are neatly aligned and are normalised to one on the y axis. However, at more positive potentials differences can clearly be seen when comparing MSCVs sampled at different times. MSCVs sampled at longer times give a noticeably steeper slope than those sampled at shorter times. Specifically, the MSCV sampled at 500 ms (Figure 4.2, ■) shows a steep slope indicative of a reversible reduction wave. As the sampling time decreases, the curve becomes more drawn out with the slope becoming less steep, which is indicative of increasing limitations from kinetic effects. This is a key advantage of the MSCV normalisation technique, as it is able to display kinetic limitations of a system by removing the varying mass transport effects at all timescales.

MSCVs for $Fe(ClO_4)_3$ reduction were then used to calculate values for E^0, k^0 and α by non-linear regression to fit experimental sigmoidal curves to the model in Equation 4.2. The kinetic parameters were allowed to vary whilst all other parameters listed were fixed. The values used are given in Table 4.1. Since kinetic parameters are independent of sampling time, multiple MSCVs were simultaneously fitted as a means of obtaining an average fit across multiple data sets. MSCVs sampled at 100, 200, 300, 400 and 500 ms were simultaneously fitted using the global fit function of Origin 9.1. According to Equation 4.1, these sampling times correspond to mass transfer coefficients between 0.0078 and 0.010 cm s^{-1}, which related to rotation rates of between 500 and 900 Hz at a rotating disc electrode. These sampling times were chosen to ensure that k_m at all sampling times was approximately equal to the heterogeneous rate constant for Fe^{III} reduction, as given in the literature. This therefore allows the quasireversible model to be applied to the full MSCV wave. The resultant fit is shown in Figure 4.3.

An excellent fit was achieved after only a few iterations. The high quality of the fit (R^2 = 0.999) is clearly seen from the match between theoretical and experimental data. Application of a Gaussian distribution of weights around the slope of the wave made a negligible difference to the obtained values. The regression analysis gave $E^0 = 0.75 \pm 0.0004$ V vs. RHE, $k^0 = 0.008 \pm 0.0001$ cm s^{-1} and $\alpha = 0.37 \pm 0.002$. The high quality of the fit is reiterated in the remarkably small errors associated with the fitted data. These

values are in good agreement with those quoted in the literature, where $k^0 = 0.008$ cm s^{-1} and 0.009 cm s^{-1} and $\alpha = 0.37$ were previously recorded on rotating disc electrodes[117,118].

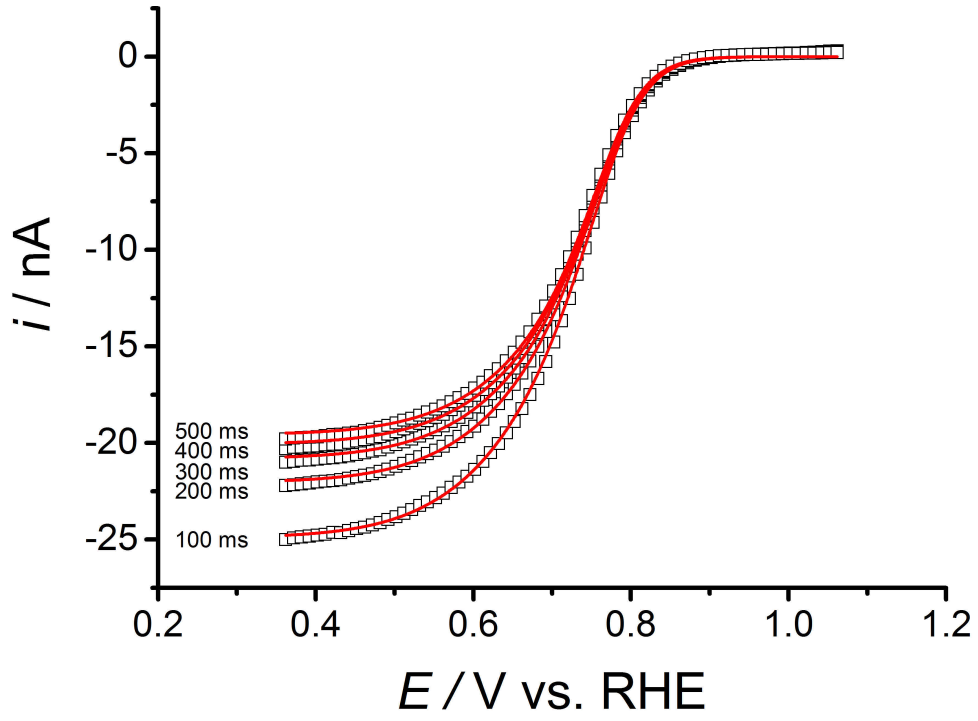

Figure 4.3: *MSCV for 5 mM $Fe(ClO_4)_3$ reduction at a 25 µm diameter platinum electrode in Ar purged 0.5 M $HClO_4$, sampled 100, 200, 300, 400 and 500 ms after the potential step, showing the experimental data (□) and the fitted model (—). Theoretical curves were produced by nonlinear curve fitting to Equation 4.2 using the parameters listed in Table 4.1.*

This method takes advantage of the ability of MSCV to alter the rate of mass transport seen across the entirety of wave, thereby giving a quasireversible voltammogram at all potentials. This allows the entirety of the MSCV to be fitted to the quasireversible model given in Equation 1.51. Calculated values of E^0, k^0 and α are in excellent agreement with the literature. To confirm the accuracy of these values for the Fe^{II}/Fe^{III} system, they were also calculated using the cyclic voltammetry method as discussed in Chapter 1.3.3. A jacketed cell was set up with 5 mM $Fe(ClO_4)_3$ in 0.5 M $HClO_4$, with a 5 mm platinum working electrode, SCE reference, and platinum gauze counter. The cell was kept at 25°C via a thermostatically controlled water bath. The reference electrode was brought into as close a position as possible to the working electrode via a Luggin capillary. A series of

cyclic voltammograms were then run at increasing scan rates, which can be seen in Figure 4.4.

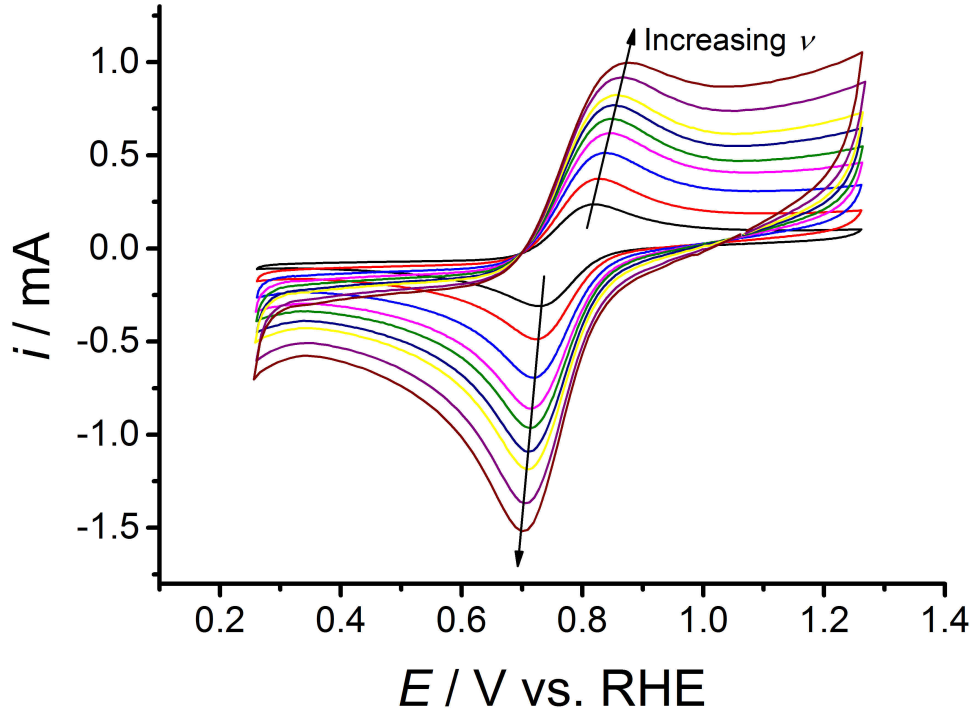

Figure 4.4: *Cyclic voltammograms for the Fe^{II}/Fe^{III} redox couple, using 5 mM $Fe(ClO_4)_3$ in Ar purged 0.5 M $HClO_4$ at a 5 mm diameter platinum electrode, showing the increase in peak separation with increasing scan rate.*

Peak potentials were read for each CV and then used to calculate the peak separation (ΔE_p). These were then used to calculate kinetic parameters for the Fe^{II}/Fe^{III} system using the Nicholson method, as given by Equation 1.19. The readily available values for the dimensionless kinetic parameter ψ from the data tables were not used, due to the limited number of values and the assumptions that $D_O = D_R$ and $\alpha = 0.5$. Instead, the approximation for ψ from Siraj *et al.*, given in Equation 1.20, was used. A non-linear regression was then performed on a plot of ΔE_p vs. ν using Equations 1.19 and 1.20, where k^0, E^0 and α are allowed to vary, and all other values are fixed as those given in Table 4.1. The fitted data is shown in Figure 4.5.

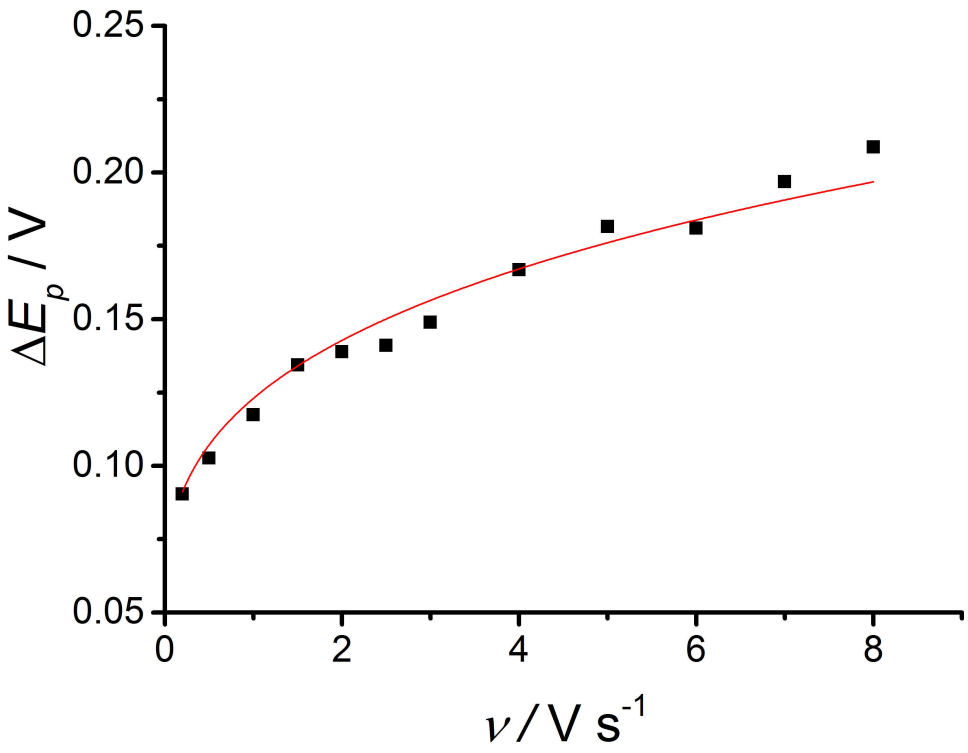

Figure 4.5: *Plot of peak separation (ΔE_p) from cyclic voltammograms (■) against the corresponding scan rates (ν) for the Fe^{II}/Fe^{III} redox system, recorded in 5 mM $Fe(ClO_4)_3$ in Ar purged 0.5 M $HClO_4$ at a 5 mm diameter Pt electrode, against a SCE reference electrode and platinum counter, with a Luggin capillary to reduce iR drop. Also shown is the fitted curve from a non-linear regression of experimental data points using Equations 1.19 and 1.20 (—).*

The resultant non-linear regression gave $k^0 = 0.009$ cm s^{-1} and $\alpha = 0.39$. These values are in excellent agreement with those determined by the novel MSCV method presented earlier. To further validate this fit, COMSOL Multiphysics v 4.4 was used to construct a number of theoretical MSCVs to match those generated in previous experiments. Values for D_O, D_R, c, a and τ were set to match those used in the model, and values for E^0, k^0 and α were set to match those gleaned from the previous fit.

MSCVs were constructed by simulating a number of current transients using the COMSOL package for the reduction of Fe^{3+} to Fe^{2+}. The simulation assumes transport only by diffusion according to Fick's second law. The boundary conditions at the domain floor, domain wall and symmetry axis are set to zero flux, and the boundary condition for the domain ceiling is set such that the concentration of Fe^{3+} and Fe^{2+} at any given position

($c|_x$) is equal to the concentration in the bulk solution (c^∞). The boundary conditions at the electroactive surface of the microelectrode surface was set to follow Butler-Volmer kinetics according to Equation 1.5. Values for c_x are determined using an expanding mesh, which gives an increased density of elements near to the electrode edge for accurate determination of concentration gradients at the edge sites. This is vital as these edge sites give significant contributions to the overall flux to the electrode surface, as discussed in Section 1.4.

With the model set up a potential step was applied, starting from a potential where no net reduction is observed to one where a significant, mass transport controlled rate of reduction is observed. For said potential step, a chronoamperogram is recorded by integrating the flux of Fe^{3+} to the electrode. This process is then repeated for a number of potentials at 10 mV intervals along the redox wave in question. MSCVs are then constructed as discussed in Section 1.3.5, by simply treating the theoretical chronoamperograms in the same way as for the experimental ones. The values for parameters used for the simulations are given in Table 4.2.

Simulated results were first validated by comparing a theoretical transient at high overpotential with $k^0 = 10$ cm s^{-1} to give full diffusion control, to one constructed using Equation 1.45. The two theoretical transients showed a difference of less than 0.1 %, indicating an excellent agreement. Chronoamperograms were simulated for the reduction of Fe^{3+} to Fe^{2+} using the parameters stated in Table 4.2. MSCVs were then constructed from data sampled 50, 100, 200 and 500 ms after the onset of the potential step. These simulated MSCVs were then compared against the corresponding experimental MSCVs from the same data set that was used to calculate the kinetic parameters, as shown in Figure 4.6.

Table 4.2: *Simulation parameters for the calculation of theoretical chronoamperograms for the single electron reduction of* $Fe(ClO_4)_3$.

Symbol	Value	Description
a	12.85 µm	Microdisc radius
r_g	3 mm	Radius of the glass around the electroactive area
r_{max}	20 mm	Radius of the solution domain
z_{max}	20 mm	Height of solution above the domain floor
z_{ede}	10 mm	Height of microelectrode above domain floor
T	298 K	Temperature of solution
c_R^∞	0 mM	Bulk concentration of Fe^{2+}
D_R	7.61 x 10^{-6} cm^2 s^{-1}	Diffusion coefficient of Fe^{2+}
c_O^∞	5 mM	Bulk concentration of Fe^{3+}
D_O	6.29 x 10^{-6} cm^2 s^{-1}	Diffusion coefficient of Fe^{3+}
E^0	0.75 V vs. RHE	Standard potential for electron transfer
k^0	0.008 cm s^{-1}	Standard rate constant for electron transfer
α	0.37	Transfer coefficient for electron transfer

The excellent agreement seen in Figure 4.6 between experimental and theoretical MSCVs constructed from the previously derived parameters gives clear indication of the accuracy of the method. Further calculation of kinetic parameters by the same means can be assumed to be accurate.

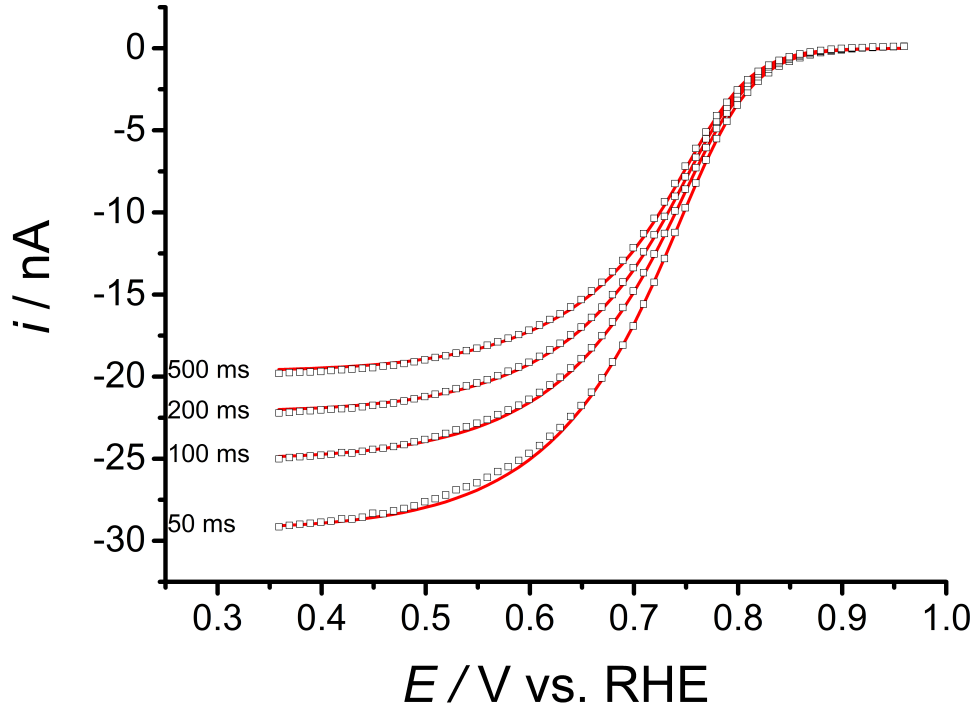

Figure 4.6: *MSCV for 5 mM $Fe(ClO_4)_3$ reduction at a 25 µm diameter platinum electrode in Ar purged 0.5 M $HClO_4$, sampled 50, 100, 200 and 500 ms after the potential step, showing the experimental data (□) and the theoretical data from COMSOL simulations (—), produced using the parameters given in Table 4.2.*

4.3 Kinetics of the ruthenium hexamine system

Section 4.1 highlighted the efficiency of MSCV for the calculation of the kinetic parameters of a redox system. The faster ferri/ferrocyanide redox couple was also successfully probed, giving E^0 = 0.88 ± 0.0006 V vs. RHE, k^0 = 0.089 ± 0.013 cm s^{-1} and α = 0.40 ± 0.03. These values are in excellent agreement with the literature, where k^0 = 0.8 cm s^{-1}, 0.9 cm s^{-1} and 0.10 cm s^{-1} and α = 0.45 were previously recorded on rotating disc electrodes and by hydrodynamic voltammetry[119–121] (see Appendix 10.5 for full details). To test the limits of the MSCV kinetic technique, an even faster system was chosen for analysis. The third species investigated for its kinetic parameters using MSCV was ruthenium hexamine. This is a single electron redox species that is well known for being extremely fast, and so will certainly test the limits of MSCV as a technique. Values for k^0 vary greatly within the literature, ranging from 0.4 ± 0.12 cm s^{-1} measured by fast scan

cyclic voltammetry[122], 4.0 ± 2.0 cm s^{-1} by SECCM[123] up to as high as 17.0 ± 0.9 cm s^{-1} measured by nanoelectrodes[124]. In fact, a search through the literature shows that the quoted value for k^0 has increased from 0.1 to many cm s^{-1}, most likely due to the advancement in the techniques used to record it[125].

Equation 4.1 was used to give a rough guide as to what timescale would be needed to give a rate of mass transfer fast enough to give quasireversible conditions. Although a range of timescales would likely be valid, an approximation was made such that quasireversible conditions would be achieved when the rate of mass transport was equal to the rate of electron transfer. Based on this assumption, the quoted heterogeneous rate constants correspond to sampling times between 20 μs and 10 ns. This makes it clear that the previous time range obtained for MSCVs is not sufficient in this case. MSCVs would need to be recorded on a much faster timescale.

Previous experiments recorded the MSCVs using the Autolab PGSTAT101. This has a limited range of acquisition conditions, where the shortest sampling time possible is 1.3 ms. The more powerful PGSTAT30 allows a data point to be recorded ever 1.3 μs, giving access to a much faster time domain for MSCV. MSCVs were therefore recorded every 10 μs for the single electron reduction of ruthenium hexamine. MSCVs were then normalised in the way previously described in Chapter 3.1 using Equation 1.45. The diffusion coefficient for D_O was calculated from a plot of limiting currents against microdisc radii for differently sized microelectrodes. D_R was then calculated assuming that D_O / $D_R = 0.71$[126]. Electrode radii were accurately measured using the environmental mode of a SEM. All parameters used are given in Table 4.3. The resultant normalised MSCVs are shown in Figure 4.7.

Table 4.3: *Parameters used during the normalisation and subsequent kinetic analysis of MSCVs for single electron reduction of ruthenium hexamine.*

Symbol	Parameter	Value
a	Electrode radius	12.6 µm
n	Number of electrons transferred	1
D_O	Diffusion coefficient for $[Ru(NH_3)_6]^{3+}$	8.4 x 10^{-6} cm^2 s^{-1}
D_R	Diffusion coefficient for $[Ru(NH_3)_6]^{3+}$	1.2 x 10^{-5} cm^2 s^{-1}
c	Concentration of $[Ru(NH_3)_6]^{3+}$	5 mM
T	Temperature	298 K

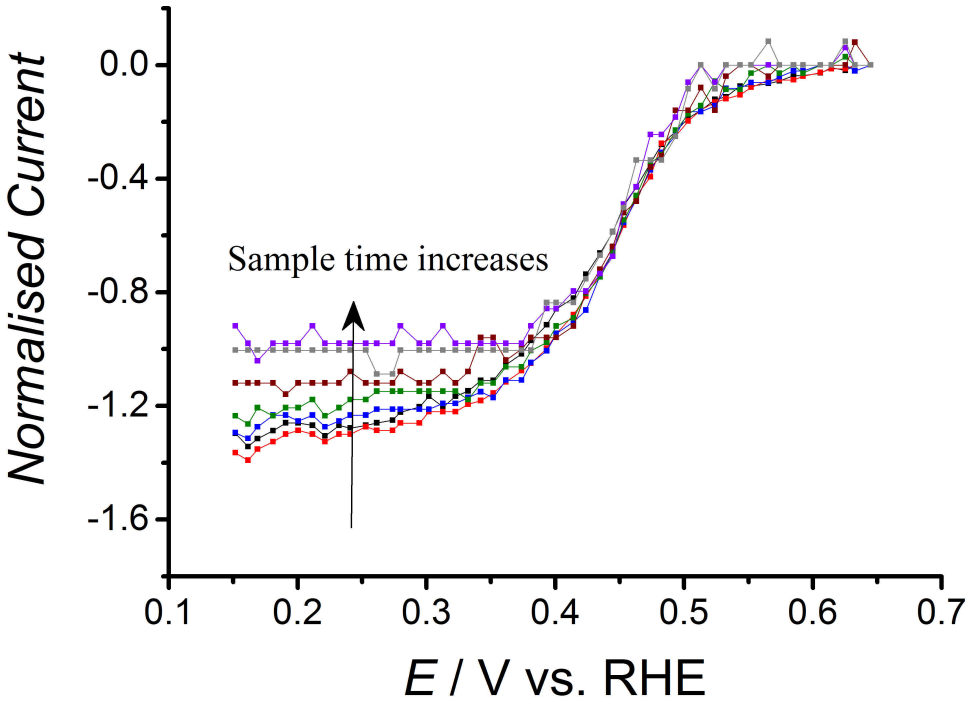

Figure 4.7: *MSCV for 5 mM $[Ru(NH_3)_6]^{3+}$ reduction at a 25 µm diameter platinum electrode in Ar purged KCl, sampled 10 µs (black), 20 µs (red), 50 µs (blue), 100 µs (green), 200 µs (brown), 500 µs (purple) and 1 ms (grey) after the potential step, normalised using the theoretical limiting current from Equation 1.45, using the parameters listed in Table 4.3.*

Clearly the normalisation is not working well at these short times. This is unlikely to be due to a failure of the model for the chronoamperometeric response at a microelectrode by Mahon and Oldham (Equation 1.45). Even though the sampling has been reduced,

the model has been previously verified by Britz *et al.* down to very short times[127]. This leaves the possibilities that there is a further source of current in solution, or that there was an error in the measurement of the timescale by the autolab equipment. The MSCVs also display significantly more noise than was the case for the previous MSCVs for Fe^{III} reduction. This is likely due to the large current range that had to be used due to the large currents recorded for chronoamperograms on the microsecond timescale.

When looking at the possibility of a source of extra current, the most likely species to be responsible is residual dissolved oxygen. It is possible that trace oxygen may have remained in solution after the argon purge. This was ruled out by repeating the MSCV measurement in the presence of an oxygen scavenger, sodium sulfite, which undergoes photooxidation through the adsorption of 265 nm light to give the sulfite radical anion[128]. This radical then reduces oxygen to water via a series of radical reactions[129].

$$SO_3^{\bullet-} + O_2 \rightarrow SO_5^{\bullet-} \tag{4.3a}$$

$$SO_5^{\bullet-} + SO_3^{2-} \rightarrow SO_5^{2-} + SO_3^{\bullet-} \tag{4.3b}$$

$$SO_5^{\bullet-} + SO_3^{2-} \rightarrow 2SO_4^{2-} \tag{4.3c}$$

Equation 4.3: *Chain mechanism by which sodium sulfite removed oxygen from solution, with the end product being sulfate in solution.*

In this way, addition of a small amount of sodium sulfite can ensure a solution free from dissolved oxygen. The effectiveness of this method can be simply demonstrated by purging a solution of $[Ru(NH_3)_6]^{3+}$ with argon and recording a CV. The solution was then exposed to air for 30 min either with or without the oxygen scavenger present, before recording a second CV. These CVs can be seen in Figure 4.8. As the cell was exposed to air, oxygen displaced argon in solution. The concentration of dissolved oxygen then increases, giving an increase in the reduction current at low potentials. In the presence of a scavenger, any oxygen that entered solution was immediately removed by the process detailed in Equation 4.3, and so the before and after CVs are identical.

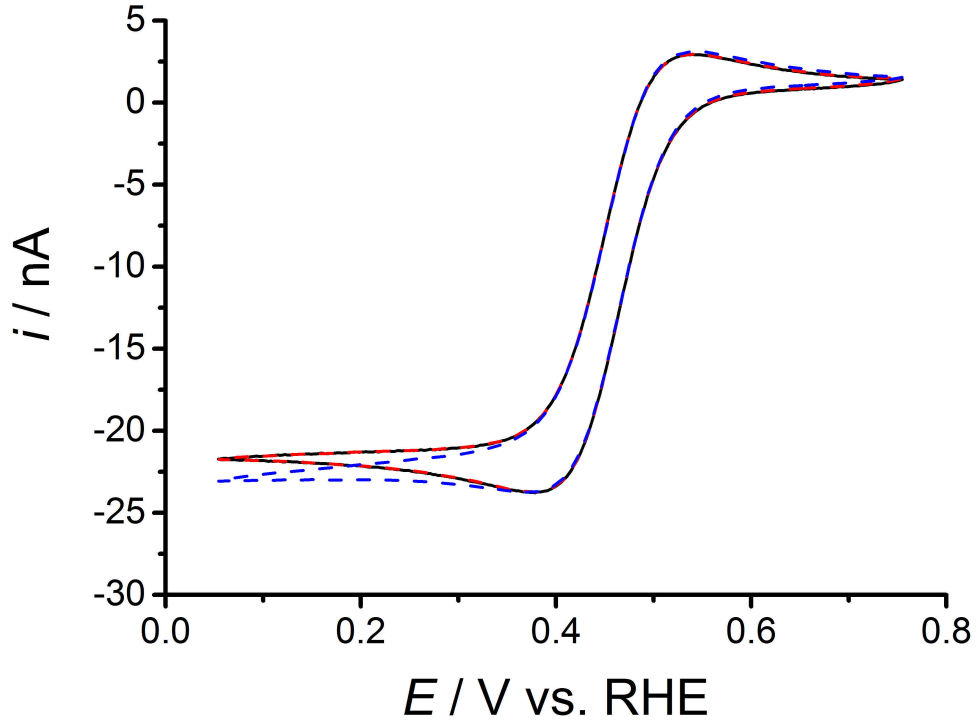

Figure 4.8: *200 mV s^{-1} CV for 5 mM $[Ru(NH_3)_6]^{3+}$ reduction at a 25 µm diameter platinum electrode in Ar purged 0.5 M KCl, showing the original CV recorded immediately after purging (black) and CVs recorded after a 30 minute exposure to air in the presence of (red dashed) and absence of (blue dashed) 0.34 mM Na_2SO_3 as an oxygen scavenger.*

For the ruthenium hexamine MSCVs, a small amount of Na_2SO_3 was added to the electrolyte after it had already been purged with argon to give 0.34 mM in solution. The Na_2SO_3 then acted to remove any trace dissolved oxygen, whilst itself having a small enough concentration so as not to interfere with the current from the reduction of $[Ru(NH_3)_6]^{3+}$. The cell was then purged for a further 20 minutes in the presence of the scavenger. An MSCV was then recorded under these conditions, and no change in the extra current was seen. Higher concentrations of the scavenger were also investigated, which had little effect on the magnitude of the extra current.

With errors in the model and the presence of trace oxygen seemingly ruled out, the likely cause of the extra current was error in the measurement of the timescale alongside current recordings when sampling at such short times. As the PGSTAT30 is a high quality potentiostat, it is likely that the interval between data recordings could be trusted to be

10 μs. However, a small pause between the end of the rest potential command and the onset of the potential step command could result in there being a shift in the start time of a few microseconds. This would have an undetectable effect on standard measurements, but would result in a noticeable shift in the timescale over the first few data points.

For this reason, a correction factor was applied to the timescales that were given by the potentiostat. This was calculated by taking a current transient for the reduction of $[Ru(NH_3)_6]^{3+}$ and performing a non-linear regression using a modified form of Equation 1.45. All terms were kept the same, except that the t term was replaced with $(t \times t_{factor})$, where t is the sampling time and t_{factor} is the correction factor that will be applied. This was done in order to calculate the offset in the recorded time data. Over the first 100 μs t_{factor} was found to be 0.6. Normalising the MSCVs using Equation 1.45 with the corrected times gave a much improved result. All MSCVs now normalise to one, as shown in Figure 4.9.

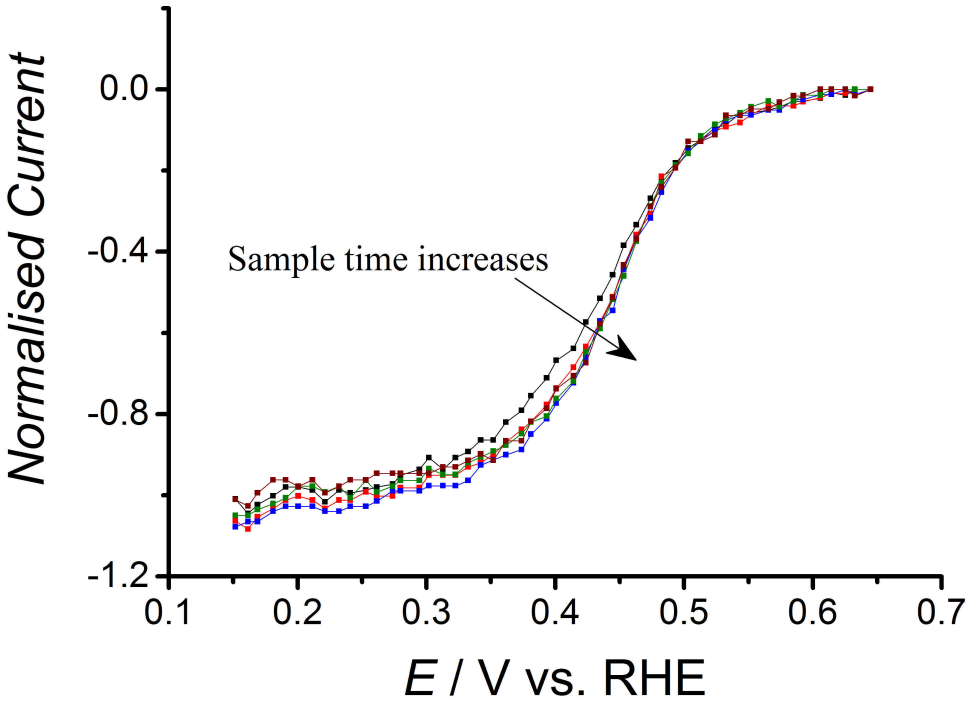

Figure 4.9: *MSCV for 5 mM $[Ru(NH_3)_6]^{3+}$ reduction at a 25 μm diameter platinum electrode in Ar purged KCl, assumed to be sampled 6 μs (black), 12 μs (red), 18 μs (blue), 24 μs (green) and 30 μs (brown) after the potential step, normalised using the theoretical limiting current from Equation 1.45, using $D = 8.4 \times 10^{-6}$ cm^2 s^{-1}, $c = 5$ mM, $a = 12.6$ μm.*

MSCVs for $[Ru(NH_3)_6]^{3+}$ reduction were then used to calculate values for E^0, k^0 and α by using non-linear regression to fit experimental sigmoidal curves to the model in Equation 4.2, with the corrected times being used in all cases. The kinetic parameters were allowed to vary whilst all other parameters listed were fixed at those given in Table 4.3. Since kinetic parameters are independent of sampling time, multiple MSCVs were simultaneously fitted as a means of obtaining an average fit across multiple data sets. MSCVs sampled at 10, 20, 30 and 50 µs were simultaneously fitted using the global fit function of Origin 9.1. Following Equation 4.1, these sampling times give k_m between 0.24 and 0.53 cm s^{-1}. This is equivalent to RDE rotation rates of between 2.5 and 5.1 MHz. The resultant fit is shown in Figure 4.10.

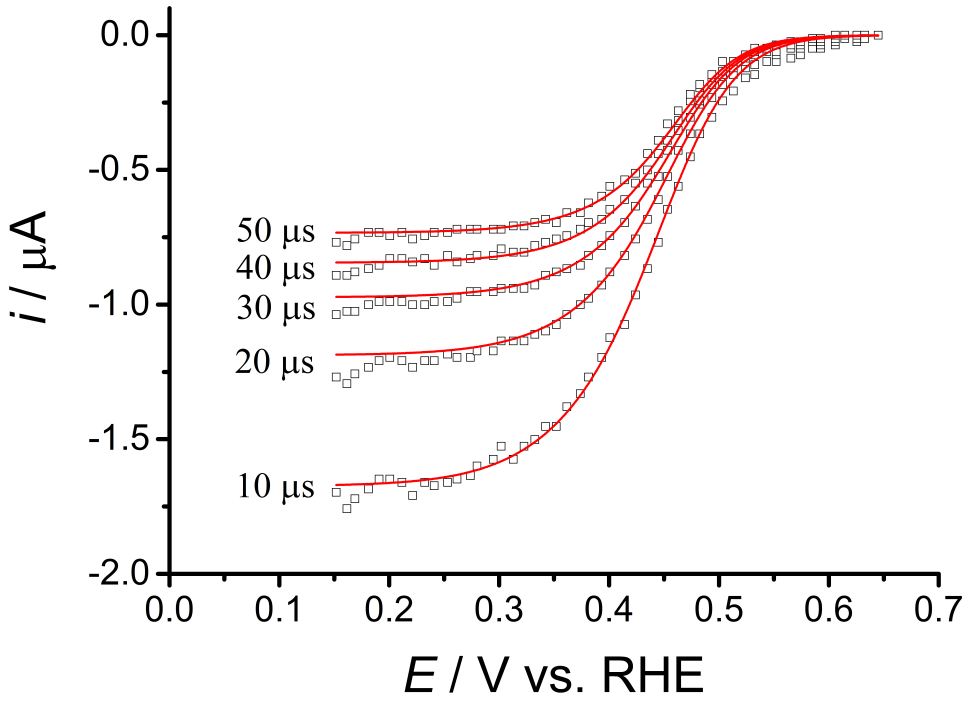

Figure 4.10: *MSCV for 5 mM $[Ru(NH_3)_6]^{3+}$ reduction at a 25 µm diameter platinum electrode in Ar purged KCl, assumed to be sampled 6, 12, 18, 24 and 30 µs after the potential step, showing the experimental data (□) and the fitted model (—). Theoretical curves were produced by nonlinear curve fitting to Equation 4.2 using the parameters listed in Table 4.3.*

The quality of the fit appears good thanks to the good matching between theoretical and experimental data, and gave $k^0 = 0.49 \pm 0.05$ cm s^{-1}, $\alpha = 0.55 \pm 0.02$ and $E^0 = 0.47 \pm 0.002$ V vs. RHE. Although the errors associated with the regression are again remarkably low, the value of k^0 is significantly lower than expected. A second fit was attempted where

the offset was defined by $t + t_{factor}$, rather than $t \times t_{factor}$, however this resulted in a visibly poor fit, and so a regression was not attempted. The low recorded value of k^0 most likely indicates that, even when sampling at times on the order of 10 μs, the sampling time is not sufficiently short to give quasireversible conditions. It appears that the elucidation of kinetic parameters for species as fast as $[Ru(NH_3)_6]^{3+}$ may not be possible using MSCV.

4.4 Operational range of the MSCV kinetic technique

Application of the MSCV model for the elucidation of kinetic parameters requires quasireversible conditions. For slow systems this is facile, as quasireversibility is observed close to the steady state. Faster systems are made to appear quasireversible by shortening the sampling time, increasing the rate of mass transport. Clearly this introduces a limit to this technique, as sampling times are often restrained by the equipment in use. To gain an idea of the range of this technique, a series of MSCVs were produced using COMSOL, as previously described. These MSCVs ranged from having slow kinetics, with k^0 of around 0.001 cm s^{-1}, up to very fast kinetics, with k^0 of up to 5 cm s^{-1}.

The constructed MSCVs were then analysed by non-linear regression against the model put forward in Equation 4.2 at a range of timescales. The calculated parameters were compared with those used in the original COMSOL simulation. The accuracies of the calculated parameters at these times were then used to find a functional timescale range for all kinetic parameters. The fits will be inherently less accurate than those achieved in previous chapters, as the fit was performed on a single MSCV for a single timescale, rather than simultaneously fitting to multiple timescales as a means of recording an average of multiple data sets. Despite this, the fits can be used to give a demonstration of the working timescale where the model is valid.

The quality of the fit was determined by the accuracy of the extracted parameters k^0, α and E^0. For k^0, a good fit was determined by an error less than a factor of 2, a poor fit by an error between a factor of 2 and 2.5, and a bad fit by an error greater than a factor

of 2.5. For α, a good fit was determined by an error of less than 0.1, a poor fit by an error between 0.1 and 0.15 and a bad fit by an error greater than 0.15. For E^0, a good fit was determined by an error less than 10 mV, a poor fit by an error between 10 and 20 mV, and a bad fit by an error greater than 20 mV.

It is often useful to express the kinetics of a system in terms of a normalised kinetic parameter, K. This is defined as the ratio between the rates of electron transfer and mass transfer, k_s / k_m. k_s is simply taken as the heterogeneous rate constant k^0 as it was entered into the simulation, and k_m was taken according to Equation 4.1. The errors on k^0, α and E^0 after the fit were then plotted against the corresponding K values. Errors on k^0 were normalised by dividing the fitted parameter by the original simulated value. Errors on α and E^0 were plotted as the difference between the simulated and fitted values. Figure 4.11 shows these errors. Irreversible, quasireversible and reversible regions are given as $K \leq 0.01$, $0.01 \leq K \leq 15$ and $K \geq 15$ respectively, as was defined in reference 130.

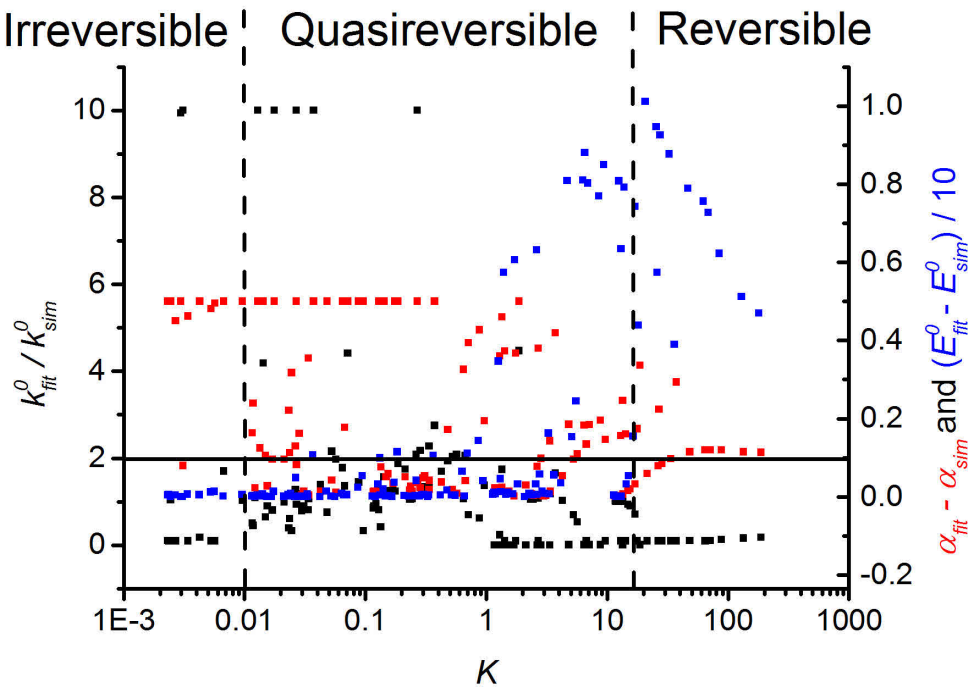

Figure 4.11: *Associated error on k^0, α and E^0 from the non-linear regression of simulated MSCVs against the model put forward in Equation 4.2. Errors on k^0 were normalised by dividing the extracted parameter from the fit (k^0_{fit}) by the original value from the simulation (k^0_{sim}), plotted in black. Errors on α were plotted as the difference between the fitted (α_{fit}) and simulated value (α_{sim}), plotted in red. Errors on E^0 were given as one tenth of the difference between the fitted (E^0_{fit}) and simulated value (E^0_{sim}), plotted in blue. A good fit requires all three parameters to be below the black line shown.*

Figure 4.11 shows that quality of the fit is not simply dependent on the nature of the kinetics of the system, as there is no clear relationship between the magnitude of the error and the reversibility of the system. Comparison of the simulated MSCVs with MSCVs constructed using Equation 4.2 show a good agreement, as indicated in Figure 4.12, and so this cannot be dismissed as a problem with the model.

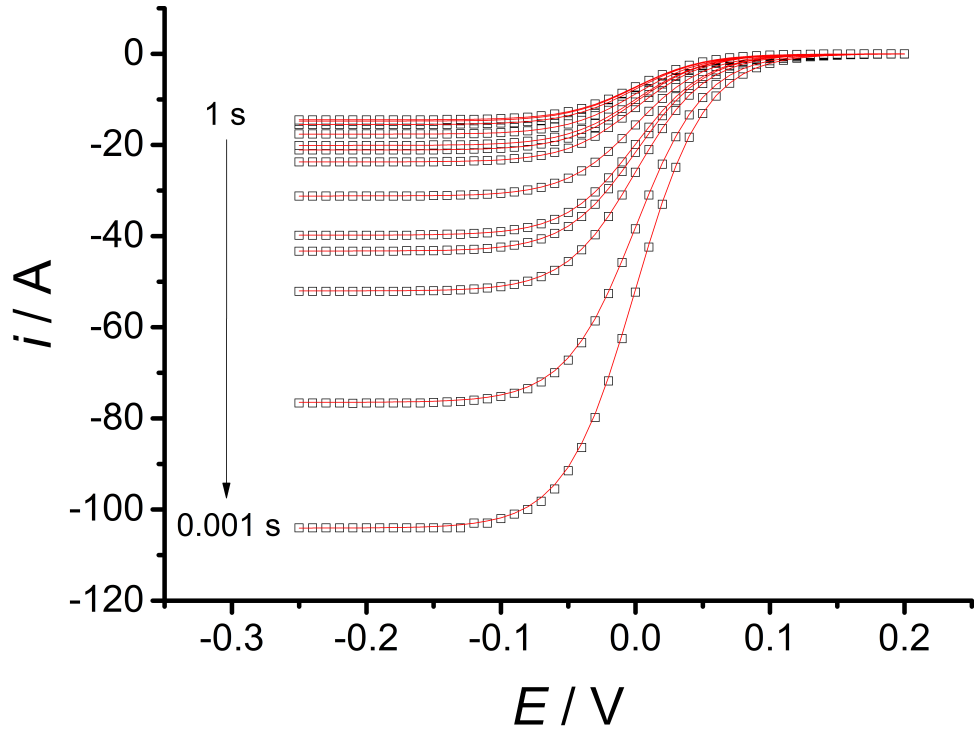

Figure 4.12: *Comparison of MSCVs that have been simulated using the COMSOL package (□) with equivalent MSCVs that have been constructed using Equation 4.2 (—). Both methods used identical paramters, such that* $k^0 = 5$ *cm* s^{-1}, $E^0 = 0$ *V,* $\alpha = 0.5$, $D_O = D_R = 5 \times 10^{-6}$ cm^2 s^{-1}, $c = 5$ *mM,* $a = 12.5 \times 10^{-4}$ *cm.*

The error is likely due to the fact that the determination of the parameters predominantly comes from the analysis of the slope of the MSCV. The resolution of the fit is therefore dependent on how greatly the slope is affected by changes in the kinetic parameters. The limitations of the method can be demonstrated by comparing theoretically constructed MSCVs where k^0 is 0.01, 0.1 and 1 cm s^{-1}, which are shown in Figure 4.13.

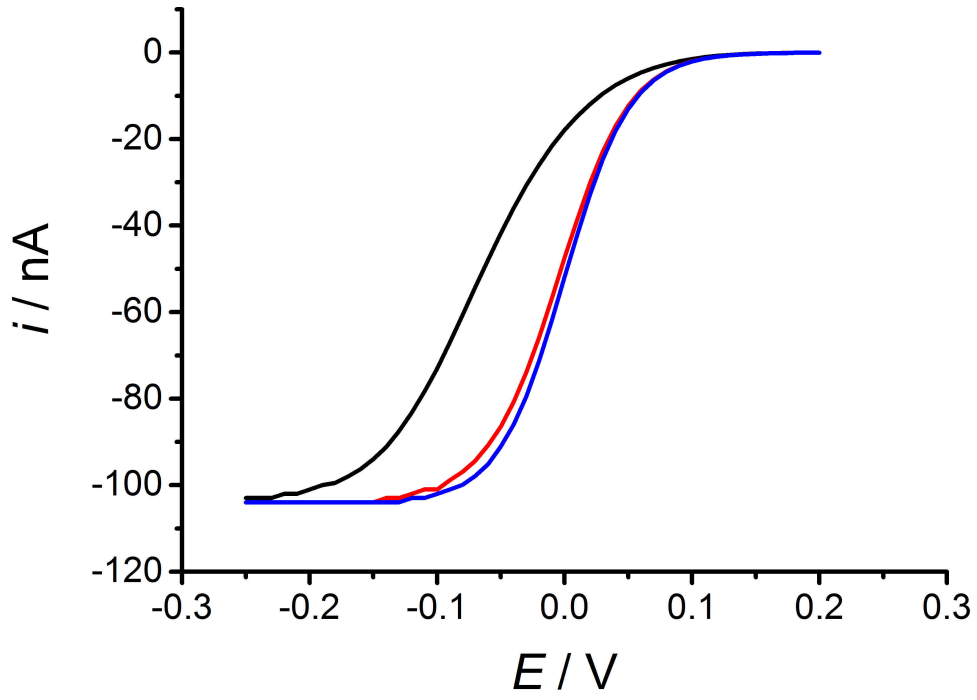

Figure 4.13: *Constructed MSCVs from simulated current transients at a 25 μm diameter electrode for a single electron reduction, sampled at 1 ms after the potential step, where kinetics were varied such that* k^0 *was 0.01 cm* s^{-1} *(black), 0.1 cm* s^{-1} *(red) and 1 cm* s^{-1} *(blue). All other parameters were identical,* $E^0 = 0$ *V,* $\alpha = 0.5$*,* $D_O = D_R = 5 \times 10^{-6}$ cm^2 s^{-1}*,* $c = 5$ *mM,* $a = 12.5 \times 10^{-4}$ *cm.*

An order of magnitude increase in k^0 from 0.01 to 0.1 cm s^{-1} gives a dramatic change in the observed slope of the MSCV. However, a further order of magnitude increase from 0.1 to 1 cm s^{-1} gives a barely observable difference in the slope. It was hoped that decreasing the sampling time could counter this effect by allowing the analysis of faster redox systems at short times. However, the poor quality of fit for fast redox systems even at short times seems to suggest that this is not possible. Indeed, it seems likely that the method of kinetic analysis by MSCV should come with a cap on the maximum possible heterogeneous rate constant with which it may be compatible.

Rather than generating a graphical representation, the workable timescales were tabulated using a simple colour coded system, where green indicates a good fit, yellow a poor fit, and red indicating that the timescale is entirely unsuitable. The parameters for determining a good, poor or unsuitable fit are the same as previously described. Rather than expressing all errors, the worst fitted parameter out of k^o, α and E^0 was chosen in

each case to represent the overall quality of the fit. The working grid can be seen in Table 4.4. A full table including the actual calculated parameters can be found in the appendix.

Table 4.4: *Workable timescales for the analysis of kinetic parameters from an MSCV using the quasireversible model given in Equation 4.2, where green indicates a good fit (k^0 error < factor 2, α error < 0.1, E^0 error < 10 mV), yellow indicates a poor fit (factor 2 < k^0 error < factor 2.5, 0.1 < α error < 0.15, 10 mV < E^0 error < 15 mV) and red indicates an unsuitable fit (k^0 error > factor 2.5, α error > 0.15, E^0 error > 15 mV)*

Sampling	k^0 **/cm s^{-1}**							
time /s	**0.001**	**0.005**	**0.01**	**0.05**	**0.1**	**0.5**	**1**	**5**
0.0001								
0.0002								
0.0005								
0.0008								
0.001								
0.002								
0.005								
0.008								
0.01								
0.02								
0.05								
0.08								
0.1								
0.2								
0.5								
0.8								
1								

Helpfully, it seems that the model is applicable for the calculation of kinetic parameters over a reasonably broad range of timescales for most kinetic parameters. This is extremely useful when it comes to practical application of MSCV as a means for determining kinetic parameters, as it means only a rough idea of the standard electrochemical rate constant is needed for an accurate fit to be achieved. However, there is a clear upper limit to the application of this model to varying kinetic parameters. Fitting to a theoretical MSCV where k^0 was 1 cm s^{-1} gave a good fit over a very narrow range of times, and it was not at all possible to fit to an MSCV where k^0 was 5 cm s^{-1}. An upper limit of $k^0 = 1$ cm s^{-1} therefore seems necessary for the practical application of the model to real world systems.

4.5 Comparison of methods

It has been shown that MSCV is a simple and useful way of determining the kinetic parameters of an electrochemical system. A functional range has been suggested where $k^0 < 1$ cm s^{-1} can be obtained with ease, providing an appropriate sampling time is selected. The model also succeeded in fitting MSCVs where k^0 was as low as 0.001 cm s^{-1}, which is sufficiently low to cover most commonly used redox mediators. For slower systems the MSCV appears irreversible at all times. Here the model for an irreversible wave, shown in Equation 1.52, could be substituted into the proposed quasireversible model, shown in Equation 4.2. This would allow a fit to be obtained. A greater degree of accuracy can be obtained in all cases by simultaneously fitting multiple MSCVs to the same equation using the global fit option, which is available in most software.

A commonly used alternative method for calculating the kinetic parameters from a redox system is using the difference between peak potentials from cyclic voltammetry (ΔE_p). The Nicholson method allows calculation of a dimensionless parameter ψ, which contained the kinetic parameters k^0 and α as described in Equation 1.19[7]. A number of other authors have suggested models linking ψ with the recorded ΔE_p in order to more easily calculate kinetic parameters, and avoid the use of the more general data tables that are available[9–12]. The functional range of the model depends on the range over which

recorded CVs appear to be quasireversible. Matsuda and Ayabe express this in terms of the dimensionless kinetic parameter Λ[5].

$$\Lambda = \frac{k^0}{(D\nu F/RT)^{1/2}} \tag{4.4}$$

Equation 4.4: *Dimensionless kinetic parameter for cyclic voltammetry at large planar electrodes* (Λ)*, from the diffusion coefficient* (D)*, sweep rate* (ν)*, Faraday's constant* (F)*, ideal gas constant* (R)*, temperature* (T) *and the heterogeneous rate constant* (k^0)*.*

A system is deemed to be quasireversible when $15 \leqslant \Lambda \leqslant 10^{-2(1+\alpha)}$. Taking $\alpha = 0.5$, $T = 298$ K, and $D_O = D_R = 5 \times 10^{-6}$ cm^2 s^{-1}, the scan rate needed to analyse a redox system where $k^0 = 1$ cm s^{-1} would be 23 V s^{-1}. Theoretically this is possible, as potentiostats capable of cycling orders of magnitude faster than this are readily available. However, when cycling this quickly it cannot be guaranteed that the observed shift in ΔE_p is entirely due to kinetic effects. This often is not true, as solution resistance leads to a greater overpotential being needed to drive the reaction according to Ohm's law, which results in a shift in the peak potential towards higher overpotentials. Faster cycling also increases the capacitive currents. If these become too large it is possible that they act to obscure the peak potentials altogether, which makes analysis by this method impossible.

Similar considerations must be made when using linear sweep voltammetry at rotating disc electrodes for the calculation of kinetic parameters. Here, kinetic parameters are obtained by recording voltammograms at varying rotation rates in order to obtain the kinetically controlled current, which is proportional to the kinetic parameters. Van der Vliet *et al.*[76] observed that, even with all good experimental practices in place, the remaining solution resistance was sufficient to give a significant shift in the observed voltammograms for the oxygen reduction reaction at RDE. They state the importance of applying corrections to account for this, as an absence of correction in their work caused significant shifts in the half wave potentials, and led to an error in the calculated kinetic currents of up to 0.37 mA cm_{Pt}^{-2}. The MSCV method offers clear advantages over these methods, thanks to its wide functional range, and the small area meaning that issues with capacitance and solution resistance do not need to be considered.

When comparing the MSCV model to the existing model for gleaning kinetic information from SCVs at planar electrodes from Bard and Faulkner[5] then advantage comes from the use of microelectrodes. In both bases, the analysis of faster electrochemical systems requires a shortening of the sampling time, so that the rate of mass transport increases whilst the rate of electron transfer is kept constant.

In the case of planar electrodes, the large area results in a significant capacitive response at short times. The characteristic time taken to resolve the charging current is proportional to its size. For example, a 1 cm diameter electrode would take around 28 ms for the charging current to decrease sufficiently for the Faradaic current to be observed, assuming the distance between the Luggin capillary and working electrode was 1 cm, the solution conductivity was 0.013 Ω^{-1} cm^{-1} and the capacitance of the electrode was 30 μF cm^{-2}. For the 25 μm microelectrode under the same condutions, this would only require around 6 μs.

Bard and Faulkner state that the quasireversible behaviour is determined by a kinetic parameter λ^0, which is given as the value of λ as was previously described by Equation 1.37 at $E = E^0$. This means that, as with our model, SCV at planar electrodes can access a range of kinetic parameters by varying the sampling time. The quasireversible range corresponds to $10^{-2\alpha} \leqslant \lambda^0 \leqslant 2$. Taking $\alpha = 0.5$ and $D_O = D_R = 5 \times 10^{-6}$ cm^2 s^{-1}, and assuming a shortest possible sampling time of 30 ms, this corresponds to a maximum accessible heterogeneous rate constant of 0.013 cm s^{-1} before the upper limit of $\lambda^0 = 2$ is reached. Our model using MSCV is functional up to values of k^0 almost two orders of magnitude larger, which demonstrates a clear improvement on the existing model.

As the proposed MSCV model is built on the model for kinetics from steady state voltammetry at microelectrodes by Oldham[29] the range of k^0 over which it is valid will likely be similar. When applied to steady state voltammetry, the quasireversible domain is defined by the dimensionless kinetic parameter κ^0.

$$\kappa^0 = \frac{\pi k^0 a}{4D} \tag{4.5}$$

Equation 4.5: *Dimensionless kinetic parameter for steady state voltammetry at microelectrodes (κ^0), from the diffusion coefficient (D), electrode radius (a) and the heterogeneous rate constant (k^0)*

A steady state voltammogram recorded at a microelectrode was determined to be quasireversible when $0.2 \leqslant \kappa^0 \leqslant 20$. Here, rather than varying the rate of mass transport by varying sampling time, it is done by varying the electrode radius. It would therefore be important to select an appropriately sized electrode depending on the species being probed.

Using our MSCV procedure, it was possible to accurately determine k^0 up to 1 cm s^{-1}. Using steady state voltammetry this would require an electrode with a radius smaller than 0.13 μm. A simple variation of the sampling time is far less experimentally challenging than the fabrication of such small electrodes. That is not to say that electrodes on this order have not been made and used for this purpose. Sun *et al.* used nanoelectrodes in order to measure the heterogeneous rate constant of tetracyanoquinodimethane[131]. A rate constant of 1.1 ± 0.04 cm s^{-1} was obtained using electrodes which had between 76 and 386 nm radii.

Another common practice is to combine the benefits of small radii electrodes with another means of varying the rate of mass transport using SECM. Here, a rapid rate of mass transport is again achieved through the use of an electrode with nanometer dimensions. This is then supplemented by bringing the electrode into close proximity to a conductive substrate. The redox probe is reduced at the electrode tip, but then regenerated at the substrate, to provide a greatly increased flux to the electrode via a positive feedback loop, as described in Figure 4.14.

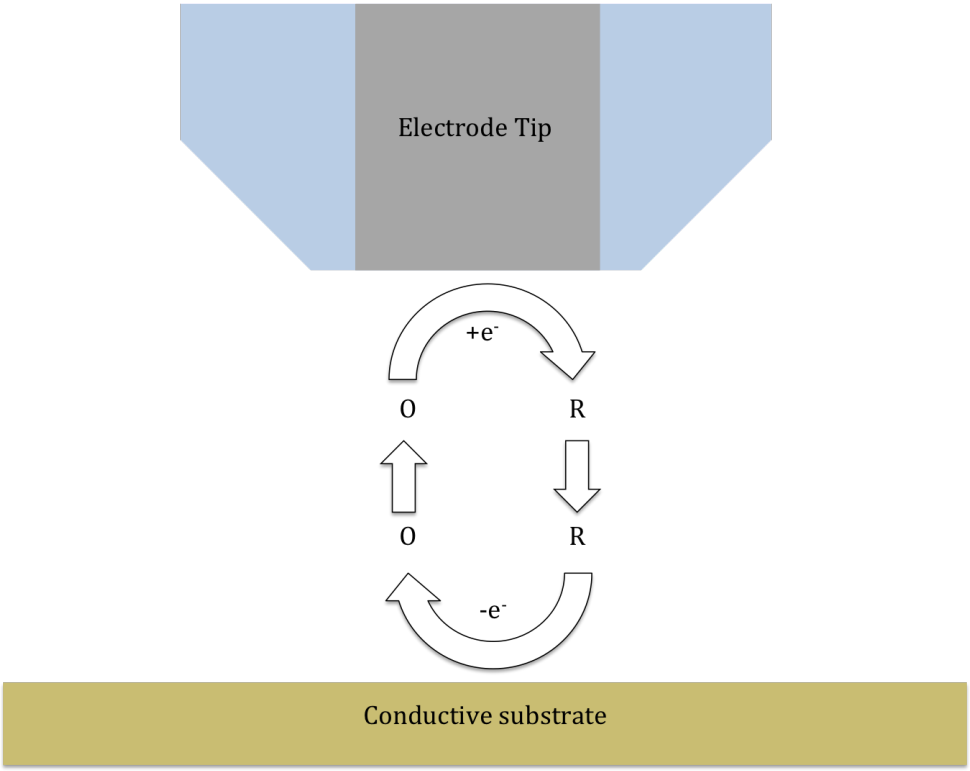

Figure 4.14: *Schematic diagram showing the positive feedback mode of SECM from the reduction of O to R, as O is regenerated at the conductive substrate, which is in close proximity to the electrode tip.*

The degree of increase in the recorded current is dependent on the normalised tip distance (L), given as the ratio between the distance of the electrode from the substrate and the electrode radius. A steady state voltammogram is recorded at a set tip-substrate distance to give the desired level of positive feedback. Kinetic parameters can then be obtained through a simple fitting of the recorded voltammogram to a model that combines the shape dependence of the voltammogram on its kinetics with the normalised tip distance, as given in Equation 4.6[132].

$$i_T = \frac{0.78377}{L(\theta + 1/\kappa)} + \frac{0.68 + 0.3315\exp(-1.0672/L)}{\theta}\left[1 + \frac{\pi}{\kappa\theta}\left(\frac{2\kappa\theta + 3\pi}{4\kappa\theta + 3\pi^2}\right)\right]^{-1} \tag{4.6a}$$

$$\kappa = \frac{\pi k^0 a}{D_O}\exp\left\{\frac{-\alpha n F(E - E^0)}{RT}\right\} \tag{4.6b}$$

$$\theta = 1 + \frac{D_O}{D_R}\exp\left\{\frac{nF(E - E^0)}{RT}\right\} \tag{4.6c}$$

Equation 4.6: *Theoretical current at a SECM electrode tip under positive feedback conditions (i_T) from the number of electrons transferred (n), diffusion coefficient for the oxidised (D_O) and reduced species (D_R), tip radius (a), normalised tip distance (L = distance/radius), standard electrochemical rate constant (k^0), transfer coefficient (α), Faraday's constant (F), potential (E), standard potential (E^0), ideal gas consant (R) and temperature (T).*

In this way, by combining the increase in mass transport due to the small electrode size with the increase due to the positive feedback loop, incredibly fast redox species may be analysed. Using this method, Velmurugan *et al.* were able to calculated k^0 for ferrocene methanol and ruthenium hexamine as 8.4 ± 0.2 cm s^{-1} and 13.5 ± 2 cm s^{-1} respectively[133]. These values are well outside of the scope of the MSCV method, as the model could not differentiate between the slopes of MSCVs recorded for such fast systems, even when sampling at short times. The SECM model is still dependent on achieving quasireversible conditions. Here, quasireversibility is determined by the dimensionless parameter λ'.

$$\lambda' = \frac{Lk^0 a}{D} \tag{4.7}$$

Equation 4.7: *Dimensionless kinetic parameter for voltammetry at a SECM tip under positive feedback conditions (λ'), from the diffusion coefficient (D), electrode radius (a), normalised tip-substrate distance (L = distance/radius) and the heterogeneous rate constant (k^0)*

Mirkin *et al.* found that the system could be said to be quasireversible providing $\lambda < 10$[134]. Assuming a 25 μm diameter electrode tip was used, $D = 5 \times 10^{-6}$ cm^2 s^{-1}, and the electrode was positioned such that $L = 0.5$, the maximum attainable value of k^0 would be 0.16 cm s^{-1}. This is still nearly an order of magnitude slower than the maximum range of the MSCV technique, again highlighting the power of the proposed model. Of course, the range of kinetic parameters accessible to the SECM technique could be greatly improved by using a smaller electrode tip. Reducing the electrode diameter to 100 nm would give

a maximum accessible value of k^0 of 20 cm s^{-1}. Of course, the same is true of the MSCV technique. The rate of mass transport is currently increased by decreasing the sampling time. The use of this technique at an already much smaller electrode would give an increase in the rate of mass transport when compared to an MSCV at a larger electrode that was sampled at the same time. The combination of MSCV with much smaller electrodes seems to be a promising way forward for this model in order to access much faster systems.

5 Oxygen Pre-adsorption During ORR

5.1 Using MSCV with the ORR

MSCV can be used for simple, visual analysis of the oxygen reduction reaction (ORR). Comparing MSCVs sampled at varying times after the potential step can clearly show how the ORR changes with time. This work is built on procedures developed for oxygen sensing in sea water. The oxygen sensor was attached to a rig which was dropped into the ocean[111,112]. It was suggested that the accuracy of the current measurements could be improved by reducing the time at which the current was sampled. This would give a much thinner diffusion layer which should therefore experience less distortion as a result of the convection.

The ORR is far more complicated than the single electron reductions that have previously been discussed. This is due to the nature of the different pathways available, predominantly the two and four electron reductions discussed in Section 1.5. Once a two electron reduction of oxygen to hydrogen peroxide has been performed, a further two electron reduction requires the peroxide to stay in close proximity to the electrode surface. Invariably some surface adsorbed peroxide diffuses into the bulk solution before being reduced to water. This leads to what could be viewed as an incomplete reduction of oxygen, as described by Equation 1.55. If the average number of electrons transferred per oxygen molecule was calculated, this apparent number of electrons transferred (n_{app}) for the reduction would be somewhere between two and four, but not as high as four.

The value of n_{app} would be expected to be mass transport dependent. High rates of mass transport result in a greater rate of diffusion of peroxide away from the electrode surface, leading to a lower value of n_{app}. This has previously been observed using rotating disc electrodes and microdisc electrodes[43] and on carbon supported platinum nanoparticles[32]. In the case of chronoamperometry, shorter sampling times result in a greater rate of mass transport. A MSCV sampled at short times could therefore be

expected to display lower values of n_{app}. This chapter will look at the reduction of oxygen on the millisecond timescale and the information that such measurements contain.

The first MSCV for ORR was recorded in aerated 0.1 M $KClO_4$ with a 25 µm diameter platinum electrode. The cell was set up as was described in Section 2.2, and the pre-conditioning waveform described in Figure 2.3 was performed. The normalisation procedure was the same as was used during the ruthenium experiments using Equation 1.45. Now, by setting the theoretical number of electrons transferred to one, the MSCV recorded should converge to n_{app} on the y axis, as was previously described in Equation 3.2. For the oxygen reduction reaction, n_{app} will be expected to be between 2 and 4. Calculated values of $n_{app} = 4$ indicates complete four-electron reduction to water, whereas $n_{app} = 2$ would indicate partial two-electron oxygen reduction to hydrogen peroxide. The recorded MSCV is shown in Figure 5.1.

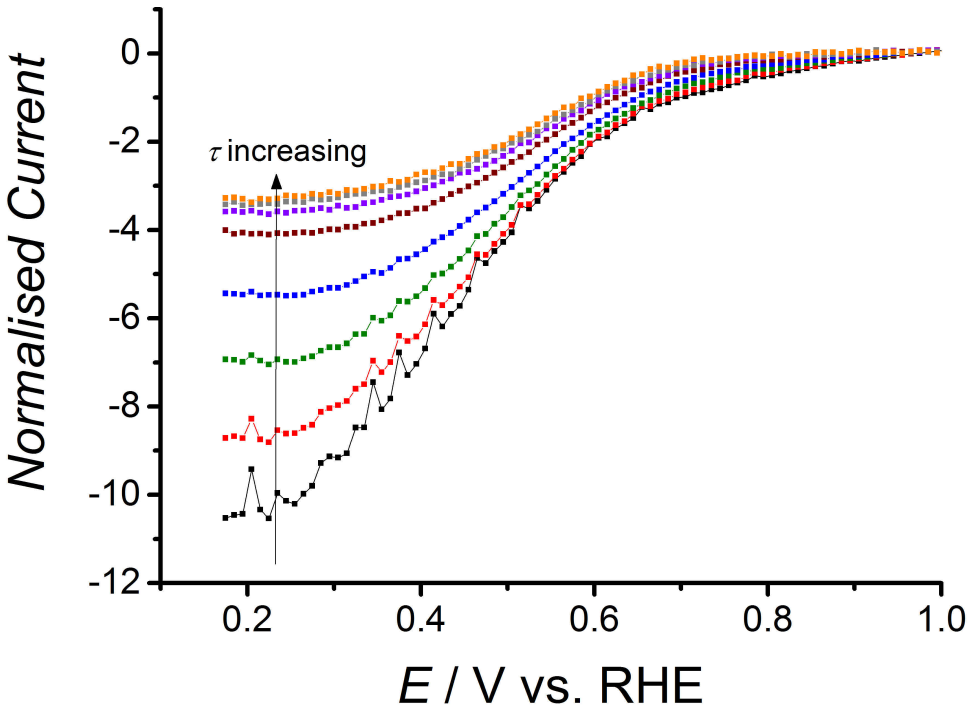

Figure 5.1: *MSCV for ORR at a pre-conditioned 25 µm platinum diameter electrode in aerated 0.1 M $KClO_4$, sampled 2.5 ms (black), 5 ms (red), 10 ms (green), 20 ms (blue), 50 ms (brown), 100 ms (purple), 200 ms (grey), and 500 ms (orange) after the potential step, normalised using the theoretical limiting current from Equation 1.45, using $D = 2.29 \times 10^{-5}$ cm^2 s^{-1}, $c = 0.257$ mM and $a = 12.85$ µm.*

It can be seen that there is significant time dependence in the normalised current for ORR calculated by MSCV. When sampling at times greater than 100 ms, the MSCVs are all normalising to a n_{app} value of around 3.3. This seems reasonable, as it indicates predominantly four-electron reduction of oxygen to water, with some two-electron to peroxide present as well. Partial reduction to peroxide is responsible for the apparent loss of current. Comparing the produced sigmoids for short and long time MSCVs, it is also noticeable that the MSCVs sampled at shorter times exhibit a more shallow slope, with the ORR plateau not being reached until a more negative potential is applied. This is indicative of kinetic limitations associated with fast sampling times, as was also seen for MSCVs recorded for the Fe^{II}/Fe^{III} redox couple in Section 4.2.

For the shorter sampling times, the calculated values of n_{app} quickly become unreasonably large. The normalisation procedure detailed in Equations 1.45 - 3.2 assumes that the current comes from a purely diffusion controlled, one-electron reduction. These large values of n_{app} indicate that there is a further source of current that is not being taken into account by the normalisation.

The successful use of the procedure with $[Ru(NH_3)_6]^{3+}$ indicates that the extra current cannot be simply explained by equipment error or a problem with the normalisation, and so the source of the extra current is likely to be chemical. The formation of an oxide layer prior to the potential step is a plausible explanation, as the reduction of this layer could generate the extra current. However, the rest potential at OCP followed a sweep from a sufficiently negative potential to ensure that no oxide remained on the electrode surface. Also, the potential range for oxygen reduction and $[Ru(NH_3)_6]^{3+}$ show significant overlap. It would therefore be expected that the reduction of a surface oxide due to the potential waveform should be seen in MSCVs for the reduction of $[Ru(NH_3)_6]^{3+}$ as well, which is clearly not the case (See Figure 3.2). The involvement of hydrogen adsorption can also be ruled out, as the extra current is seen across the whole of the ORR wave, which is well outside of the potential range for hydrogen adsorption. It therefore seems appropriate to look for another reaction or series of reactions that may be responsible.

5.2 Pre-adsorbed oxygen under transient conditions

The extra current seen for MSCV of the ORR at short times seems likely to be due to the presence of pre-adsorbed oxygen on the surface of the electrode[135]. The waveform used for the collection of the current transients from which MSCVs are sampled involves a short rest at OCP prior to the potential step being performed (see Figure 2.3). During this rest, a small amount of oxygen may adsorb onto the electrode surface. When the potential step is then performed, the pre-adsorbed oxygen will be simultaneously reduced along with oxygen arriving at the electrode surface due to mass transport. This concurrent reduction of two sources of oxygen would be responsible for an apparent number of electrons for the reduction being greater than four. Once this pre-adsorbed oxygen was consumed, the only source of oxygen would be by mass transport control. A diffusion limited response would then be seen, as is observed for MSCVs sampled at times longer than around 100 ms. A schematic diagram of this process is given in Figure 5.2.

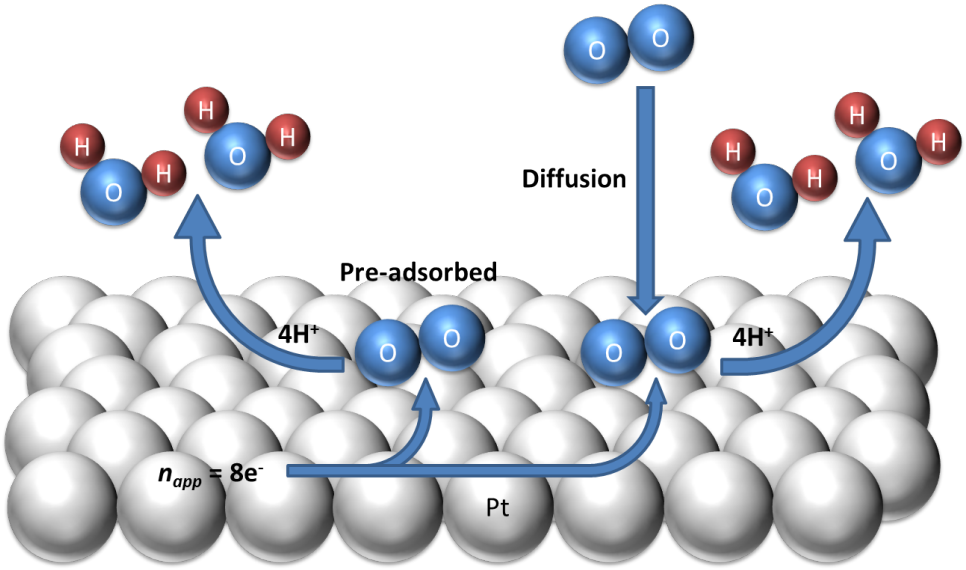

Figure 5.2: *Schematic diagram for the concurrent reduction of pre-adsorbed oxygen with oxygen arriving at the electrode surface by mass transport, resulting in an apparent number of electrons transferred greater than 4.*

The presence of a pre-adsorbed oxygen species agrees with current knowledge about the nature of the ORR and also the understanding about the interactions between aqueous

oxygen and a metal surface. Whilst there is much discussion about the full mechanistic route of the ORR, it is generally agreed that the reaction starts with an initial adsorption step onto the electrode surface[53]. Whilst the presence of adsorbed oxygen has been confirmed during the ORR using EQCM[136], it was not possible to find any study into the adsorption of oxygen onto the electrode surface under aqueous conditions prior to the ORR being electrochemically driven.

Looking at the MSCV for ORR presented in Figure 5.1, the extra current seen at short times is clearly evident at all potentials along the redox wave. The sigmoidal shape of the oxygen reduction curve is preserved despite the increase in the overall current. This indicates that the process responsible for the extra current exhibits the same potential dependence as the dissolved oxygen, which is consistent with the assignment of pre-adsorbed oxygen as the source. This also rules out any contributions from the adsorption of hydrogen onto the electrode during the reduction, as this occurs on platinum at more negative potentials than where the extra current is observed. So far this has been discussed in terms of the extra apparent electrons being transferred. It is also possible to see the reduction of this pre-adsorbed oxygen by means of a direct comparison of the experimental current transient with the theoretical diffusion controlled response that is predicted by Equation 1.45. The comparison is shown in Figure 5.3.

The extra current seen at short times is immediately seen when comparing the experimental and theoretical transients. The current at short times is apparently increased due to the consumption of pre-adsorbed oxygen. The current eventually returns to the expected diffusion controlled response at around 100 ms, once the pre-adsorbed oxygen is consumed. The background response in argon purged solution shows a slight current response. The nature of this response is outside of the scope of this report, however it cannot be modelled by Equation 1.45, and so does not appear to be due to a diffusion controlled redox process. It seems likely that this is due either to some small amount of hydrogen adsorption, or the reorganisation of charged species adsorbed onto the electrode surface caused by the sudden onset of a negative potential difference. Importantly, the background response does not approach the magnitude of the difference between the

theoretical diffusion controlled current and the experimental current, and so should not be suspected as a cause.

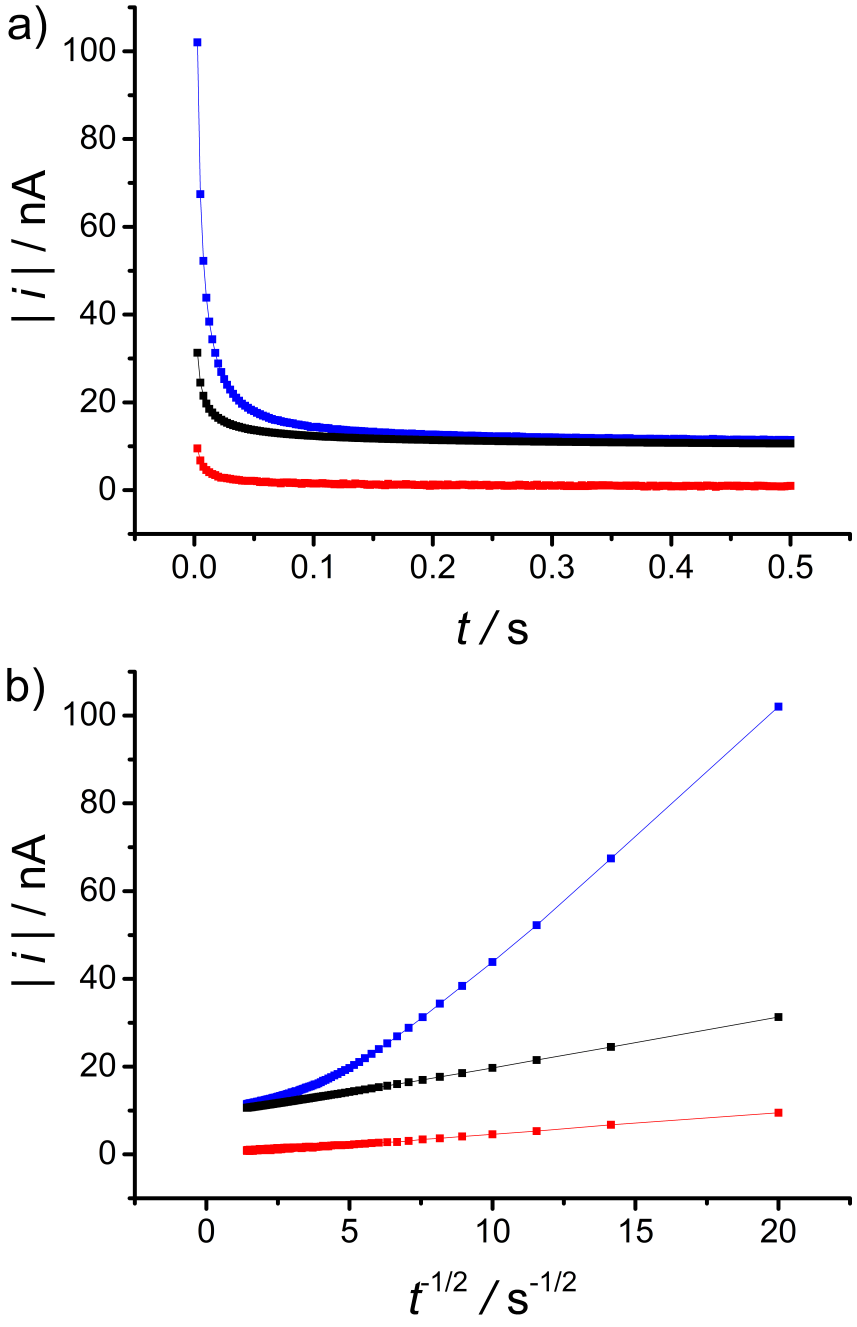

Figure 5.3: *Experimental chronoamperogram recorded after performing a potential step from OCP (1.0 V vs. RHE) to 0.17 V vs. RHE at a pre-conditioned 25 μm diameter Pt electrode in 0.1 M $KClO_4$ (blue), compared to the background current recorded under the same conditions in argon purged solution (red), the theoretical limiting current from Equation 1.45, using $D = 2.29 \times 10^{-5}$ cm^2 s^{-1}, $c = 0.257$ mM, $a = 12.85$ μm (black), plotted against both t (a) and $t^{-1/2}$ (b).*

As the reduction of the pre-adsorbed oxygen is seen as a current signal, it is possible to express the quantity of adsorbed oxygen in terms of a charge. This is simply done by integrating the difference between the experimental current from the potential step (i_{exp}) and the theoretical diffusion controlled response from Equation 1.45 (i_{theo}), as is described by Equation 5.1. Normalisation of the 500 ms MSCV for oxygen reduction using Equation 3.2 gave n_{app} as 3.3, and so this value will be used in the calculation of the i_{theo}. The charge associated with the reduction of pre-adsorbed oxygen as calculated by this subtraction method will hence be referred to as $Q_{ads,sub}$.

$$Q_{ads,sub} = \int (i_{exp} - i_{theo})\,\mathrm{d}t \tag{5.1}$$

Equation 5.1: *Extra charged seen during chronoamperometry for the oxygen reduction reaction in fully aerated solution ($Q_{ads,sub}$) from the integral of the difference between the experimental current recorded in fully aerated solution (i_{exp}) and the theoretical diffusion limited current response as determined by Equation 1.45 (i_{theo}) with respect to time. i_{theo} was taken assuming n = 3.3, D = 2.29 × 10^{-6} cm^2 s^{-1}, c = 0.257 mM and a = 12.85 μm.*

This process was repeated with five current transients taken from the ORR plateau of the MSCV shown in Figure 5.1. An average was then taken, giving $Q_{ads,sub}$ as 0.738 nC. Importantly, the low value of the calculated charge acts to highlight the sensitivity of MSCV as a technique for recording n_{app} for multi-electron reductions, as even a small amount of extra charge translates as a significant change in the observed value for n_{app}. It is possible to express this extra charge in terms of the number of monolayers of oxygen pre-adsorbed onto the electrode surface. This was done by first calculating the number of moles of oxygen that would make up a complete monolayer (N_{O_2}) from the surface area of the electrode in question, and the number of active sites available for oxygen pre-adsorption. The number of platinum atoms per square centimetre was taken as 1.3 × 10^{15}, which is the generally accepted value for polycrystalline platinum[137].

$$N_{O_2} = \frac{A \cdot N_{Pt,cm^{-2}}}{2N_A} \tag{5.2}$$

Equation 5.2: *Number of adsorption sites available for oxygen pre-adsorption on a platinum electrode surface (N_{O_2}) from the surface area of the electrode (A) the number of platinum atoms found in a square centimetre of polycrystalline platinum ($N_{Pt,cm^{-2}}$) and Avogadro's constant (N_A).*

The factor of two given is needed as oxygen is assumed to bind side-on according to the bridge model (Figure 1.22), giving one molecule of oxygen adsorbing onto two platinum atoms. Importantly, the surface area taken for Equation 5.2 is not simply the geometric surface area, but the true electrocatalytic active area. This takes into account the roughness of the electrode surface along with any site defects that inevitable give microelectrodes a larger surface area than is determined by its radius. This was found from the charge under the hydride adsorption region of a 20 mV s^{-1} CV recorded in 1 M H_2SO_4 [138].

$$A_{echem} = \frac{0.71}{210\ \mu C\ cm^{-2}} \int_{0.02\ V}^{0.35\ V} i\,dt \tag{5.3}$$

Equation 5.3: *Electroactive area of a platinum electrode (A_{echem}) from the integral of the current in the hydride adsorption region of a 20 mV s^{-1} CV in 1 M H_2SO_4 between set limits vs. RHE (i), the charge taken to strip a complete monolayer of adsorbed hydrogen from polycrystalline platinum (210 $\mu C\ cm^{-2}$) and the number of monolayers of hydrogen that are adsorbed over the given potential range at that cycling speed, as determined by Biegler et al[138] (0.71).*

Precise knowledge of the electrode area allows expression of the extra charge in terms of the charge density, 54.0 μC cm^{-2}. This method is only possible for a platinum electrode thanks to its well defined and well studied hydrogen adsorption region. For a 25 μm diameter platinum microelectrode, the number of adsorption sites for oxygen was found to be 1.02 x 10^{10}, which corresponds to 1.69 x 10^{-14} mol of pre-adsorbed oxygen. The number of moles of oxygen that was actually present on the electrode surface due to pre-adsorption was found from the extra charge passed, using Faraday's law of electrolysis.

$$Q = mnF \tag{5.4}$$

Equation 5.4: *Faraday's law of electrolysis, where measured charge (Q) is equal to the product of the number of moles (m), number of electrons transferred (n) and Faraday's constant (F).*

Taking the previously calculated value of $Q_{ads,sub}$ as described by Equation 5.1, the number of moles of oxygen pre-adsorbed onto the electrode surface was found to be 2.03 x 10^{-15} mol. This value corresponds to 0.12 monolayers of adsorbed oxygen. Again, this

clearly highlights the sensitivity of the MSCV technique, as as little as 0.12 monolayers of adsorbate clearly showed up on the short time MSCVs.

5.3 Direct reduction of pre-adsorbed oxygen

It is worth noting that a number of assumption are made in the calculation of $Q_{ads,sub}$, most notably that n_{app} is constant at all sampling times. For this reason, a second method for the calculation of this charge was also investigated. If the extra current seen is purely due to the pre-adsorption of oxygen onto the electrode surface, it should be possible to quantify the adsorbed oxygen through a simple reduction, as could be done with any other adsorbate. A potential step was performed from OCP to the ORR plateau on an electrode with a certain amount of adsorbed oxygen on its surface whilst in an environment with no further source of current. The resultant current transient could then be purely ascribed to the reduction of the adsorbed O_2 layer.

This was achieved by setting up an experiment with a 25 μm diameter platinum electrode and SCE reference electrode in aerated 0.1 M $KClO_4$, and pre-treating as detailed in Chapter 2.2. The cleaning waveform detailed in Figure 2.3 was then employed and the electrode allowed to rest at OCP for 10 s. After the 10 s rest was completed, the electrolyte was purged with argon whilst OCP was maintained for 30 minutes. As adsorbed oxygen has a relatively strong interaction with platinum metal, the adsorbed oxygen layer was maintained for the duration of the argon purge. A potential step was then performed to 0.15 V vs. RHE, giving a current transient for the reduction of adsorbed oxygen. A second potential step was then immediately performed from OCP to the same potential, which showed a dramatically reduced current response, indicating that the source of current in the first step had been removed. This ruled out contaminants or surface oxide as the source of the current in the first step, as these should still be capable of causing a significant current response in the absence of oxygen. The negligible current response of the second step was ascribed to background processes. This second step was therefore subtracted from the first step, so as to remove any background effects. The remaining

current response was solely due to the reduction of the pre-adsorbed oxygen layer. These current transients are shown in Figure 5.4.

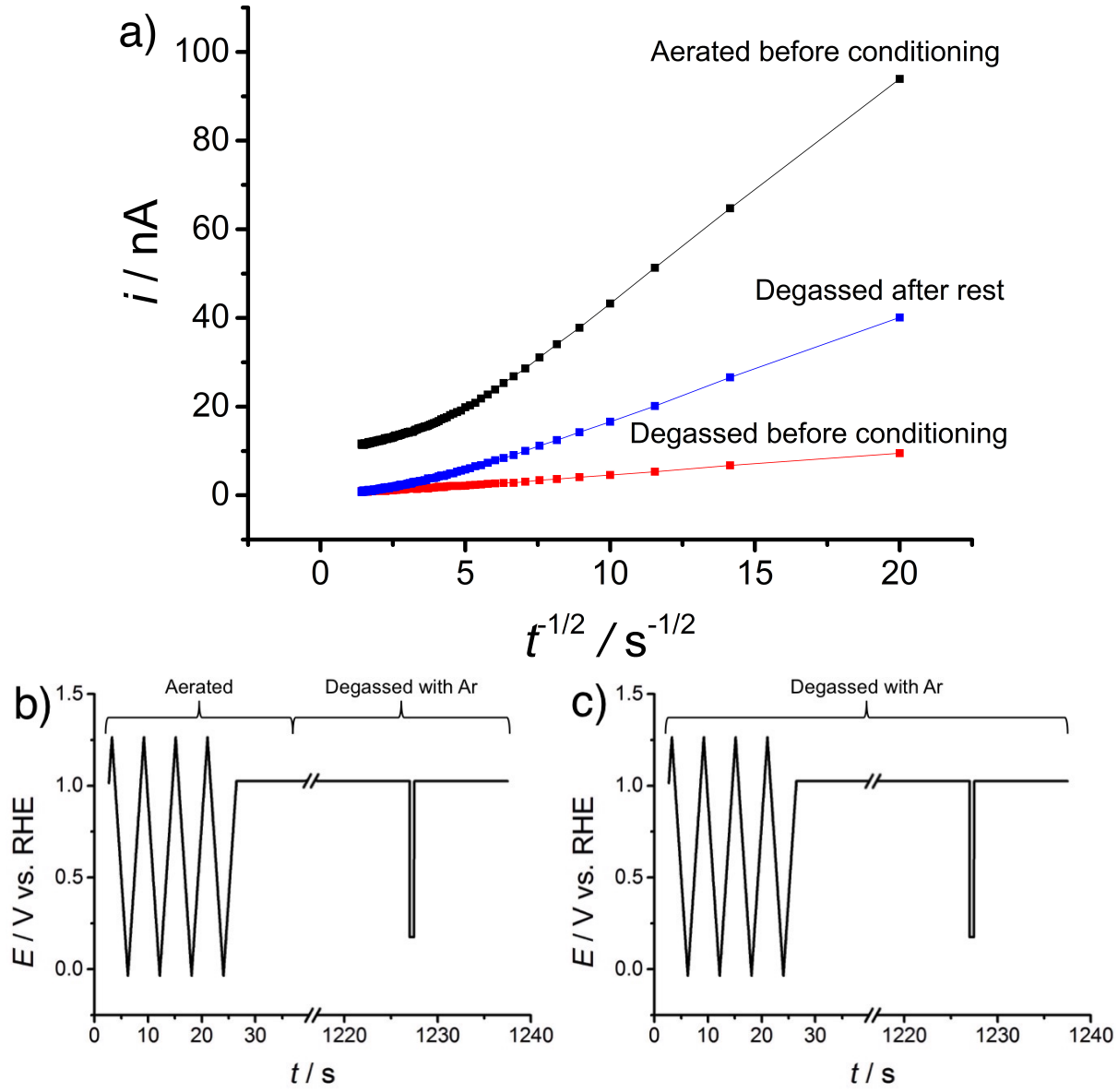

Figure 5.4: *a) Chronoamperograms for ORR in aerated 0.1 M $KClO_4$, at a pre-conditioned 25 µm diameter platinum electrode, stepped from OCP to 0.15 V vs. RHE, showing the current in fully aerated solution with no controls in place (I_{air}, black), the current in argon purged solution with the adsorbed oxygen layer (I_{O_2}, blue) and the background current recorded in argon purged solution after the pre-adsorbed oxygen layer had been consumed (I_b, red). b) Potential waveform used for collecting the blue current transient for the reduction of pre-adsorbed oxygen. c) Potential waveform used to collect the red current transient for the background current. The black current transient was collected using the potential waveform given in Figure 2.3.*

Figure 5.4 clearly shows that the first potential step yields a significantly greater current response than the second, more so than could possibly be explained by experimental error or background processes. This gives a strong indication of the presence of pre-adsorbed oxygen on the electrode surface prior to the first step, which was not replaced prior to the second step due to the argon purged conditions. Integration of the difference between the current response from the reduction of the pre-adsorbed oxygen layer (I_{ads}) and the background current response (I_b) with respect to time gives the associated charge for the reduction of this adsorbed oxygen layer ($Q_{ads,step}$).

$$Q_{ads,step} = \int (I_{ads} - I_b)\, \mathrm{d}t \tag{5.5}$$

Equation 5.5: *Charge from the reduction of pre-adsorbed oxygen ($Q_{ads,step}$) from the integral of the difference between the current from the reduction of the pre-adsorbed oxygen (I_{ads}) and the background current response (I_b) with respect to time.*

$Q_{ads,step}$ was then compared to the extra charged recorded using the subtraction method ($Q_{ads,sub}$), as previously described by Equation 5.1. These calculations found $Q_{ads,step}$ to be 40.0 μC cm^{-2}, compared to the previously determined value of $Q_{ads,sub}$, 54.0 μC cm^{-2}. After performing the same calculations for $Q_{ads,step}$ as for $Q_{ads,sub}$ (Equations 5.2 - 5.4), the number of moles of adsorbed oxygen was found to be 1.5 x 10^{-15} mol, corresponding to 0.09 monolayers. The similarity between these figures further supports the suggestion that the extra current is due to the presence of adsorbed oxygen, and also validates the assumptions made during the use of the theoretical equation in the subtraction method. This is important, as the subtraction method is significantly easier experimentally, requiring only a single current transient in aerated conditions, as opposed to multiple degassing steps. For this reason, Q will be calculated by the subtraction method throughout this report. The slightly larger value of $Q_{ads,sub}$ is to be expected, as some loss of adsorbed oxygen whilst the solution was being purged with argon is likely. Importantly, the similarity between the two values gives a strong indication that pre-adsorbed oxygen is the sole cause of the extra charge recorded, and so further sources do not need to be investigated.

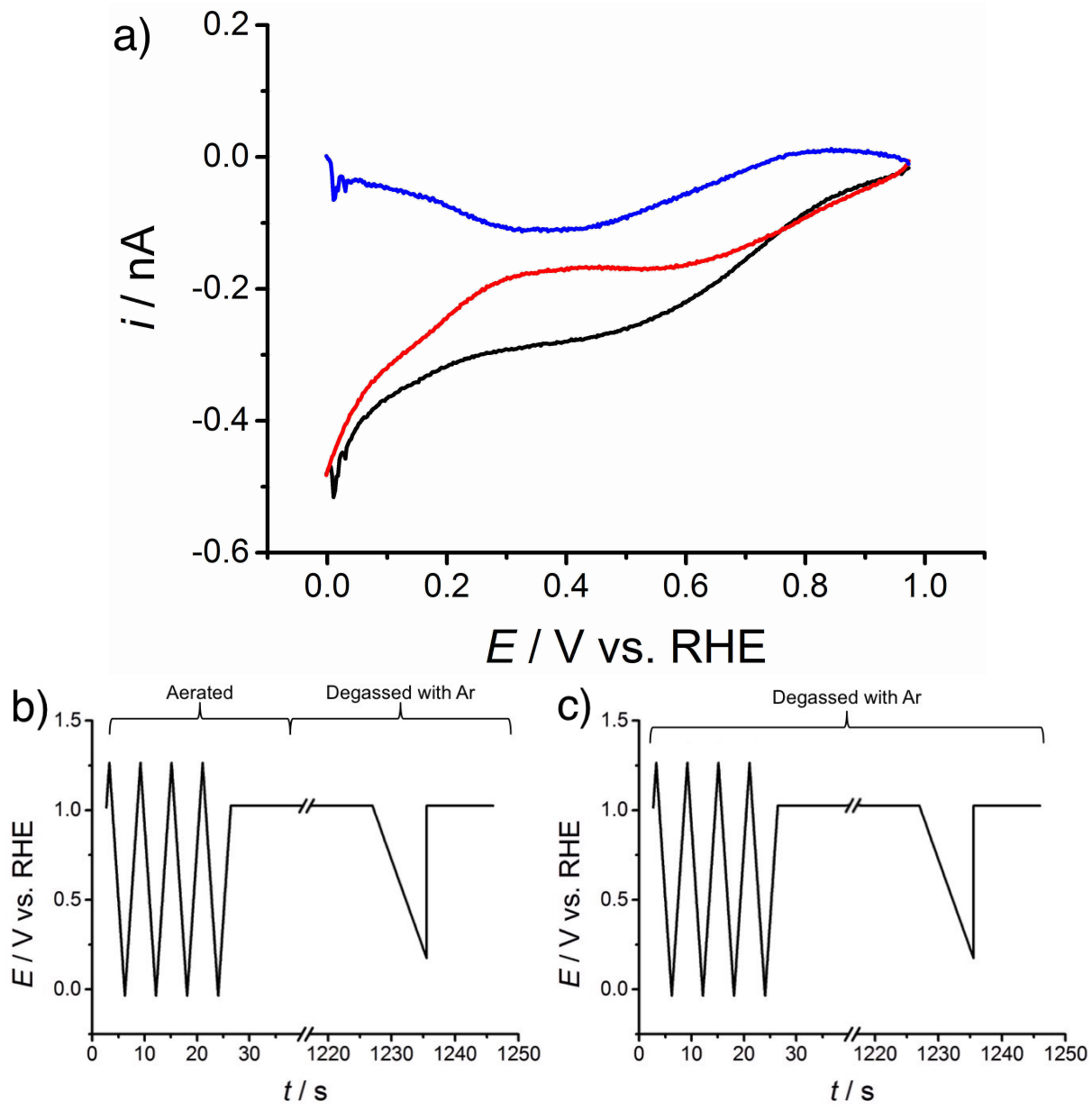

Figure 5.5: *a) Linear sweeps for the ORR at A 25 μm diameter platinum electrode in 0.1 M $KClO_4$ recorded by sweeping from OCP to 0.0 V vs. RHE at 100 mV s^{-1}, showing the current response in argon purged solution with the adsorbed oxygen layer (I_{exp}, black), the background current response recorded in argon purged solution after the pre-adsorbed oxygen layer had been consumed (I_b, red) and the result of the subtraction of the background from the experimental linear sweep, showing a peak due to the reduction of the pre-adsorbed oxygen layer (I_{ads}, blue). b) Potential waveform used for recording the black linear sweep voltammogram for the reduction of pre-adsorbed oxygen. c) Potential waveform used for recording the red linear sweep voltammogram for the background processes.*

Alternatively, the extra charge could be calculated through the use of a linear sweep rather than a potential step. The start of the method was identical to that previously described. The electrode was pre-conditioned using the waveform in Figure 2.3, to ensure the surface is oxide free before the oxygen was allowed to adsorb onto the electrode surface for 10 s. The cell was then purged with argon, so that any reduction could be ascribed to the reduction of the pre-adsorbed oxygen only. After this, instead of stepping the potential to give diffusion controlled oxygen reduction, the potential was swept to give a complete ORR wave at 100 mV s^{-1}. This was then repeated in fully argon purged solution to give a background sweep. The background was then subtracted from the initial linear sweep to show the sweep from the reduction of the pre-adsorbed oxygen. The resultant voltammograms are shown in Figure 5.5.

This method has the advantage over the chronoamperogram method as it gives a clear visual indication that an adsorption process is occurring, as the peak observed in the subtracted voltammogram is indicative of a stripping process. Slight modification of this process can be used to construct a similar plot for the reduction of a deposited platinum oxide. The procedure is initiated in degassed solution, with the rest potential being sufficiently positive to deposit a small amount of oxygen onto the electrode surface. The comparison is shown in Figure 5.6.

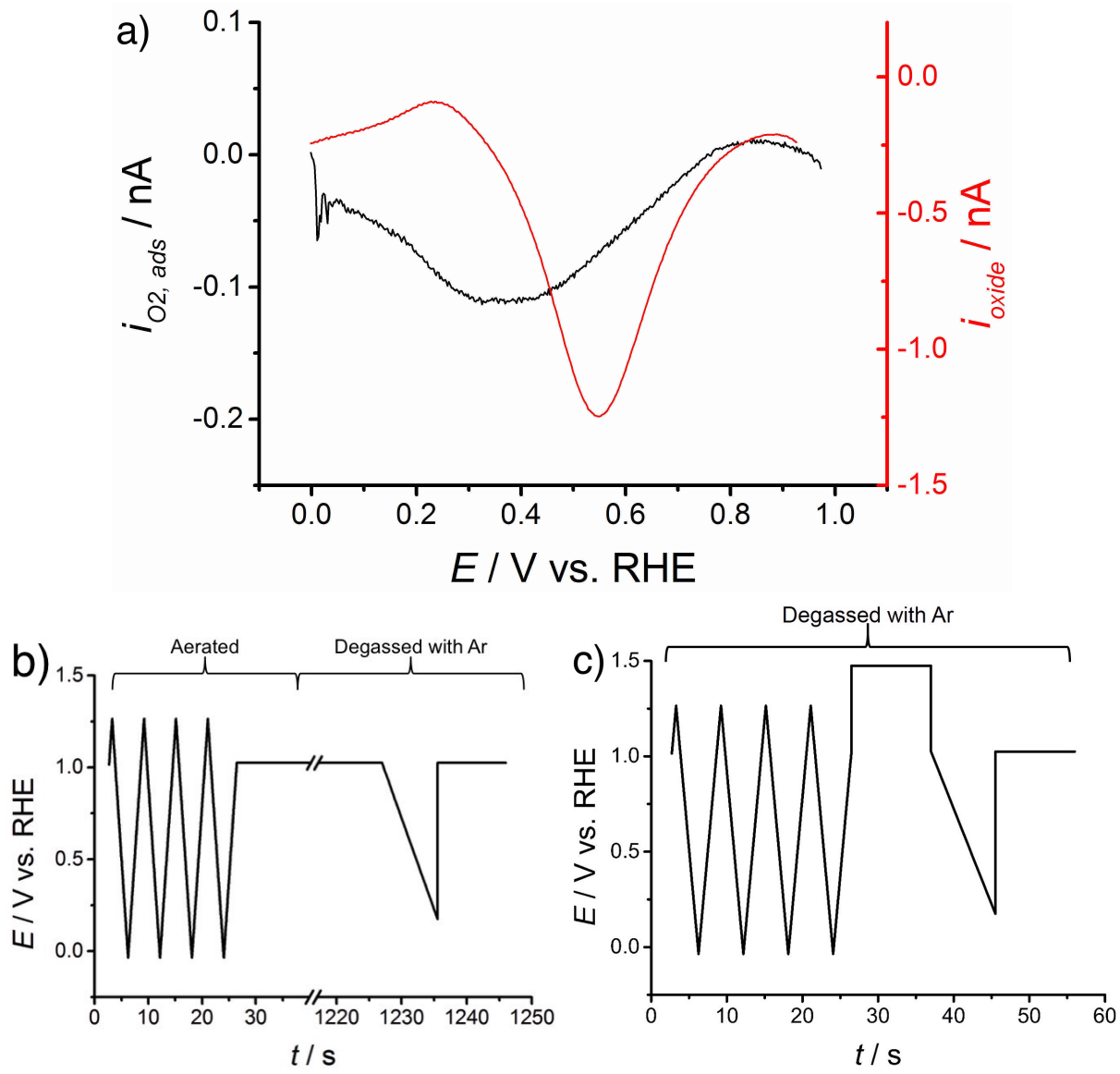

Figure 5.6: *a) Linear sweeps for the reduction of adsorbed oxygen species at a pre-conditioned 25 µm diameter platinum electrode in 0.1 M $KClO_4$ using the same method as described in Figure 5.5, showing the difference in the position of the reduction peak when reducing pre-adsorbed oxygen, adsorbed at OCP (black), compared to when reducing a platinum oxide deposited at OCP + 0.5 V (red). b) Potential waveform used for recording the black linear sweep voltammogram for the reduction of pre-adsorbed oxygen. c) Potential waveform used for recording the red linear sweep voltammogram for the reduction of the platinum oxide deposited at OCP + 0.5 V.*

It can be clearly seen that there is a significant difference between the peak potential for the reduction of pre-adsorbed oxygen and the reduction of intentionally deposited oxide at a higher overpotential. This is a good indication that the source of the extra charge is different in nature from the oxide that is electrochemically grown at positive potentials.

The area under the peak of Figure 5.5 can be calculated through simple integration of current against time to give $Q_{ads,sweep}$, according to Equation 5.5. The procedure described in Equations 5.2 - 5.4 could then be used in the same way to calculate the number of moles of oxygen which had pre-adsorbed. This was found to be 1.4 x 10^{-15} mol. This is in excellent agreement with the 1.5 x 10^{-15} mol calculated by the chronoamperometry method, validating the sweep method.

It is important to note that a number of assumptions have been made in these calculations. For example, it is assumed that the pre-adsorbed oxygen is reduced by four electron reduction, that all oxygen is bound side on, and that all crystal faces found in the polycrystalline platinum surface are behaving equally. However, the calculation does again highlight the sensitivity of the MSCV procedure, as this minute fraction of a monolayer is clearly observable on the millisecond timescale. These calculations also highlight how small an amount of oxygen is needed to generate a significant transient current response.

The success of this method also reveals interesting information about the nature of the binding of oxygen onto the metal surface. If the oxygen was physisorbed onto the electrode surface, the adsorption would be in a state of equilibrium. This would mean that when the cell was purged with argon, the adsorbed oxygen would desorb as soon as the concentration of oxygen in solution became low. This is not what is seen, as the pre-adsorbed oxygen remains adsorbed throughout the argon purge. This indicates that the adsorption onto the electrode surface is irreversible. This will involve a chemisorption of the oxygen onto the electrode, allowing the oxygen to remain adsorbed during the argon purge. This indicates that the oxygen adsorbs via a dissociative mechanism to allow a formal bond to be formed between the oxygen and the metal. The irreversible nature of the pre-adsorption should therefore be considered throughout the rest of this work.

5.4 MSCVs after varied rest conditions

All data presented thus far agree with the assertion that the extra current seen at short times is due to the reduction of pre-adsorbed oxygen. If this is indeed the case, then the recorded extra current and the calculated extra charge should be predictably tuned by manipulating the experimental conditions. Experiments that are designed to maximise oxygen adsorption should result in the greatest increase in the measured current, and vice versa. The first such series of experiments manipulated the rest time at open circuit prior to the potential step being recorded. Reducing the time spent at OCP should allow less oxygen to pre-adsorb, resulting in a reduction in the current response.

Current transients for the ORR on platinum were recorded by performing the cleaning waveform given in Figure 2.3, and then stepping from OCP to 0.15 V vs. RHE in 0.1 M $KClO_4$ as before. This was repeated with rest times of 10 s, 5 s, 2 s, 1 s and 0 s. A 0 s rest is defined as the potential step being performed immediately after the cleaning waveform had finished. All other conditions were kept the same. For the ease of analysis, the current transients are plotted as current vs. the inverse square root of time, as this draws out the data at short times. All of the transients were normalised by dividing the experimental current by the average current over the last 100 ms of the transient, in order to account for any differences in the concentration of dissolved oxygen or any other factors between experiments. As a point of reference, the theoretical transient for the reduction of oxygen according to Equation 1.45, assuming $n_{app} = 3.3$, is also plotted. All transients can be seen in Figure 5.7.

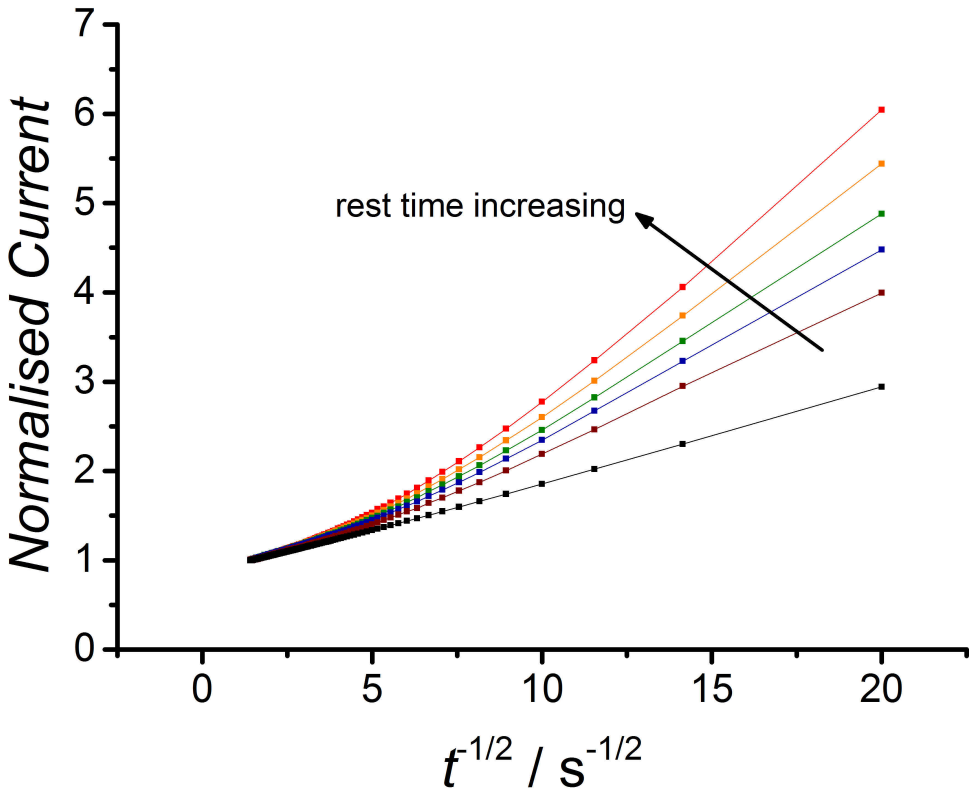

Figure 5.7: *Current transients after stepping from OCP to 0.15 V vs. RHE in aerated 0.1 M $KClO_4$ on a pre-conditioned 25 µm diameter Pt electrode. Transients were normalised by dividing by the average current over the last 100 ms. The rest at OCP was for 10 s (red), 5 s (orange), 2.5 s (green), 1 s (blue) and 0 s (brown). Also shown is the theoretical current transient according to Equation 1.45 (black), using $D = 2.29 \times 10^{-5}$ cm^2 s^{-1}, $c = 0.257$ mM, $a = 12.85$ µm and $n_{app} = 3.3$.*

It can be seen from Figure 5.7 that there is a clear trend whereby shortening the rest time before the potential step also reduces the current at short times. However, even when there is essentially no rest period, the current at short times is still clearly larger than the current predicted by Equation 1.45. It may be that the time spent during the final sweep of the cleaning waveform is enough to adsorb a considerable amount of oxygen. It seems that special measures are needed in order to ensure that the electrode is free of adsorbed oxygen prior to the potential step.

It is worth noting that Equation 1.45 assumes that the potential step is being performed from a starting point of zero current, where the concentration of reactant, in this case oxygen, is the same at the electrode surface as in the bulk. When removing the rest period and performing the potential step directly from the cleaning waveform, the diffusion layer

around the electrode tip is in a dynamic state of change, and so it cannot be guaranteed that the model applies. Furthermore, if the concentration of oxygen at the electrode surface is not given time to replenish, it would be expected that the concentration of dissolved oxygen, and therefore the measured current would also be smaller. Care must therefore be taken when analysing transients recorded after very short rest times. However, as the trend is seen when reducing the rest time from 10 s to 2.5 s, it seems reasonable to draw the conclusion that the rest period is directly affecting the magnitude of the extra current.

An important distinction to make is that the extra current is due to the reduction of pre-adsorbed oxygen rather than the reduction of oxide. When oxide is formed on platinum, further oxidation is possible even after a complete monolayer is formed, as the oxide may be intercalated into the bulk platinum structure[17]. This would result in a further increase in current. Oxygen pre-adsorption on the other hand would reach a saturation point once a certain amount of oxygen had absorbed[44]. Attempting to saturate the surface with pre-adsorbed oxygen would result in a plateau in the amount of extra charge, whereas oxide formation would give a consistent increase in the amount of extra charge. This was achieved by recording chronoamperograms for the ORR in 0.1 M $KClO_4$ after resting at increasing lengths of time at OCP prior to the potential step. The electrode was pre-conditioned using the waveform in Figure 2.3 prior to each step to ensure the surface was oxide free. The amount of extra charge seen in each case was then calculated using the procedure detailed in Equation 5.1, and plotted against the corresponding rest time at OCP. $Q_{ads,sub}$ was plotted in terms of charge density by dividing by the electrochemically active area, as determined by Equation 5.3. The change in charge density with rest time is shown in Figure 5.8.

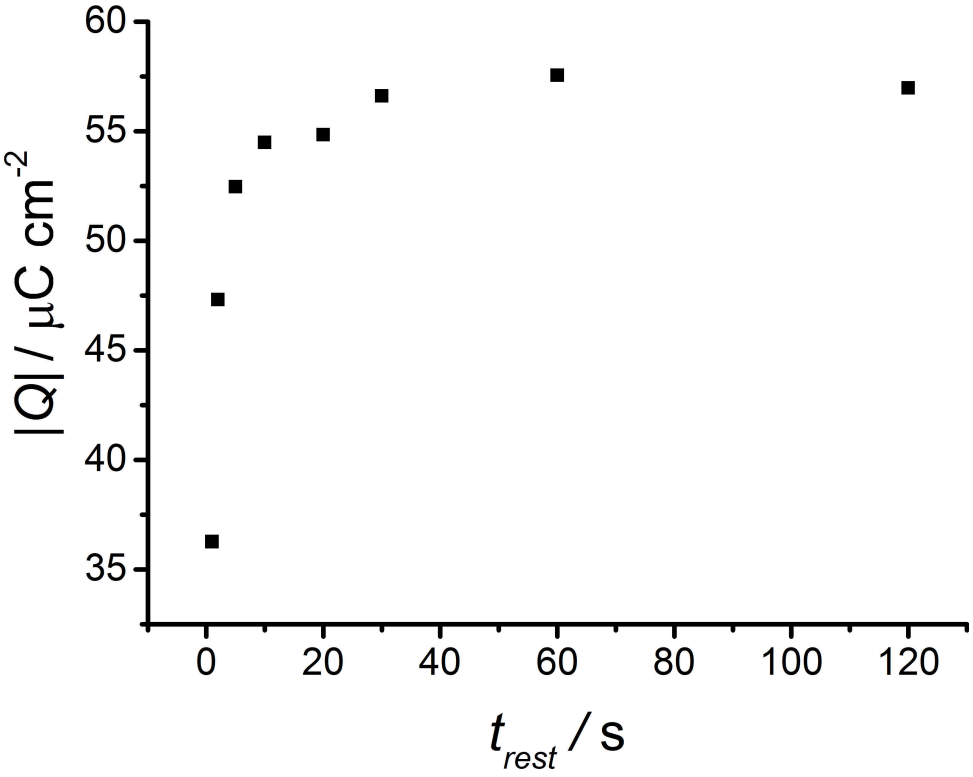

Figure 5.8: *Calculated extra charge density ($Q_{ads,sub}$) due to the reduction of pre-adsorbed oxygen, calculated using Equation 5.1, plotted against the time spent resting at OCP. Data was recorded using a pre-conditioned 25 μm diameter Pt electrode in aerated 0.1 M $KClO_4$.*

The extra charge can be clearly seen to plateau after resting for around 30 s, indicating that a maximum quantity of oxygen had pre-adsorbed. As well as probing the effect of changing the rest time on the charge density, this same method can also be used to find the effect of varying the rest potential. This was achieved by recording chronoamperograms for the ORR in 0.1 M $KClO_4$ after resting at varied potentials for 10 s prior to the potential step. The electrode was pre-conditioned using the waveform in Figure 2.3 prior to each step to ensure the surface was oxide free. The amount of extra charge seen in each case was then calculated using the procedure detailed in Equation 5.1, and plotted against the corresponding rest potential. $Q_{ads,sub}$ was plotted in terms of charge density by dividing by the electrochemically active area, as determined by Equation 5.3. The trend in charge density with rest potential is shown in Figure 5.9.

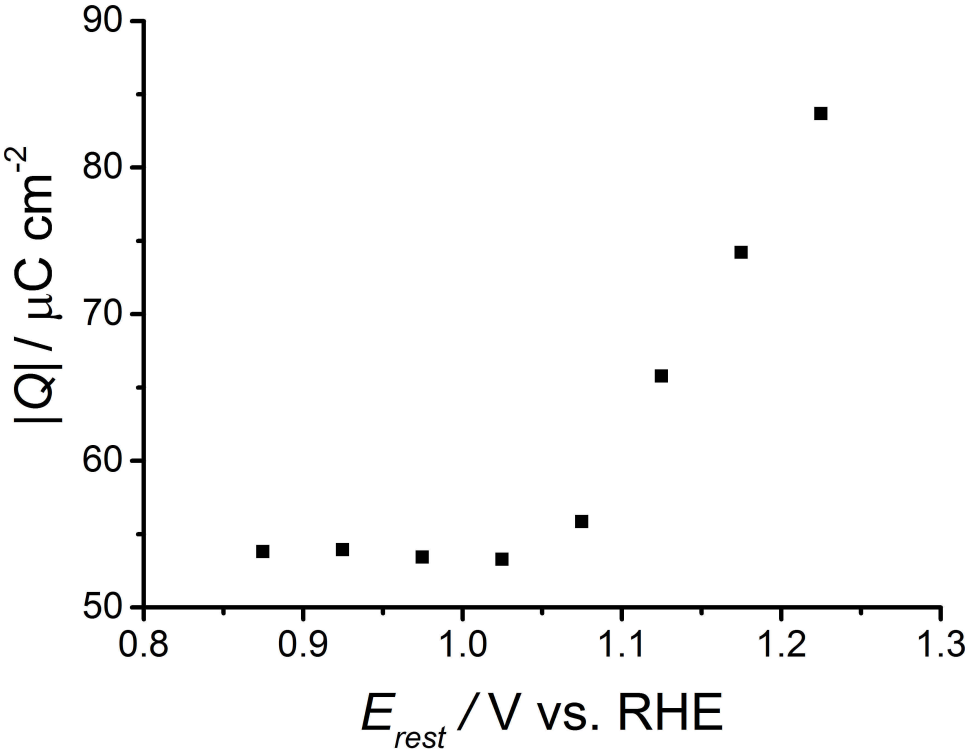

Figure 5.9: *Calculated extra charge density ($Q_{ads,sub}$) due to the reduction of pre-adsorbed oxygen, calculated using Equation 5.1, plotted against the rest potential, showing the sudden increase where oxide starts to form, and the plateaued region where a stable quantity of pre-adsorbed oxygen is being reduced. Data was recorded using a pre-conditioned 25 μm diameter Pt electrode in aerated 0.1 M $KClO_4$.*

A plateaued region of constant extra charge is seen as long as the potential is kept sufficiently negative not to induce oxide formation. The potentiostatically driven formation of platinum oxide is clearly seen as the steep rising slope on the right and side of the plot. This is consistent with the linear relationship between charge and potential for oxide formation that has been previously reported using SECM[139]. At lower potentials, the extra charge seen is constant over a wide potential range of around 150 mV. This rules out a potentially driven mechanism for the extra current, as such a wide plateau would not be seen. In combination with the apparent maximum adsorption seen at relatively short rest times seen in Figure 5.8, this data gives a good indication that a potentiostatically driven oxide formation is not responsible for the extra current. Instead, the pre-adsorption of molecular oxygen is a more likely source.

5.5 Poisoning the electrode with anions

As the extra charge is down to the reduction of pre-adsorbed oxygen, the charge should be proportional to the number of active sites available for oxygen adsorption. The number of active sites could be reduced by using a strongly adsorbing anion. It has been previously reported that the binding strength of anions on platinum follows the pattern I^- > Br^- > Cl^- > ClO_4^- [61]. It would therefore be expected that experiments performed in an iodide electrolyte would have fewer free sites available for oxygen adsorption, and therefore show less extra charge due to the reduction of pre-adsorbed oxygen. The electrode was first cleaned using the same pre-conditioning waveform as in previous experiments, to ensure a clean, oxide free surface. Chronoamperograms were then recorded by stepping from OCP to a potential significantly negative to give mass transport controlled reduction. Strongly adsorbing anions can cause a shift in the ORR wave to more negative potentials, and so the potentials used were adjusted appropriately in each case. This was done to ensure all experiments are comparable. Extreme precision was not needed in the choice of rest potential, as the wide plateau seen in Figure 5.9 gives a considerable margin for error with little or no effect on the calculated extra charge.

It can clearly be seen that as the binding strength of the anion increases, the short time current decreases. This continues from $KClO_4$, which gives the maximum amount of extra current, until KI, which gives close to the expected diffusion controlled response at all sampling times. This demonstrates a strong dependence on the number of available active sites, as would be expected for a process determined by the pre-adsorption of molecular oxygen. Although an approximately diffusion controlled response is seen for ORR in KI, it was thought possible that the current at short times would decrease with respect to the theoretical transient. This was suspected as rapid mass transport at short times would result in a greater proportion of hydrogen peroxide being lost into bulk of the solution.

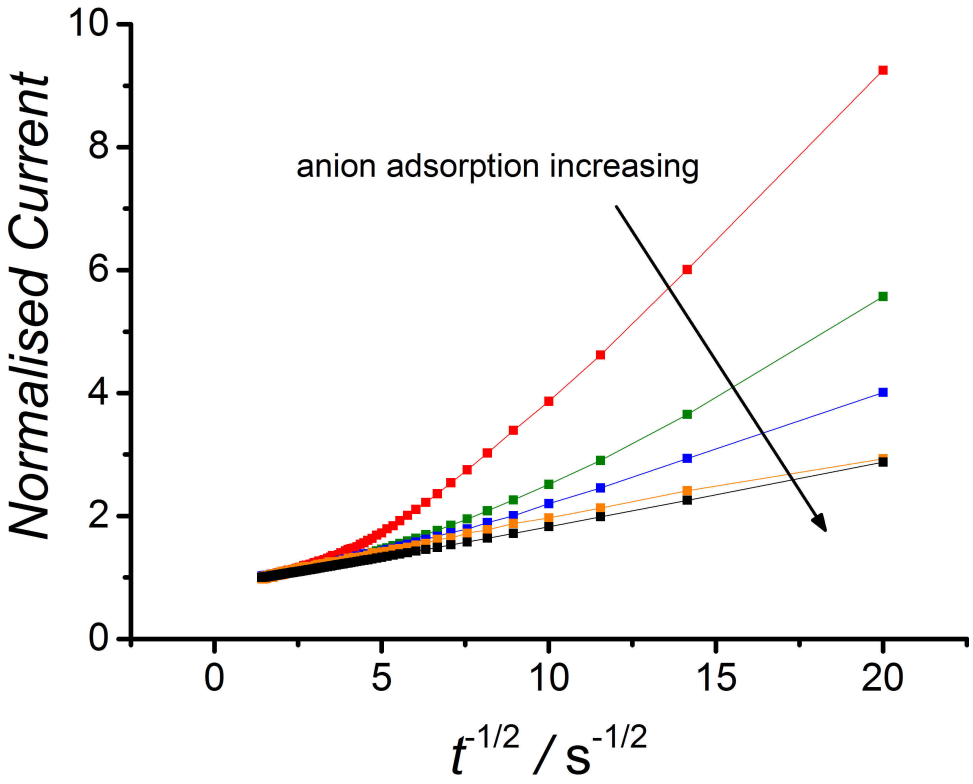

Figure 5.10: *Current transients after stepping from OCP to 0.15 V vs. RHE in 0.1 M potassium electrolytes on a pre-conditioned 25 μm diameter Pt electrode. Transients were normalised by dividing by the average current over the last 100 ms. The electrolyte used was $KClO_4$ (red), KCl (green) KBr (blue), and KI (orange). Also shown is the theoretical limiting current from Equation 1.45 (black), using $D = 2.29 \times 10^{-5}$ cm^2 s^{-1}, $c = 0.257$ mM, and $n_{app} = 3.3$ and $a = 12.85$ μm.*

It seems unlikely that the sampling time is not short enough to give sufficiently fast mass transport to reduce n_{app}. Work by Pletcher and Sotiropoulos[43] showed a noticeable reduction in n_{app} from 3.3 at a 25 μm diameter to electrode to around 2.8 at a 10 μm diameter electrode. 25 μm and 10 μm diameter electrodes correspond to mass transfer coefficients of 0.022 and 0.056 cm s^{-1}, according to Equation 1.48. Using Equation 4.1, this equates to sampling times of 500 and 5 ms respectively. The sampling times used should therefore be short enough to show a reduction in n_{app} with time. Instead, the absence of the reduction in n_{app} with time is likely to be due to a small amount of pre-adsorbed oxygen present despite the strong adsorption of iodide. Close inspection of the transient in the presence of iodide (Figure 5.10, ■) seems to show that the data point at 2.5 ms ($t^{-1/2}$ = 20 $s^{-1/2}$) is trending downwards. It is possible that even shorter sampling times would

give data points below the diffusion controlled response where n_{app} is assumed to be 3.3 as this downward trend continued. This would indicate the expected greater production of peroxide at shorter times, as the reduced n_{app} would appear as a reduced normalised current. This merits further work.

5.6 MSCV for the ORR with pH controls in place

It is well known that the oxygen reduction reaction is strongly dependent on the pH of the solution being used. The ORR also actively makes the environment around the microelectrode tip more alkaline, which can be explained by the proton consumption in Equation 1.53, or the hydroxide ion generation in Equation 1.54. As the solution becomes more basic, the ORR wave is shifted to more negative potentials. A transient change in the local pH could therefore affect the measured extra current compared to the diffusion controlled response. Alternatively, a pH change would disturb the distribution of ions within the diffuse layer, which could then be generating a capacitive current at short times. This required investigation, as it could potentially lead to an overestimation of the amount of oxygen adsorbed. .

If this is indeed the case, controlling the pH to prevent transient changes could reduce the extra current seen. This could be achieved by recording the MSCV in the presence of a neutral buffered solution, such as a phosphate buffer. Any role played by the glass insulation surrounding the microelectrode could be elucidated by using an epoxy sealed electrode rather than a glass one. Glass has a certain capacity for the storage of protons. Protons are exchanged for the metal ions which act to charge balance the silicate structure, a process known as dealkalization. Epoxy does not have the same capacity for proton storage as glass, and so if the glass surround is responsible, MSCVs at the epoxy electrode should show no extra current. An MSCV was recorded under identical conditions to those previously described, but using an epoxy sealed electrode in place of a glass sealed one. The results are shown in Figure 5.11.

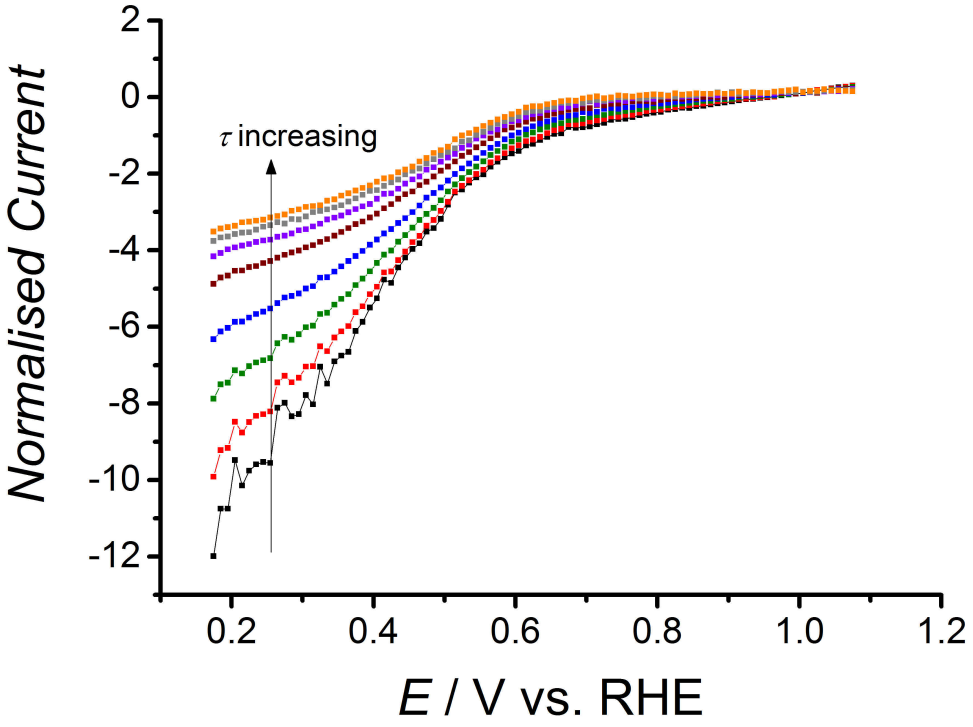

Figure 5.11: *MSCV for ORR at a pre-conditioned 25 μm diameter platinum electrode in aerated 0.1 M $KClO_4$ with epoxy insulation, sampled 2.5 ms (black), 5 ms (red), 10 ms (green), 20 ms (blue), 50 ms (brown), 100 ms (purple), 200 ms (grey), and 500 ms (orange) after the potential step, normalised using the theoretical limiting current from Equation 1.45, using $D = 2.29 \times 10^{-5}$ cm^2 s^{-1}, $c = 0.257$ mM, $a = 12.85$ μm*

The extra current is still seen with an epoxy-insulated electrode, which ruled out any involvement by the glass insulation, although it did not altogether rule out transient pH change as the cause of the extra current. After saturation with humidified air, the pH of the electrolyte was measured to be 7.34. An MSCV was therefore recorded in 0.1 M $KClO_4$ in the presence of 10 mM phosphate buffer at pH 7.34. The MSCV is shown in Figure 5.12.

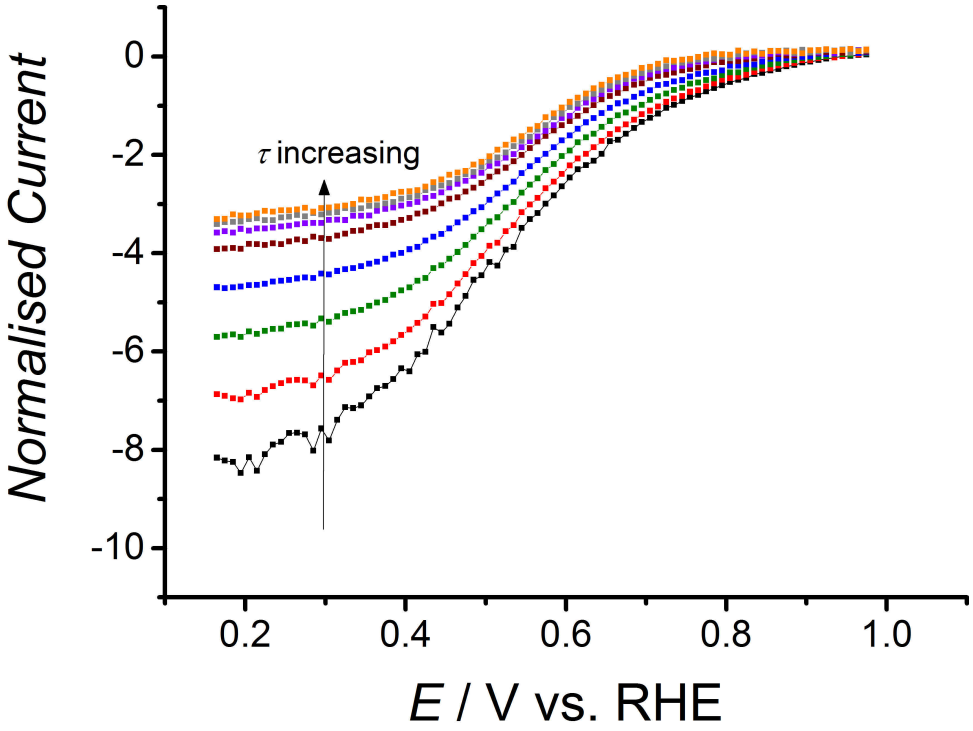

Figure 5.12: *MSCV for ORR at a pre-conditioned 25 μm diameter platinum electrode in aerated 0.1 M $KClO_4$ with 10 mM pH 7.34 phosphate buffer, sampled 2.5 ms (black), 5 ms (red), 10 ms (green), 20 ms (blue), 50 ms (brown), 100 ms (purple), 200 ms (grey), and 500 ms (orange) after the potential step, normalised using the theoretical limiting current from Equation 1.45, using $D = 2.29 \times 10^{-5}$ cm^2 s^{-1}, $c = 0.257$ mM, $a = 12.85$ μm*

Again, the extra current is still seen. A slight reduction in the extra current at short times is observed, with the 2.5 ms MSCV converging to around 8 in the presence of the buffer (Figure 5.12), compared to around 10.5 in the absence of the buffer (Figure 5.1). This reduction is likely due to the relatively strong adsorption of phosphate having a poisoning effect, hindering the adsorption of oxygen. One further option to prevent transient changes in pH is to conduct experiments in strong acid or base. This gives a large excess of H^+ and OH^- in solution, and so would prevent a noticeable local change in the pH environment around the electrode during the ORR. MSCVs for the ORR were therefore performed in 0.1 M $HClO_4$ and 0.1 M KOH. These are shown in Figures 5.13 and 5.14 respectively.

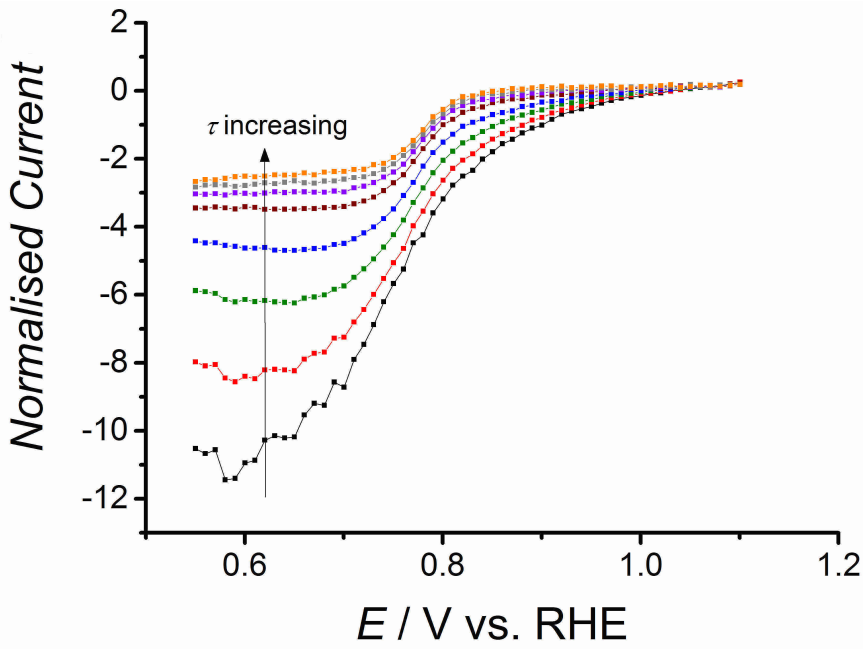

Figure 5.13: *MSCV for ORR at a pre-conditioned 25 μm diameter platinum electrode in aerated 0.1 M KOH, sampled 2.5 ms (black), 5 ms (red), 10 ms (green), 20 ms (blue), 50 ms (brown), 100 ms (purple), 200 ms (grey), and 500 ms (orange) after the potential step, normalised using the theoretical limiting current from Equation 1.45, using* $D = 1.83 \times 10^{-5}$ cm^2 s^{-1} *and* $c = 0.256$ *mM and* $a = 12.85$ *μm.*

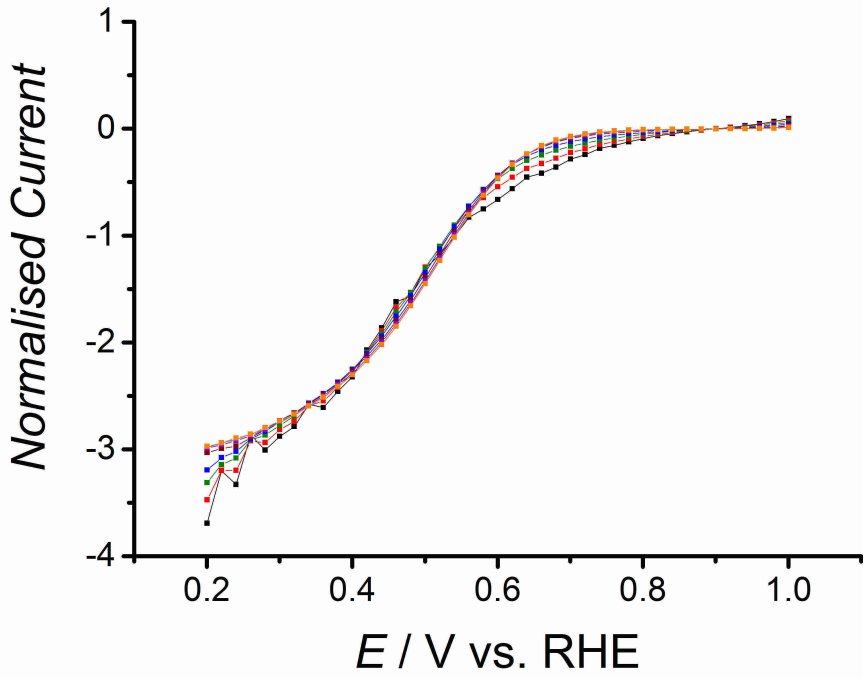

Figure 5.14: *MSCV for ORR at a pre-conditioned 25 μm diameter platinum electrode in aerated 0.1 M* $HClO_4$*, sampled 2.5 ms (black), 5 ms (red), 10 ms (green), 20 ms (blue), 50 ms (brown), 100 ms (purple), 200 ms (grey), and 500 ms (orange) after the potential step, normalised using the theoretical limiting current from Equation 1.45, using* $D = 1.83 \times 10^{-5}$ cm^2 s^{-1} *and* $c = 0.256$ *mM and* $a = 12.85$ *μm.*

It can clearly be seen that conducting the experiment in strong base will not remove the extra current seen at short times. However, when probing the ORR in strong acid, the extra current now seems to have disappeared at all sampling times. Whilst the previous experiments indicate that a transient change in pH do not affect the extra current, there is clearly a strong pH dependence. Indeed, by adding aliquots of $HClO_4$ into a cell containing $KClO_4$, it was possible to reduce the extra current seen at short times. The extra current was eventually removed once the pH was made significantly low. To demonstrate this, current transients were recorded after performing a potential step from OCP to the plateau of the ORR wave in neutral unbuffered solution. An aliquot of acid was then added, and the solution was homogenised with a glass sealed magnetic stirrer bar before the next potential step was performed. The average of ten current transients recorded in this way was used in each case for this comparison, as shown in Figure 5.15.

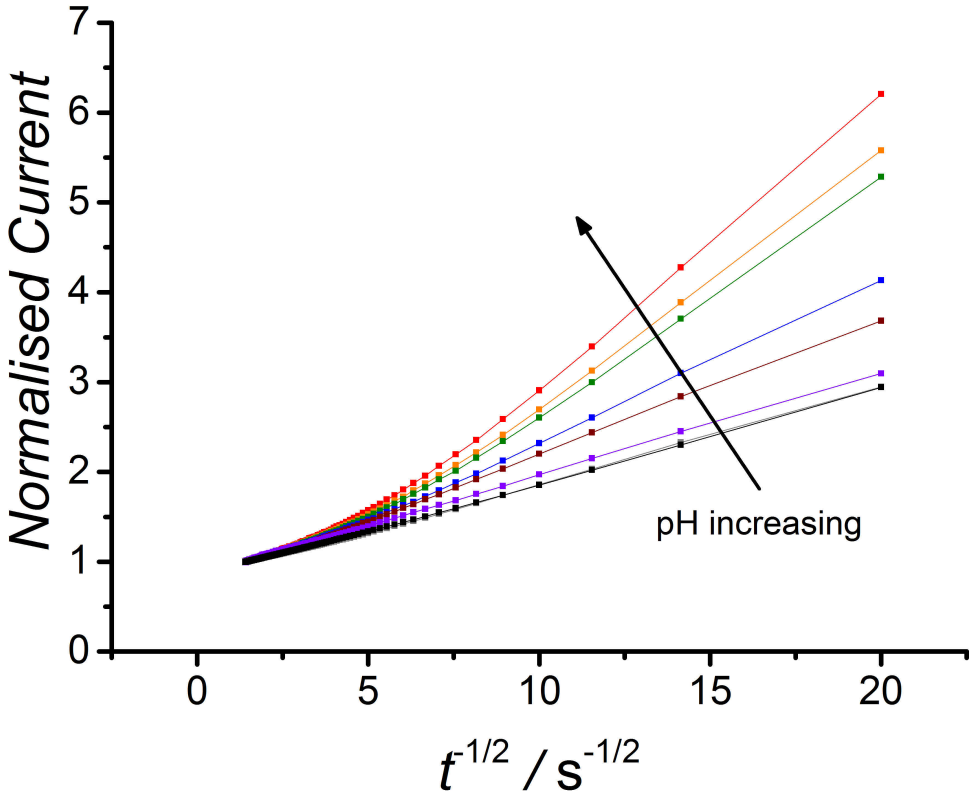

Figure 5.15: *Current transients after stepping from OCP to 0.15 V vs. RHE in aerated 0.1 M $KClO_4$ on a pre-conditioned 25 μm diameter Pt electrode, normalised by dividing by the average current over the last 100 ms, where the aliquot of $HClO_4$ added was 0 μl (red), 0.1 μl (orange), 0.5 μl (green), 1 μl (blue), 10 μl (brown), 20 μl (purple), 50 μl (grey), and the theoretical current transient according to Equation 1.45 (black) using $D = 2.29 \times 10^{-5}$ cm^2 s^{-1}, $c = 0.257$ mM, $a = 12.85$ μm and $n_{app} = 3.3$*

It is clear that a low pH is able to remove the extra current seen for the ORR at short times. However, it is worth noting that it is not clear whether the absence is due to an inhibition of the pre-adsorption of oxygen, an inhibition of the reduction of the pre-adsorbed oxygen, or an enhancement that is sufficient to consume the oxygen layer prior to the first data point being recorded at 2.5 ms. The ORR has been reported to be more facile in alkaline media than in acid[140]. This makes it unlikely that acidic media is showing a rapid consumption of adsorbed oxygen. More likely it seems that the acidic environment is helping to block the adsorption of oxygen on to the electrode.

A further possibility is a change in the mechanism of the ORR when moving from basic to neutral to acidic solutions. In basic and neutral solutions, the oxygen reduction involves a combination of oxygen with water molecules, as described in Equation 1.54. In acidic solution the reduction involves a combination of oxygen with protons in solution, as described in Equation 1.53. The change between the two mechanisms has been reported to be around pH 2.7[34,35]. It may be that the presence of pre-adsorbed oxygen is not as favourable when the acidic mechanism is in play, as any pre-adsorbed oxygen would have to wait for the diffusion of protons to the electrode surface before reduction. The diffusion coefficient of protons is incredible fast thanks to the small size of the ion and due to the Grotthus mechanism[141]. The diffusion coefficient for protons has been measured as 8.59 x 10^{-5} cm^2 s^{-1} in 0.1 M $NaClO_4$, by Lanning *et al.*[142] which is more than four times the measured diffusion coefficient of oxygen. It therefore seems doubtful that the diffusion of H^+ could be a limiting factor. However when looking at the reduction of pre-adsorbed oxygen, there is no oxygen diffusion term. It is possible that in this case the diffusion on protons may become significant. Of course, it is possible that it is not just one but a combination of factors that is causing the inhibition of the extra charge at short times. This distinction merits further work.

5.7 Concentration dependence of pre-adsorbed oxygen

It appears that the oxygen is adsorbing prior to a potential being applied to the electrode, making the adsorption a passive process. If this is the case, it is likely that the number of monolayers of oxygen adsorbing onto the electrode surface is dependent on the concentration of oxygen in the bulk solution. To probe this, a cell was set up with argon purged electrolyte, a 25 μm diameter platinum electrode and SCE. The cell was then sealed from the environment using a Suba-Seal septum. The electrode was then treated as with all previous experiments, as was detailed in Section 2.2. A series of current transients were then performed by stepping from OCP to 0.15 V vs. RHE five times, with the cleaning waveform from Figure 2.3 being inserted between each step. A 0.1 ml aliquot of aerated electrolyte was then introduced into the cell using a syringe through the septum. The electrolyte was then homogenised using a glass sealed magnetic stirrer bar for one minute. A Teflon coated stirrer bar was not used as Teflon has the capacity to store oxygen, and so would give uncertainty around the dissolved oxygen concentration[111]. A further five current transients were recorded, where the electrolyte now contains a small amount of dissolved oxygen. This was repeated until a total of 15 ml had been added to the cell.

In order to calculate the amount of extra charge associated with each of these solutions, the exact concentration of dissolved oxygen needed to be known in each case. This was determined by performing a non-linear regression analysis of the last 100 ms of each experiment against the model in Equation 1.45, where values of D and a were fixed at the same values as were previously used for the MSCV analyses, and n_{app} was fixed as 3.3, as determined by the long time MSCV measurements. Once the concentration was determined, Equation 1.45 was used to generate a theoretical current transient for each concentration, which was then subtracted from the corresponding experimental transient. These were all then integrated against time to give a collection of extra charges for each concentration of dissolved oxygen. The method detailed in Section 6.1 was followed, taking electrode radius, atoms per cm^{-2} and R_f into account. The relationship between the extra charge and dissolved oxygen concentration is shown in Figure 5.16.

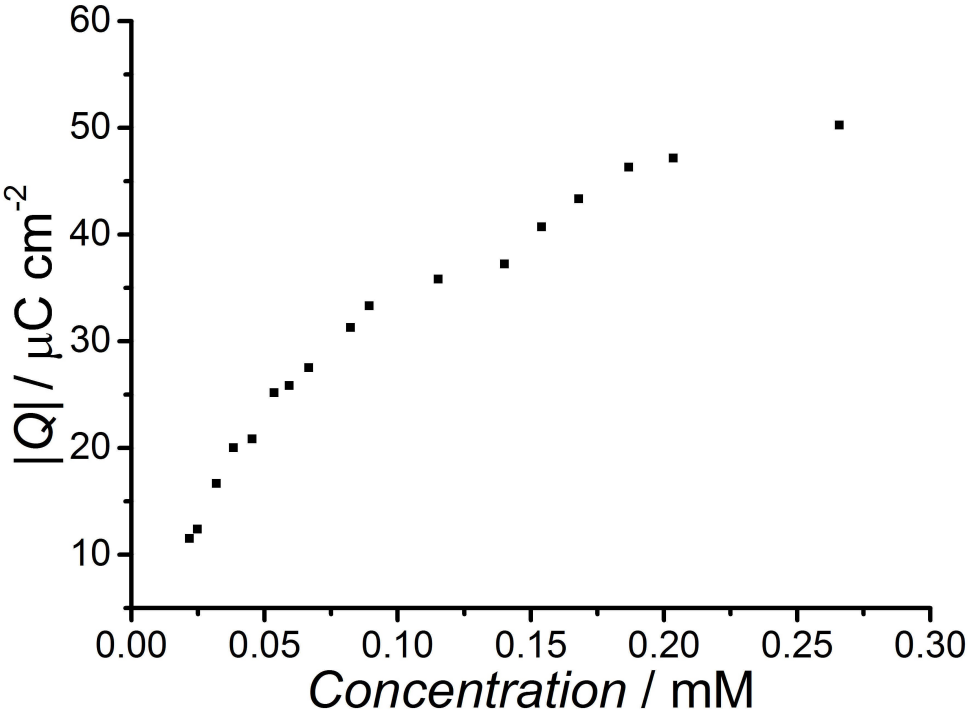

Figure 5.16: *Calculated extra charge density ($Q_{ads,sub}$) due to the reduction of pre-adsorbed oxygen, calculated using Equation 5.1, vs. the concentration of dissolved oxygen in solution, as determined by non-linear regression of the last 100 ms of the average current transient using Equation 1.45, assuming $D = 2.29 \times 10^{-5}$ cm^2 s^{-1}, $a = 12.8$ μm and $n_{app} = 3.3$.*

It can be seen that even at low concentrations of dissolved oxygen, it is possible to detect a small amount of extra current. The extra charge rapidly increases as the concentration is marginally increased up to around 0.1 mM. The extra charge then seems to start to reach a plateau as a fully aerated solution is approached. The assumption that n_{app} remains constant at all concentrations of dissolved oxygen was seen to be appropriate as the steady state current observed on the chronoamperograms indicated n_{app} was around 3.3 at all concentrations. This appears to resemble an adsorption isotherm, which gives weight to the suggestion that it is an adsorption process that we are seeing. However, as the pre-adsorption has been shown to be irreversible, it would be more accurate to refer to this as a dosing curve, as an isotherm assumes that the adsorption is in a state of equilibrium. Importantly, there is a clear dependence of the extra charge on the concentration of oxygen in solution. This indicates that it is aqueous oxygen that is the cause, as opposed to oxide formed from the splitting of water, which would be possible in degassed solution.

6 Elucidation of ORR activity

6.1 MSCVs on varying metals

Chapter 5 has shown evidence that the extra current seen over the first few milliseconds of the oxygen reduction reaction is caused by the pre-adsorption of oxygen prior to the potential step. This chapter looks at the potential for the charge from the reduction of pre-adsorbed oxygen being used as a descriptor for oxygen reduction activity.

The adsorption of oxygen onto a metal electrode is related to the energy of the formed bonds between molecular oxygen and the metal in question. Stronger bonds between the oxygen atoms and the partially empty d orbitals of the metal will result in more energetically favourable adsorption. The energy gain from the forming of strong M-O bonds is needed to outweigh the repulsive interactions between more densely packed oxygen atoms. It would therefore be expected that more oxygen will adsorb during a rest at open circuit on a strongly adsorbing metal than on a weakly adsorbing metal.

To test this, MSCVs were recorded for electrodes made of metals with varying binding energies towards dissolved oxygen (ΔE_O). There values have been previously calculated by Nørskov *et al.*[102] using density functional theory (DFT). There are a number of ways that binding energies can be calculated. In this case, values for the ΔE_O are taken as the enthalpy of the formation of a surface bound oxygen atom from the splitting of a water molecule, following the reaction given in Equation 6.1.

$$M + H_2O \rightarrow M - O + H_2 \tag{6.1}$$

Equation 6.1: *Reaction scheme used for the calculation of oxygen binding energy at a metal surface (ΔE_O) from the enthalpy of the reaction to form M-O from M and H_2O.*

Metals that bind more strongly to dissolved oxygen would be likely to have a greater level of oxygen coverage after being exposed to aerated solutions for the same length of time. A trend would therefore be expected between binding energy and the extra current, with larger currents being seen on more strongly adsorbing metals thanks to the greater degree of oxygen pre-adsorption. MSCVs were recorded on nickel, copper, silver and gold, which are shown in Figures 6.1, 6.2, 6.3 and 6.4 respectively. The pre-conditioning waveform shown in Figure 2.3 was used in each case, with the potentials being adjusted to those given in Table 2.5. The trend in ΔE_O is Ni < Cu < Pt < Ag < Au, as seen in Figure 1.25, where a more negative ΔE_O indicates stronger binding to the metal surface.

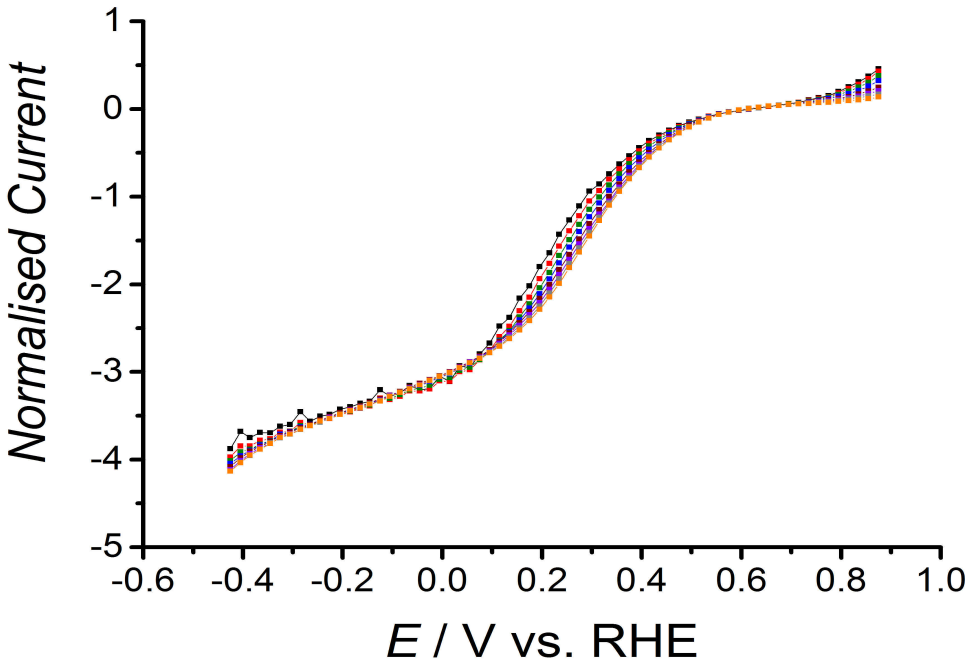

Figure 6.1: *MSCV for ORR at a pre-conditioned 25 μm diameter gold electrode in aerated 0.1 M $KClO_4$, sampled 2.5 ms (black), 5 ms (red), 10 ms (green), 20 ms (blue), 50 ms (brown), 100 ms (purple), 200 ms (grey), and 500 ms (orange) after the potential step, normalised using the theoretical limiting current from Equation 1.45, using $D = 2.29 \times 10^{-5}$ cm^2 s^{-1}, $c = 0.257$ mM, $a = 12.1$ μm.*

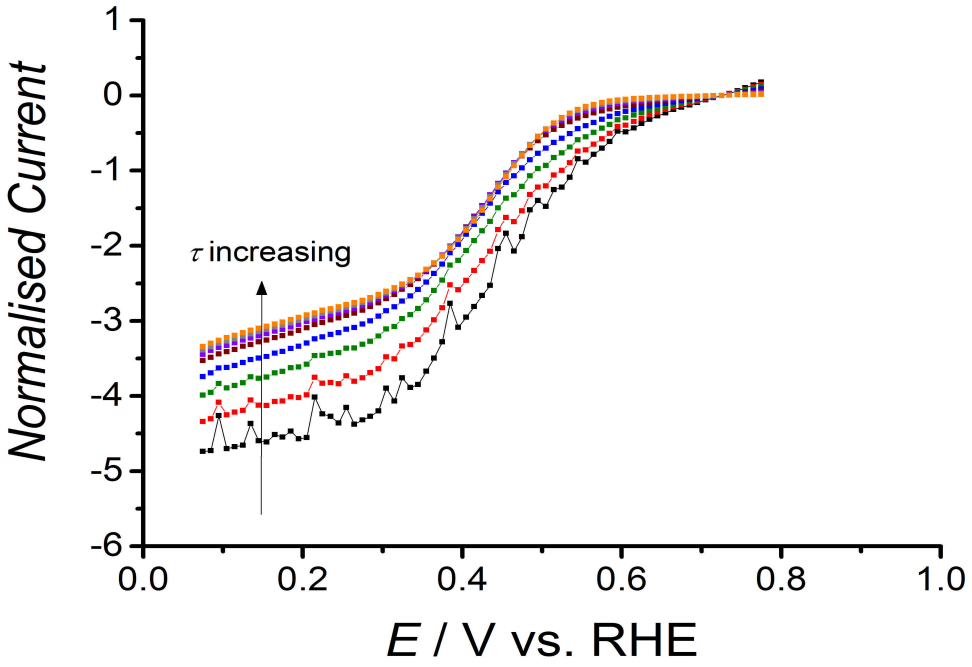

Figure 6.2: *MSCV for ORR at a pre-conditioned 25 μm diameter silver electrode in aerated 0.1 M $KClO_4$, sampled 2.5 ms (black), 5 ms (red), 10 ms (green), 20 ms (blue), 50 ms (brown), 100 ms (purple), 200 ms (grey), and 500 ms (orange) after the potential step, normalised using the theoretical limiting current from Equation 1.45, using $D = 2.29 \times 10^{-5}$ cm^2 s^{-1}, $c = 0.257$ mM, $a = 11.5$ μm.*

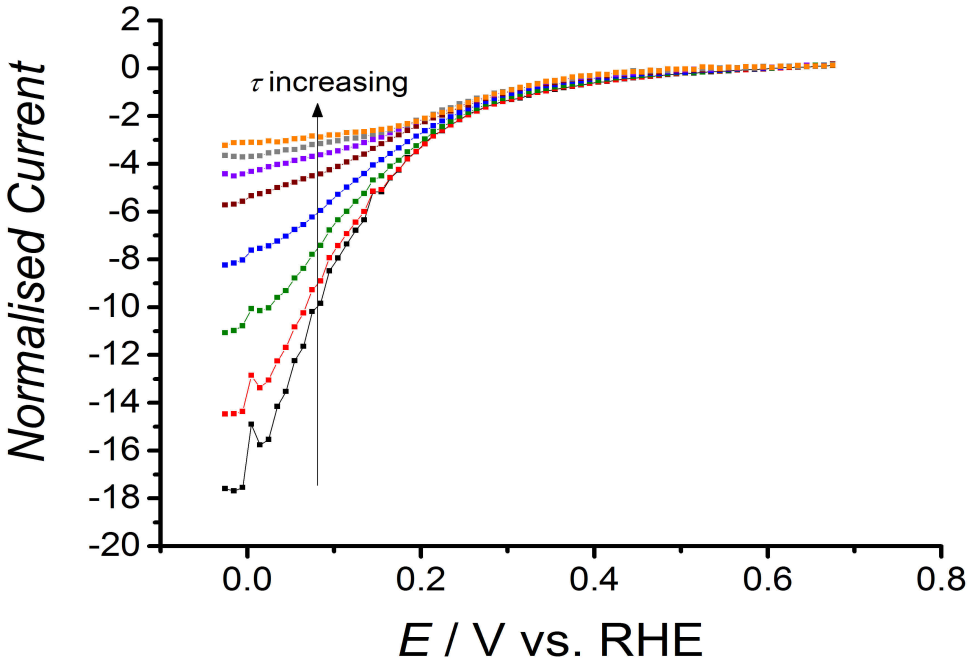

Figure 6.3: *MSCV for ORR at a pre-conditioned 25 μm diameter copper electrode in aerated 0.1 M $KClO_4$, sampled 2.5 ms (black), 5 ms (red), 10 ms (green), 20 ms (blue), 50 ms (brown), 100 ms (purple), 200 ms (grey), and 500 ms (orange), normalised using the theoretical limiting current from Equation 1.45, using $D = 2.29 \times 10^{-5}$ cm^2 s^{-1}, $c = 0.257$ mM, $a = 14.0$ μm.*

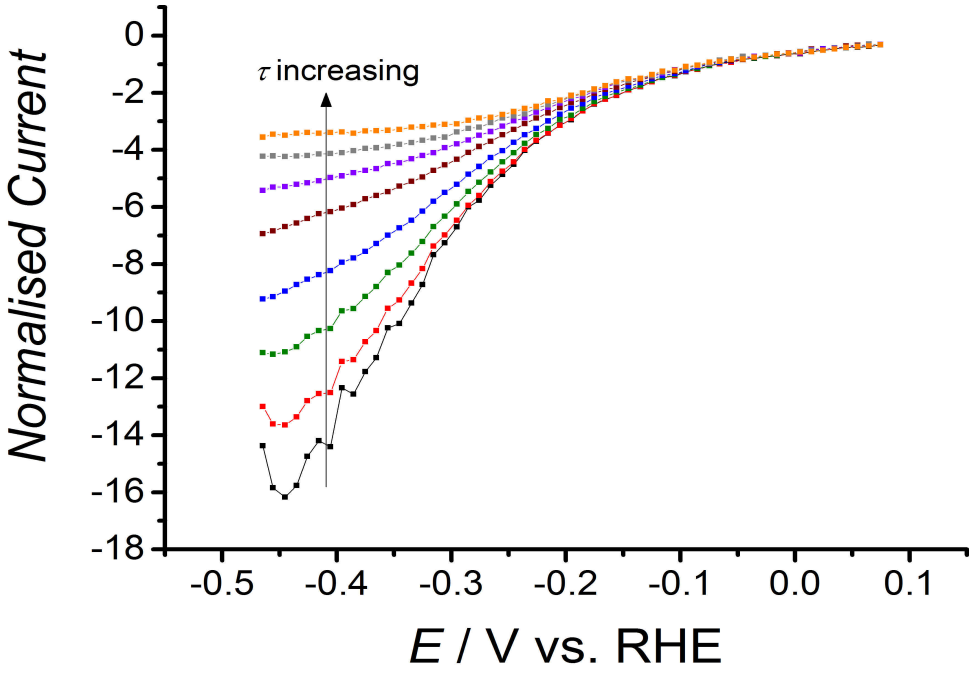

Figure 6.4: *MSCV for ORR at a pre-conditioned 25 μm diameter nickel electrode in aerated 0.1 M $KClO_4$, sampled 2.5 ms (black), 5 ms (red), 10 ms (green), 20 ms (blue), 50 ms (brown), 100 ms (purple), 200 ms (grey), and 500 ms (orange) after the potential step, normalised using the theoretical limiting current from Equation 1.45, using $D = 2.29 \times 10^{-5}$ cm^2 s^{-1}, $c = 0.257$ mM, $a = 12.8$ μm.*

Comparison of MSCVs recorded at the five metals shows that the trend in extra current appears to follow the same trend as is found in ΔE_O. To confirm the relationship, it would be more useful to express this extra current in terms of the extra charge compared to the theory. This was done for all metals in the same way as for platinum, where transients from the plateau of the MSCV were taken and averaged, before the theoretical transient from Equation 1.45 was subtracted. The resultant current after the subtraction was due to the adsorbed oxygen, as the model assumes an entirely diffusion controlled current. The result of the subtraction was then integrated with respect to time to give the corresponding charge $Q_{ads,sub}$, as was described in Equation 5.1.

$Q_{ads,sub}$ was then normalised by dividing by the electrochemically active area of the electrode. However, it is not as simple to calculate the number of active sites in non-platinum metals, as the surface behaviour is not as well defined as for platinum. The procedure detailed in Equation 5.3 is therefore not valid for the other metals. For this reason, a different approach to finding the true surface area was needed. First, the true

electroactive area of a platinum electrode was determined by the method given in Equation 5.3, after the platinum electrode had undergone a strict, and reproducible polishing regime. This was then compared to the geometric area to give the roughness factor of that electrode (R_f).

$$R_f = \frac{A_{echem}}{\pi a^2} \tag{6.2}$$

Equation 6.2: *Calculation for the roughness factor of an electrode (R_f) from the electrochemically active area of an electrode as given by Equation 5.3 (A_{echem}) and the geometric area taken from the electrode radius (a) determined by SEM.*

For a well polished platinum electrode, R_f was found to be 2.8. With the R_f calculated for the platinum electrode, it can then be assumed that the same R_f applies to all other metal electrodes, as long as they go through the same reproducible polishing regime. Their electrochemically active surface areas were determined by multiplying the geometric area of each electrode by 2.8. A further issue with calculating the number of adsorption sites on the electrode surface for varying metal electrodes is that different metals have a different number of atoms per cm^2. This leads to a different number of oxygen binding sites in the same area of metal electrode. The calculation of the number of adsorption sites on the electrode was therefore determined individually for each metal using Equation 5.2, with the number of atoms per square centimetre being taken from the literature, and the radius being accurately determined by SEM. With all of these controls in place, the calculated values of A_{echem} can be assumed accurate.

The calculated charge density was plotted against the ΔE_O values from Nørskov[102] to look for a correlation. Binding energies are also available in the form of Gibbs energies (ΔG_O) of the reaction shown in Equation 6.1, which are also plotted against the same charge data. Error bars were calculated by recording five separate current transients for a narrow range of potentials that all gave a diffusion controlled current response, and calculating the extra charge for each one. The error bar was then taken as the maximum difference between one of these charges and the mean value.

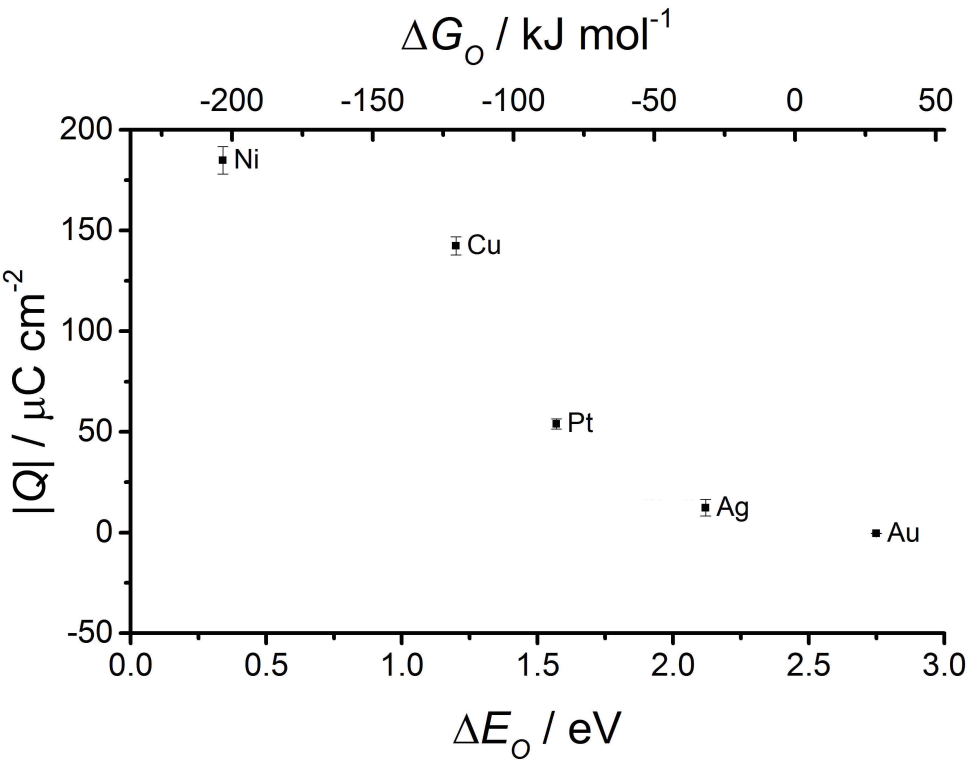

Figure 6.5: *Calculated extra charge density ($Q_{ads,sub}$) due to the reduction of pre-adsorbed oxygen, calculated using Equation 5.1 against the binding energy of those metals toward oxygen (ΔE_O) and the Gibbs energies of the reaction detailed in Equation 6.1 (ΔG_O). ΔG_O and ΔE_O were both taken from reference 102.*

There is a clear trend where as ΔE_O becomes more negative, the charge density rapidly increases. This is due to the increased strength of the interaction between oxygen and metal surface resulting in a greater quantity of oxygen adsorbing onto the electrode surface during the same rest period. The small size of the error bars give good confidence in the resolution of the difference between extra charges of different metals. As with platinum, the extra charge can be expressed in terms of a number of moles of surface adsorbate using Faraday's law of electrolysis (Equation 5.4). If it is assumed that the reduction of the adsorbed oxygen layer is a four electron process, then the number of moles of oxygen pre-adsorbed onto the electrode surface can be calculated. For Au, Ag, Pt, Cu and Ni this gave 1.1 x 10^{-12}, 3.0 x 10^{-11}, 1.3 x 10^{-10}, 3.4 x 10^{-10} and 4.4 x 10^{-10} mol cm^{-2} respectively.

To find the number of monolayers of oxygen, the number of moles in a complete monolayer is required. This is taken as half the number of active sites on each electrode,

as molecule of O_2 is able to bridge across two metal atoms on the electrode surface. This follows the bridge adsorption model[47], as described in Figure 1.22. This mode has been reported to favour four electron reduction, as is commonly observed on platinum metal surfaces, and so is assumed to be the predominant mode of adsorption. The number of moles of O_2 in a complete monolayer is given by Equation 5.2. By calculating the number of active sites on each electrode using the method detailed in Equations 5.2, 5.3 and 6.2, it was possible to express this in terms of the number of monolayers adsorbed onto the electrode. This takes into account the number of atoms cm^{-2}, the surface roughness, and precise size of each electrode individually. For Ni, Cu, Ag and Au the number of atoms cm^{-2} for the polycrystalline metals were taken as 1.6, 1.8, 1.0 and 1.2×10^{15} respectively[143–146]. The number of monolayers for each metal are shown in Figure 6.6.

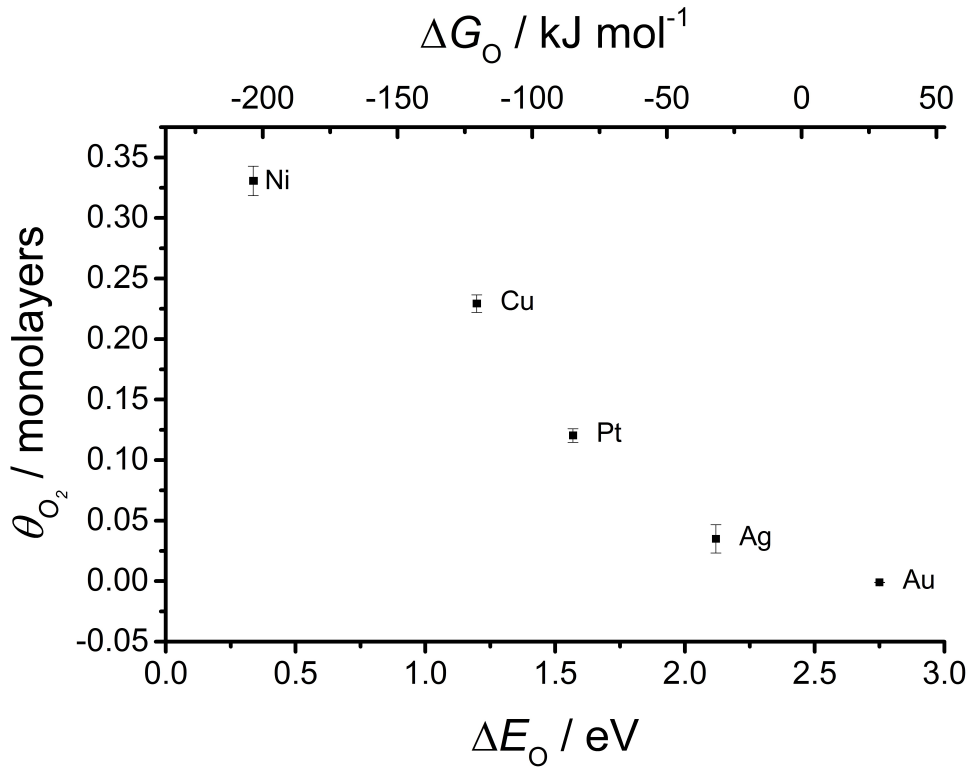

Figure 6.6: *Calculated number of monolayers of adsorbed O_2 (θ_{O_2}) from the ratio of the extra charge seen in ORR experiments to the theoretical charge for a complete monolayer for Ni, Cu, Pt, Ag and Au against the binding energy of those metals toward oxygen (ΔE_O) and the Gibbs energies of the reaction detailed in Equation 6.1 (ΔG_O). ΔG_O and ΔE_O were both taken from reference 102.*

As with the platinum calculation, it is important to note that a number of assumptions are made in this calculation, which have been previously discussed. Whilst the given values should be treated with caution, it is still worth noting that the number of monolayers involved are low. This makes the suggestion that adsorbed oxygen is the sole cause of the extra current more likely, as it does not require the presence of multiple, or even nearly complete monolayers of adsorbed oxygen to cause significant extra current. It also further highlights the sensitivity of the MSCV technique, as the small fractions of a monolayer of adsorbed oxygen are very easily observed.

6.2 Experimental calculation of ΔG_O

Figure 6.5 reveals a sigmoidal relationship between $Q_{ads,sub}$ and ΔG_O. However, it is important to note that the values given for ΔG_O are entirely theoretical, having come from DFT calculations. To confirm the sigmoidal relationship, an experimental approach for the calculation of ΔG_O was sought. This came from the determination of $Q_{ads,sub}$ from linear sweep voltammetry in argon purged solution in the presence of a pre-adsorbed oxygen layer. After the background subtraction, the reduction of the pre-adsorbed oxygen resembled a stripping peak, which had a peak potential (E_p) associated with its reduction (Figure 5.5). E_p is therefore a measure of the potential difference needed to drive the reduction of the pre-adsorbed oxygen. This was repeated for the silver, copper and nickel electrodes, as shown in Figure 6.7. Two trends can clearly be seen from the plot. One is that as the binding energy with the metal electrode increases, the charge under the peak increases, reflecting the greater quantity of oxygen that pre-adsorbs as the binding energy increases. It can also be seen that as the binding energy increases, the peak potential shifts to the left. This indicates that a greater overpotential is needed to reduce the pre-adsorbed oxygen layer when the binding energy of that oxygen layer increases.

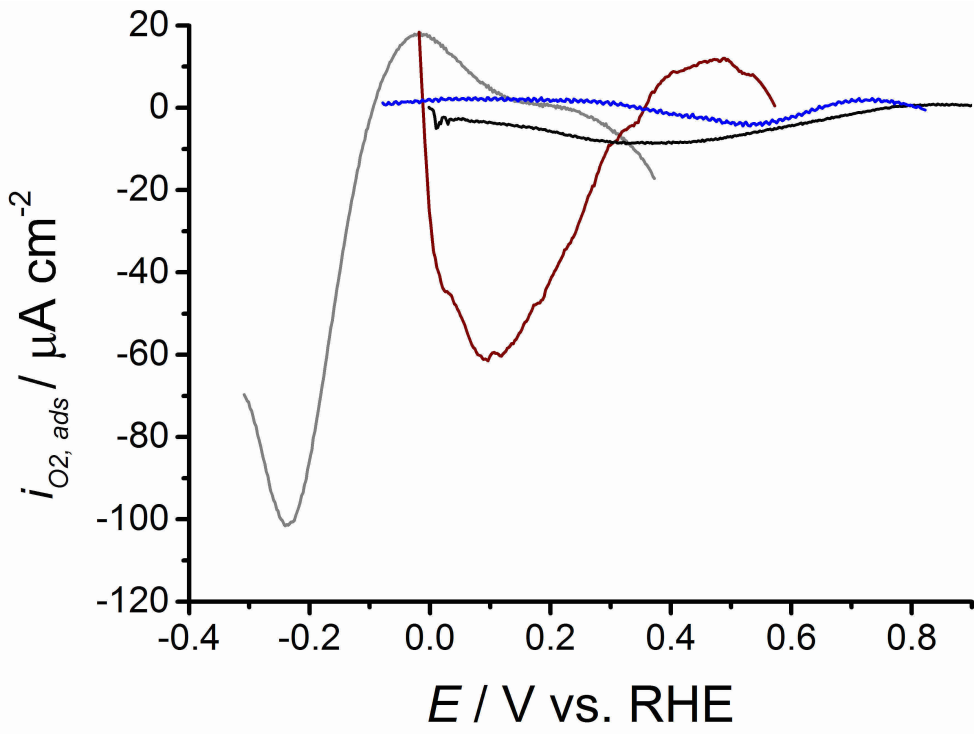

Figure 6.7: *Linear sweep voltammograms for the reduction of pre-adsorbed oxygen ($i_{O_2,ads}$), from the subtraction of a background voltammogram from one recorded in argon purged solution in the presence of a pre-adsorbed oxygen layer. Voltammograms were recorded using the procedure and waveforms described in Figure 5.5. These were recorded for Ni (grey), Cu (brown), Pt (black), and Ag (blue) electrodes.*

These trends both agree with previous data, and reflect the expected pattern in the metals. E_p is therefore an indication of how strongly the oxygen is adsorbed onto the electrode surface, but it is not a formal binding energy. The energy of the bonds between the metal of the electrode and the oxygen on the surface can be described as the difference between the potential at which the adsorbed oxygen is stripped (E_p) and the potential at which the oxygen desorbs. This potential is taken as the thermodynamic potential for oxygen reduction, E_{ORR}. The energy of binding in volts is therefore the difference between E_p and the thermodynamic potential for oxygen reduction. The binding energy (ΔG_{peak}) can be simply converted into J mol^{-1} using Equation 6.3.

$$\Delta G_{peak} = -nF(E_{ORR} - E_p) \tag{6.3}$$

Equation 6.3: *Binding energy of oxygen onto an electrode (ΔG_{peak}) from the difference between the peak from the stripping voltammogram of the reduction of pre-adsorbed oxygen (E_p) and the thermodynamic potential for oxygen reduction (E_{ORR}), multiplied by the number of electrons transferred (n) and Faraday's constant (F).*

E_{ORR} is difficult to determine experimentally, and so was taken as the thermodynamic value of 1.229 V vs. RHE, adjusted to the previously measured value of pH 7.34 using Equation 6.4.

$$E_{ORR} = E^0 - (59\ \text{mV} \times \text{pH}) \tag{6.4}$$

Equation 6.4: *PH adjusted thermodynamic potential for oxygen reduction (E_{ORR}) from the standard thermodynamic potential (E^0) and the pH.*

For pH 7.34, this equated to 0.796 V vs. RHE. The number of electrons was taken as two, as the binding of oxygen to the metal surface was determined theoretically according to a single oxygen atom bound to a single metal atom. In this way, ΔG_{peak} was calculated for all metals shown in Figure 6.5. Extra charges were then plotted against both ΔG_O from the literature, and ΔG_{peak} from the experiments simultaneously as a way validating the calculated ΔG_{peak}. Both plots are overlaid in Figure 6.8.

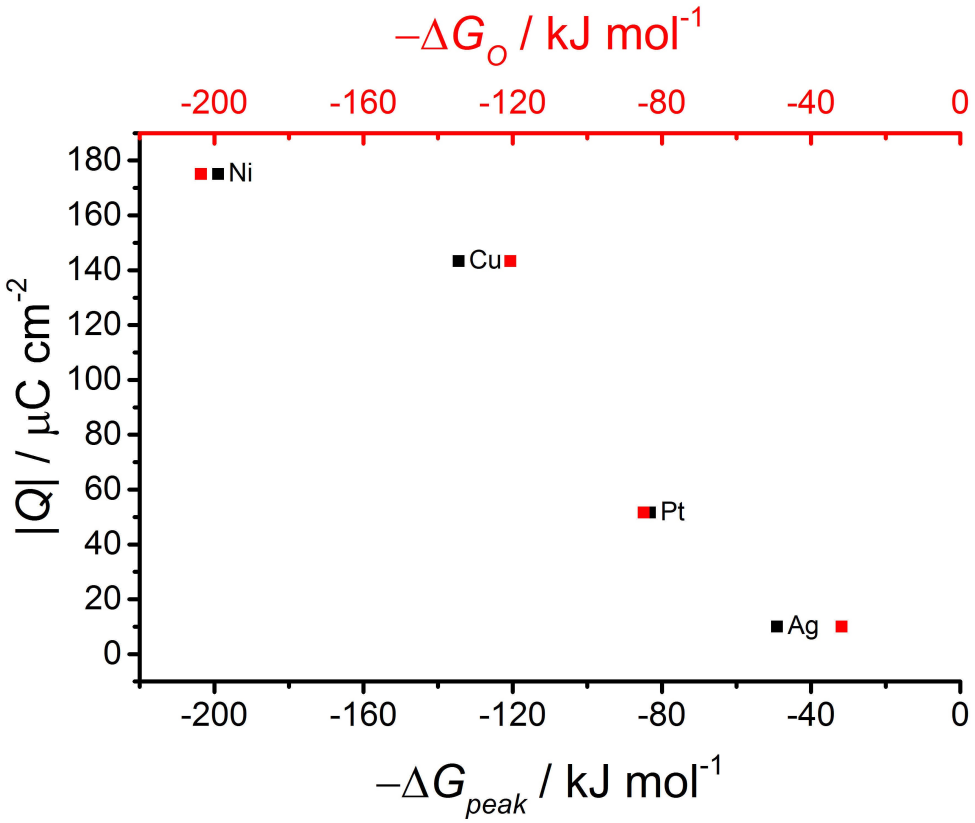

Figure 6.8: *Calculated extra charge density ($Q_{ads,sub}$) due to the reduction of pre-adsorbed oxygen, calculated using Equation 5.1 against the Gibbs energies of adsorption, taken from reference 102 (ΔG_O, red), and the Gibbs energy as calculated experimentally (ΔG_{peak}, black).*

The remarkable similarity between the two curves gives good indication that the experimentally calculated values of ΔG_{peak} are a true representation of the strength of the binding between the pre-adsorbed oxygen and the metal surface. A plot of Q against ΔG_O can therefore be used as a calibration curve for the calculation of binding energies of unknown materials. $Q_{ads,sub}$ is very simply calculated from the integral of the difference between the experimental current transient for oxygen reduction, and the theoretical diffusion controlled response, according to Equation 5.1. If $Q_{ads,sub}$ is calculated for an unknown material, then ΔG_O can simply be read off of the x axis of the plot. This was done for $Pt_{0.9}Rh_{0.1}$ and $Pt_{0.9}Ir_{0.1}$ alloys. MSCVs for both alloys were first recorded for both metals to check the position of the ORR wave in each case. The electrode was pre-conditioned using the waveform in Figure 2.3, using the potentials listed in Table 2.5 in both cases. The recorded MSCVs are shown in Figures 6.9 and 6.10 respectively.

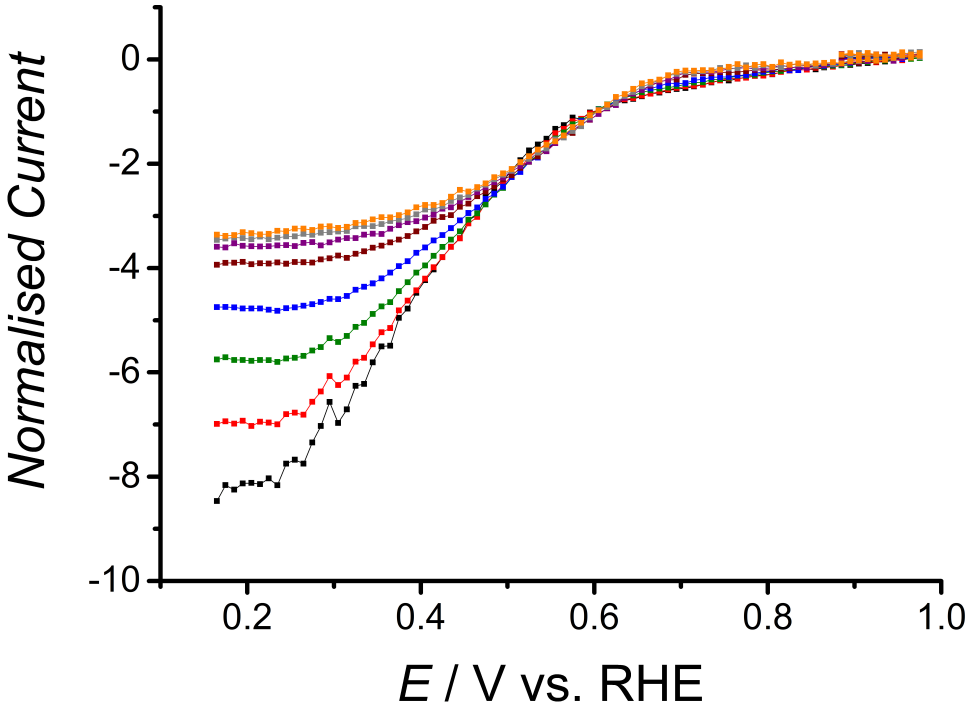

Figure 6.9: *MSCV for ORR at a pre-conditioned 25 µm diameter $Pt_{0.9}Rh_{0.1}$ electrode in aerated 0.1 M $KClO_4$, sampled 2.5 ms (black), 5 ms (red), 10 ms (green), 20 ms (blue), 50 ms (brown), 100 ms (purple), 200 ms (grey), and 500 ms (orange) after the potential step, normalised using the theoretical limiting current from Equation 1.45, using $D = 2.29 \times 10^{-5}$ cm^2 s^{-1}, $c = 0.261$ mM, $a = 13.8$ µm*

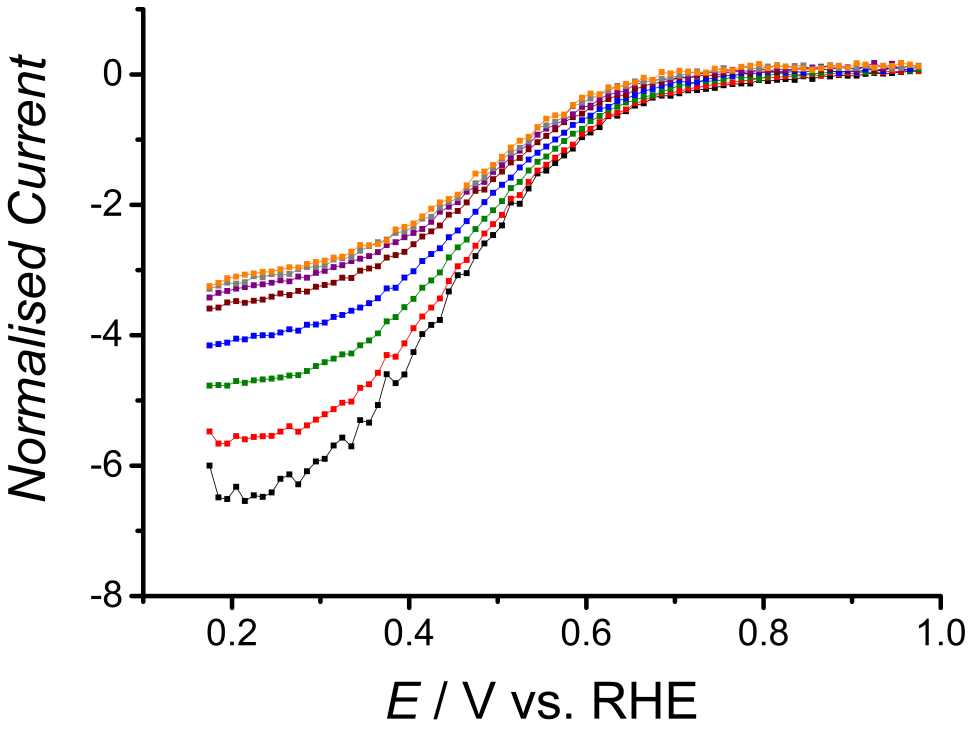

Figure 6.10: *MSCV for ORR at a pre-conditioned 25 μm diameter $Pt_{0.9}Ir_{0.1}$ electrode in aerated 0.1 M $KClO_4$, sampled 2.5 ms (black), 5 ms (red), 10 ms (green), 20 ms (blue), 50 ms (brown), 100 ms (purple), 200 ms (grey), and 500 ms (orange) after the potential step, normalised using the theoretical limiting current from Equation 1.45, using $D = 2.29 \times 10^{-5}$ cm^2 s^{-1}, $c = 0.264$ mM, $a = 12.5$ μm*

Using an average of current transients at the plateau for oxygen reduction on both metals, the extra charge was calculated as previously described using Equation 5.1. The calculated charges for $Pt_{0.9}Ir_{0.1}$ and $Pt_{0.9}Rh_{0.1}$ were then plotted along with the previously calculated values for Au, Ag, Pt, Cu and Ni. The extra charges were then aligned with the curve in Figure 6.5 in order to calculate an approximate binding energy, as shown in Figure 6.11. The curve drawn has no mathematical basis, it is only intended as a guide for calculation of ΔG_O and ΔE_O. This gave ΔE_O for $Pt_{0.9}Ir_{0.1}$ and $Pt_{0.9}Rh_{0.1}$ as 1.75 eV and 1.70 eV respectively, and ΔG_O as -67.5 kJ mol^{-1} and -72.4 kJ mol^{-1} respectively. Again, the small size of the error bars highlight the precision of the method, as a small percentage of alloyed metal gives a significant change in the calculated charge, which is well outside of the error bars. This gives confidence that the method can resolve the difference between different alloys, even when the alloyed metal is only present in a small percentage.

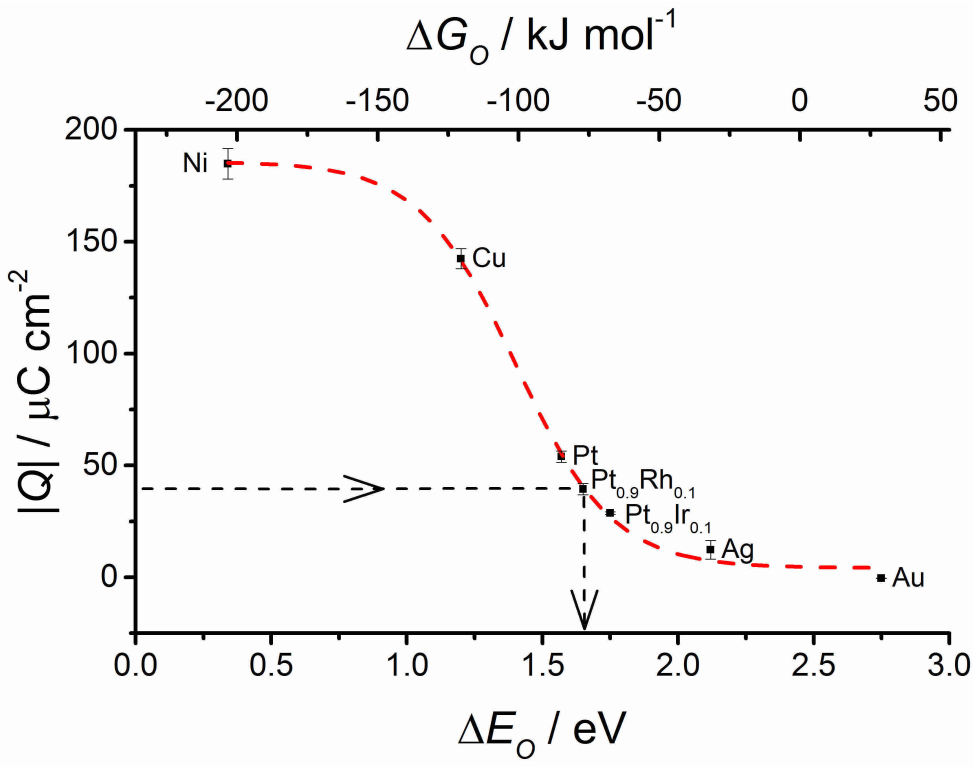

Figure 6.11: *Calculated extra charge density ($Q_{ads,sub}$) due to the reduction of pre-adsorbed oxygen, calculated using Equation 5.1 against the binding energy of those metals toward oxygen (ΔE_O) and the Gibbs enthalpies of the reaction detailed in Equation 6.1 (ΔG_O). Experimental values for $Q_{ads,sub}$ for $Pt_{0.9}Ir_{0.1}$ and $Pt_{0.9}Rh_{0.1}$ were aligned with the calibration curve (- - -) to give calculated values of ΔG_O and ΔE_O for both.*

Of course, values for ΔG_O can also be calculated using the peak potential method shown in Equation 6.3. These were found to be -56.8 kJ mol^{-1} and -62.5 kJ mol^{-1} respectively. Again a good agreement between the two values is seen. Both methods can be used as a means of calculating ΔG_O. The calibration curve method offers an advantage in that the experimental method to collect the data is far more simple, requiring only a single chronoamperogram to calculate ΔG_O, as opposed to a complex combination of linear sweeps and degassing procedures. Increased accuracy is gained by recording a collection of chronoamperograms and taking an average, but simple automation procedures mean this makes a negligible difference to the time taken to conduct the experiments. The calibration curve also allows the simple reading of ΔG_O off an axis rather than using the peak potential E_p. This is potentially advantageous as E_p can sometimes be difficult to determine if the subtraction experiment results in a long, broad peak. The subtraction

method does offer the advantage that it is entirely experimental, with no reliance on theoretical models of computer simulation. However, the good agreement between the two methods suggests that simulations and use of model are valid, and so can readily be used in the calculation of ΔG_O.

6.3 Catalytic activity towards ORR from MSCV

A common method of determining the catalytic activity of a material is via a Koutecky-Levich analysis using a rotating disc electrode (RDE). This takes advantage of the relative contributions of the kinetically controlled (i_k) and the mass transport limited current (i_D) towards the experimentally measured current (i_{exp}) at varying points along a linear sweep voltammogram, as described by Equation 1.35. Rearrangement of this allows calculation of i_k through the following simple equation.

$$i_k = \frac{i_D \; i_{exp}}{i_D - i_{exp}} \tag{6.5}$$

Equation 6.5: *Calculation of the kinetic current at a given overpotential (i_k) from the diffusion limited current (i_D) and the experimentally recorded current at that potential (i_{exp}).*

In order for this approach to be valid the reaction at the surface of the electrode must be first order with respect to the species being oxidised or reduced, as was previously discussed in Section 1.3.4. For this reason, i_k was calculated from MSCVs sampled at 500 ms after the potential step in order to give steady state reduction of oxygen in all voltammograms. As long as the diffusion coefficient, electrode area and concentration of dissolved oxygen are known, then it is possible to calculate i_k at a given point along the voltammogram. Selection of a low overpotential minimises contributions from i_D, and so allows more precise calculation of i_k.

Care needs to be taken over the selection of the potential for the calculation of i_k. If the overpotential is too high, it results in an entirely diffusion controlled current being observed, where as if the overpotential is too low the reduction is not sufficiently

driven to observe the Faradaic current over background processes. A number of authors have investigated links between the measurement of i_k and the selected overpotential. Mayrhofer *et al.* have suggested a potential range that gives between 10 and 80 % of i_D as the recorded current[75], whereas Vidal-Inglesias *et al.* suggest that the error in i_k was reduced by up to a factor of three if a potential giving an upper limit of 50 % of i_D was used[147].

Kinetic currents were calculated using this method for Ni, Cu, Pt, $Pt_{0.9}Ir_{0.1}$, $Pt_{0.9}Rh_{0.1}$, Ag and Au at 0.45 V vs. RHE, corresponding to kinetic currents of 50 % of i_D, where i_D was determined from the plateau of the 500 ms MSCV for oxygen reduction at the Pt microelectrode. All values of i_k were then calculated from 500 ms MSCVs recorded at the corresponding metal microelectrodes, in order to give steady state oxygen reduction in all cases. These were found to be 2.09 x 10^{-5}, -3.6 x 10^{-5}, -1.87 x 10^{-3}, -2.37 x 10^{-3}, -1.02 x 10^{-3}, -1.02 x 10^{-3}, -3.01 x 10^{-4} and -9.24 x 10^{-5} A cm^{-2} respectively.

It is clear immediately that the platinum metal electrodes have the greatest kinetic currents, with i_k decreasing as the binding energy is either decreasing or increasing. This follows the same pattern as the volcano plot shown in Figure 1.25, which showed a maximum catalytic activity for metals with an intermediate binding energy (ΔG_O). As the binding energy has been shown in the previous chapter to be related to the extra charge seen in transient experiments (Q), it would be expected that a plot of i_k vs. Q would show the same volcano relationship. This is shown in Figure 6.12.

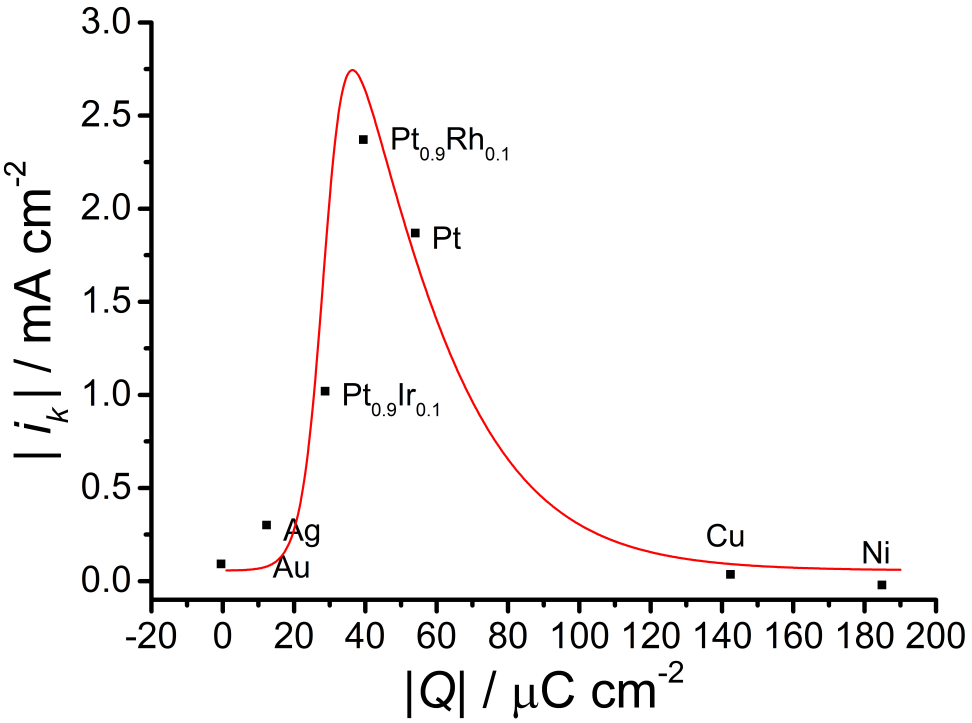

Figure 6.12: *Calculated kinetic current at 0.45 V vs. RHE (i_k) for varying metal microelectrodes, plotted against the extra charge due to the reduction of pre-adsorbed oxygen (Q), calculated using Equation 5.1. The red line has no mathematical basis, but is given as a guide to the eye to show the volcano relationship.*

Immediately it can be seen that there is an asymmetric volcano relationship between Q and i_k, as was seen in the original volcano plot in Figure 1.25. The points have here been joined with a sloped curve rather than two straight lines due to the apparent sigmoidal relationship between Q and ΔG_O that was previously proposed. Ideally more data points would be needed for metals and/or metal alloys with charges in between those of Pt and Cu in order to confirm or reject this suggestion. This justification is highlighted in a 3D plot of i_k vs. Q vs. ΔG_O.

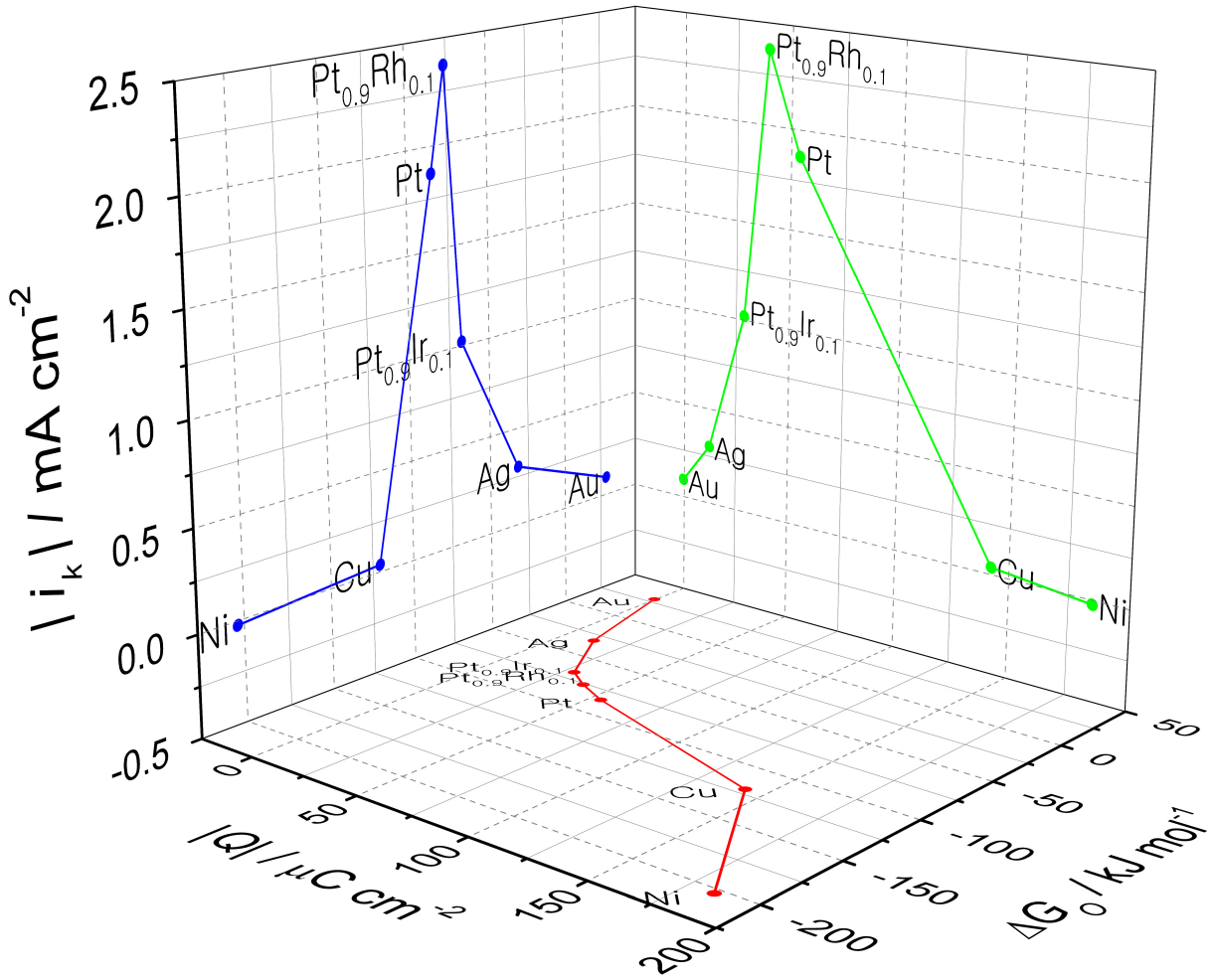

Figure 6.13: *Calculated kinetic current at 0.45 V vs. RHE (i_k, y axis) for varying metal microelectrodes, plotted against the extra charge due to the reduction of pre-adsorbed oxygen (Q, x axis), calculated using Equation 5.1 and also against the Gibbs energies of adsorption from the stripping peak potentials (ΔG_O, z axis).*

In both the x-y and z-y planes, a volcano plot can be clearly seen. The z-y plane shows i_k against the binding energy, which is analogous to the Nørskov volcano plot in Figure 1.25. The x-y plane shows i_k against the extra charge seen due to the reduction of pre-adsorbed oxygen. The sigmoidal relationship between Q and i_k acts to draw out the right hand side of the volcano in the x-y plane, which is why a curve was chosen to join the data points in Figure 6.12. Despite the good agreement, further work should be done to fill this plot with a greater number of data points to discern the true nature of the relationship between i_k and Q over this range.

The broader volcano offers the advantage of giving a greater resolution when it comes to distinguishing between points on the volcano outside of experimental error. A steeper gradient of any calibration curve will always result in small errors having a greater impact on extrapolated values. More importantly, the z-y plane of Figure 6.13 offers an entirely experimental interpretation of the relationship between oxygen adsorption onto an electrode surface and the catalytic activity of the electrode in question. This provides a purely experimental means of evaluating the catalytic activity of a novel oxygen reduction catalyst using simple chronoamperometric experiments. To our knowledge this has not previously been observed experimentally.

The ease of construction of this plot offers a clear example of the usefulness of MSCV as a technique over other more conventional voltammetric methods. Calculation of i_k using rotating disc electrodes, for example, requires a number of corrections and considerations to be made in order to ensure the accuracy of the extrapolated values. For example, large surface area electrodes have considerable iR drop, thanks to the relatively large resistance of these electrodes, as determined by Equation 1.10. The iR drop acts to distort the ORR wave, resulting in an increased error in calculated kinetic currents[76]. Varying correction factors have been applied in the literature, most being between a factor of 1.46 and 2.09 depending on conditions[62]. This is why low overpotentials are often chosen for the calculation of kinetic currents in order to minimise the experimental current, thereby also minimising the iR drop. This is not an issue for the kinetic analysis of MSCV, as the small electrode area means that iR drop is negligible. This gives access to a much wider range of potentials where the kinetic current may be calculated.

Kinetic currents are also affected by the presence of oxides on the electrode surface. The presence of oxides acts to inhibit the ORR, as was discussed in Section 1.5. A greater extent of surface oxidation will result in a decrease in the measured kinetic current. The use of a cleaning waveform with MSCV ensures an oxide free surface, and so this does not affect the recorded data. Experiments at RDE also require corrections for capacitive currents, usually through the subtraction of an equivalent voltammogram which has been

recorded in the the absence of oxygen, using a nitrogen or argon purge[62]. Again, this is not necessary for MSCV, as the capacitance is proportional to the electrode area.

6.4 Tafel analysis with MSCV

Section 1.5 covered how the construction of a Tafel plot gave a simple indication of the number of electrons transferred in the rate determining step of a redox reaction. In the case of oxygen reduction, it has been commonly reported that the Tafel slope changes from around 120 mV dec^{-1} to 60 mV dec^{-1} slope. This indicates a switch from a single electron transfer rate determining step to a pseudo-two electron transfer rate determining step. It has been proposed that this change is due to the presence of a surface oxide acting to hinder oxygen reduction at the metal surface, resulting in an apparent decrease in kinetics[33,47,50,51].

As the MSCV procedure gave a sigmoidal voltammogram for the reduction of oxygen, it was possible to use the MSCV to carry out a Tafel analysis. This was first done for the 25 μm diameter platinum metal electrode in aerated 0.1 M $KClO_4$, by plotting the overpotential against the log of the current. The overpotential was calculated as the difference between the applied potential and the thermodynamic potential for oxygen reduction, which was corrected for pH using Equation 6.4. The kinetic current was calculated as described in Equation 6.5. A potential range was then chosen which corresponded to a measured current of between 10 and 50 % of the diffusion limited current, as was previously discussed[75,147]. This was then compared to the same plot from a cyclic voltammogram, which was recorded at 20 mV s^{-1} on a 5 mm diameter platinum RDE, rotating at 1600 rpm in the same solution. Steps were taken to minimise the effects of iR drop in rotating disc experiments by using a conductive electrolyte and luggin capillary. Both the forward and the reverse scans were plotted. All three Tafel plots are shown in Figure 6.14.

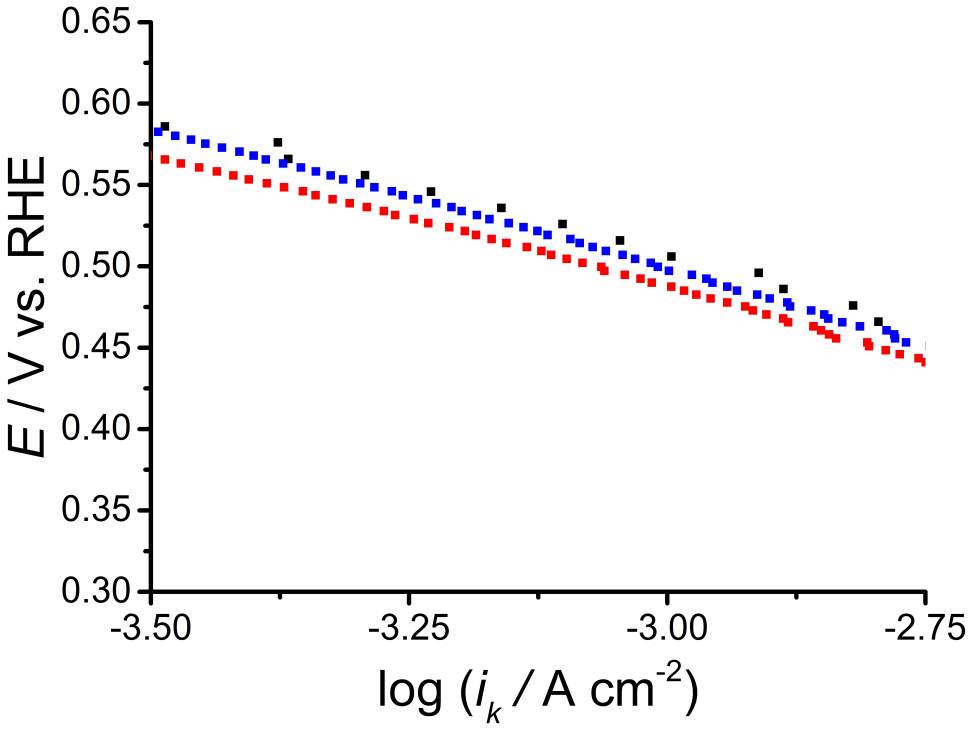

Figure 6.14: *Tafel plots of potential (E) against the log of the kinetic current (i_k), calculated using Equation 6.5, shown for an MSCV (black) recorded at a pre-conditioned 25 μm diameter platinum microelectrode, and the positive going (blue) and negative going (red) sweeps of a 20 mV s^{-1} CV recorded at a 5 mm diameter platinum rotating disc at 1600 rpm. Both experiments were recorded in aerated 0.1 M $KClO_4$.*

Comparison of the MSCV Tafel plot with CV Tafel plots show that the MSCV aligns much more closely with the positive going sweep than the negative going sweep. The calculated kinetic current at 0.45 V vs. RHE for the MSCV is -1.01 mA cm^{-2} compared to -0.931 mA cm^{-2} for the positive going sweep and -0.80 mA cm^{-2} for the negative going sweep. The positive going sweep started from an initially reducing environment, and so the bulk of the wave should be recorded on an oxide free surface. The negative going sweep spends the initial portion of the sweep in a potential range where oxide may adsorb onto the surface. The difference between the Tafel slopes of the forward and backward sweeps is due to the presence of oxide on the surface hindering the ORR, and so giving an apparent reduction in the ORR kinetics. The slow scan rate was deliberately chosen to give a significant amount of time at positive potentials, resulting in a greater degree of surface oxidation and therefore a greater hinderance of ORR kinetics[74].

The close agreement of the MSCV slope with the positive going linear sweep is a good indication that the electrode surface is oxide free at all potentials, most likely due to the presence of the cleaning waveform. Closer inspection of the MSCV Tafel slope shows it to be slightly above the slope for the positive going sweep at the RDE. The reason for this discrepancy is unclear, but could potentially be explained by differences in the proportions of the various crystal faces on the two different polycrystalline electrodes.

The close agreement between the Tafel slopes from MSCV and RDE experiments is interesting, as the significant corrections needed for iR drop and capacitive currents are not needed with MSCV, as was previously discussed. However, it is worth noting that the application of MSCVs to the construction of Tafel plots does have the limitation in that the density of data points is far lower on the MSCV than for the conventional linear sweep voltammogram. Data points for the MSCV come from individual chronoamperometric experiments, whereas the data points for the CV are taken as sampled potentials on a potential ramp. This could easily be remedied by reducing the potential increment between sequential potential step experiments. As the Tafel slope tends to focus on a relatively narrow potential range, it would be easy to increase the density of data points over the desired range, whilst omitting potentials over the rest of the voltammogram. This would give a high resolution Tafel slope without significantly increasing the length of the experiment.

The construction of Tafel plots from MSCVs provides a further means of evaluating catalytic activities of novel materials. This can be seen through the comparison of Tafel plots for Pt, $Pt_{0.9}Ir_{0.1}$ and $Pt_{0.9}Rh_{0.1}$, which are shown in Figure 6.15.

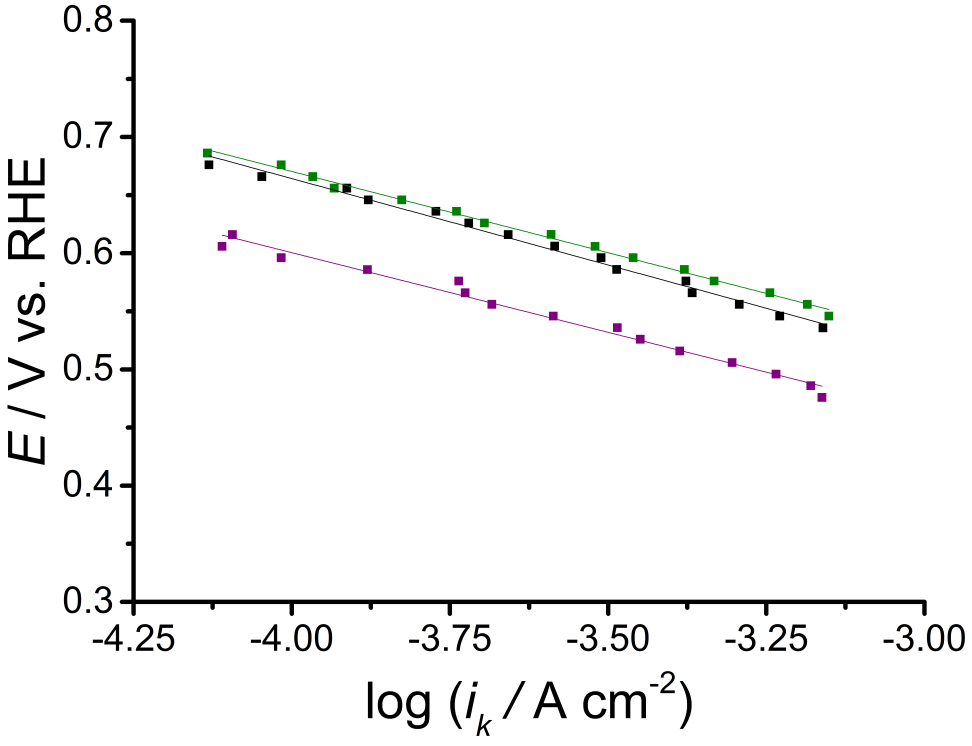

Figure 6.15: *Tafel plots of potential (E) against the log of the kinetic current (i_k), calculated using Equation 6.5, shown for MSCVs recorded at Pt (black), $Pt_{0.9}Ir_{0.1}$ (purple) and $Pt_{0.9}Rh_{0.1}$ (green), all recorded at a 25 μm platinum microelectrode in aerated 0.1 M $KClO_4$.*

The similarity between the Tafel slopes of Pt (-140 mV dec^{-1}), $Pt_{0.9}Ir_{0.1}$ (-143 mV dec^{-1}) and $Pt_{0.9}Rh_{0.1}$ (-137 mV dec^{-1}) show that the rate determining step is the same for Pt and both metal alloys, and so comparison between the materials is valid. The key difference between the alloys comes from the intercepts with the y axis. Extrapolation of the plotted trendline to zero overpotential allows calculation of the exchange current density (i_0). This is measure of the current for concurrent oxidation and reduction processes at the electrode at the point where the measured current is zero. This makes i_0 is a good indicator of the catalytic activity of a material, with larger i_0 indicating that the material is more catalytically active. Taking the potential at equilibrium as the thermodynamic potential for oxygen reduction, as given by Equation 6.4, i_0 for Pt, $Pt_{0.9}Ir_{0.1}$ and $Pt_{0.9}Rh_{0.1}$ was calculated as 1.08, 1.28 and 0.47 mA cm^{-2} respectively.

It has been reported that there is a large scope for error in these calculated values, particularly around the potential range chosen and the definition of the equilibrium

potential, E^0 [62], and so these numbers should be treated with caution. However, the Tafel slopes themselves provide a useful means of comparing the catalytic activities of multiple materials by simply comparing the positions of the slopes. Slopes with a higher position on the y axis can be seen to be more catalytically active. The displayed trend in activity of $Pt_{0.9}Ir_{0.1}$ < Pt < $Pt_{0.9}Rh_{0.1}$ is in agreement with the trends shown in the previously recorded plots of i_k vs. Q and ΔG_O shown in Figures 6.12 - 6.13. The consistency in the calculation of this order of activities across multiple MSCV methods gives confidence in the extrapolated trend.

7 Conclusions

Transient experiments conducted through short timescale sampling of chronoamperometric experiments give access to useful information thanks to the high mass transport regime, whilst measured currents are not obscured by capacitive currents. Analysis of such data was done using models that have been manipulated to take into account the small electrode size and short sampling time to reveal kinetic information and adsorption phenomena.

Sampled current voltammetry is a useful way of recording voltammograms whilst ensuring that every data point has the same history, rather than depending on the previous state of the electrode. Although the technique is cumbersome, due to the necessity to perform separate chronoamperometric experiments for each data point, this technique is probably unique in its ability to give a standardised electrode history for across the entirety of the voltammogram. The use of microelectrodes when measuring the data (MSCV) allows the recording of meaningful information even at very short times, when macroelectrodes would give far too large capacitive currents to be useful. MSCVs sampled at increasingly short times display increased kinetic limitations, seen as a decrease in the slope of the sigmoid, thanks to the increased rate of mass transport to electrode surface. This makes it possible to compare the shapes of voltammograms recorded on different timescales. This is important for microelectrodes as the change in diffusion regime at rapid rates of mass transport would usually result in an increase in charging current and the appearance of peaks in the voltammogram. This is not the case for MSCVs, as the smooth sigmoid is maintained at all rates of mass transport.

This effect can be reliably manipulated in order to record MSCVs under quasireversible conditions, where the rate of mass transport (k_m) is roughly equal to the rate of electron transfer (k_s). This was desirable as a number of models exist where kinetic parameters k^0, E^o and α can be calculated from a quasireversible voltammogram. Although models were available for a number of different types of voltammetry, one had not previously been developed for SCV. This is presumably due to its use with larger electrodes, and

so short timescale SCVs had never previously been considered. A model was therefore constructed based on an expression for the calculation of kinetic parameters from the slope of a microelectrode. A time dependent k_m parameter was added in order to take into account the relative development of the hemispherical diffusion field to the microdisc, depending on the sampling time (Equations 4.1 - 4.2). This is a novel method for the determination of kinetic parameters for a redox species that takes advantage of the key characteristics of a microelectrode, whilst also being simple to perform experimentally, if a little time consuming.

This model was tested by calculating k^0, α and E^0 for the Fe^{II} / Fe^{III} redox couple. This was done by fitting experimental MSCVs for the reduction of $Fe(ClO_4)_3$ to Equation 4.2 by means of a non-linear regression, where all parameters were fixed except for k^0, α and E^0, which were permitted to vary. Five MSCVs constructed from different sampling times were simultaneously fit as a means of averaging multiple data sets. The resultant non-linear regression gave $k^0 = 0.008 \pm 0.0001$ cm s^{-1}, $\alpha = 0.37 \pm 0.002$ and $E^0 = 0.75 \pm 0.0004$ V vs. RHE, which are in excellent agreement with the literature[117,118]. The values were further validated using the peak potentials from cyclic voltammetry at varying scan rates, as described by the Nicholson method[7,9–12], detailed in Equations 1.19 - 1.20. Parameters were also verified by comparing experimental MSCVs with theoretical MSCVs, which were constructed from a collection of theoretical chronoamperograms produced by COMSOL. Simulations had been programmed to assume the same kinetic parameters as were given by the regression.

Shortening the sampling time allowed kinetic parameters to also be calculated for the ferri/ferrocyanide redox couple, which were found to be $k^0 = 0.089 \pm 0.013$ cm s^{-1}, $\alpha = 0.40 \pm 0.03$, and $E^0 = 0.88 \pm 0.0006$ V vs. RHE. Again these values are in good agreement with the literature[119–121], and can be easily verified by comparing the experimental MSCVs with theoretical MSCVs produced by the COMSOL package. The same technique was also attempted for the much faster $[Ru(NH_3)_6]^{3+}$ reduction. A good quality fit did appear to be achieved, but the extracted parameters were significantly slower than were expected. This appears to be due to a limitation in the method in that, even at very short sampling

times, MSCVs with rapid kinetics show little difference in their slopes. An upper limit of $k^0 = 1$ cm s^{-1} has therefore been proposed. For slower systems than this, a good quality fit is possible as long as an appropriate sampling time is selected. A guide to the selection of a viable sampling time is shown in Table 4.4, where in a table of kinetic parameters against sampling times, an appropriate fit is indicated by a green box.

Normalising MSCVs using a theoretical, time dependent diffusion limiting current allows the time dependence of MSCVs to be removed. This allows all SCVs to be compared regardless of sampling time. This normalisation procedure can be manipulated to determine the value of the number of electrons transferred during a complex, multi-electron reduction (n_{app}). This was applied to the oxygen reduction reaction (ORR), as n_{app} was expected to vary with k_m, and therefore also with sampling time. At sampling times greater than around 100 ms, the method for determining n_{app} is valid. Normalisation yields reasonable results regardless of sampling time, typically giving $n_{app} \approx 3.3$. At shorter sampling times, the calculated values of n_{app} are unreasonably large, indicating that, at short times, there is some further source of current present. This work suggests that the observed extra current is due to the presence of pre-adsorbed oxygen on the electrode surface. This would be rapidly consumed after the onset of a potential step experiment, and so would explain why the extra current is only seen at very short times. A simple subtraction of the expected diffusion controlled response allowed the adsorbed oxygen to be expressed as a current response. Subsequent integration gives a charge, which allowed for an approximate number of moles of adsorbed oxygen to be calculated. Although a number of approximations were made, the values indicated the remarkable sensitivity of the novel MSCV technique when it comes to detecting small fractions of a monolayer of adsorbates.

The extra current was found to be reduced by shortening the rest time spend at OCP prior to the potential step, or by poisoning the electrode surface prior to the potential step being performed. Both of these steps were taken to reduce the amount of oxygen that was able to pre-adsorb. The quantity of adsorbed oxygen also appears to be dependent on the concentration of oxygen in solution. A significant increase was seen when small

quantities of aerated solution was added to an argon purged electrolyte. The number of monolayers involved then seemed to tend towards a plateau once a fully aerated solution was reached. Varying the potential of the rest prior to the potential step had no effect on the extra charge over a range of around 150 mV, demonstrating a potential independent adsorption. This constant extra charge was maintained until the rest potential resulted in the deposition of a surface oxide, which resulted in a linear increase in the extra charge.

It was also possible to directly reduce the pre-adsorbed oxygen by removing oxygen from the solution through argon purging once the oxygen had been allowed to adsorb. The charge passed during this reduction was close to the extra charge seen when comparing the experimental transients with those predicted by the theoretical model used. Importantly it is possible to differentiate between the reduction of this pre-adsorbed oxygen from the reduction of an intentionally deposited oxide. There is much discussion in the literature regarding the reduction of adsorbed oxygen, but the oxygen is most often referred to as 'adsorbed oxygen species' without much discussion as to the source of the formed oxygen. As far as we are aware this work offers the first experimental distinction between the reduction of adsorbed molecular oxygen and adsorbed oxide.

The extra charge could be predictably tuned by varying the binding energy between the metal electrode and the dissolved oxygen (ΔG_O). The extra current followed the trend in binding energy, where Ni > Cu > Pt > Ag > Au. The greatest extra charge was seen with the most strongly binding nickel electrodes. The extra charge was then predictably reduced by reducing the binding energy according to this trend. Reducing the pre-adsorbed oxygen in argon purged solution revealed a peak current after background subtraction. This allowed calculation of a peak potential (E_p) for the reduction of the pre-adsorbed oxygen. From this, an experimental method to calculate ΔG_O was devised, through calculation of the difference between E_p and the thermodynamic potential for the oxygen reduction reaction. These calculated values were in excellent agreement with those in the literature, which validates the approach of plotting the extra charge against binding energy for oxygen.

The sigmoidal relationship between the extra charge and ΔG_O allows the calculation of ΔG_O for novel materials by way of a calibration curve. Once the magnitude of the extra charge is known ΔG_O can be simply read off of the x axis. This is useful in the development of novel oxygen reduction catalyst materials, as ΔG_O is often used as a descriptor for the indication of a high quality catalyst for the ORR. Alternatively, plots of the kinetic current against the extra charge reveal a volcano-like relationship, akin to the plots of catalytic activity against binding energy from Nørskov *et al.*[102]. This novel approach provides a direct experimental means to evaluate the catalytic activity of a material for the ORR from a single chronoamperometric experiment. The strong correlation between the extra charge, kinetic current and binding energies of all materials studied opens up the possibility of Q being used as a descriptor for ORR activity.

Tafel analysis of MSCVs for Pt, $Pt_{0.9}Ir_{0.1}$ and $Pt_{0.9}Rh_{0.1}$ show similar Tafel slopes, indicating the same rate limiting step, whilst the change in intercept with the y-axis reveals a trend in catalytic activity of $Pt_{0.9}Ir_{0.1}$ < Pt < $Pt_{0.9}Rh_{0.1}$. This is in agreement with previously calculated kinetic currents. Importantly, the Tafel slope from a MSCV was in agreement with one recorded at a platinum metal rotating disc electrode that was swept from an initially reducing environment, indicating that the MSCV cleaning waveform does indeed keep the metal surface oxide free. Importantly, the Tafel slope from the MSCV shows a slight offset from the Tafel slope from the MSCV, which is likely due to iR drop at the much larger RDE. This demonstrates a key advantage to the MSCV technique, where the small active area of the microelectrode means corrections for iR drop are not necessary.

8 Future work

8.1 Kinetics from MSCV

The application of an experimental model for the calculation of kinetic parameters using voltammetry requires the redox system being probed to be quasireversible. This work uses a decreased sampling time with MSCV to increase the rate of mass transport to the electrode surface, thereby allowing a system to be quasireversible simply through careful selection of an appropriate sampling time. The limitation of this method comes in the finite ability to shorten the sampling time. Many conventional potentiostats are unable to sample at times shorter than around 1 ms. Even with those that are, microelectrodes are still subject to capacitive currents on the microsecond timescale, which provides an absolute limit to the range of sampling times that may be applied.

In order to gain a wider range of the application of the model to even faster redox system, a further range of increase of mass transport would be needed. This provides the possibility of making even extremely fast systems such as ruthenium hexamine quasireversible, and so would allow the calculation of kinetic parameters using the proposed model. One possibility would be through the use of MSCV with much smaller electrodes. Smaller radii give much greater rates of mass transport according to Equation 4.1. This should increase the range of kinetic parameters that are accessible to the technique. A new range table such as the one given in Table 4.4 would need to be generated for all radii used. Further increase in the rate of mass transport through the use of nanoelectrode arrays or single nanoparticles could also be used, although the model used for kinetic analysis (Equation 4.2) would need to be altered to take into account the differing diffusion fields to these electrodes. With certain redox systems such as the oxygen reduction reaction, the wave is shifted to more negative potentials as the radius is reduced, so this would have to be taken into account before using this technique. The validity of the technique with much smaller electrodes would need to be tested with COMSOL simulations in the same way as described in Chapter 4.1.

8.2 ORR with MSCV

This work has presented a sigmoidal relationship between the extra charge seen due to the pre-adsorption of oxygen (Q), and the binding energy of the metal towards oxygen (ΔG_O). Also shown is a volcano relationship between the kinetic current (i_k) and both ΔG_O and Q. The calculated values of i_k and Q for two platinum alloys were also found to fit into the proposed relationships. Whilst the presented data is in good agreement with the proposed relationships, the accuracy could be greatly improved through the study of additional materials. This would help to confirm the sigmoidal relationship proposed in Figure 6.5, and give insight to whether a straight or curve volcano plot would be more appropriate in Figures 6.12 and 6.13. The pure metals studied were Ni, Cu, Pt, Ag and Au. These were chosen as they take up a range of positions on the volcano plot of catalytic activity against binding energy given by Nørskov *et al.*, shown in Figure 1.25. This figure shows a number of other metals, such as Ir, Rh, Ru and Co, that take up intermediate positions on this scale. These metals would be ideal to increase the resolution of the figures given in this work.

The use of more metal alloys could also help to increase the number of data points in the plot. Only 10 % of a secondary metal alongside platinum gave a significant shift in the calculated Q, as well as a predictable shift in the other calculated parameters. In the case of the alloys, ΔG_O was determined by simply reading the value off of the calibration curve after Q had been calculated. It would be helpful to confirm these values using DFT. This could model the adsorption of oxygen onto the alloy surface, using the same parameters as for the Nørskov volcano plot. This would be far more complicated than for the pure metals, as the effect of the interactions between Pt and alloyed metal orbitals on the Pt d-band would have to be calculated, as well as taking into account the relative surface contributions of both metals. This would make the whole process computationally expensive. However, in the interests of accuracy, this should be done for all alloys if they are to be used in the construction of a true calibration curve. To start, the use of multiple metals would therefore be the most favourable way to proceed.

When it comes to the practical applications of fuel cell catalysts, it is more common to investigate mixed metal alloys as carbon supported nanoparticles than as pure metals. It would therefore be useful to apply this work to such catalysts. The use of carbon supported nanoparticles provides added complexity as the activity of a supported nanoparticle tends to differ from the equivalent pure metal. This is due to the faster mass transport to nanoparticles, the impact of interactions between the metal and support on the electronic nature of the metal, and also the porous structure of the support affecting the diffusion to the metal particles. It would therefore likely be necessary to construct a new calibration curve and/or volcano plot for application to nanoparticle materials. Care should be taken to ensure that all catalysts are prepared in the same way so that all results are comparable. For the same reason, the normalisation should be done to take into account the large variation in active areas and activities that come from variances in nanoparticle size, crystal face, distribution of edge, step and defect sites and particle distribution [68,69,86,148].

Construction of MSCVs and other similar analysis could be done through the deposition of a nanoparticle materials into a shallow recessed microelectrode. This could then be polished down in order to give a smooth disc of the catalyst material with a known small radius. As long as a flat disc is produced, the recorded current should still follow diffusion control, as predicted by Equation 1.45. This would make all analytical techniques and assumptions made in this work still applicable to these new materials. The increase in active area with the use of nanoparticles would also increase the associated capacitive currents. It may be that a large range of sampling times would not be possible with nanoparticle catalysts as with the flat metal surface. Capacitive currents could potentially be minimised by having as thin a layer of the catalyst as possible. Certainly this merits further work.

The choice of materials used in this work was limited to those that were available fabricated as microwires. It would be possible to extend the study to further materials by combining MSCV with scanning electrochemical cell microscopy (SECCM). SECCM works on the same principle to SECM, with a tip electrode approaching a substrate. However, with SECCM the tip is a hollow glass pipette filled with the electrolyte, in this case aerated

$KClO_4$. A reference electrode is then linked to the electrolyte using a flexible capillary. The working electrode is then the substrate being used. The electrode tip is brought close to the substrate, so that the meniscus of solution at the tip opening is brought into contact with the substrate. This completes the circuit, and so electrochemistry can be done at the exposed portion of the substrate. Once a connection is confirmed it is possible to conduct voltammetry or amperommetry as if at a standard microelectrode. Mass transport regimes will here be dominated by the diameter of the tip, as this will be proportional to the exposed area of the metal substrate[32,149,150].

The diffusion field will be different to that at a microelectrode, as the edge diffusion that gives significant contributions to the flux to a microelectrode will be hindered by the presence of the glass walls of the pipette. This would need to be taken into account before the same procedures for kinetic analysis used in this report are applied to the case of MSCV with SECCM. This should not be complicated, as the effect of the change in diffusion field on the diffusion controlled, time dependent current could be evaluated as was done here, using ruthenium hexamine as a model single electron reduction. Differences between the measured current and the theoretical diffusion controlled current according to Equation 1.45 could then be used to establish a correction factor, which would then be confirmed using numerical simulations. Once confirmed, MSCV with SECCM could be used to analyse the catalytic activity of numerous materials that cannot be easily fabricated into microwires, such as glassy carbon, boron doped diamond or single crystal metal surfaces.

9 References

[1] Y. Qing, C. Xing, Z. Jing, Z. Hai-Feng, C. Wang-Sheng, Z. Xu-Sheng, A. Marcelli, W. Zi-Yu; Local hydrated structure of an Fe^{2+}/Fe^{3+} aqueous solution: an investigation using a combination of molecular dynamics and X-ray absorption fine structure methods; *Chin. Phys. C*, **2013**, *37*, 038003, 1–6.

[2] J. K. Burdett; Electronic paradoxes in the structure of minerals *in* The Stability of Minerals; G. Price, N. Ross (Eds.), *Springer, Netherlands*, **1992**, 88–131.

[3] R. Davis, C. A. McAuliffe, D. M. Johns; Elements of the first transitional period *in* Inorganic Chemistry of the Transition Elements; B. Johnson (Ed.), *Chemical Society, London*, **1977**, 149–301.

[4] P. Brezonik; Chemical Kinetics and Process Dynamics in Aquatic Systems; *Taylor & Francis, USA*, **1993**.

[5] A. J. Bard, L. R. Faulkner; Electrochemical Methods: Fundamentals and Applications 2nd Edition; *John Wiley & Sons, Ltd, New York*, **2001**.

[6] M. V. Mirkin; Determination of electrode kinetics *in* Handbook of electrochemistry; C. G. Zoski (Ed.), *Elsevier Science, Netherlands*, **2007**, 639–660.

[7] R. S. Nicholson, I. Shain; Theory of stationary electrode polarography: single scan and cyclic methods applied to reversible, irreversible and kinetic systems; *Anal. Chem.*, **1964**, *36*, 706–723.

[8] C. G. Zoski; Handbook of electrochemistry; *Elsevier Science, Netherlands*, **2007**.

[9] R. Lavagnini, R. Antiochia, F. Magno; An extended method for the practical evaluation of the standard rate constant from cyclic voltammetry data; *Electroanalysis*, **2004**, *16*, 505–506.

[10] D. Dragu, M. Buda, T. Vişan; Cyclic voltammetry simulation using orthogonal collocation: comparison with experimental data and measuring the electrochemical rate constant; *U.P.B. Sci. Bull. Series B*, **2009**, *71*, 77–90.

[11] T. Swaddle; Homogeneous vs. heterogeneous self-exchange electron transfer reactions of metal complexes: Insights from pressure effects; *Chem. Rev.*, **2005**, *106*, 2573–2608.

[12] N. Siraj, G. Grampp, K. Landgraf, K. Punyain; Cyclic voltammetric study of heterogeneous electron transfer rate constants of various organic compounds in ionic liquids: Measurements at room temperature; *Z. Phys. Chem.*, **2012**, *227*, 105–120.

[13] H. Li, K. Lee, J. Zhang; Electrocatalytic H_2 oxidation reaction *in* PEM Fuel Cell Electrocatalysts and Catalyst Layers: Fundamentals and Applications; J. Zhang (Ed.), *Springer, London*, **2008**, 135–164.

[14] R. Compton, C. Banks; Understanding Voltammetry, *Vol. 2nd Revised Edition*; *Imperial College Press, London*, **2010**.

[15] G. Jerkiewicz, G. Vatankhah, J. Lessard, M. P. Soriaga, Y.-S. Park; Surface-oxide growth at platinum electrodes in aqueous H_2SO_4: Reexamination of its mechanism through combined cyclic-voltammetry, electrochemical quartz-crystal nanobalance, and Auger electron spectroscopy measurements; *Electrochim. Acta*, **2004**, *49*, 1451 – 1459.

[16] A. A. Topalov, S. Cherevko, A. R. Zeradjanin, J. C. Meier, I. Katsounaros, K. J. J. Mayrhofer; Towards a comprehensive understanding of platinum dissolution in acidic media; *Chem. Sci.*, **2014**, *5*, 631–638.

[17] Y.-F. Yang, G. Denuault; Scanning electrochemical microscopy (SECM): Study of the formation and reduction of oxides on platinum electrode surfaces in Na_2SO_4 solution (pH = 7); *J. Electroanal. Chem.*, **1998**, *443*, 273 – 282.

[18] H. Angerstein-Kozlowska, B. Conway, W. Sharp; The real condition of electrochemically oxidized platinum surfaces: Part I. Resolution of component processes; *J. Electroanal. Chem. Interfacial Electrochem.*, **1973**, *43*, 9 – 36.

[19] E. L. Redmond, B. P. Setzler, F. M. Alamgir, T. F. Fuller; Elucidating the oxide growth mechanism on platinum at the cathode in PEM fuel cells; *Phys. Chem. Chem. Phys.*, **2014**, *16*, 5301–5311.

[20] T. Jacob; Theoretical investigations on the potential-induced formation of Pt-oxide surfaces; *J. Electroanal. Chem.*, **2007**, *607*, 158 – 166.

[21] M. Gattrell, B. MacDougall; Reaction mechanisms of the O_2 reduction/evolution reaction *in* Handbook of Fuel Cells, *Vol. 5-6*; W. Vielstich, A. Lamm, H. Gasteiger (Eds.), *John Wiley & Sons, Ltd, New York*, **2010**, 443–464.

[22] H. A. Laitinen, C. G. Enke; The Electrolytic Formation and Dissolution of Oxide Films on Platinum; *J. Electrochem. Soc.*, **1960**, *107*, 773–781.

[23] T. Tsuda, C. L. Hussey; Electrochemistry of room temperature ionic liquids and melts *in* Modern Aspects of Electrochemistry, No. 45; R. E. White (Ed.), *Springer, New York*, **2009**, 63–174.

[24] J. Newman; Resistance for flow of current to a disk; *J. Electrochem. Soc.*, **1966**, *113*, 501–502.

[25] D. Malleo, J. T. Nevill, A. van Ooyen, U. Schnakenberg, L. P. Lee, H. Morgan; Characterization of electrode materials for dielectric spectroscopy; *Rev. Sci. Instrum.*, **2010**, *81*, 016104, 1-3.

[26] J. Zuo, Q. Deng, L. Cui, Y. Sun, X. Li; Electricity generation from organic wastewater using a continuous-flow single chamber microbial fuel cell; *ECS Trans.*, **2008**, *13*, 19–26.

[27] D. Shoup, A. Szabo; Chronoamperometric current at finite disk electrodes; *J. Electroanal. Chem. Interfacial Electrochem.*, **1982**, *140*, 237 – 245.

[28] P. J. Mahon, K. B. Oldham; Diffusion-controlled chronoamperometry at a disk electrode; *Anal. Chem.*, **2005**, *77*, 6100–6101.

[29] K. B. Oldham, J. C. Myland, C. G. Zoski, A. M. Bond; Kinetic parameters from steady-state voltammograms at microdisc electrodes; *J. Electroanal. Chem.*, **1989**, *270*, 79–101.

[30] A. C. Michael, R. M. Wightman, C. Amatore; Microdisk electrodes 1. Digital-simulation with a conformal-map; *J. Electroanal. Chem. Interfacial Electrochem.*, **1989**, *267*, 33–45.

[31] K. B. Oldham; Steady-state voltammetry *in* Microelectrodes: Theory and Applications; I. Montenegro, A. Queirós, J. Daschbach (Eds.), *Springer Netherlands*, **1991**, 35–50.

[32] S. L. Chen, A. Kucernak; Electrocatalysis under conditions of high mass transport rate: Oxygen reduction on single submicrometer-sized Pt particles supported on carbon; *J. Phys. Chem. B*, **2004**, *108*, 3262–3276.

[33] C. Song, J. Zhang; Electrocatalytic Oxygen Reduction Reaction *in* PEM Fuel Cell Electrocatalysts and Catalyst Layers; J. Zhang (Ed.), *Springer London*, **2008**, 89–134.

[34] S. Mentus; The evidence of limitation of oxygen reduction reaction by proton diffusion in low-concentration acid solutions; *J. Electroanal. Chem.*, **2015**, *738*, 47 – 50.

[35] M. F. Li, L. W. Liao, D. F. Yuan, D. Mei, Y.-X. Chen; pH effect on oxygen reduction reaction at Pt(1 1 1) electrode; *Electrochim. Acta*, **2013**, *110*, 780 – 789.

[36] M. Sosna; Oxygen Reduction at Microelectrodes: Application to the Dissolved Oxygen Sensor for in situ Oceanographic Measurements; *Southampton University*, **2006**.

[37] H. S. Wroblowa, Y. C. Pan, G. Razumney; Electroreduction of Oxygen - New Mechanistic Criterion; *J. Electroanal. Chem.*, **1976**, *69*, 195–201.

[38] M. Gara, E. Laborda, P. Holdway, A. Crossley, C. J. V. Jones, R. G. Compton; Oxygen reduction at sparse arrays of platinum nanoparticles in aqueous acid: hydrogen peroxide as a liberated two electron intermediate; *Phys. Chem. Chem. Phys.*, **2013**, *15*, 19487–19495.

[39] J. M. Noël, A. Latus, C. Lagrost, E. Volanschi, P. Hapiot; Evidence for OH Radical Production during Electrocatalysis of Oxygen Reduction on Pt Surfaces: Consequences and Application; *J. Am. Chem. Soc.*, **2012**, *134*, 2835–2841.

[40] M. H. Shao, P. Liu, R. R. Adžić; Superoxide anion is the intermediate in the oxygen reduction reaction on platinum electrodes; *J. Am. Chem. Soc.*, **2006**, *128*, 7408–7409.

[41] A. Bard, R. Parsons, J. Jordan; Standard Potentials in Aqueous Solution; *Taylor & Francis, New York*, **1985**.

[42] P. R. Birkin, J. M. Elliott, Y. E. Watson; Electrochemical reduction of oxygen on mesoporous platinum microelectrodes; *Chem. Commun.*, **2000**, 1693–1694.

[43] D. Pletcher, S. Sotiropoulos; A Study of Cathodic Oxygen Reduction at Platinum Using Microelectrodes; *J. Electroanal. Chem.*, **1993**, *356*, 109–119.

[44] N. M. Marković, P. N. Ross, Jr.; Surface science studies of model fuel cell electrocatalysts; *Surf. Sci. Rep.*, **2002**, *45*, 117 – 229.

[45] A. Damjanovic, V. Brusic; Electrode kinetics of oxygen reduction on oxide-free platinum electrodes; *Electrochim. Acta*, **1967**, *12*, 615 – 628.

[46] E. Yeager; Electrocatalysts for O_2 reduction; *Electrochim. Acta*, **1984**, *29*, 1527 – 1537.

[47] E. Yeager, A. Razaq, D. Tryk; The electrolyte factor in O_2 reduction electrocatalysis; *Pro. Electrochem. Soc.*, **1992**, *92*, 440–473.

[48] R. A. Sidik, A. B. Anderson; Density functional theory study of O_2 electroreduction when bonded to a Pt dual site; *J. Electroanal. Chem.*, **2002**, *528*, 69 – 76.

[49] M. M. Ghoneim, S. Clouser, E. Yeager; Oxygen Reduction Kinetics in Deuterated Phosphoric Acid; *J. Electrochem. Soc.*, **1985**, *132*, 1160–1162.

[50] A. Damjanovic, J. Bockris; The rate constants for oxygen dissolution on bare and oxide-covered platinum; *Electrochim. Acta*, **1966**, *11*, 376 – 377.

[51] N. Marković, R. Adžić, B. Cahan, E. Yeager; Structural effects in electrocatalysis: oxygen reduction on platinum low index single-crystal surfaces in perchloric acid solutions; *J. Electroanal. Chem.*, **1994**, *377*, 249 – 259.

[52] C. Song, Y. Tang, J. L. Zhang, J. Zhang, H. Wang, J. Shen, S. McDermid, J. Li, P. Kozak; {PEM} fuel cell reaction kinetics in the temperature range of 23-120 C; *Electrochim. Acta*, **2007**, *52*, 2552 – 2561.

[53] J. A. Keith, T. Jacob; Theoretical studies of potential-dependent and competing mechanisms of the electrocatalytic oxygen reduction reaction on Pt(111); *Angew. Chem. Int. Ed.*, **2010**, *49*, 9521–9525.

[54] E. Yeager; Dioxygen electrocatalysis: mechanisms in relation to catalyst structure; *J. Mol. Catal.*, **1986**, *38*, 5 – 25.

[55] J. S. Griffith; On the Magnetic Properties of Some Haemoglobin Complexes; *Proc. R. Soc. Lon. A*, **1956**, *235*, 23–36.

[56] R. Adžić; Recent Advances in the Kinetics of Oxygen Reduction *in* Electrocatalysis; J. Lipkowski, P. Ross (Eds.), *John Wiley & Sons, Ltd, New York*, **1998**, 197–242.

[57] L. Pauling; Nature of the Iron-Oxygen Bond in Oxyhaemoglobin; *Nature*, **1964**, *203*, 182–183.

[58] J. L. Gland, B. A. Sexton, G. B. Fisher; Oxygen interactions with the Pt(111) surface; *Surf. Sci.*, **1980**, *95*, 587 – 602.

[59] J. Schmidt, C. Stuhlmann, H. Ibach; Oxygen adsorption on the Pt(110)(1 x 2) surface studied with EELS; *Surf. Sci.*, **1993**, *284*, 121 – 128.

[60] J. C. Amphlett, R. M. Baumert, R. F. Mann, B. A. Peppley, P. R. Roberge, A. Rodrigues; The Effect of Carbon Monoxide Contamination on Anode Efficiency in PEM Fuel Cells; *Am. Chem. Div. Fuel Chem.*, **1993**, *38*, 1477–1482.

[61] I. Katsounaros, W. B. Schneider, J. C. Meier, U. Benedikt, P. U. Biedermann, A. Cuesta, A. A. Auer, K. J. Mayrhofer; The impact of spectator species on the interaction of H_2O_2 with platinum: implications for the oxygen reduction reaction pathways; *Phys. Chem. Chem. Phys.*, **2013**, *15*, 8058–68.

[62] K. Shinozaki, J. W. Zack, R. M. Richards, B. S. Pivovar, S. S. Kocha; Oxygen Reduction Reaction Measurements on Platinum Electrocatalysts Utilizing Rotating Disk Electrode Technique: I. Impact of Impurities, Measurement Protocols and Applied Corrections; *J. The Electrochem. Soc.*, **2015**, *162*, F1144–F1158.

[63] H. Yano, T. Uematsu, J. Omura, M. Watanabe, H. Uchida; Effect of adsorption of sulfate anions on the activities for oxygen reduction reaction on Nafion®-coated Pt/carbon black catalysts at practical temperatures; *J. Electroanal. Chem.*, **2015**, *747*, 91 – 96.

[64] J. P. Collman, P. Denisevich, Y. Konai, M. Marrocco, C. Koval, F. C. Anson; Electrode catalysis of the four-electron reduction of oxygen to water by dicobalt face-to-face porphyrins; *J. Am. Chem. Soc.*, **1980**, *102*, 6027–6036.

[65] M. Teliska, V. S. Murthi, S. Mukerjee, D. E. Ramaker; Site-Specific vs Specific Adsorption of Anions on Pt and Pt-Based Alloys; *J. Phys. Chem. C*, **2007**, *111*, 9267–9274.

[66] E. G. Ciapina, P. P. Lopes, R. Subbaraman, E. A. Ticianelli, V. Stamenković, D. Strmcnik, N. M. Marković; Surface spectators and their role in relationships between activity and selectivity of the oxygen reduction reaction in acid environments; *Electrochem. Commun.*, **2015**, *60*, 30 – 33.

[67] B. Grgur, N. Marković, P. Ross; Temperature-dependent oxygen electrochemistry on platinum low-index single crystal surfaces in acid solutions; *Can. J. Chem.*, **1997**, *75*, 1465–1471.

[68] V. Komanicky, A. Menzel, H. You; Investigation of Oxygen Reduction Reaction Kinetics at (111)(100) Nanofaceted Platinum Surfaces in Acidic Media; *J. Phys. Chem. B*, **2005**, *109*, 23550–23557.

[69] G. A. Attard, A. Brew; Cyclic voltammetry and oxygen reduction activity of the Pt(1 1 0)-(1 x 1) surface; *J. Electroanal. Chem.*, **2015**, *747*, 123 – 129.

[70] T. Imaoka, H. Kitazawa, W.-J. Chun, K. Yamamoto; Finding the Most Catalytically Active Platinum Clusters With Low Atomicity; *Angew. Chem. Int. Ed.*, **2015**, *54*, 9810–9815.

[71] H. A. Gasteiger, S. S. Kocha, B. Sompalli, F. T. Wagner; Activity benchmarks and requirements for Pt, Pt-alloy, and non-Pt oxygen reduction catalysts for {PEMFCs}; *Appl. Catal. B*, **2005**, *56*, 9 – 35.

[72] U. Paulus, A. Wokaun, G. Scherer, T. Schmidt, V. Stamenković, N. Marković, P. Ross; Oxygen reduction on high surface area Pt-based alloy catalysts in comparison to well defined smooth bulk alloy electrodes; *Electrochim. Acta*, **2002**, *47*, 3787 – 3798.

[73] Q. Jia, K. Caldwell, J. M. Ziegelbauer, A. Kongkanand, F. T. Wagner, S. Mukerjee, D. E. Ramaker; The Role of OOH Binding Site and Pt Surface Structure on ORR Activities; *J. Electrochem. Soc.*, **2014**, *161*, F1323–F1329.

[74] N. Hodnik, C. Baldizzone, S. Cherevko, A. Zeradjanin, K. Mayrhofer; The Effect of the Voltage Scan Rate on the Determination of the Oxygen Reduction Activity of Pt/C Fuel Cell Catalyst; *Electrocatal.*, **2015**, *6*, 237–241.

[75] K. Mayrhofer, D. Strmcnik, B. Blizanac, V. Stamenković, M. Arenz, N. Marković; Measurement of oxygen reduction activities via the rotating disc electrode method: From Pt model surfaces to carbon-supported high surface area catalysts; *Electrochim. Acta*, **2008**, *53*, 3181 – 3188.

[76] D. Van der Vliet, D. S. Strmcnik, C. Wang, V. Stamenković, N. Marković, M. Koper; On the importance of correcting for the uncompensated Ohmic resistance in model experiments of the Oxygen Reduction Reaction; *J. Electroanal. Chem.*, **2010**, *647*, 29–34.

[77] P. S. Ruvinskiy, A. Bonnefont, C. Pham-Huu, E. R. Savinova; Using Ordered Carbon Nanomaterials for Shedding Light on the Mechanism of the Cathodic Oxygen Reduction Reaction; *Langmuir*, **2011**, *27*, 9018–9027.

[78] A. E. Sleightholme, J. R. Varcoe, A. R. Kucernak; Oxygen reduction at the silver/hydroxide-exchange membrane interface; *Electrochem. Commun.*, **2008**, *10*, 151 – 155.

[79] J. L. Fernández, M. Wijesinghe, C. G. Zoski; Theory and Experiments for Voltammetric and SECM Investigations and Application to ORR Electrocatalysis at Nanoelectrode Ensembles of Ultramicroelectrode Dimensions; *Anal. Chem.*, **2015**, *87*, 1066–1074.

[80] V. Stamenković, T. J. Schmidt, P. N. Ross, N. M. Marković; Surface Composition Effects in Electrocatalysis: Kinetics of Oxygen Reduction on Well-Defined Pt_3Ni and Pt_3Co Alloy Surfaces; *J. Phys. Chem. B*, **2002**, *106*, 11970–11979.

[81] S. Mukerjee, S. Srinivasan, M. P. Soriaga, J. McBreen; Role of Structural and Electronic Properties of Pt and Pt Alloys on Electrocatalysis of Oxygen Reduction: An In Situ XANES and EXAFS Investigation; *J. Electrochem. Soc.*, **1995**, *142*, 1409–1422.

[82] N. M. Marković, T. J. Schmidt, V. Stamenković, P. N. Ross; Oxygen Reduction Reaction on Pt and Pt Bimetallic Surfaces: A Selective Review; *Fuel Cells*, **2001**, *1*, 105–116.

[83] I. Spanos, K. Dideriksen, J. J. K. Kirkensgaard, S. Jelavic, M. Arenz; Structural disordering of de-alloyed Pt bimetallic nanocatalysts: the effect on oxygen reduction reaction activity and stability; *Phys. Chem. Chem. Phys.*, **2015**, *17*, 44–53.

[84] H. Xin, A. Holewinski, N. Schweitzer, E. Nikolla, S. Linic; Electronic Structure Engineering in Heterogeneous Catalysis: Identifying Novel Alloy Catalysts Based on Rapid Screening for Materials with Desired Electronic Properties; *Top. Catal.*, **2012**, *55*, 376–390.

[85] V. Jalan, E. J. Taylor; Importance of Interatomic Spacing in Catalytic Reduction of Oxygen in Phosphoric Acid; *J. Electrochem. Soc.*, **1983**, *130*, 2299–2302.

[86] P. C. Jennings, H. A. Aleksandrov, K. M. Neyman, R. L. Johnston; DFT studies of oxygen dissociation on the 116-atom platinum truncated octahedron particle; *Phys. Chem. Chem. Phys.*, **2014**, *16*, 26539–26545.

[87] V. Stamenković, B. S. Mun, M. Arenz, K. J. J. Mayrhofer, C. A. Lucas, G. Wang, P. N. Ross, N. M. Marković; Trends in electrocatalysis on extended and nanoscale Pt-bimetallic alloy surfaces; *Nature Mat.*, **2007**, *6*, 241–247.

[88] K. R. Lee, Y. Jung, S. I. Woo; Combinatorial Screening of Highly Active Pd Binary Catalysts for Electrochemical Oxygen Reduction; *ACS Comb. Sci.*, **2012**, *14*, 10–16.

[89] R. Gentil, H. Villullas; Oxygen reduction activity and methanol tolerance of carbon-supported PtV nanoparticles and the effects of heat treatment at low temperatures; *J. Solid State Electrochem.*, **2015**, 1–11.

[90] S. Knani, L. Chirchi, W. Napporn, S. Baranton, J. Léger, A. Ghorbel; Promising ternary Pt-Co-Sn catalyst for the oxygen reduction reaction; *J. Electroanal. Chem.*, **2015**, *738*, 145 – 153.

[91] M. Lefévre, E. Proietti, F. Jaouen, J.-P. Dodelet; Iron-Based Catalysts with Improved Oxygen Reduction Activity in Polymer Electrolyte Fuel Cells; *Science*, **2009**, *324*, 71–74.

[92] Y.-C. Wang, Y.-J. Lai, L. Song, Z.-Y. Zhou, J.-G. Liu, Q. Wang, X.-D. Yang, C. Chen, W. Shi, Y.-P. Zheng, M. Rauf, S.-G. Sun; S-Doping of an Fe/N/C ORR Catalyst for Polymer Electrolyte Membrane Fuel Cells with High Power Density; *Angew. Chem. Int. Ed.*, **2015**, 9907–9910.

[93] V. B. Baez, D. Pletcher; Preparation and characterization of carbon/titanium dioxide surfaces the reduction of oxygen; *J. Electroanal. Chem.*, **1995**, *382*, 59 – 64.

[94] J. Masa, W. Xia, M. Muhler, W. Schuhmann; On the Role of Metals in Nitrogen-Doped Carbon Electrocatalysts for Oxygen Reduction; *Angew. Chem. Int. Ed.*, **2015**, 10102–10120.

[95] Z. Wu, E. M. Benchafia, Z. Iqbal, X. Wang; N_8 Polynitrogen Stabilized on Multi-Wall Carbon Nanotubes for Oxygen-Reduction Reactions at Ambient Conditions; *Angew. Chem. Int. Ed.*, **2014**, *53*, 12555–12559.

[96] H.-J. Zhang, H. Li, C. Deng, B. Zhao, J. Yang; Electrocatalysis of Oxygen Reduction Reaction on Carbon Nanotubes Modified by Graphitization and Amination; *ECS Electrochem. Lett.*, **2015**, *4*, H33–H37.

[97] J. Liu, P. Song, Z. Ning, W. Xu; Recent Advances in Heteroatom-Doped Metal-Free Electrocatalysts for Highly Efficient Oxygen Reduction Reaction; *Electrocatalysis*, **2015**, *6*, 132–147.

[98] D.-W. Kim, O. L. Li, N. Saito; Enhancement of ORR catalytic activity by multiple heteroatom-doped carbon materials; *Phys. Chem. Chem. Phys.*, **2015**, *17*, 407–413.

[99] M. Zhang, Y. Yan, K. Gong, L. Mao, Z. Guo, Y. Chen; Electrostatic Layer-by-Layer Assembled Carbon Nanotube Multilayer Film and Its Electrocatalytic Activity for O_2 Reduction; *Langmuir*, **2004**, *20*, 8781–8785.

[100] V. M. Andoralov, M. R. Tarasevich, O. V. Tripachev; Oxygen reduction reaction on polycrystalline gold. Pathways of hydrogen peroxide transformation in the acidic medium; *Russ. J. Electrochem.*, **2011**, *47*, 1327–1336.

[101] R. W. Zurilla, R. K. Sen, E. Yeager; The Kinetics of the Oxygen Reduction Reaction on Gold in Alkaline Solution; *J. Electrochem. Soc.*, **1978**, *125*, 1103–1109.

[102] J. K. Nørskov, J. Rossmeisl, A. Logadottir, L. Lindqvist, J. R. Kitchin, T. Bligaard, H. Jonsson; Origin of the overpotential for oxygen reduction at a fuel-cell cathode; *J. Phys. Chem. B.*, **2004**, *108*, 17886–17892.

[103] B. Hammer, J. K. Nørskov; Theoretical surface science and catalysis - calculations and concepts; *Adv. Catal.*, **2000**, *45*, 71–129.

[104] B. Hammer; Special Sites at Noble and Late Transition Metal Catalysts; *Top. Catal.*, **2006**, *37*, 3–16.

[105] J. R. Kitchin, J. K. Nørskov, M. A. Barteau, J. G. Chen; Modification of the surface electronic and chemical properties of Pt(111) by subsurface 3d transition metals; *J. Chem. Phys.*, **2004**, *120*, 10240–10246.

[106] H. Xin, A. Holewinski, S. Linic; Predictive Structure Reactivity Models for Rapid Screening of Pt-Based Multimetallic Electrocatalysts for the Oxygen Reduction Reaction; *ACS Catal.*, **2012**, *2*, 12–16.

[107] M. E. Scofield, H. Liu, S. S. Wong; A concise guide to sustainable PEMFCs: recent advances in improving both oxygen reduction catalysts and proton exchange membranes; *Chem. Soc. Rev.*, **2015**, *44*, 5836–5860.

[108] H. Xin, N. Schweitzer, E. Nikolla, S. Linic; Communications: Developing relationships between the local chemical reactivity of alloy catalysts and physical characteristics of constituent metal elements; *J. Chem. Phys.*, **2010**, *132*, 111101, 1-4.

[109] E. M. Erickson, M. E. Oruc, D. J. Wetzel, M. W. Cason, T. T. H. Hoang, M. W. Small, D. Li, A. I. Frenkel, A. A. Gewirth, R. G. Nuzzo; A Comparison of Atomistic and Continuum Approaches to the Study of Bonding Dynamics in Electrocatalysis: Microcantilever Stress and in Situ EXAFS Observations of Platinum Bond Expansion Due to Oxygen Adsorption during the Oxygen Reduction Reaction; *Anal. Chem.*, **2014**, *86*, 8368–8375.

[110] K. Akita; Diffusivities of gases in aqueous electrolyte solutions; *Ind. Eng. Chem. Fundam.*, **1981**, *20*, 89–94.

[111] M. Sosna, G. Denuault, R. W. Pascal, R. D. Prien, M. Mowlem; Development of a reliable microelectrode dissolved oxygen sensor; *Sensor. Actuat. B-Chem.*, **2007**, *123*, 344–351.

[112] M. Sosna, G. Denuault, R. W. Pascal, R. D. Prien, M. Mowlem; Field assessment of a new membrane-free microelectrode dissolved oxygen sensor for water column profiling; *Limnol. Oceanogr.-Meth.*, **2008**, *6*, 180–189.

[113] D. Tromans; Modeling oxygen solubility in water and electrolyte solutions; *Ind. Eng. Chem. Res.*, **2000**, *39*, 805–812.

[114] J. Colt; Computation of dissolved gas concentrations in water as functions of temperature, salinity, and pressure; *American Fisheries Society, Bethesda Maryland*, **1984**.

[115] N. Leventis, X. R. Gao; In the presence of very fast comproportionation, sampled current voltammetry and rotating disk electrode voltammetry yield equal two versus one-electron limiting current ratios. Reconciliation through analysis of concentration profiles; *J. Electroanal. Chem.*, **2001**, *500*, 78–94.

[116] S. C. Perry, L. M. Al Shandoudi, G. Denuault; Sampled-Current Voltammetry at Microdisk Electrodes: Kinetic Information from Pseudo Steady State Voltammograms; *Anal. Chem.*, **2014**, *86*, 9917–9923.

[117] J. Suzuki; Hydrodynamic Voltammetry with Convection Electrode .4. Measurements of Kinetic Parameters of Electrode Reaction .2.; *Bull. Chem. Soc. Jpn.*, **1970**, *3*, 755–758.

[118] D. H. Angell, T. Dickinson; Kinetics of ferrous/ferric and ferro/ferricyanide reactions at platinum and gold electrodes 1. Kinetics at bare metal surfaces; *J. Electroanal. Chem.*, **1972**, *35*, 55–72.

[119] M. D. Wijnen, W. M. Smit; Square wave electrolysis IV. Results and discussion; *Rec. Trav. Chim.*, **1960**, *79*, 289.

[120] J. E. B. Randles, K. W. Somerton; Kinetics of rapid electrode reactions. Part 3. - Electron exchange reactions; *Trans. Faraday. Soc.*, **1952**, *1952*, 937–950.

[121] J. Jordan, R. A. Javick; Electrode kinetics by hydrodynamic voltammetry - study of ferrous-ferric, ferrocyanide-ferricyanide and iodine-iodide systems; *Electrochim. Acta*, **1962**, *6*, 22–33.

[122] D. O. Wipf, E. W. Kristensen, M. R. Deakin, R. M. Wightman; Fast-scan cyclic voltammetry as a method to measure rapid, heterogeneous electron-transfer kinetics; *Anal. Chem.*, **1988**, *60*, 306–310.

[123] A. G. Güell, N. Ebejer, M. E. Snowden, K. McKelvey, J. V. Macpherson, P. R. Unwin; Quantitative nanoscale visualization of heterogeneous electron transfer rates in 2D carbon nanotube networks; *Proc. Nat. Acad. Sci.*, **2012**, *109*, 11487–11492.

[124] A. J. Wain; Electrochemistry at Nanoelectrodes *in* Electrochemistry: Nanoelectrochemistry, *Vol. 12*; R. Compton, J. Wadhawan (Eds.), *Royal Society of Chemistry, Cambridge*, **2013**, 44–86.

[125] A. M. Bond, E. A. Mashkina, A. N. Simonov; A Critical Review of the Methods Available for Quantitative Evaluation of Electrode Kinetics at Stationary Macrodisk Electrodes *in* Developments in Electrochemistry: Science Inspired by Martin Fleischmann; D. Pletcher, Z. Tian, D. Williams (Eds.), *John Wiley & Sons, Ltd, Chichester*, **2014**, 21–48.

[126] Y. J. Wang, J. G. Limon-Petersen, R. Compton; Measurement of the diffusion coefficients of $[Ru(NH_3)_6]^{3+}$ and $[Ru(NH_3)_6]^{2+}$ in aqueous solution using microelectrode double potential step chronoamperometry; *J. Electroanal. Chem.*, **2011**, *652*, 13–17.

[127] D. Britz, K. Poulsen, J. Strutwolf; Reference values of the diffusion-limited current at a microdisk electrode; *Electrochim. Acta*, **2004**, *50*, 107 – 113.

[128] H. L. J. Bäckström; The chain mechanism in the autoxidation of sodium sulfite solutions; *Z. Physik. Chem.*, **1934**, *B25*, 122–138.

[129] P. K. Hui; Uncatalyzed oxidation of aqueous sodium sulfite and its ability to stimulate bacterial respiration; *Biotechnol. Bioeng.*, **1991**, *37*, 392–396.

[130] D. Brownson, C. Banks; The Handbook of Graphene Electrochemistry; *Springer London*, **2014**.

[131] P. Sun, M. Mirkin; Kinetics of Electron-Transfer Reactions at Nanoelectrodes; *Anal. Chem.*, **2006**, *78*, 6526–6534.

[132] M. V. Mirkin, F. Fan, A. J. Bard; Scanning electrochemical microscopy part 13. Evaluation of the tip shapes of nanometer size microelectrodes; *J. Electroanal. Chem.*, **1992**, *238*, 47–62.

[133] J. Velmurugan, P. Sun, M. Mirkin; Scanning Electrochemical Microscopy with Gold Nanotips: The Effect of Electrode Material on Electron Transfer Rates; *J. Phys. Chem.*, **2009**, *131*, 459–464.

[134] M. V. Mirkin, T. Richards, A. J. Bard; Scanning Electrochemical Microscopy 20. Steady-State Measurements of the Fast Heterogeneous Kinetics in the Ferrocene/Acetonitrile System; *Anal. Chem.*, **1993**, *97*, 7672–7677.

[135] S. C. Perry, G. Denuault; Transient study of the oxygen reduction reaction on reduced Pt and Pt alloys microelectrodes: evidence for the reduction of pre-adsorbed oxygen species linked to dissolved oxygen; *Phys. Chem. Chem. Phys.*, **2015**, *17*, 30005–30012.

[136] J. Omura, H. Yano, M. Watanabe, H. Uchida; Electrochemical quartz crystal microbalance analysis of the oxygen reduction reaction on Pt-based electrodes. Part 1. Effect of adsorbed anions on the oxygen reduction activities of Pt in HF, $HClO_4$ and H_2SO_4 solutions; *Langmuir*, **2011**, *27*, 6464–6470.

[137] S. Sun, G. Zhang, D. Geng, Y. Chen, R. Li, M. Cai, X. Sun; A Highly Durable Platinum Nanocatalyst for Proton Exchange Membrane Fuel Cells: Multiarmed Starlike Nanowire Single Crystal; *Angew. Chem. Int. Ed.*, **2011**, *50*, 422–426.

[138] T. Biegler, D. A. J. Rand, R. Woods; Limiting Oxygen Coverage on Platinized Platinum - Relevance to Determination of Real Platinum Area by Hydrogen Adsorption; *J. Electroanal. Chem.*, **1971**, *29*, 269–277.

[139] Y.-F. Yang, G. Denuault; Scanning electrochemical microscopy (SECM) study of pH changes at Pt electrode surfaces in Na_2SO_4 solution (pH 4) under potential cycling conditions; *J. Chem. Soc., Faraday Trans.*, **1996**, *92*, 3791–3798.

[140] N. Ramaswamy, S. Mukerjee; Fundamental Mechanistic Understanding of Electrocatalysis of Oxygen Reduction on Pt and Non-Pt Surfaces: Acid versus Alkaline Media; *Adv. Phys. Chem.*, **2012**, *2012*, 1–17.

[141] N. Agmon; The Grotthuss mechanism; *Chem. Phys. Lett.*, **1995**, *244*, 456 – 462.

[142] J. A. Lanning, J. Q. Chambers; Voltammetry study of hydrogen ion/hydrogen couple in acetonitrile/water mixtures; *Anal. Chem.*, **1973**, *45*, 1010–1016.

[143] J. W. Geus; Characterization of Surface Hydrogen on Catalysts *in* Hydrogen Effects in Catalysis: Fundamentals and Practical Applications; Z. Paál, P. G. Menon (Eds.), *Taylor & Francis, New York*, **1987**, 399–610.

[144] S. Průša, P. Procházka, P. Bábor, T. Šikola, R. ter Veen, M. Fartmann, T. Grehl, P. Brüner, D. Roth, P. Bauer, H. H. Brongersma; Highly Sensitive Detection of Surface and Intercalated Impurities in Graphene by LEIS; *Langmuir*, **2015**, *31*, 9628–9635.

[145] M. Pedio, C. Cepek, R. Felici; Organic Molecules on Noble Metal Surfaces: The Role of the Interface *in* Nobel Metals; Y.-H. Su (Ed.), *InTech Open Access Publisher, Shanghai*, **2012**, 249–286.

[146] S. Mu Adsorption, initial growth and desorption kinetics of p-quaterphenyl on polycrystalline gold surfaces; *App. Surf. Sci.*, **2004**, *221*, 184 – 196.

[147] F. J. Vidal-Iglesias, J. Solla-Gullón, A. Rodes, E. Herrero, A. Aldaz; Errors in the use of the Koutecky-Levich plots; *Electrochem. Comm.*, **2012**, *15*, 42–45.

[148] M. Watanabe, H. Sei, P. Stonehart; The influence of platinum crystallite size on the electroreduction of oxygen; *J. Electroanal. Chem.*, **1989**, *261*, 375–387.

[149] N. Ebejer, M. Schnippering, A. W. Colburn, M. A. Edwards, P. R. Unwin; Localised high resolution electrochemistry and multifunctional imaging: scanning electrochemical cell microscopy; *Anal. Chem.*, **2010**, *82*, 9141–9145.

[150] S. C. Lai, P. V. Dudin, J. V. Macpherson, P. R. Unwin; Visualising zeptomole (electro)catalysis at single nanoparticles within an enemble; *J. Am. Chem. Soc.*, **2011**, *133*, 10744–10747.

10 Appendix

10.1 Sample procedure for MSCV collection for 0.1 M $KClO_4$

>Nested procedure (DATA)	
>Timed procedure	
>Set potential (V)	0.3
>Set cell	On
>Repeat for multiple values	
>Number of repetitions	100
>Potential /V	-0.5
>Preconditioning	
>CV staircase	0.3, 0.6, -0.7, 0.35, 7, 0.5
>Start potential (V)	0.3
>Upper vertex potential (V)	0.6
>Lower vertex potential (V)	-0.7
>Stop potential (V)	0.3
>No. stop crossings	7
>Step potential	0.00244
>Scan rate (V/s)	0.5
>Potential step	
>Set potential (V)	0.3
>Record signals (>1 ms)	10,0.01
>Duration (s)	10
>Interval time (s)	0.01
>Set potential (V)	-0.5

>Record signals (>1 ms)	0.5, 0.0025
>Duration (s)	0.5
>Interval time (s)	0.0025
>Calculate signal	My Current
>Calculate signal	My Potential
>Calculate signal	My Time
>Calculate signal	My Index
>Set potential (V)	0.3
>Record signals (>1 ms)	10, 0.01
>Duration (s)	10
>Interval time (s)	0.01
>Nested Procedure (Data Handling)	
>My Current (A)	<..array.. >(A)
>My Potential (V)	<..array.. >(V)
>My Time (s)	<..array.. >(s)
>My Index	<..array.. >
>Build signal	
>Export ASCII data	C://
>Filename	C://dump.txt
>Number of columns	4
>Column delimiter	Tab
>Decimal separator	.
>Column 1	My Potential (V)
>Column 2	My Current (A)
>Column 3	My Time (s)
>Column 4	My Index

10.2 Procedure used to produce MSCV from raw data

>Import ASCII data	C://dump
>Filename	C://dump
>Number of columns	4
>Column delimiter	Tab
>Decimal separator	.
>Current	<..array..>(A)
>Potential	<..array..>(V)
>Time	<..array..>(s)
>Index	<..array..>
>Counter	<..array..>
>Calculate signal	MAX(index)
>index	Counter
>Repeat n times special	200
>Number of repetitions	200
>Count	Count 1
>Nested procedure	
>Counter	0
>Calculate signal	Rep-Count
>Windower	
>Potential	Potential (V)
>Current	Current (A)
>Time	Time (s)
>Index	Index
>Counter	Counter
>Special plot	
>X	Potential (V)
>Y	Current (A)
>Z	Counter

10.3 Kinetic range of MSCV technique - full table

Table 10.1: *Workable timescales for the analysis of kinetic parameters from an MSCV, where green indicates a good fit (k^0 error < factor 2, α error < 0.1, E^0 error < 10 mV), yellow indicates a poor fit (factor 2 < k^0 error < factor 2.5, 0.1 < α error < 0.15, 10 mV < E^0 error < 15 mV) and red indicates an unsuitable fit (k^0 error > factor 2.5, α error > 0.15, E^0 error > 15 mV).*

Sampling time /s	Kinetic Parameter	k^0 cm s^{-1}							
		0.001	**0.005**	**0.01**	**0.05**	**0.1**	**0.5**	**1**	**5**
0.0001	k^0	0.18	0.10	0.10	1.16	4.47	2.75	1.87	10.00
	α	0.11	0.29	0.34	0.42	0.5	0.50	0.50	0.50
	E^0	0.05	0.04	0.04	0.01	0.00	0.01	0.01	0.01
0.0002	k^0	0.16	0.10	0.10	0.10	1.74	10.00	0.42	10.00
	α	0.12	0.22	0.25	0.38	0.46	0.50	0.50	0.50
	E^0	0.05	0.06	0.06	0.06	0.00	0.00	0.01	0.00
0.0005	k^0	0.13	0.10	0.10	0.10	0.62	1.24	1.45	10.00
	α	0.12	0.17	0.20	0.37	0.43	0.50	0.50	0.50
	E^0	0.06	0.07	0.08	0.06	0.01	0.00	0.00	0.00
0.0008	k^0	0.11	0.10	0.10	0.10	0.70	1.57	4.42	4.19
	α	0.12	0.16	0.18	0.37	0.39	0.50	0.50	0.50
	E^0	0.07	0.08	0.08	0.06	0.01	0.00	0.00	0.00
0.001	k^0	0.10	0.10	0.10	0.24	1.07	0.81	1.78	10.00
	α	0.12	0.15	0.18	0.36	0.33	0.50	0.50	0.50
	E^0	0.08	0.08	0.08	0.03	0.01	0.00	0.00	0.00
0.002	k^0	0.10	0.10	0.10	1.38	1.94	0.34	0.76	1.03
	α	0.11	0.15	0.19	0.19	0.17	0.50	0.50	0.50
	E^0	0.08	0.08	0.08	0.00	0.00	0.01	0.00	0.00
0.005	k^0	0.10	0.10	0.67	2.06	2.28	1.36	0.81	1.70
	α	0.10	0.13	0.14	0.04	0.02	0.18	0.36	0.50
	E^0	0.09	0.09	0.02	0.00	0.00	0.00	0.00	0.00
0.008	k^0	0.10	0.53	1.02	2.08	2.18	1.97	1.18	0.10
	α	0.08	0.11	0.10	0.01	0.02	0.01	0.16	0.50
	E^0	0.09	0.02	0.01	0.00	0.00	0.00	0.00	0.00
0.01	k^0	0.10	0.70	1.14	2.03	2.08	2.16	1.27	0.10
	α	0.08	0.10	0.08	0.02	0.04	0.04	0.13	0.48
	E^0	0.09	0.02	0.00	0.00	0.00	0.00	0.00	0.00

Continued on next page

Table 10.1: *continued from previous page*

Sampling time /s	**Kinetic Parameter**	k^0 **cm s^{-1}**							
		0.001	**0.005**	**0.01**	**0.05**	**0.1**	**0.5**	**1**	**5**
0.02	k^0	0.10	1.03	1.31	1.70	1.75	1.39	0.99	0.18
	α	0.06	0.05	0.03	0.04	0.05	0.01	0.10	0.50
	E^0	0.10	0.00	0.00	0.00	0.00	0.00	0.00	0.00
0.05	k^0	0.71	1.18	1.28	1.42	1.26	1.07	0.81	0.10
	α	0.03	0.01	0.00	0.04	0.03	0.00	0.10	0.46
	E^0	0.02	0.00	0.00	0.00	0.00	0.00	0.00	0.00
0.08	k^0	0.90	1.16	1.25	1.34	1.25	0.90	0.90	10.00
	α	0.02	0.01	0.01	0.05	0.06	0.10	0.03	0.08
	E^0	0.01	0.00	0.00	0.00	0.00	0.00	0.00	0.00
0.1	k^0	0.94	1.17	1.17	1.30	1.20	0.79	0.65	9.93
	α	0.02	0.00	0.01	0.05	0.05	0.00	0.10	0.50
	E^0	0.01	0.00	0.00	0.00	0.00	0.00	0.00	0.00
0.2	k^0	0.94	1.08	1.18	1.13	1.26	0.94	1.17	0.10
	α	0.02	0.00	0.02	0.04	0.08	0.08	0.13	0.45
	E^0	0.00	0.00	0.00	0.00	0.00	0.00	0.00	0.00
0.5	k^0	1.01	1.05	1.10	1.06	0.95	0.33	1.09	1.05
	α	0.01	0.00	0.02	0.01	0.01	0.32	0.02	0.50
	E^0	0.00	0.00	0.00	0.00	0.00	0.00	0.00	0.00
0.8	k^0	1.01	1.05	1.13	1.06	0.89	0.61	0.45	0.10
	α	0.01	0.01	0.02	0.03	0.01	0.11	0.24	0.50
	E^0	0.00	0.00	0.00	0.00	0.00	0.00	0.00	0.00
1	k^0	1.01	1.06	1.08	1.05	0.86	0.40	0.51	0.11
	α	0.00	0.01	0.01	0.02	0.01	0.22	0.16	0.50
	E^0	0.00	0.00	0.00	0.00	0.00	0.00	0.00	0.00

10.4 Sample cyclic voltammograms

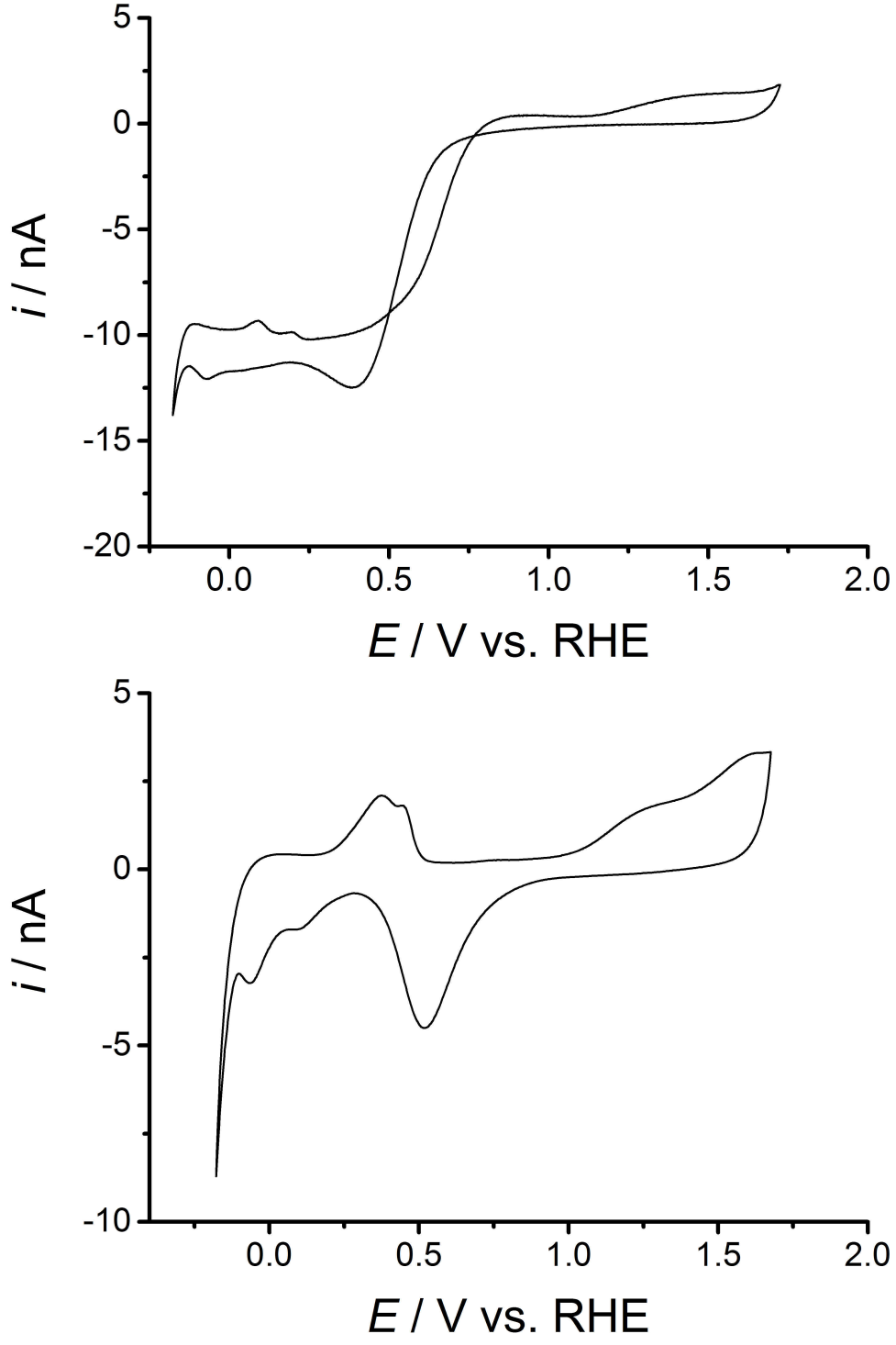

Figure 10.1: *Cyclic voltammograms of a pre-conditioned 25 μm diameter Pt microelectrode in 0.1 M $KClO_4$, ν = 200 mV s^{-1}, recorded in aerated (top) and degassed (bottom), solutions.*

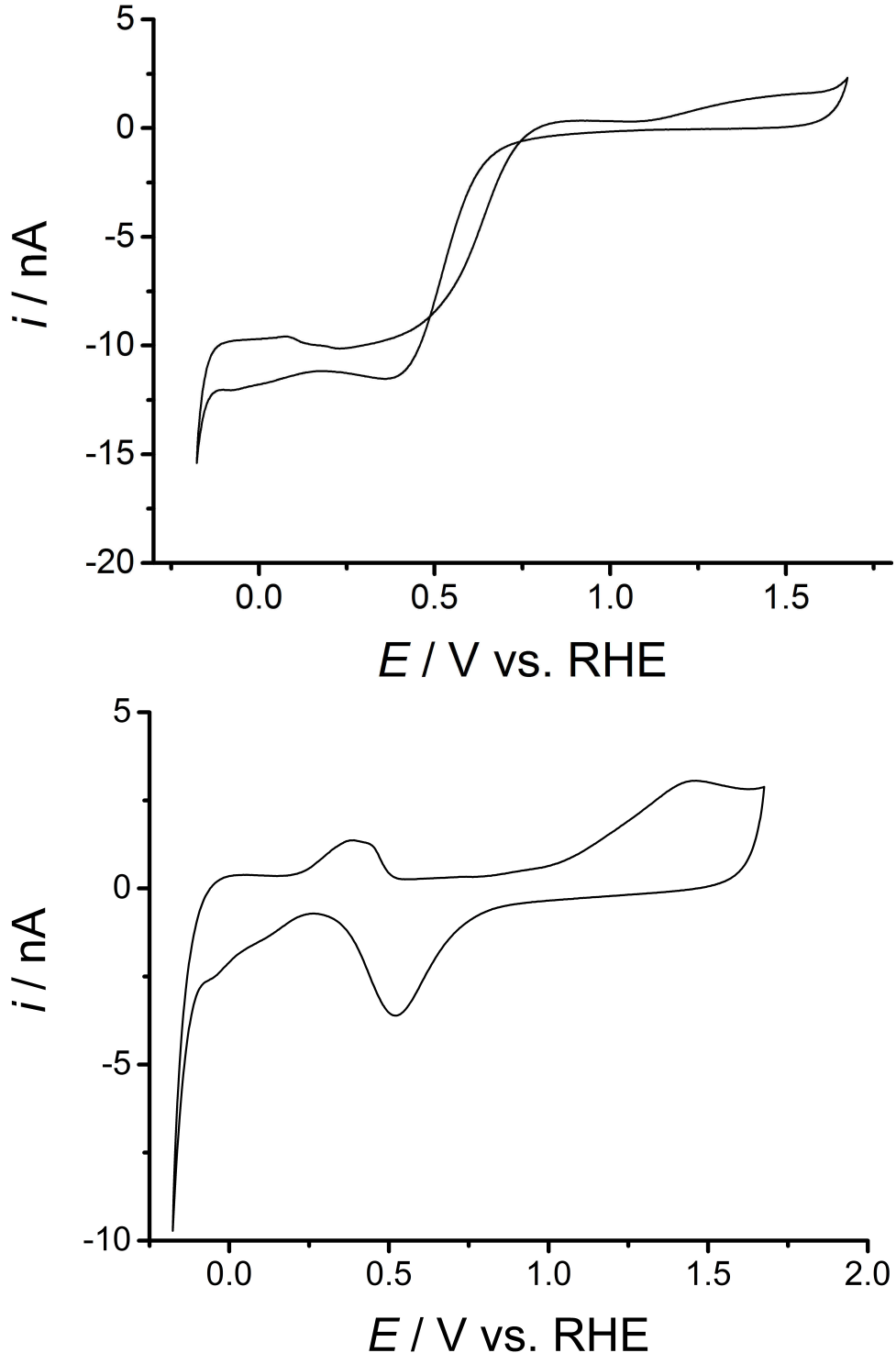

Figure 10.2: *Cyclic voltammograms of a pre-conditioned 25 μm diameter $Pt_{0.9}Ir_{0.1}$ microelectrode in 0.1 M $KClO_4$, ν = 200 mV s^{-1}, recorded in aerated (top) and degassed (bottom), solutions.*

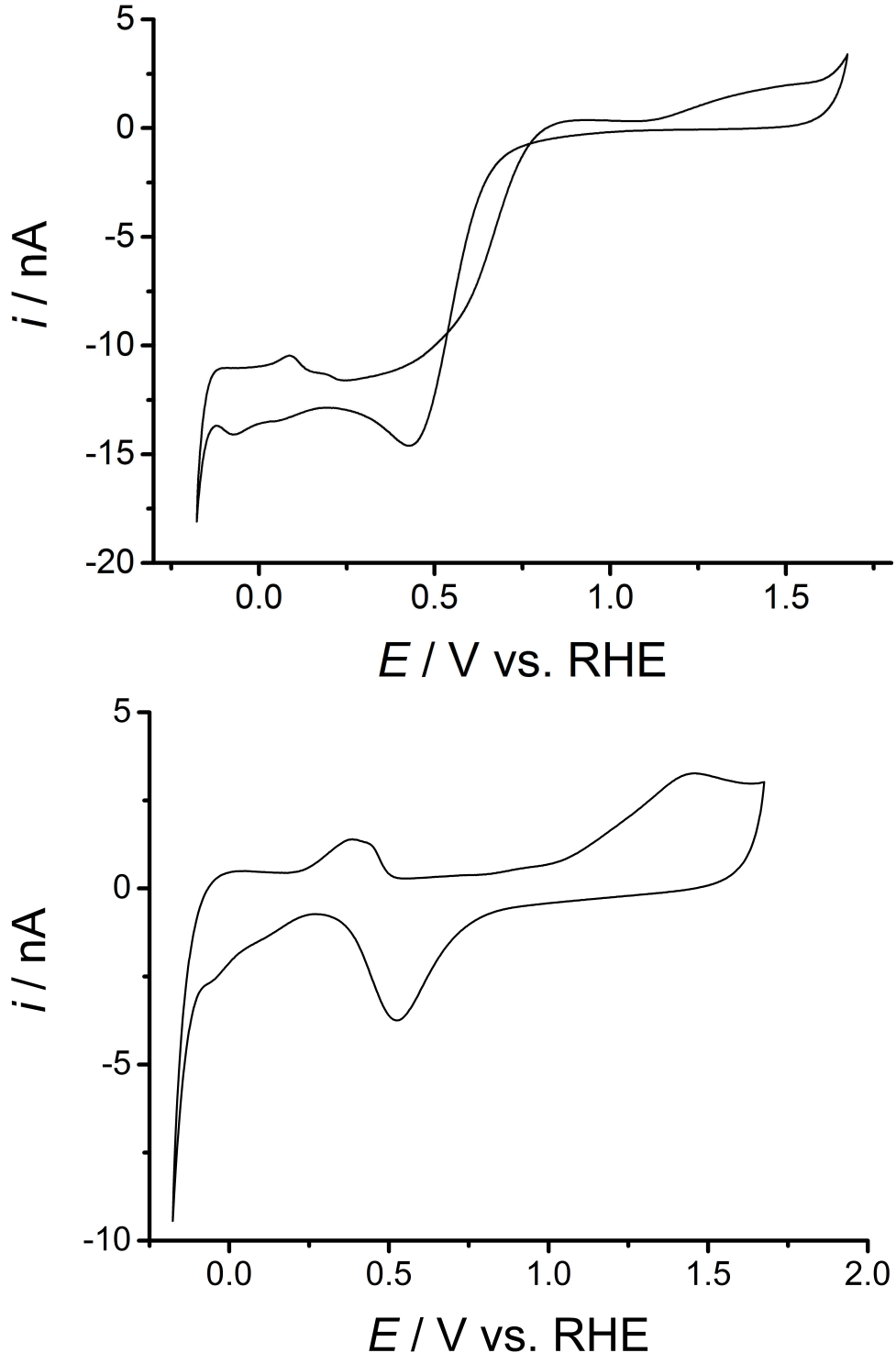

Figure 10.3: *Cyclic voltammograms of a pre-conditioned 25 μm diameter $Pt_{0.9}Rh_{0.9}$ microelectrode in 0.1 M $KClO_4$, ν = 200 mV s^{-1}, recorded in aerated (top) and degassed (bottom), solutions.*

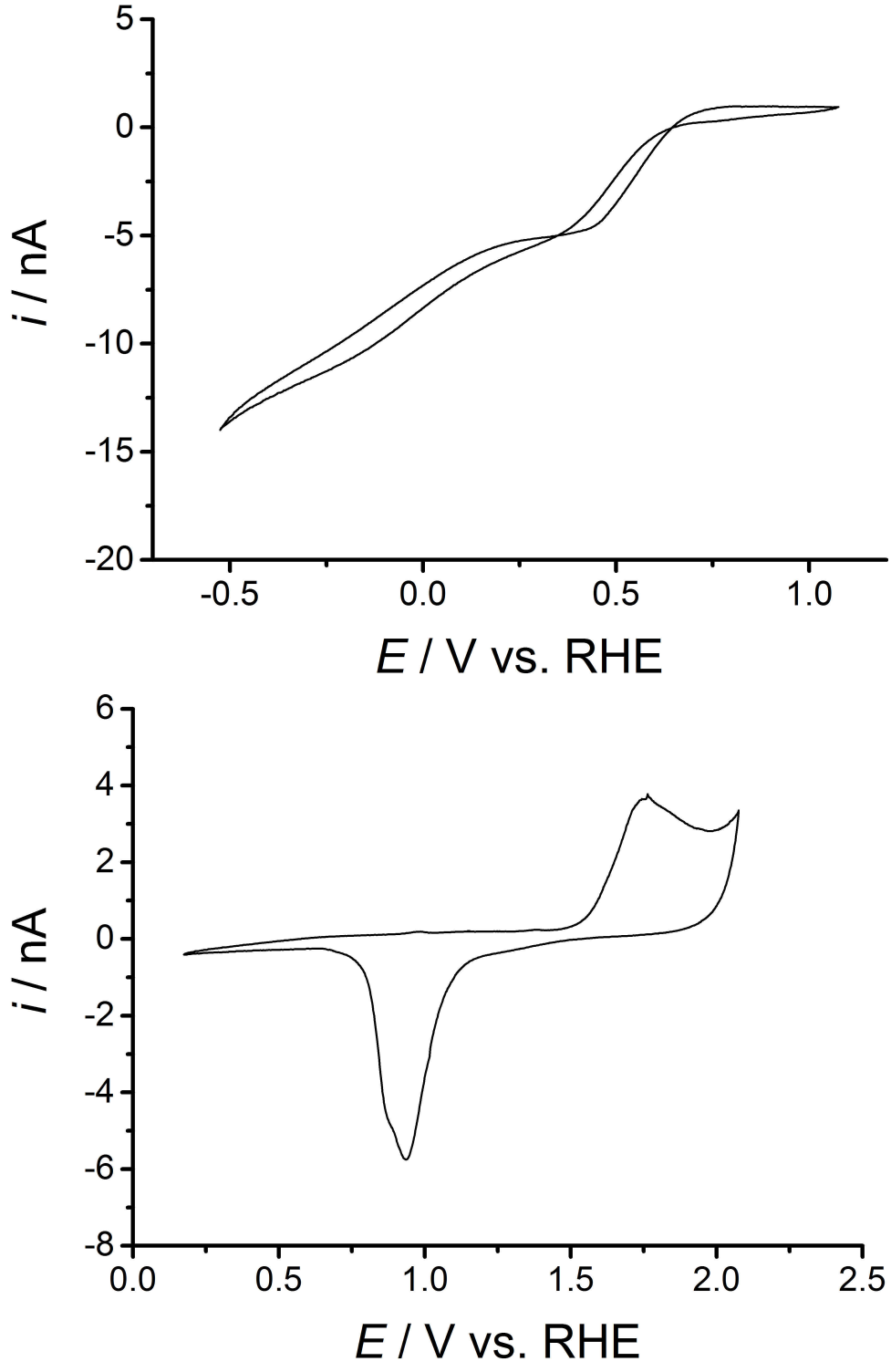

Figure 10.4: *Cyclic voltammograms of a pre-conditioned 25 μm diameter Au microelectrode in 0.1 M* $KClO_4$, ν = *200 mV* s^{-1}, *recorded in aerated (top) and degassed (bottom), solutions.*

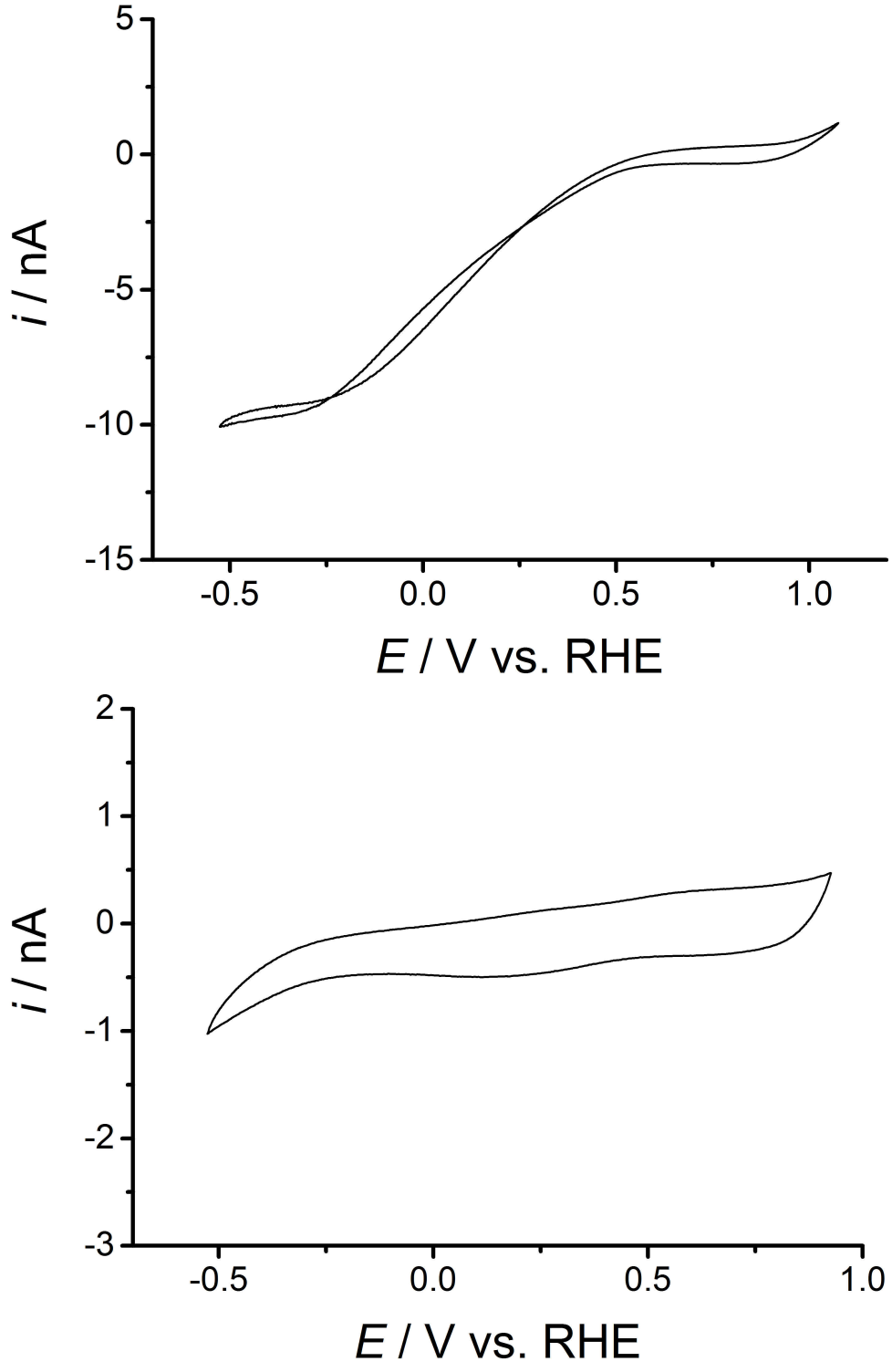

Figure 10.5: *Cyclic voltammograms of a pre-conditioned 25 μm diameter Ag microelectrode in 0.1 M* $KClO_4$, ν = *200 mV* s^{-1}, *recorded in aerated (top) and degassed (bottom), solutions.*

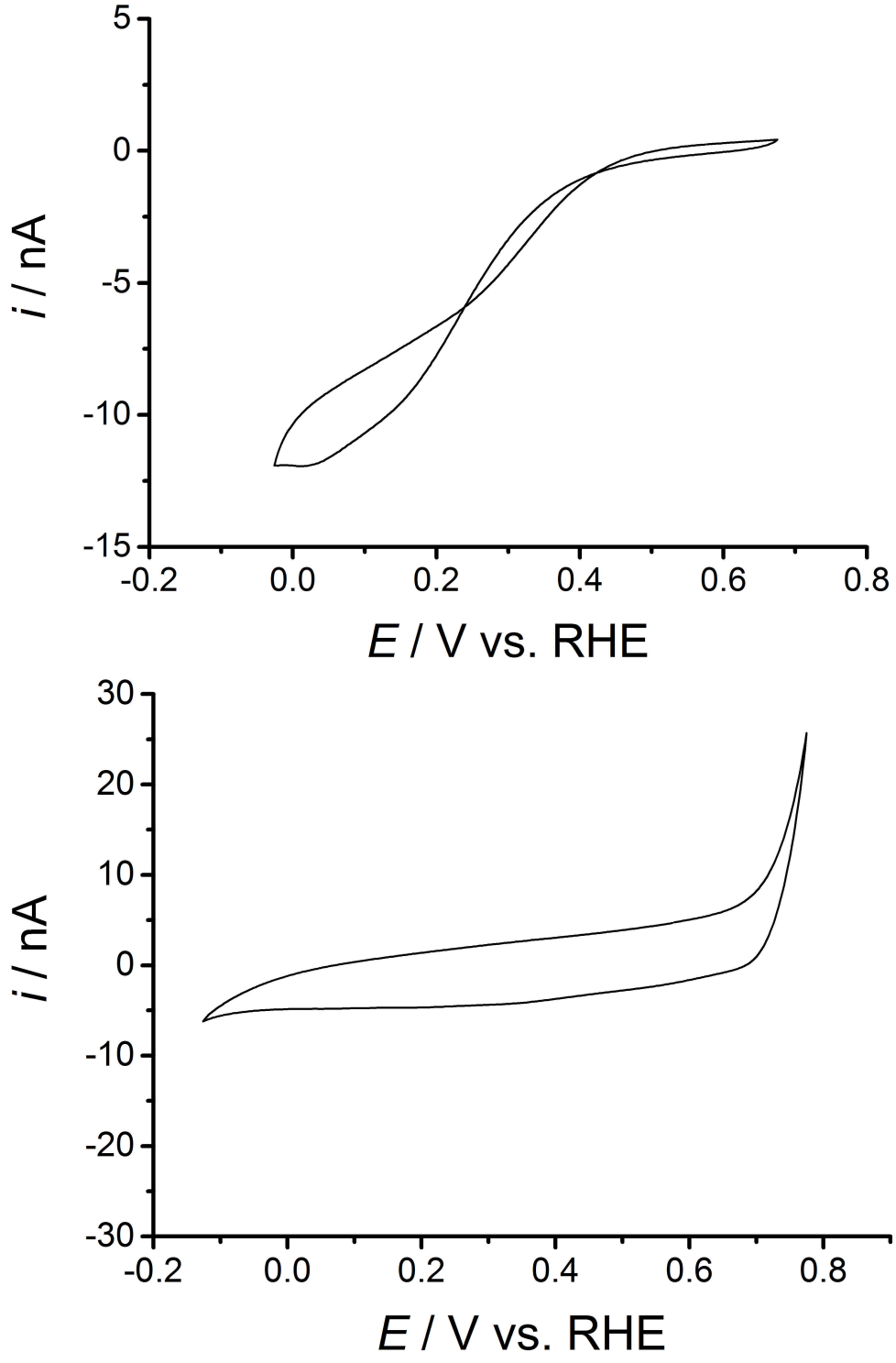

Figure 10.6: *Cyclic voltammograms of a pre-conditioned 25 μm diameter Cu microelectrode in 0.1 M* $KClO_4$, ν = *200 mV* s^{-1}, *recorded in aerated (top) and degassed (bottom), solutions.*

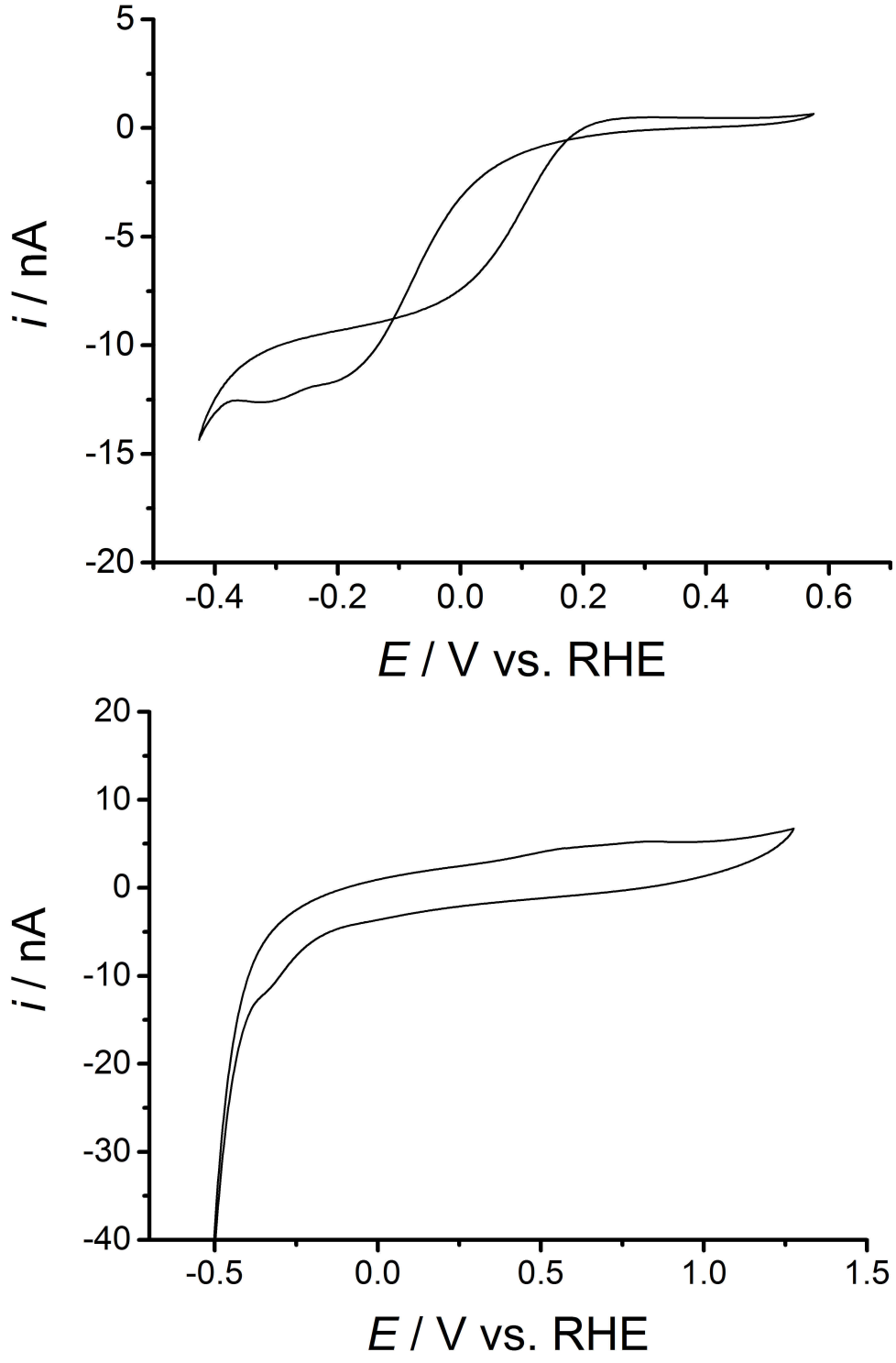

Figure 10.7: *Cyclic voltammograms of a pre-conditioned 25 μm diameter Ni microelectrode in 0.1 M $KClO_4$, ν = 200 mV s^{-1}, recorded in aerated (top) and degassed (bottom), solutions.*

10.5 Kinetics of the ferri/ferrocyanide system

Chapter 4.1 highlighted the efficiency of MSCV for the calculation of kinetic parameters of a redox system. However, as the Fe^{II}/Fe^{III} system is not particularly fast, it did not push the limits of MSCV as a method. To test the flexibility of the application of this method, a faster redox system was probed. MSCVs were therefore recorded for the ferri/ferrocyanide redox couple. As with the Fe^{II}/Fe^{III}, ferricyanide is a simple, single electron transfer with well documented kinetic parameters in the literature for comparison[118]. MSCVs were recorded for the reduction of $K_3Fe(CN)_6$ in 0.5 M KCl using a 25 µm platinum electrode.

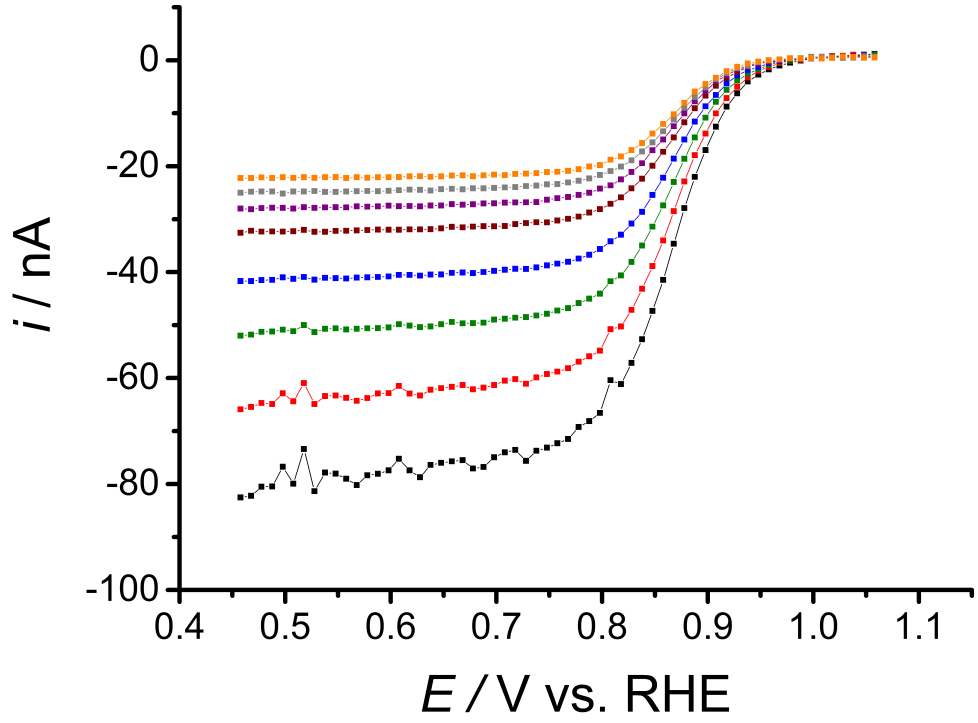

Figure 10.8: *MSCV for 5mM $K_3Fe(CN)_6$ reduction at a pre-conditioned 25 µm diameter platinum electrode in Ar purged 0.5 M $HClO_4$, sampled 2.5 ms (black), 5 ms (red), 10 ms (green), 20 ms (blue), 50 ms (brown), 100 ms (purple), 200 ms (grey), and 500 ms (orange) after the potential step.*

MSCVs were then normalised as previously described in Chapter 3.1 using Equation 1.45. The diffusion coefficient for D_O was calculated from a plot of limiting currents against microdisc radii for differently sized microelectrodes. The value for D_R was calculated assuming that $D_O/D_R = 1.11$[118]. Electrode radii were accurately measured using the

environmental mode of a SEM. All parameters used are given in Table 10.2. The resultant normalised MSCVs are shown in Figure 10.9.

Table 10.2: *Parameters used during the normalisation and subsequent kinetic analysis of MSCVs for the ferri/ferrocyanide redox couple.*

Symbol	Parameter	Value
a	Electrode radius	12.6 µm
n	Number of electrons transferred	1
D_O	Diffusion coefficient for $K_3Fe(CN)_6$	7.37 x 10^{-6} cm^2 s^{-1}
D_R	Diffusion coefficient for $K_4Fe(CN)_6$	6.62 x 10^{-6} cm^2 s^{-1}
c	Concentration of $Fe(ClO_4)_3$	5 mM
T	Temperature	298 K

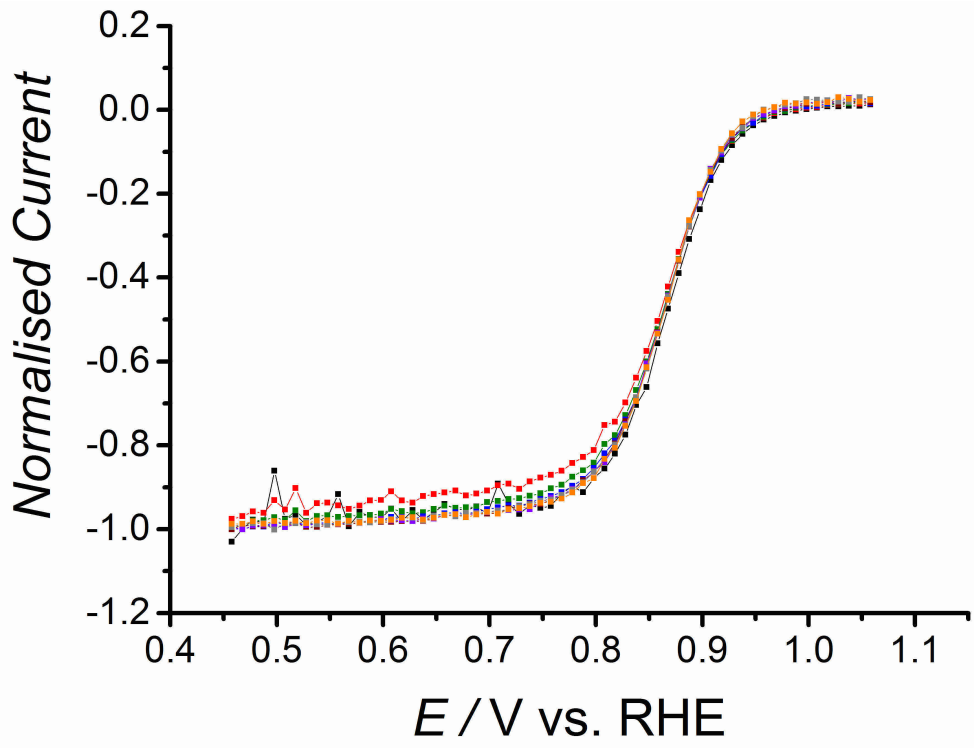

Figure 10.9: *MSCV for 5mM $K_3Fe(CN)_6$ reduction at a pre-conditioned 25 µm diameter platinum electrode in Ar purged 0.5 M $HClO_4$, sampled 2.5 ms (black), 5 ms (red), 10 ms (green), 20 ms (blue), 50 ms (brown), 100 ms (purple), 200 ms (grey), and 500 ms (orange) after the potential step, normalised using the theoretical limiting current from Equation 1.45, using the parameters listed in Table 10.2.*

As with $[Ru(NH_3)_6]^{3+}$ (Figure 3.2), at large overpotentials all MSCVs are neatly aligned and are normalised to one on the y axis. Unlike $Fe(ClO_4)_3$ (Figure 4.2), the differences

in the slopes of MSCVs at varying sampling times are too subtle to be clearly seen. This is due to the faster electron transfer seen in the ferri/ferrocyanide couple when compared to the Fe^{II}/Fe^{III} couple. Gleaning kinetic information from these MSCVs will therefore require much shorter sampling times in order to give the same quasireversible conditions.

MSCVs for $K_3Fe(CN)_6$ reduction were then used calculate values for E^0, k^0 and α by using non-linear regression to fit experimental sigmoidal curves to the model in Equation 4.2. The kinetic parameters were allowed to vary whilst all other parameters listed were fixed at those given in Table 10.2. Since kinetic parameters are independent of sampling time, multiple MSCVs were simultaneously fitted as a means of obtaining an average fit across multiple data sets. MSCVs sampled at 10, 20, 50 and 100 ms were simultaneously fitted using the global fit function of Origin 9.1. The resultant fit is shown in Figure 10.10.

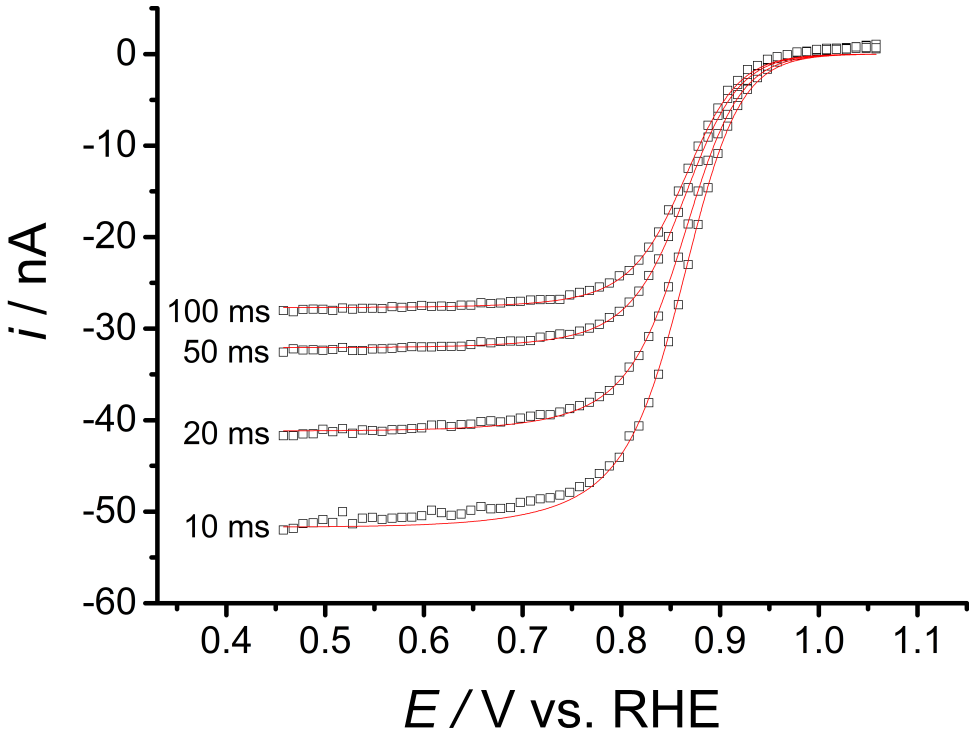

Figure 10.10: *MSCV for 5mM $K_3Fe(CN)_6$ reduction at a pre-conditioned 25 μm diameter platinum electrode in Ar purged 0.5 M KCl, sampled 10, 20, 50 and 100 ms after the potential step, showing the experimental data (□) and the fitted model (—). Theoretical curves were produced by nonlinear curve fitting to Equation 4.2 using the parameters listed in Table 10.2.*

An excellent fit was achieved after only a few iterations. The high quality of the fit (R^2 = 0.999) is clearly seen from the match between theoretical and experimental data. Application of a Gaussian distribution of weights around the slope of the wave made a negligible difference to the obtained values. The regression analysis gave E^0 = 0.88 ± 0.0006 V vs. RHE, k^0 = 0.089 ± 0.013 cm s^{-1} and α = 0.40 ± 0.03. These values are in good agreement with those quoted in the literature, where k^0 = 0.8 cm s^{-1}, 0.9 cm s^{-1} and 0.10 cm s^{-1} and α = 0.45 were previously recorded on rotating disc electrodes and by hydrodynamic voltammetry[119–121].

To further validate this fit, COMSOL Multiphysics v 4.4 was used to construct a number of theoretical MSCVs to match those generated in previous experiments. Values for D_O, D_R, c, a and τ were set to match those used in the model, and values for E^0, k^0 and α were set to match those gleaned from the previous fit. MSCVs were constructed by simulating a number of current transients using the COMSOL package for the reduction of ferricyanide to ferrocyanide. All simulation parameters were kept the same as described in the previous case for the simulation of MSCVs for the Fe^{II}/Fe^{III} couple.

With the model set up, a potential step was applied starting from a potential where no net reduction is observed to one where a significant, mass transport controlled rate of reduction is observed. For said potential step, a chronoamperogram is recorded by integrating the flux of ferricyanide to the electrode. This process is then repeated for a number of potentials at 10 mV intervals along the redox wave in question. MSCVs are the constructed as discussed in Chapter 1.3.5, by simply treating the theoretical chronoamperograms in the same way as for the experimental ones. Chronoamperograms were simulated for the reduction of ferricyanide to ferrocyanide using the parameters stated in Table 10.3. MSCVs were then constructed from data sampled 50, 100, 200 and 500 ms after the onset of the potential step. These simulated MSCVs were then compared against the corresponding experimental MSCVs from the same data set that was used to calculate the kinetic parameters. The excellent fit between the experimental and theoretical value gives good indication that the derived parameters are accurate.

Table 10.3: *Simulation parameters for the calculation of theoretical chronoamperograms for the single electron reduction of ferricyanide.*

Symbol	Value	Description
a	12.6 µm	Microdisc radius
r_g	3 mm	Radius of the glass around the electroactive area
r_{max}	20 mm	Radius of the solution domain
z_{max}	20 mm	Height of solution above the domain floor
z_{ede}	10 mm	Height of microelectrode above domain floor
T	298 K	Temperature of solution
c_R^∞	0 mM	Bulk concentration of ferrocyanide
D_R	6.32 x 10^{-6} cm^2 s^{-1}	Diffusion coefficient of ferrocyanide
c_O^∞	5 mM	Bulk concentration of ferricyanide
D_O	7.34 x 10^{-6} cm^2 s^{-1}	Diffusion coefficient of ferricyanide
E^0	0.88 V vs. RHE	Standard potential for electron transfer
k^0	0.089 cm s^{-1}	Standard rate constant for electron transfer
α	0.40	Transfer coefficient for electron transfer

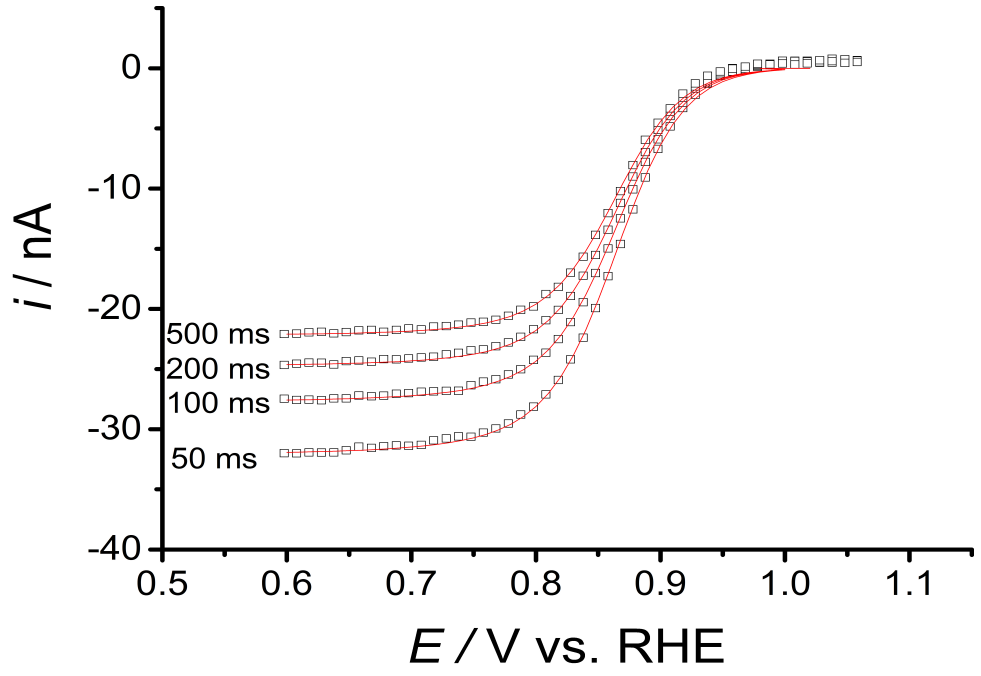

Figure 10.11: *MSCV for 5mM $K_3Fe(CN)_6$ reduction at a pre-conditioned 25 µm diameter platinum electrode in Ar purged 0.5 M KCl, sampled 50, 100, 200 and 500 ms after the potential step, showing the experimental data (□) and the theoretical data from COMSOL simulations (—), produced using the parameters given in Table 10.3.*